

# Superconductivity in Two-Dimensional Crystals

El-Bana, Mohammed

*Award date:*
2013

*Awarding institution:*
University of Bath

# Superconductivity in Two-Dimensional Crystals

Mohammed Sobhy El Sayed El Bana

A thesis submitted for the degree of Doctor of Philosophy

**University of Bath**

Department of Physics

June 2013

## COPYRIGHT

# Abstract

Since the first isolation of graphene in 2004 interest in superconductivity and the superconducting proximity effect in monolayer or few-layer crystals has grown rapidly. This thesis describes studies of both the proximity effect in single and few-layer graphene flakes, as well as the superconducting transition in few unit cell chalcogenide flakes. Optical and atomic force microscopy and Raman spectroscopy have been used to characterise the quality and number of molecular layers present in these flakes. Graphene structures with superconducting Al electrodes have been realised by micromechanical cleavage techniques on $Si/SiO_2$ substrates. Devices show good normal state transport characteristics, efficient back-gating of the longitudinal resistivity, and low contact resistances. Several trials have been made to investigate proximity-induced critical currents in devices with junction lengths in the range 250-750 nm. Unfortunately, no sign of proximity supercurrents was observed in any of these devices. Nevertheless the same devices have been used to carefully characterise proximity doping, (due to the deposited electrode), and weak localisation/anti-localisation contributions to the conductivity in them. In addition this work has been extended to investigations of the superconducting transition in few unit-cell dichalcogenide flakes. Four-terminal devices have been realised by micromechanical cleavage from a 2H-$NbSe_2$ single crystal onto $Si/SiO_2$ substrates followed by the deposition of Cr/Au contacts. While very thin $NbSe_2$ flakes do not appear to conduct, slightly thicker flakes are superconducting with an onset $T_c$ that is only slightly depressed from the bulk value (7.2K). The resistance typically shows a small, sharp, high temperature transition followed by one or more broader transitions, which end in a wide tail to zero resistance at low temperatures. These multiple transitions appear to be related to disorder in the layer stacking rather than lateral inhomogeneity. The behaviour of several flakes has been characterised as a function of temperature, applied field and back-gate voltage. The resistance and transition temperatures are found to depend weakly on the gate voltage. Results have been analysed in terms of available theories for these phenomena.

# Acknowledgment

I am truly grateful to numerous people who have helped and encouraged me for my doctoral study at the University of Bath.

I would particularly like to express my deepest gratitude to my supervisor Prof. Dr. Simon Bending for his sincere supervision and precious remarks regarding this research.

I acknowledge the financial support I received from the Egyptian government and Ain Shams University as well as the EPSRC in the UK under grant no. EP/G036101/1.

I am indebted to many colleagues that I have met during my study at the University of Bath. A great deal of help was provided by the technicians; in particular I would like to thank Dr. Spartaco Landi, Wendy Lambson, Bob Draper, Paul Reddish, Dr. Sivapathasundaram Sivaraya and Dr. Stephen Wedge for their generous help with my research.

In addition, my deepest thanks go to all members of the Physics Department, especially our group members for their many insightful discussions (Dr. Andy Moskalenko, Dr. Sara E. C. Dale, Dr. Miles A. Engbarth, Dr. Ke Wang, Dr. Peter Curran, Dr. Waled Desoky, Hussen Mohammed and Murali). Further, I would like to thank Dr. Sam Littlejohn who provided invaluable help when writing my LabVIEW programs.

I also have to thank Wendy Lambson, Dr. Peter Curran and Max Harris for proof reading this work.

Finally, my deepest gratitude goes to my family for their wholehearted encouragement and constant support. My parents and my sisters have been supporting me so patiently through all of my life. As to my wife, her support, encouragement, quiet patience and unwavering love have undeniably formed the bedrock upon which the past eight years of my life have been built. Last but certainly not least, there are my kids (Fatma and Ahmed) who provide the greatest reason for living and working hard.

# Common Symbols

| | |
|---|---|
| $E_F$ | Fermi Energy |
| $k_F$ | Fermi Wavelength |
| $n$ | Carrier Concentration |
| $e$ | The Electronic Charge |
| $R_{xx}$ | Longitudinal Resistance |
| $\sigma$ | Conductivity |
| $\mu$ | Carrier Mobility |
| $D$ | Diffusion Constant |
| $V_g$ | Gate Voltage |
| $V_{DP}$ | Dirac Point Gate Voltage |
| $\varepsilon_r$ | The Relative Permittivity |
| $\varepsilon_0$ | The Permittivity of Free Space |
| $T$ | Temperature |
| $T_c$ | Critical Temperature |
| $B$ | Applied Magnetic Field $(\mu_0 H)$ |
| $M$ | The Magnetisation |
| $H_c$ | The Critical Magnetic Field |
| $\lambda_L$ | Magnetic Field Penetration Depth |
| $\xi$ | Coherence Length |
| $\Delta$ | Superconducting Gap |
| $n_{SF,2D}$ | The Two Dimensional Superfluid Density |
| $T_{BKT}$ | The BKT Transition Temperature |
| $I_c$ | Critical Current |
| $V_H$ | Hall Voltage |

| | |
|---|---|
| $\boldsymbol{d}$ | Flake Thickness |
| $\boldsymbol{L_{\varphi}}$ | Phase Coherence Length |
| $\boldsymbol{\tau_{\varphi}^{-1}}$ | The Phase-Breaking Rate |
| $\boldsymbol{\tau_{i}^{-1}}$ | The Inter-Valley Scattering Rate |
| $\boldsymbol{\tau_{*}^{-1}}$ | The Intra-Valley Scattering Rate |
| $\boldsymbol{G}$ | Conductance |
| $\boldsymbol{H_P}$ | Penetration Field |
| $\boldsymbol{R_{squ}}$ | Room Temperature Sheet Resistance |
| $\boldsymbol{\rho_{Bulk}}$ | Bulk Resistivity |
| $\boldsymbol{RRR}$ | Reduced Resistance Ratio |
| $\boldsymbol{H_{c2}(0)}$ | Zero-Temperature Upper Critical Field |
| $\boldsymbol{\xi(0)}$ | Zero-Temperature Ginzburg-Landau Coherence Length |

# Contents

# List of Figures

# List of tables

# Chapter 1

# Introduction

## 1.1 Motivation

The ultimate goal of this project is to investigate two-dimensional superconducting crystals in common layered materials such as $NbSe_2$ using the same micromechanical cleavage and device preparation techniques developed for graphene. In order to develop the key technological steps for these studies, initial work is focussed on reproducing earlier research on the superconducting proximity effect in few-layer graphene flakes. The isolation of graphene (single layer graphite) in 2004 demonstrated for the first time that truly two-dimensional crystals can be stable on $Si/SiO_2$ substrates and as free-standing membranes, opening up the possibility of new and exciting physics in a new class of materials. It was subsequently exhibited that single layer graphene can carry significant proximity supercurrents, even when the Fermi energy is at the Dirac point, and there are theoretically no free carriers. Fabrication of graphene Josephson junctions enables us to study the rare intersection of relativity and superconductivity. The initial work has been expanded on within this project and extended to investigate two-dimensional superconducting crystals of the layered chalcogenide $NbSe_2$. Building on the knowledge gained in this work on graphene, new techniques for the mechanical exfoliation of few-layer $NbSe_2$ flakes have been developed which give a large number of bigger "thin and few unit-cell" flakes. This new mechanical exfoliation protocol enabled fabrication and measurement of superconductivity in several 4-point $NbSe_2$ devices.

The main motivation for the thesis has been to overcome the challenges of fabricating field effect transistor (FET) devices for both graphene and $NbSe_2$ flakes. These challenges relate to the difficulties of establishing reliable fabrication processes for making low resistance Ohmic contacts to these flakes, as well as developing reliable measurement protocols to prevent completed devices from being

damaged by static shock. A great deal has been done to overcome these obstacles and very interesting original data have been collected.

## 1.2 Thesis Overview

In the light of the above, chapter two gives an overview of the theory of graphene and $NbSe_2$ including their crystalline and electronic properties. In addition, an introduction to field effect structures will be provided.

Chapter three covers the theoretical background of superconductivity, its basic theories and a brief description of the Josephson effect. A review of prior work on superconductivity in graphene and few-unit cell $NbSe_2$ is also presented.

Chapter four discusses the various fabrication techniques which were established for producing and characterising FET devices for both graphene and $NbSe_2$ flakes. Also, a brief summary of the way that Hall probes can be used to characterise the magnetic properties of $NbSe_2$ flakes is described.

The next two chapters (chapters five and six) detail the results that have been obtained for graphene and $NbSe_2$ devices respectively.

Finally, conclusions drawn from results that have been presented in the previous two chapters are indicated in chapter seven along with suggestions for future work.

# Chapter 2

# Two – Dimensional Crystals

## 2.1 Introduction to the structure and properties of Graphene

### 2.1.1 The isolation of graphene

The isolation of graphene as a true two-dimensional material (2D) opened the way for investigation of a new class of materials in low dimensional physics. Graphene was isolated for the first time in 2004 by Andre Geim's team from the University of Manchester [1]. It has become a hot topic in both the materials science and condensed matter physics communities. The importance of graphene arises from its physical properties as it exhibits excellent crystalline uniformity and transport properties which make it a promising material for future nanoelectronic devices and spintronics. Other unique properties (mechanical, thermal) mean it could have a wide array of other practical uses.

### 2.1.2 What is graphene?

Graphene's name came from Graphite + ENE and it acquired this name as it is considered to be the basic building unit of graphite. Graphite consists of multi layers of graphene sheets. A graphene sheet is a one-atom thick layer of $sp^2$ bonded carbon atoms. The C-C bond length in graphene is about 0.142 nm. Graphene sheets consist of hexagonal rings that are similar to benzene rings, and graphene has a honeycomb lattice made out of hexagons as shown in Fig. 2-1.

Graphene is considered to be the building block for all graphitic forms and is the building unit in three of the four basic allotropes of the carbon atom (Nanotubes, Buckyballs and Graphite).

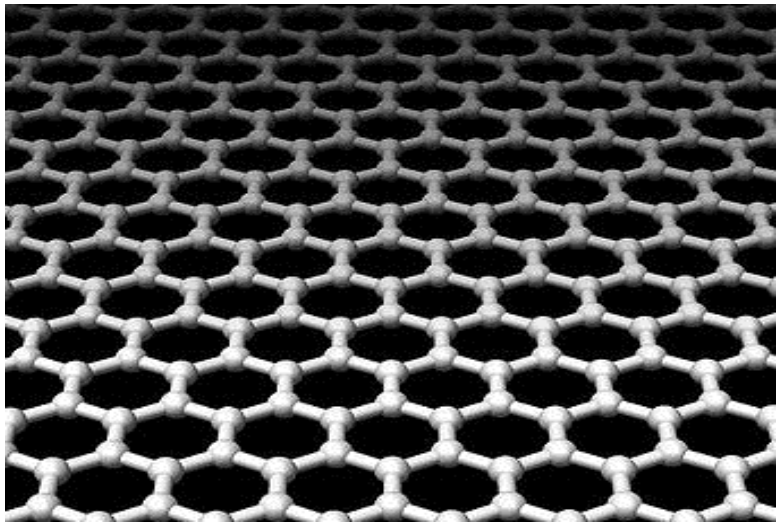

**Figure 2-1:** Carbon atoms arranged in hexagonal rings forming a honeycomb sheet of graphene. Image is in the public domain.

Although four different allotropes can be formed from carbon, they can have very different properties. In Diamond, which is a hard material, the $sp^3$ bonding (often induced under extreme pressure and temperature) is what causes its different properties and makes diamond an electrical insulator. Rolling single graphene sheets forms carbon nanotubes. Nanotubes can exhibit metallic or semiconducting characteristics according to the rolling direction of the graphene sheet. Carbon nanotubes are a one dimensional material (1D) and their conductivity depends on their structure.

Fullerenes were discovered in 1986 by Smalley, Kroto and Curl. Fullerenes have a caged structure which can be obtained by modifying the hexagonal structure of graphene into pentagons and heptagons. Fullerenes are zero dimensional materials (0D). Finally, graphite is obtained from stacking graphene sheets which are $sp^2 + p_z$ bonded. The layers are stabilized by van der Waals interactions. These four allotropes of the carbon atom are represented in the following Fig. 2-2.

To summarize graphene properties, we can say that graphene is considered to be a 2-dimensional hexagonal lattice of $sp^2$ hybridized carbon atoms, the basis for C-60 (Bucky balls), nanotubes, and graphite, and contains bonds which are among the strongest found in nature [2, 3].

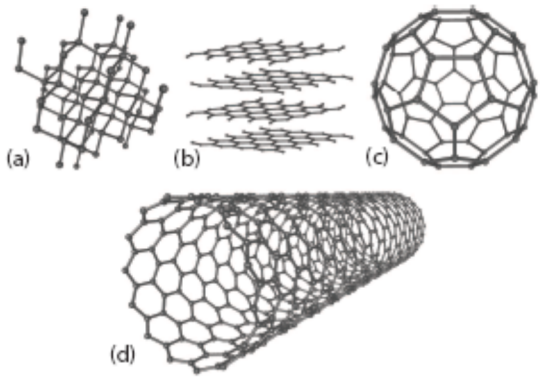


**Figure 2-2:** Carbon forms the following four allotropes [a) Diamond (3D), b) Graphite (2D), c) Fullerenes (OD), and d) Nanotubes (1D)] [2].

### 2.1.3 Graphene structure

Graphene is made up of a hexagonal carbon network in which three adjacent carbon atoms can form strong covalent bonds easily, in a process called $sp^2$ hybridization. Figure 2-3 explains the $sp^2$ hybridization mechanism. In $sp^2$ hybridization one 2s atomic orbital hybridizes with two 2p atomic orbitals yielding three hybridized $sp^2$ orbitals.

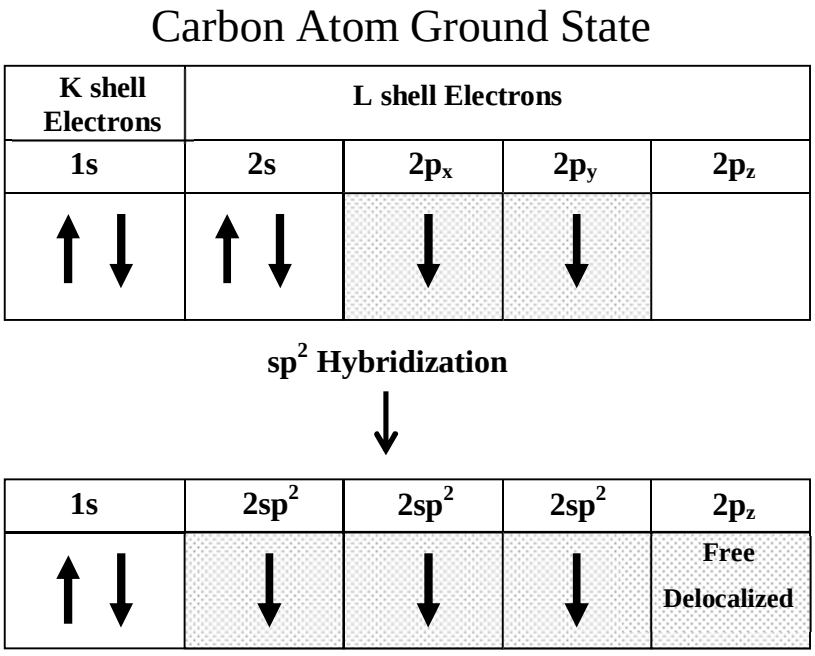


**Figure 2-3:** The $sp^2$ hybridization mechanism [4].

At the same time a free delocalized (unhybridized) p electron orbital is obtained. The $sp^2$ hybridization has a valence state of four (V4).

The angle between three identical $sp^2$ orbitals is 120 degrees and all of them are in the same plane. The orientation of the $sp^2$ structure is shown in Fig. 2-4. The unhybridized p orbital is responsible for forming the pi ($\pi$) bond with other atoms, and this fourth orbital is perpendicular to the plane of the three $sp^2$ orbitals [4].

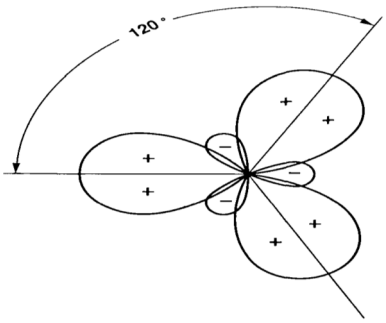


**Figure 2-4:** The orientation of $sp^2$ orbitals in space [4].

As a result of the small size of the atom and the three $sp^2$ valence electrons, the covalent $sp^2$ bond is a strong one. The $sp^2$ bond is stronger than the $sp^3$ bond as it is shorter and has higher bond energy. The $sp^2$ orbital is a $\sigma$ orbital like the $sp^3$ orbital and the bond is called a $\sigma$ bond. A three dimensional schematic of the graphite structure is shown in Fig. 2-5.

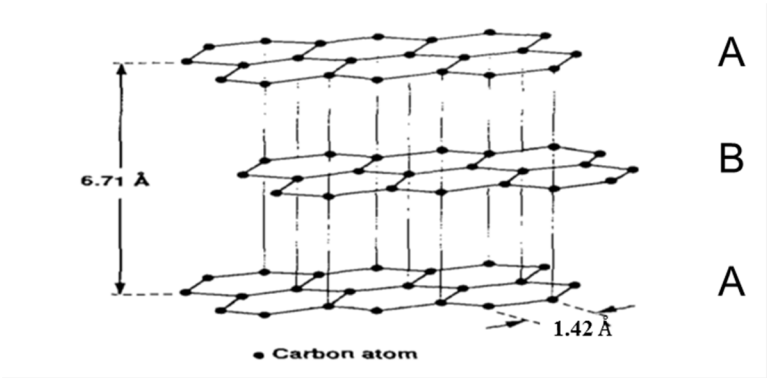


**Figure 2-5:** Schematic diagram of the graphite crystal structure [4].

In this sketch each $sp^2$ hybridized carbon atom makes three bonds with other $sp^2$ hybridized atoms forming an array of hexagonal rings. These hexagonal structure layers are stacked in planes parallel to each other. The unhybridized ($p_z$-orbital) that forms a subsidiary pi ($\pi$) bond contains delocalised electrons that cannot move from one plane to another but can move within the plane, and this leads to the anisotropic properties of graphite. Figure 2-6 shows both sigma bonds and the $2p_z$ free electrons of the $sp^2$ hybridized structure of graphite [4].

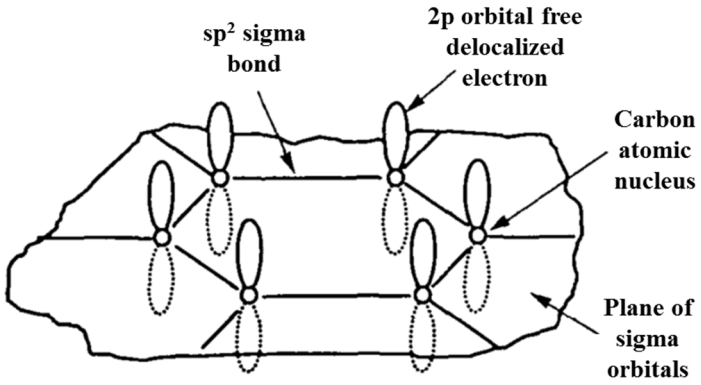


**Figure 2-6:** Schematic diagram of graphite structure [4].

Single layer graphene (1LG) has a unit cell containing two atoms A and B as presented in Fig. 2-7 (a), each forming a triangular 2D network. AB stacking (Bernal stacking) of two layers forms the bilayer graphene structure (2LG). Four carbon atoms $A_1$, $A_2$, $B_1$ and $B_2$ form the (2LG) unit cell. Atoms $A_1$, $A_2$, for instance, will overlap whilst $B_1$ and $B_2$ will be placed in the vacant centres of the hexagons of the other layer respectively as shown in Fig. 2-7 (b). One of the interesting features of 1LG is that its electronic structure reveals massless Dirac fermions with linear dispersion, $E \propto p$, where $p$ is the momentum and $E$ is the kinetic energy (cf., Fig. 2-7 (c)), while massive Dirac fermions with quadratic dispersion, $E \propto p^2$, are revealed by the electronic structure of 2LG, as shown in Fig. 2-7 (d) [5]. In trilayer graphene (3LG), two different possibilities can exist according to the way the third layer is added. Firstly the Bernal ABA stacking, in which two AB layers act as bilayer graphene and the third AB layer mirrors the first layer. Secondly, the other possibility is the rhombohedral or ABC stacking [5, 6]. This structure possesses inversion symmetry, in which the third layer is displaced with respect to the second layer, similar to the case of the second layer with respect to the first one. 3LG with either ABA or ABC stacking is presented in Figs. 2-7 (e) and 2-7 (f). The electronic structure of ABA trilayer graphene presents an overlap between 1LG linear dispersion and the quadratic dispersion of 2LG as can be seen in Fig. 2-7 (g), whereas, a cubic dispersion, $E \propto p^3$, represents the electronic structure of ABC trilayer graphene (cf., Fig. 2-7 (h)) [5]. Another stacking of two bilayer unit cells presents the structure of four layer graphene (4LG). To acquire more layers, another AB stacking is required each time. Furthermore, the 3D graphite structure is obtained

by stacking of graphene layers. A sketch of multilayer graphene is represented in Fig 2-7 (i), where two scenarios of replication of the ABA or ABC stacking case can occur [7-9].

Schematic band structures of 1LG, 2LG, and 3LG graphene are illustrated in Figs 2-7 (c), 2-7 (d) and 2-7 (g) and 2-7 (h), respectively. These graphs show the band structure with, and without an applied perpendicular electric field. Solid lines refer to data with an applied field, whilst the dotted lines are data without the field. In addition, there is no effect of the electric field on the band structure of 1LG [10]. Also, in the case of 2LG applying an electric field opens up a band gap and a suppression of the density of states at $E_F$ occurs [11]. Furthermore, applying a perpendicular electric field to 3LG has two scenarios. 3LG with ABA stacking exhibits a tuneable band overlap, whilst 3-LG with ABC stacking exhibits a tuneable band gap [12].

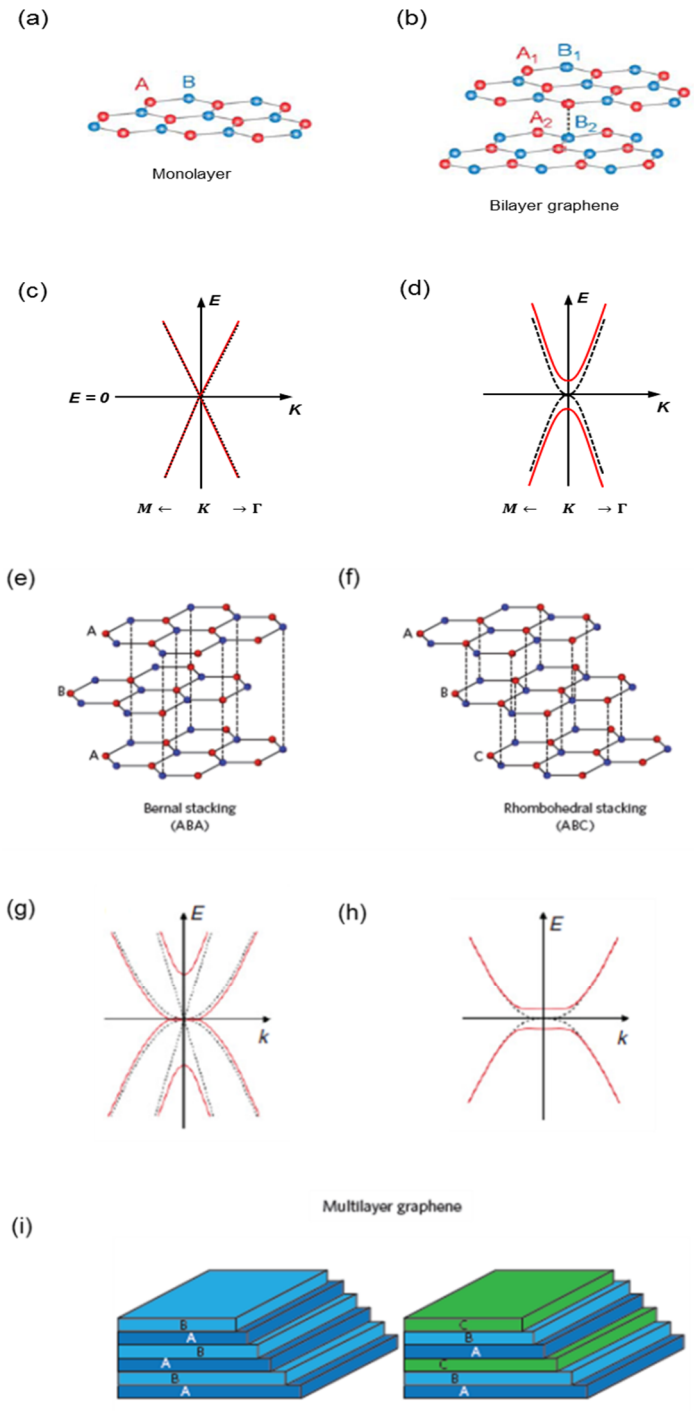


**Figure 2-7:** Top view of the crystal structure for a) monolayer graphene, b) bilayer. e, f) Trilayer and i) multilayer graphene. The effect of an applied perpendicular electric field on these graphene layers is shown by solid lines in c) 1LG, d) 2LG g, h) 3LG graphene, whereas the dotted lines in these sketches refer to the absence of an electric field [5, 10, 12].

### 2.1.4 Graphene Band Structure

Graphene is a one atom thick layer of graphite and it is considered to be a 2D material. The separation between parallel layers of graphene in graphite is 3.35 Å and this separation distance is much larger than the spacing between atoms in the same plane which is 1.42 Å.

As a result of these two spacing values, the interaction between atoms in the same plane is much stronger than that between atoms in different layers. Figure 2-8 illustrates the form of the unit cell of graphene that has two atomic sublattices called A and B and describes the Brillouin zone referring to the high symmetry points Γ, K and M.

The real space unit vectors $\overrightarrow{a_1}$ & $\overrightarrow{a_2}$ of the hexagonal lattice in the x, y plane and the displacement vector d between the sublattices A and B have the following values,

$$\overrightarrow{a_1} = \left(\frac{\sqrt{3}}{2}a, \frac{a}{2}\right), \overrightarrow{a_2} = \left(\frac{\sqrt{3}}{2}a, -\frac{a}{2}\right), \& \; d = \left(\frac{a\sqrt{3}}{2}, 0\right), \tag{2-1}$$

where $a$ is the lattice constant and has the following value,

$a = |\overrightarrow{a_1}| = |\overrightarrow{a_2}| = 1.42 \times \sqrt{3} = 2.46$ Å.

Figure 2-8 (b) illustrates the graphene lattice showing the first Brillouin zone and high symmetry points of 2D graphene. Dotted lines in Fig. 2-8 (b) represent the path along which the energy is calculated. The three high symmetry points Γ, K & M have the following definitions; Γ is the zone centre, K is the zone corner and M is the centre of the edge of the first Brillouin zone as introduced in Fig. 2-8 (b) [13].

**(a) π Energy Bands of Graphene**

Carbon atoms in graphene have $sp^2$ hybridization so have 4 orbital shells, three of them are $\sigma$ orbitals that lie in the plane and the fourth orbital is the π orbital which lies perpendicular to the plane. The π orbital is responsible for the most important electronic transport properties of graphene [13].

The first tight-binding calculation for graphite confirmed that graphene is a zero band gap semiconductor [14]. In this calculation the value of the π energy bands $(E_{\pm})$ can be obtained from the following equation,

$$E_{\pm}(k) = \frac{\varepsilon_{2p} \pm t\sqrt{1+4\cos\left(\sqrt{3}ak_y/2\right)cos(ak_x/2)+4cos^2(ak_x/2)}}{1\pm s\sqrt{1+4\cos\left(\sqrt{3}ak_y/2\right)cos(ak_x/2)+4cos^2(ak_x/2)}} \quad (2\text{-}2)$$

where the positive and negative signs refer to the bonding and anti-bonding orbitals respectively, $a$ is the lattice constant $k_x$ & $k_y$ are the wave-vectors, $t$ is the transfer integral which determines the probability for an electron to jump from one sublattice to the other and is usually taken as a constant value, $\varepsilon_{2p}$ is the energy of the orbital and $s$ is the overlap integral.

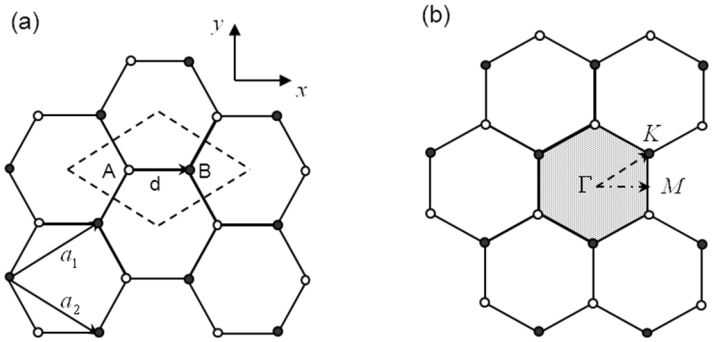


**Figure 2-8:** a) Diagram showing the real space unit vectors $\overrightarrow{a_1}$ & $\overrightarrow{a_2}$ in the hexagonal rings of graphene. b) The three high symmetry points Γ, K and M are represented in the first Brillouin zone.

Figure 2-9 displays the π energy bands of two-dimensional graphene that were obtained using the following parameters $\varepsilon_{2p}$ = 0, $t$ = -3.033 eV and $s$ = 0.129 in equation 2-2. We see that the two π bands meet only at the K points where the Fermi energy sits. The two π bands consist of the upper ($\pi^*$ anti-bonding band) and the lower ($\pi$- bonding band).

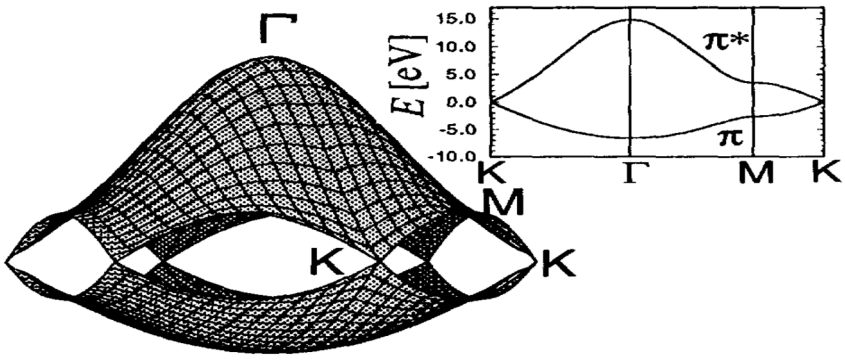


**Figure 2-9:** The π bands of 2D graphene [13].

The lower π band is fully occupied by the two π electrons of the unit cell. An important feature is observed in Fig. 2-9 where $\pi^*$ and π bands are separated by a finite gap except at the K points. This feature is responsible for many of the interesting properties of graphene as it ensures that the density of states at the Fermi level (K points) is zero.

**(b) σ Energy Bands of Graphene**

The $\sigma$ bands as well as the π bands are represented in Fig. 2-10, in which there are six $\sigma$ bands and two π bands in the two atom unit cell. Three of the six $\sigma$ bands are bonding $\sigma$ bands and appear below the Fermi energy while the other three $\sigma$ bands that lie above the Fermi level are anti-bonding $\sigma$ bands.

A large gap between $\sigma$ and π bands is found around the K points; at the same time, the $\sigma$ bands lie very far from the Fermi level. These two observations provide another proof of the role of that the π bands in graphene play in determining both its phenomena and electronic properties [13].

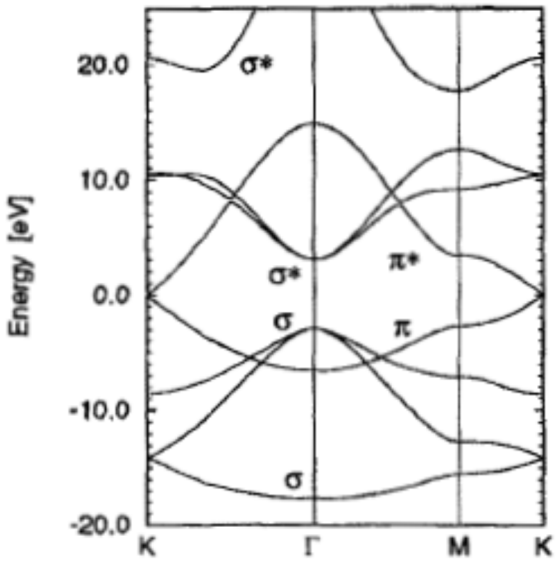


**Figure 2-10:** $\sigma$ and $\pi$ bands of 2D graphite [13].

## 2.1.5 Linear dispersion relation

Graphene is considered to be a semi-metal or zero gap semiconductor. The charges in it, including both electrons and holes near to the six corners of the 2D hexagonal Brillouin zone, behave like relativistic massless particles. The reason for

this behaviour lies in the linearity of the dispersion relation (E-k) for low energies close to these points, and because both electrons and holes follow the Dirac equation. The Dirac equation for spin ½ particles is used to explain the behaviour of the relativistic particles. The six $k$ points are known as Dirac points, and the electrons and holes they describe are called Dirac fermions [15]. The relation between E & k has the following form,

$$E = \pm \hbar v_F \left|\vec{k}\right| \tag{2-3}$$

where the ± sign relates to the conduction and valence band respectively. A constant carrier group velocity $v_g = \left|\frac{\partial E}{\hbar \partial \vec{k}}\right| = v_F$, is indicated by the linear dispersion relation, where $v_F \simeq 10^6\ \mathrm{ms}^{-1}$ is the Fermi velocity [16]. Graphite is a semi-metal in which the conduction and valence bands slightly overlap. Decreasing the number of graphene layers initiates a change in the dispersion relation; the overlap between conduction and valence bands becomes smaller and smaller and vanishes completely for single layer graphene [7]. Therefore, the relativistic behaviour is only present in monolayer graphene and it disappears with two or more layers.

### 2.1.6 Physics of 2D conductors

At zero temperature (T = 0), the induced carrier concentration as a function of the Fermi energy is given by,

$$n = \int_0^{E_F} g(E) dE, \tag{2-4}$$

where, $E_F$ is the energy of Fermi level and $g(E)$ is the two-dimensional (2D) density of states for graphene. From the linear dispersion relation, the graphene density of states $g(E)$ can be evaluated to be,

$$g(E) = \frac{1}{S}\frac{dN}{dE}\frac{g_v g_s}{2\pi\hbar^2 v_F^2} E, \tag{2-5}$$

where S is the area of the sample, N is the number of states and $g_v, g_s$ are the two-fold valley and spin degeneracies respectively $(g_v = g_s = 2)$ [17]. Therefore, similar to the case of the two-dimensional electron gas (2DEG) in [18],

$$k_F^2 = \frac{4\pi n}{g_v g_s}. \tag{2-6}$$

Substituting $g_v = 2$ and $g_s = 2$, then,

$$k_F = \sqrt{\pi n}\,, \tag{2-7}$$

where $k_F$ is the Fermi wavelength.

The longitudinal resistivity in a 2DEG is defined as,

$$\rho_{xx}^{2D} = R_{xx}^{2D}\,\frac{W}{L}\,, \tag{2-8}$$

where $L$ is the length of the device, and W is the width of the device.

The standard Boltzmann transport equation [19] is used to describe diffusive transport in most graphene samples in regimes far from the electroneutrality region. In zero magnetic field the 2D electrical conductivity, $\sigma_{xx}$ , can be determined experimentally from the inverse of the resistivity, $\sigma_{xx} = \frac{1}{\rho_{xx}}$. The 2D electrical conductivity is a measure of how easily charge carriers can move in a system and it relies on two material parameters that appear in the Drude formula,

$$\sigma = n\,e\,\mu\,, \tag{2-9}$$

where μ is the mobility and is a measure of how easily each charge carrier can move in response to an electric field in the system.

$$\mu = \frac{e\,v_F^2}{E}\,\tau\,, \tag{2-10}$$

where $\tau$ is the momentum relaxation time and $v_F$ is the Fermi velocity ($\simeq 10^6$ m/s in graphene).

By combining equations 2-3 and 2-10, the momentum relaxation time can be obtained as,

$$\tau = \frac{\hbar k_F \mu}{e\,v_F}\,, \tag{2-11}$$

where $k_F$ is the Fermi wave vector.

Another important quantity is the scattering mean free path, $l$, which can be calculated from,

$$l = \frac{2D}{v_F}\,. \tag{2-12}$$

where D is the diffusion constant. The diffusion constant is determined from the following relation,

$$D = {}^{1}/_{2}\, v_F^2\, \tau\ . \qquad (2\text{-}13)$$

Above all, mobility is an indication of the scattering rate for charge carriers in the material. The mobility of graphene flakes can be limited by several different scattering mechanisms. Examples of scatterers are: charge doping from the inhomogeneous charge distribution in the substrate, phonon coupling at elevated temperatures, strain or bending deformations of the flake, and adsorbed impurities on the flake. To date there has been little agreement on the precise factors responsible for limiting the graphene mobility [20]. Despite the existence of these limiting factors studying the electronic properties of graphene is an increasingly important issue as graphene electronics is potentially a rival to conventional semiconductor technology. Some scientists have predicted that graphene could one day replace silicon, which is the currently material of choice for transistors.

## 2.2 Introduction to the structure and properties of 2H-$NbSe_2$

In recent years, there has been renewed interest in studying layered materials. Layered materials exhibit a rich and diverse source of two-dimensional (2D) crystals. The importance of these 2D crystals arises from their unusual electronic properties and high specific surface areas, which make them useful for applications ranging from electronics to energy storage [21].

Several different approaches have been used to realise these 2D crystals. For example, these materials can usually be mechanically exfoliated as in the case of graphene [22]; hence they can be extracted from their bulk crystals [1, 23]. Even though, graphene was the first isolated layered material and has attracted a great deal of attention, other groups of materials are also important such as transition metal dichalcogenides (TMDs), transition metal oxides (TMOs) and other 2D compound such as BN, $Bi_2Te_3$ and $Bi_2Se_3$ (topological insulators) [21].

Transition metal dichalcogenides (TMDs) are promising materials for nanoscience research. In addition, TMDs possess a rich variety of electronic properties (such as metallic, semiconductor, superconductor, and charge density waves (CDWs)) and represent very interesting systems for studying mesoscopic transport in two-dimensional samples. Also, they provide possible new

functionalities for practical applications which are complementary to those of graphene [24].

### 2.2.1 Transition metal dichalcogenides (TMDs)

The past forty years have seen rapid advances in the study of TMDs. Several researchers have studied these materials as they have a wide range of unique mechanical, thermal, electronic and optical properties [25, 26]. Recently, the physical understanding of 2D materials obtained from graphene as well as the possibility to prepare and manipulate these materials at the nanoscale, have led to a renewed interest in studying the atomically thin 2D forms of TMDs. Moreover, the need to induce a band gap, as is the case in graphene, is absent in the case of some 2D TMDs. It was found that several of 2D TMDs possess sizeable band gaps, where decreasing the number of layers from the bulk to single layer changes the gaps from indirect to direct as is the case in $MoS_2$, $MoSe_2$, $WS_2$ and $WSe_2$. The TMD family has a common formula $MX_2$, where (M) is the transition metal (Mo, W, Nb, Ta, Ti) and (X) is the chalcogen (Se, S, or Te). These compounds have a rich variety of physical and electronic properties that span from semiconducting to superconducting, according to the specific choice of metal and chalcogen atoms. A sandwich structure X-M-X is the common form for these materials, where the metal atom (M) lies between hexagonally packed chalcogen atoms (X).

The coordination and oxidation states of the metal atoms play an important role in changing the properties of TMD materials, making them potentially useful in many areas of electronics. The bonding within these trilayer sheets is covalent, whereas adjacent sheets in the three dimensional (3D) crystal of TMD materials, are bound together via weak van der Waals bonds.

The TMD crystals have either hexagonal or rhombohedral symmetry. Also, two different crystals structures either trigonal prismatic (t.p) or octahedral (oct), are obtained according to the relative arrangement of the two sheets of the atoms of chalcogens around the (M) atom. Polytypism (1T, 2H, 3R, 4H, ….) has been widely reported [27]; where (1, 2, … n) represents the number of layers in the unit cell, and the capital letters indicate the type of crystal symmetry (T-trigonal, H-hexagonal and R-rhombohedral). Sketches of the most common three TMD polytypes, which are (1T, 2H and 3R) are presented in Fig. 2-11. The advantages of using 2D TMDs

materials for the fabrication of field effect transistors comes mainly from the processing ease, lack of short-channel effects, and the tuneable band gaps with high on/off ratios [28, 29].

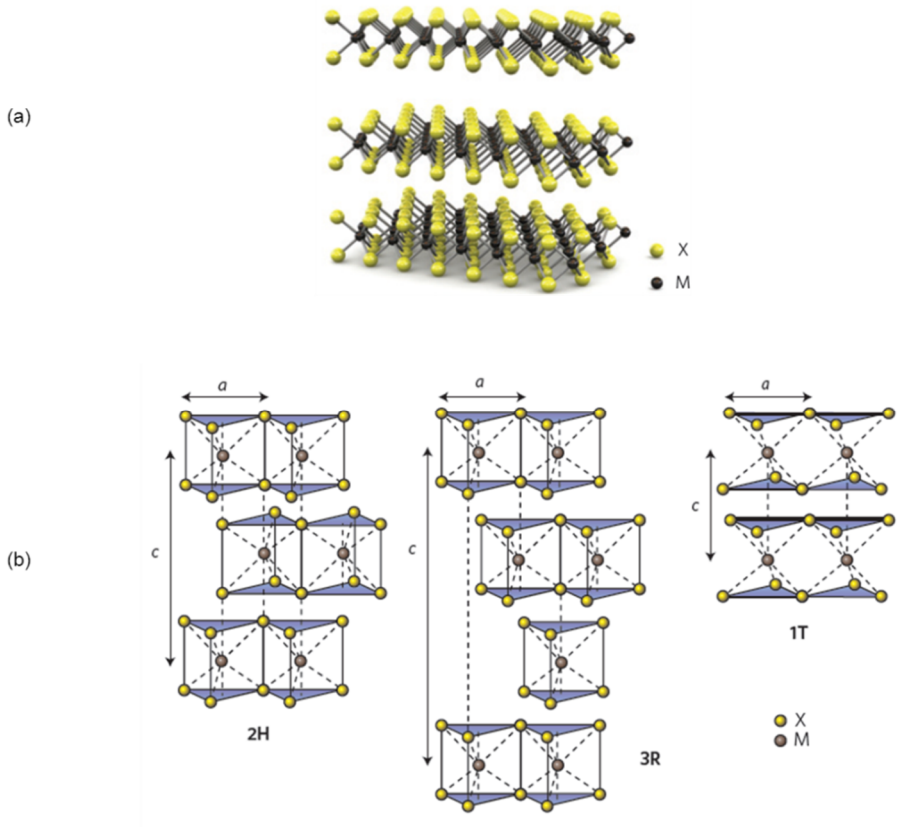


**Figure 2-11:** a) 3D structure of $MX_2$. b) Sketches of common polytypes for 2H, 3R and 1T structures respectively [30].

### 2.2.2 The structure of 2H-$NbSe_2$

The quasi two-dimensional TMD Niobium diselenide ($NbSe_2$) has a hexagonal crystal structure. It has two common crystalline forms 2H-$NbSe_2$ and 4H-$NbSe_2$. The number of $NbSe_2$ molecules in the unit cell is implied by the numbers 2 and 4, while H represents the hexagonal crystal symmetry. The 2H-$NbSe_2$ unit cell contains two $NbSe_2$ units with ABAB stacking. Each unit is formed from a sandwich of two layers of Se atoms with Nb atom layer between them. The coordination number of Se atoms is 3, while it is equal to 6 for Nb atoms. Each selenium atom is surrounded by three Niobium atoms. Strong covalent bonds exist inside the layers, while there is a weak interaction between adjacent layers as a result of van der Waals coupling. The Se-Nb bonds within a sandwich are covalent bonds, and they form the 2D-hexagonal lattice [30, 31].

The $NbSe_2$ molecular layers are bound by van der Waals coupling. Thus, 2H-$NbSe_2$ is easy to cleave along a plane parallel to the layers (as is also the case for graphite). The Se sheet is usually the termination layer after exfoliation [32]. The spacing between Nb sheets is 6.3 Å. Therefore, the c-axis of the unit cell is 12.6 Å, while the a-axis lattice constant is 3.6 Å [33]. Figure 2-12 shows a schematic diagram of the 2H-$NbSe_2$ unit cell.

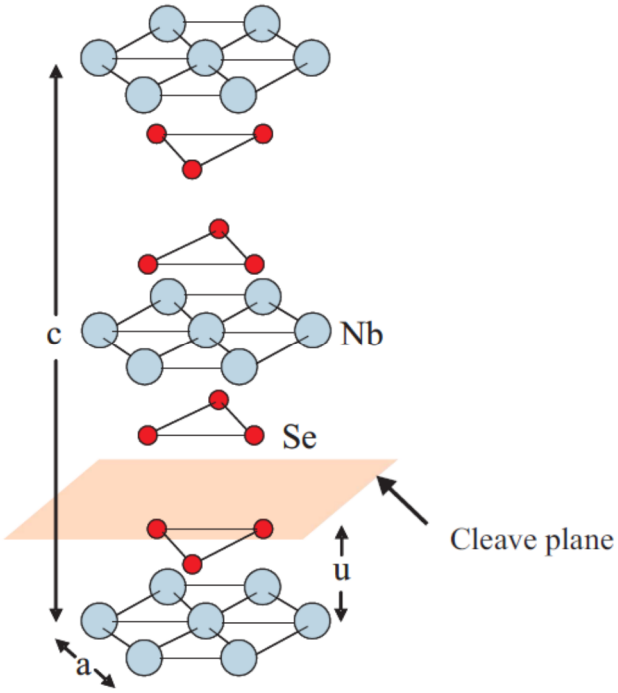


**Figure 2-12:** The 2H-$NbSe_2$ unit cell. This material can easily be cleaved at a plane situated between the two Se layers [34].

### 2.2.3 The properties of 2H-$NbSe_2$

2H-$NbSe_2$ is a type II superconductor; it is a layered material, and its single crystals can be easily cleaved to obtain few-molecular layer flakes. Electrons can move freely inside the layers, whilst at the same time an overlap of the electronic wave function occurs between the layers due to the van der Waals character of the layer interaction. This fact is intimately connected with the anisotropy of the electronic properties of 2H-$NbSe_2$ [35]. Hence, $NbSe_2$ represents a new model system for studying superconductivity in low-dimensional systems [31, 32]. 2H-$NbSe_2$ is believed to be a conventional superconducting material as well as a

highly anisotropic layered material. 2H-$NbSe_2$ is a normal metal above $\backsimeq$ 7.2 K, whilst, it becomes a type II superconductor below $\backsimeq$ 7.2 K.

In general, the 2D nature of TMD materials promotes the occurrence of electronic instabilities that are driven by Fermi surface nesting; this generates the formation of charge density waves (CDW) in them. 2H-$NbSe_2$ is a well-known material that shows the coexistence of two interesting phases at low temperature; CDW and superconductivity. To date there has been little agreement on the nature of, and the competition between these two ground states [36]. 2H-$NbSe_2$ undergoes a charge density wave (CDW) transition near T = 32 K. Several investigations of the band structure have been made in the normal and superconducting states of $NbSe_2$. These reveal the small and cylindrical shape of the Fermi surface, which enables the CDW to persist in the superconducting state [37].

Understanding the electronic band structure of $NbSe_2$ is key in order to interpret various results. In a 2H-$NbSe_2$ unit cell there are two Nb atoms and four Se atoms. Studying the interaction of the d-orbitals of Nb atoms with the outer p-orbitals of Se atoms in the unit cell helps to interpret the band structure and understand shifts of the Fermi energy, $E_F$. Figure 2-13 presents the 2D band structure of a single molecular layer of 2H-$NbSe_2$ that has been reported by Lebègue *et al.* [38]. Lots of similarities have been noticed between the energy bands of 2D 2H-$NbSe_2$ and 3D 2H-$NbSe_2$ [33]. Two features have been observed in the vicinity of the Fermi level. Firstly, the bands around the band gap are relatively flat as a consequence of the "d" character of the electron states at these energies, and secondly, a separation in energy from all other states is observed for the band state that is pinned at the Fermi level, which primarily originated from the Nb d-orbitals [38]. The evolution of the band structure with the number of layers can be seen in Fig. 2-14, where a simple comparison between the calculated energy bands of monolayer, bilayer and bulk 2H-$NbSe_2$ is presented. The differences observed in the band structure relate to the Se-Se interplanar interaction. Since it is not present in the monolayer and was reduced in the bilayer, such that there was a sinking of the antibonding Se $p_z$ band below the Fermi level and hence the presence of Nb-bands crossing the Fermi level alone, which confirms that monolayer and bilayer 2H-$NbSe_2$ are both strictly two-dimensional [39].

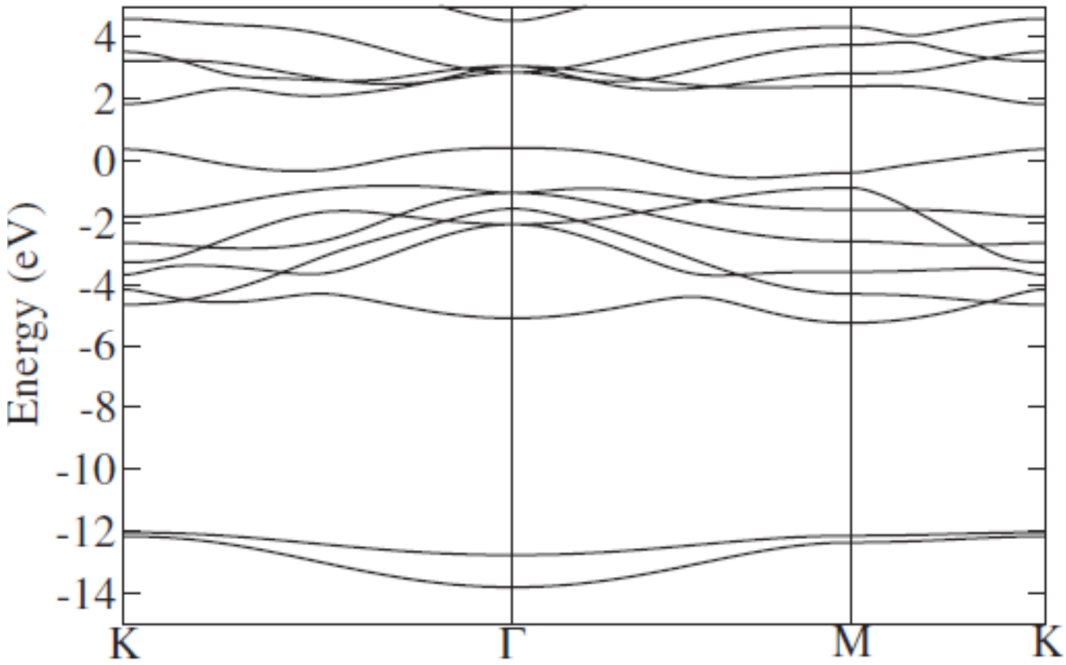


**Figure 2-13:** Two-dimensional 2H-$NbSe_2$ band structure. The Fermi level lies at 0 eV [38].

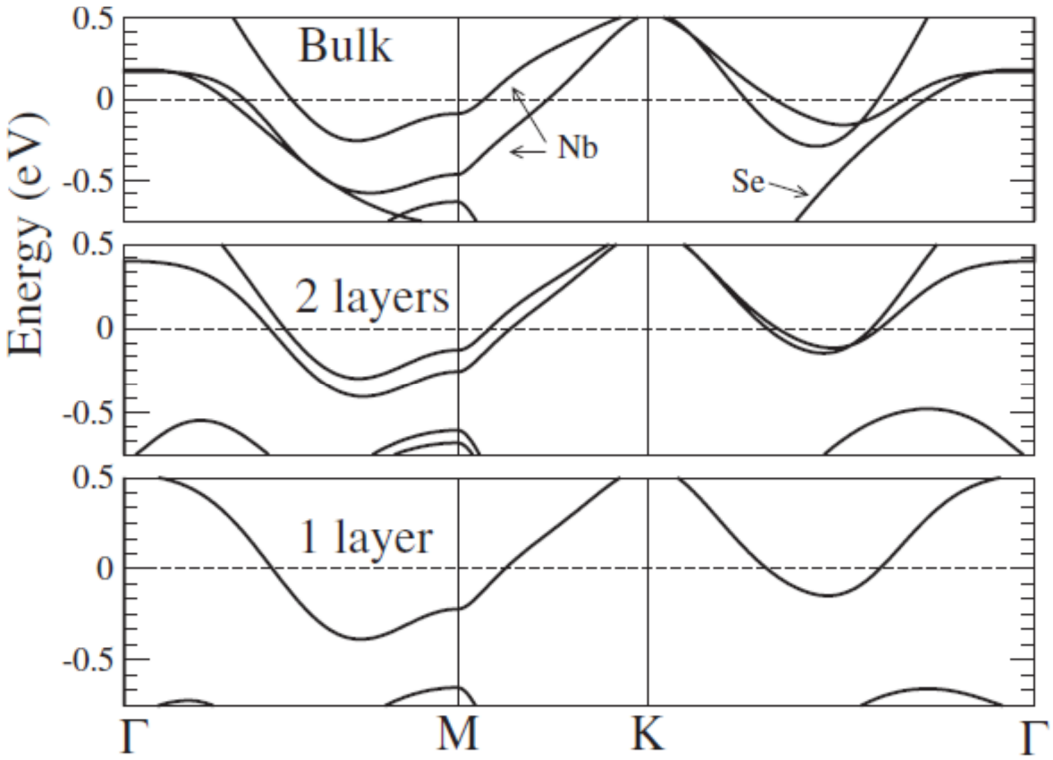


**Figure 2-14:** Band structure of monolayer, bilayer and bulk 2H-$NbSe_2$ [39].

The calculated density of states (DOS) for two-dimensional 2H-$NbSe_2$ is shown in Fig. 2-15, which reveals a large hybridization between the Nb and Se states. Two band gaps are present, a smaller one that lies between the bands derived mainly from the Nb-d states and a larger one located in the occupied states, which separates the Se-s states (in the range -13.6 to -12 eV) from the hybridized Nb and Se-p states (in the range -5 to 1 eV) [38]. In addition, Fig. 2-16 illustrates how the DOS evolves with the number of layers from bulk 2H-$NbSe_2$ to a monolayer, where the DOS has a pronounced downward slope at $E_F$ with a reduction in the layer number. This is also consistent with similar falls in the DOS as observed in Fig. 2-15. [39].

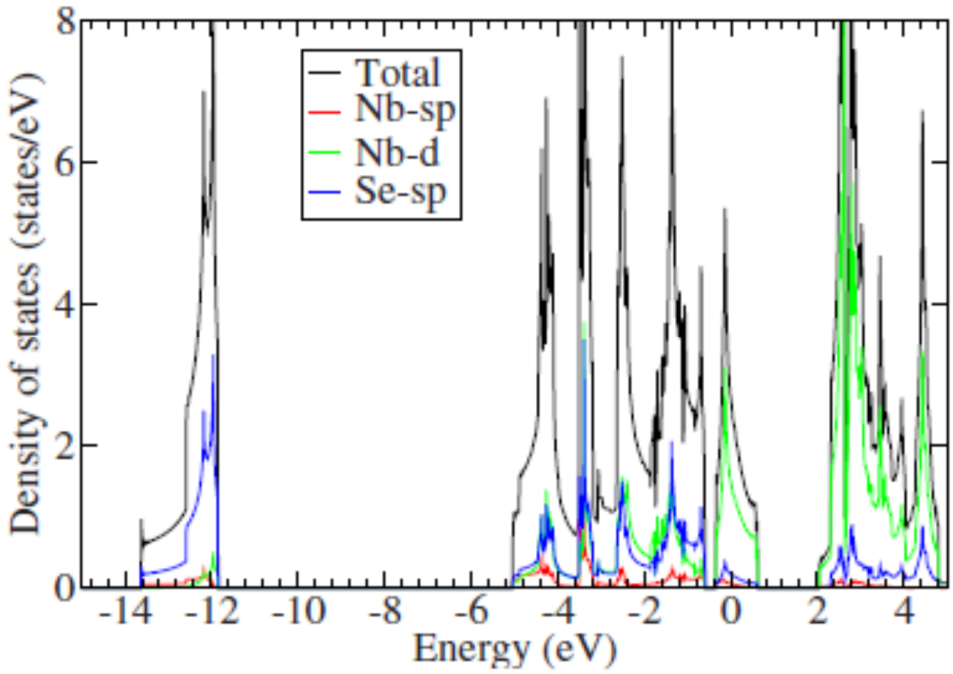


**Figure 2-15:** The DOS of two-dimensional 2H-$NbSe_2$. The Fermi level lies at 0 eV [38].

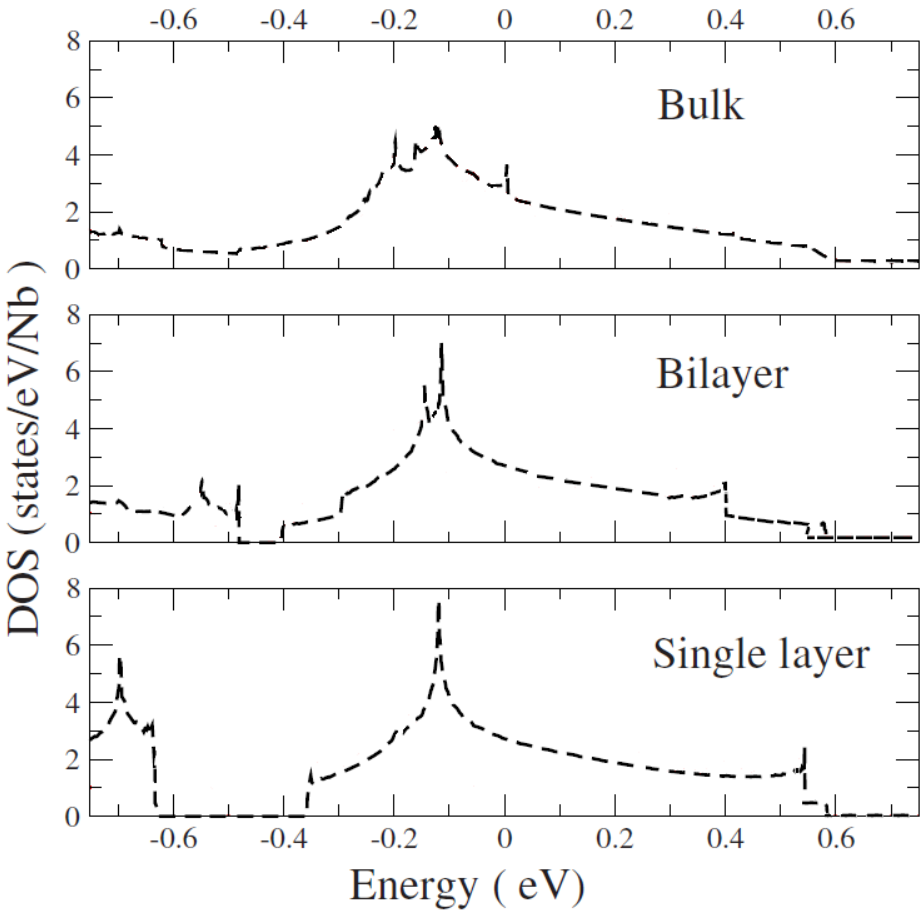


**Figure 2-16:** The evolution of DOS in 2H-$NbSe_2$ with number of layers [39].

## 2.3 Field Effect Structures and back gating

In the 1930s the German scientist Julius Lilienfeld demonstrated that a strong electrical field could cause the flow of electricity within a nearby semiconductor. This represented a new principle for making solid state devices out of semiconductors and led to the concept of the field effect transistor (FET). More recently in 1974 William Shockley reported the first working FET. Since the first appearance of the FET it has become one of the most important transistors used in both analogue and digital circuits. It is a device in which the current through the conducting region is modulated by an electric field and has three terminals, source, drain and gate. The source terminal permits the majority carriers to enter the channel, and these leave the channel through the drain terminal. The gate terminal is responsible for controlling the channel conductivity.

As mentioned earlier there are some similarities in the structure of graphene and $NbSe_2$. In both materials quite weak van der Waals coupling is responsible for

binding molecular layers into unit cells. Because of these weak bonds, the surface of the material has an intrinsically low density of dangling bonds, which can act as charge traps. Thus, these materials can in principal be very good candidates for the fabrication of FETs.

### 2.3.1 Graphene field effect transistor (GFET)

Central to the entire discipline of graphene research is the understanding and utilisation of its unusual electronic properties. The discovery of the ambipolar electric field effect in graphene [22] initiated enormous interest in graphene field effect transistors (GFET). Semiconductors generally require impurity doping in order to conduct electricity. In contrast, graphene can conduct electricity without impurity doping as it displays the phenomenon of self-doping. Both the charge carrier type and its concentration can be modulated with an external electrical field, (or gate voltage). The possibility of having a transistor which operates with either electrons, holes or both simultaneously is introduced in the GFET.

A schematic view of a GFET is given in Figs. 2-17 (a) and 2-18 (a). A GFET is effectively a parallel plate capacitor. It has the following structure from bottom to top: a heavily doped bulk substrate working as a back gate (the first plate), the dielectric medium which is the silicon dioxide $SiO_2$ layer, the top plate of the capacitor (graphene flake) and the source-drain electrodes.

Similar to a conventional capacitor an accumulation of surface charge density, *n*, is established upon applying a gate voltage. This effect can be described by the following equation,

$$n = \frac{\varepsilon_r \varepsilon_0 V_g}{d\, e} = \alpha V_{bg} \,, \tag{2-14}$$

where $n$ is the 2D carrier density, $\varepsilon_r$ is the relative permittivity of $SiO_2$, $\varepsilon_0$ is the permittivity of free space, $d$ is the thickness of the dielectric and $e$ is the electronic charge. The silicon substrate of graphene devices frequently has a 300 nm thick $SiO_2$ layer grown thermally on top with a typical value for the relative permittivity of 3.9. Substituting the above values in equation 2-14 gives the following value for the proportionality coefficient, $\alpha = 7.18 \times 10^{14}\ \mathrm{m^{-2}V^{-1}}$.

The band structure of graphene presents the opportunity for the carrier type to be switched from electrons to holes and vice versa by varying the Fermi level

position. The movement of the Fermi level relies on the applied potential difference, $V_{bg}$, between graphene and the doped silicon substrate, which locally induces charges in the graphene.

Figure 2-17 (b), illustrates the influence of the gate voltage on the resistance of a graphene device at 300 K. The maximum value of the resistance is found at the Dirac point, which is known as the charge neutrality point (CNP). Electrons and holes are induced in the graphene layer as a result of tuning the gate voltage to the right (+V) and to the left (-V) of the Dirac point respectively. The position of the Dirac point, as well as the symmetry of the electron and hole branches, are influenced by extrinsic doping effects. Consequently equation 2-14 can be used in case of neutral graphene (no extrinsic doping), whilst the charge carrier density for doped graphene can be extracted from the relation,

$$n = \alpha\,(V_{bg} - V_{DP})\,, \tag{2-15}$$

where $V_{DP}$ is the gate voltage at which the Dirac point is found and it serves as an offset value in this relation.

Several factors influence the transport properties of graphene such as the quality of the graphene layer and the interface with both $SiO_2$ and the metal contacts. The fabrication process usually strongly influences the quality of graphene flakes [40]. Carefully choosing appropriate metal contacts as well as the dielectric material for a GFET is crucial to avoid destroying its interesting properties. The metal contacts are chosen with higher work functions than that of graphene to reduce contact resistivity and locally raise the graphene density of states. In contrast, a thin, uniform layer of a high dielectric constant is selected to minimize the density of states at the graphene/dielectric interface. Finally, dielectric performance can be affected by the number of graphene layers in the channel, and the electronic properties of the flake vary strongly with the number of graphene layers.

### 2.3.2 $NbSe_2$ field effect transistor ($NbSe_2$-FET)

The modulation of the charge carrier density in a superconductor can change its physical properties such as its superconducting transition temperature, $T_c$. In the past chemical doping has been used to control the charge carrier density in a superconductor. However, various disadvantages are associated with this doping

approach such as the introduction of unwanted chemical, structural or other changes into the material as well has high levels of disorders.

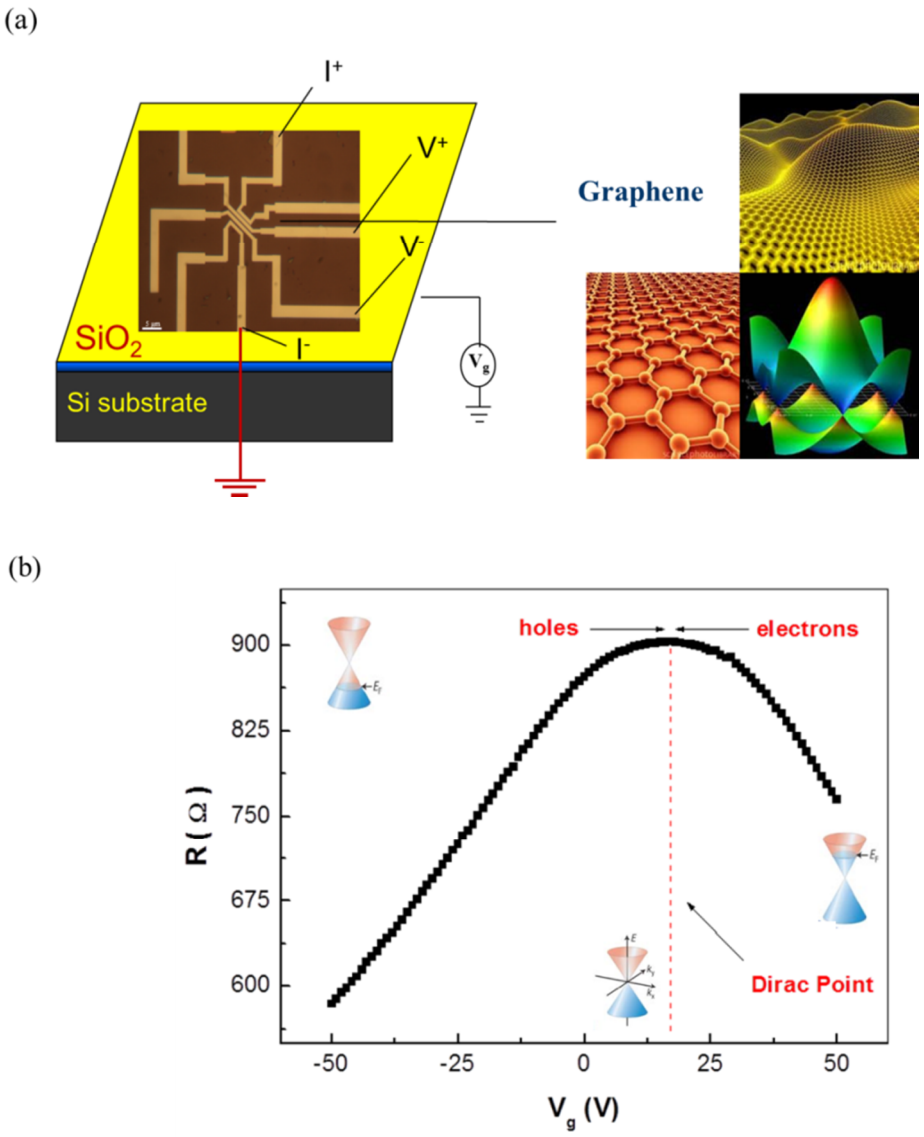


**Figure 2-17:** a) Sketch describing the structure of a GFEFT. b) Plot showing the dependence of the resistance of a graphene device on gate voltage. The inset cones indicate the changes in the position of the Fermi level as a function of the applied gate voltage.

A new technique is introduced here to minimize the potential complications of chemical doping. In this approach an external electric field is applied to change the charge carrier density. Several conditions must be satisfied to allow one to study the electric field effect on superconductivity. Since the carrier density for most superconducting materials is high two features of a good device are required. A very

thin layer of superconductor is needed to enable the electric field to control the charge carriers in it. Also, a high-quality dielectric is important to enhance the electric field and allow high gate voltages to be applied. Furthermore, one must ensure that the behaviour of such electric field devices is not undesirably controlled by the flake/substrate and flake/dielectric interfaces rather than the intrinsic properties of the superconducting flake itself [31].

Niobium diselenide $NbSe_2$ field effect transistors ($NbSe_2$-FETs) have been realised by micromechanical cleavage from a 2H-$NbSe_2$ single crystal onto $Si/SiO_2$ substrates followed by the deposition of Chromium/Gold (Cr/Au) contacts. A schematic diagram of a $NbSe_2$-FET four terminal device is shown in Fig. 2-18 (b).

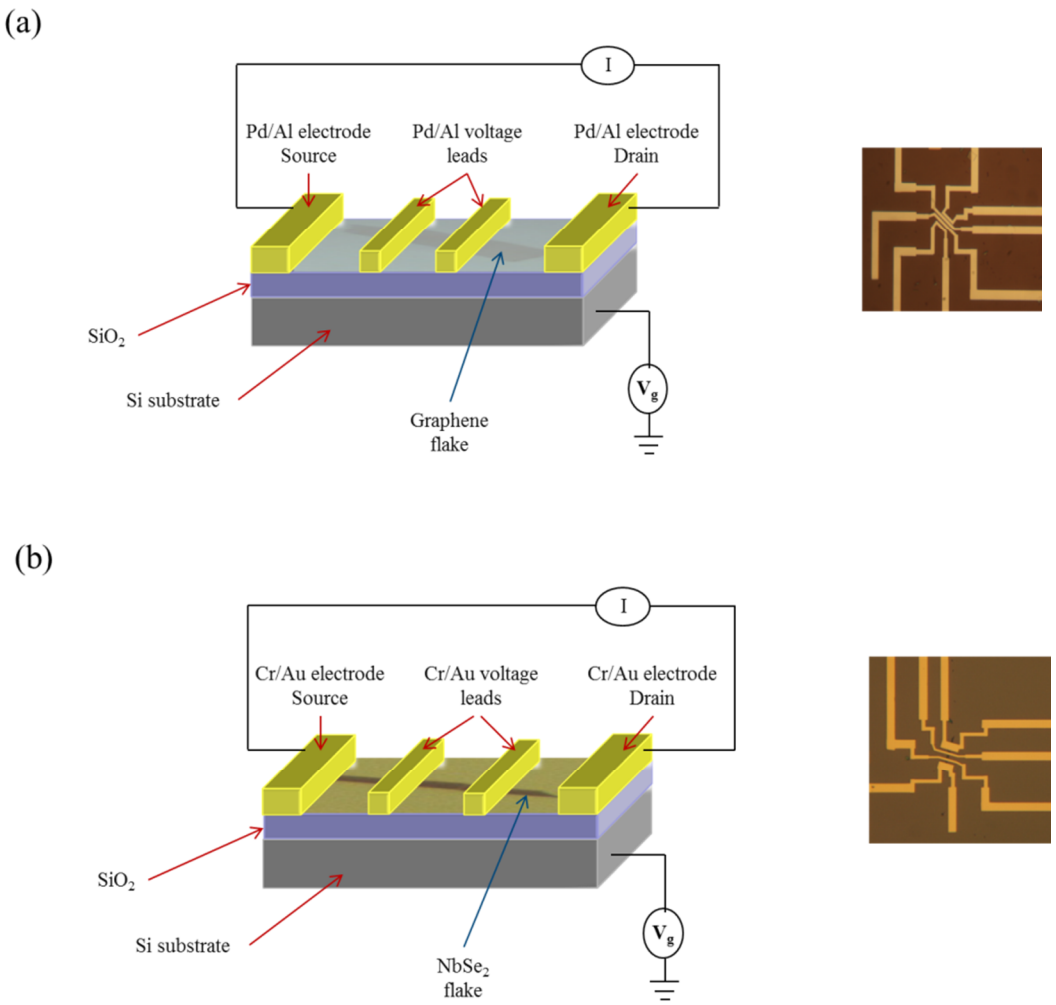


**Figure 2-18:** Schematic representations and optical images of a) a GFET and b) a $NbSe_2$-FET.

# Chapter 3

# Superconductivity

## 3.1 Historical background

In the beginning of the last century, a new branch of physics was opened up. This was made possible in 1908 when Kamerlingh Onnes liquefied helium for the first time allowing him to measure the resistance of different materials at low temperatures down to ~ 3 K.

In 1911 Onnes achieved a big breakthrough in physics by discovering the property of superconductivity in mercury at a temperature of a few degrees Kelvin above absolute zero [41]. Mercury at this time was the purest metal available, and for this reason Onnes tried to measure its resistivity at low temperature using liquid helium. By accident he found that at ~ 4 K the resistivity of mercury abruptly dropped to zero. Onnes later repeated the same measurements for other elements & alloys and so discovered the superconducting behaviour of several different materials. The temperature at which the resistance of the materials drops to zero is now known as the critical temperature, $T_c$, and is a phase transition between a normal & superconducting state of the material. The superconducting behaviour of a material depends on the nature of the material itself and each element or alloy has its own characteristic critical temperature, $T_c$. Onnes also found that the breakdown of superconductivity occurs with very high currents as well as at high magnetic fields [42].

Numerous studies have attempted to explain the main characteristic of a superconductor, namely the property of zero resistance. In 1933, more interesting findings were made by Walther Meissner and Robert Ochsenfeld. They discovered that the complete expulsion of the magnetic field from the interior of the superconductor occurs at $T < T_c(H)$, now called the Meissner-Ochsenfeld effect.

In 1953 the London brothers Fritz and Heinz published a famous article entitled “The electromagnetic equations of the superconductor” [43]. Their equations

were developed to correctly explain the Meissner effect. Also, they introduced a characteristic parameter for the superconductor, the London penetration depth $\lambda_L$, which can be defined as the depth to which a magnetic field is able to penetrate the sample.

In 1957 a new theory, which is considered a milestone in the history of condensed matter physics, was introduced by three physicists, J. Bardeen, L. Cooper and J.R. Schrieffer [44]. This so-called BCS theory described a mechanism of superconductivity that is based on Cooper pairing. A few years later, a new interesting effect was discovered, called the Josephson effect [45]. Josephson introduced the possibility of the flow of Cooper pairs between two superconductors connected by a weak link. The DC Josephson effect is obtained when Cooper pair supercurrent flow in the absence of an applied voltage, whilst the AC Josephson effect is exhibited when the flow of Cooper pairs occurs with an applied voltage between the two superconductors.

The main limitation of using superconductors in many applications has been the low temperatures that are required to keep the material in its superconducting state. This situation changed dramatically in 1986 with the discovery of high temperature superconductors (High-$T_c$). In 1986 Bednorz and Müller, [46] published a paper entitled "Possible High $T_c$ Superconductivity in the Ba-La-CuO system" which discussed the synthesis of a metallic oxygen-deficient compound with the composition $Ba_xLa_{5-x}Cu_5O_{5(3-y)}$ with a transition temperature above 30 K. This discovery of high $T_c$ superconductivity has led to a new era in the field. The discovery was the culmination of painstaking research on oxides such as $SrTiO_3$, Li-Ti oxide system [47], $BaPb_{1-x}Bi_xO$ [48] and LaBaCuO [49].

Chu's group at the University of Texas observed an increase in $T_c$ to 52 K in the LaBaCuO system by application of pressure [50] and subsequently made a major contribution to the field of high temperature superconductivity. This led them to look for a new chemical composition with smaller atoms. They reported superconductivity up to 93 K in a ceramic $YBa_2Cu_3O_{7-\delta}$ sample. This discovery of a superconducting critical temperature well above the boiling point of liquid nitrogen (77 K) opened up new avenues for technologists and condensed matter physicists throughout the world, in part because liquid nitrogen is cheaper than liquid helium.

Maeda *et al*. [51] in Japan first reported the existence of superconductivity with a $T_c$ of around 105 K in the BiSrCaCuO system. Other scientists around the world quickly stabilized related Bi-systems with structural formula $Bi_2Sr_2Ca_{n-1}Cu_nO_{2n-4}$ and $T_c$s of 10K, 85 K and 110K for n=1, 2, 3 respectively. Shortly afterwards, Sheng and Hermann [52] announced superconductivity above 100K in the thallium-CuO system, and the structural formula for the system was established by Hazen *et al.* [53] as $Tl_2Ba_2Ca_{n-1}Cu_nO_{2n+4}$ with $T_c$ of 80K, 110K and 125 K for n=1, 2, 3 respectively. Tl-2223 held the record for the highest $T_c$ of 125K for quite some time until Ott's group in Zürich [54] reported superconductivity at about 130K in the HgBaCaCuO system. When subjected to a high-pressure of 150 kbar, this mercury compound saw an increase in $T_c$ up to the present record of 150K.

More than two decades have passed since the discovery of the first high temperature superconducting (HTS) materials and this period has been fascinating and exciting for physicists as well as material scientists, electrical engineers and chemists alike working in the area of superconductivity. Enormous progress has been made in most of the physical and engineering aspects of superconductivity and there is still a tremendous scope to do more and try to resolve some of the very intricate unsolved problems. Many commercial applications of HTS can now be realised in communication and remote sensing systems with significantly improved performance. Channel filters for mobile communications are now routinely found in many base stations around the world [55].

Several new materials have been developed in recent years that are of considerable interest, both from the point of view of their structure and from the point of view of the role played by their charge carriers. Hebard discovered potassium-doped $C_{60}$ with the formula $K_3C_{60}$ and a $T_c$ of 18K in 1991, and still higher critical temperatures have been found in other doped fullerenes [56, 57]. This has opened up an entirely new exciting area of superconductivity in C-based materials. Since then, hundreds of HTS with varying transition temperatures have been synthesised. In 2001 [58] a conventional superconductor, $MgB_2$, with $T_c$ = 39 K was discovered. In 2008 Hosono [59] introduced a new family of HTS called iron-based Oxypnictides. A pnictide is an element from group V of the periodic table. Oxypnictides generally contain oxygen and rare earth elements and they are layered

tetragonal compounds. Oxypnictide materials are similar to high $T_c$ cuprate materials as both of them have conduction layers and spacer layers (charge reservoirs). In the oxypnictide LaOFeAs, FeAs planes are the conducting layers whereas LaO forms the charge reservoirs.

To summarise, even though the first observation of superconductivity was over a century ago there still seems to be much more to discover in this expanding area of physics.

### 3.1.1 The Meissner Effect

In 1933 a new property of superconducting materials was discovered that is known as the Meissner Effect. At this time Meissner and Ochsenfeld [60] observed the complete expulsion of magnetic flux from the interior of superconducting materials implying that superconductors exhibit perfect diamagnetism. This property is explained in the sketch in Fig. 3-1. Inside the sample there is a cancellation of the external applied field as the material produces a magnetic flux density that is equal and opposite to the applied field. The magnetic flux density is formed as a result of induced screening currents that flow around the perimeter of the superconductor.

Generally, the relation between the applied magnetic field $H$, the magnetic induction $B$, the permeability of vacuum $\mu_0$ and the magnetisation $M$ of a sample is [61],

$$B = \mu_0 (H + M) \quad \text{or} \quad B = \mu_0 H (1 + \chi), \tag{3-1}$$

where $M = \chi H$, (3-2)

and $\chi$ is the magnetic susceptibility ($\chi = -1$ for a perfectly diamagnetic material).

Hence, $B = \mu_0 H(1 - 1) = 0$ inside the superconducting sample.

Where $B = 0$ the material has expelled the magnetic field from that region.

Figure 3-2 indicates the relation between magnetisation, $M$, and the magnetic field, $H$. Below a certain value of the magnetic field, which is known as the critical magnetic field, $H_c$, the material behaves as a perfect diamagnet and it is in the superconducting state. However, at $H \geq H_c$ superconductivity will be destroyed and the material returns to its normal state.

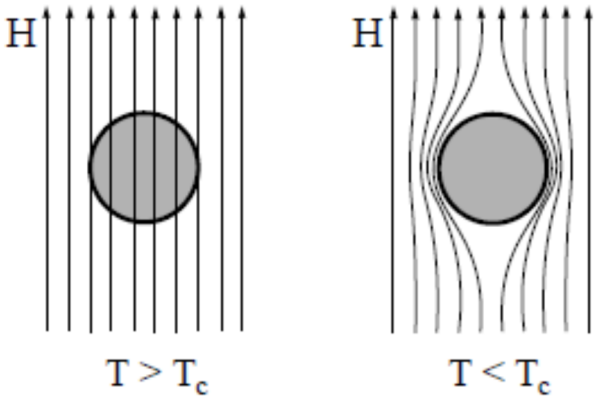


**Figure 3-1:** The Meissner effect, a) An external applied magnetic field penetrates the sample $(T > T_c)$. b) The expulsion of flux from the interior of the sample $(T < T_c)$ [62].

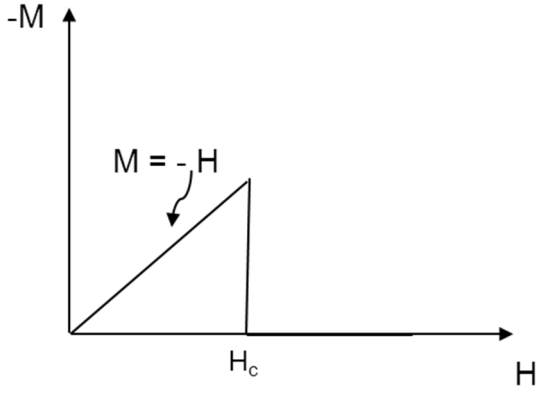


**Figure 3-2:** The M-H diagram that arises due to the Meissner effect in a type I superconductor.

In the presence of, an external applied field, $H_a$, changes in the free energy of the material per unit volume occur as a result of gaining a magnetisation, $M$.

$$\Delta f(H_a) = -\mu_0 \int_0^{H_a} M dH. \tag{3-3}$$

In the Meissner state $M = -H$ and

$$\Delta f(H_a) = -\mu_0 \int_0^{H_a} (-H) dH = \frac{\mu_0 H_a^2}{2}. \tag{3-4}$$

The onset of superconductivity lowers the overall energy of the system due to the superconducting condensation energy. When this energy is exactly balanced by the increase in energy due to the increasing magnetization, the material reverts to its normal state and superconductivity will be destroyed. The difference between the free energy of the normal and superconducting states of the material is given by

$$f_n(T,0) - f_s(T,0) = \frac{\mu_0 H_c^2(T)}{2}. \quad (3\text{-}5)$$

Hence, the critical magnetic field $H_c$ is given by

$$H_c(T) = \left(\frac{2}{\mu_0}[f_n(T,0) - f_s(T,0)]\right)^{1/2}, \quad (3\text{-}6)$$

and is a material-specific parameter.

An empirical relation that describes the temperature dependence of the critical field, $H_c$, in many superconductors is given by [63],

$$H_c(T) = H_c(0)\left[1 - \left(\frac{T}{T_c}\right)^2\right]. \quad (3\text{-}7)$$

Figure 3-3 shows the Superconducting (S) – Normal state (N) phase diagram that is described by this empirical relation.

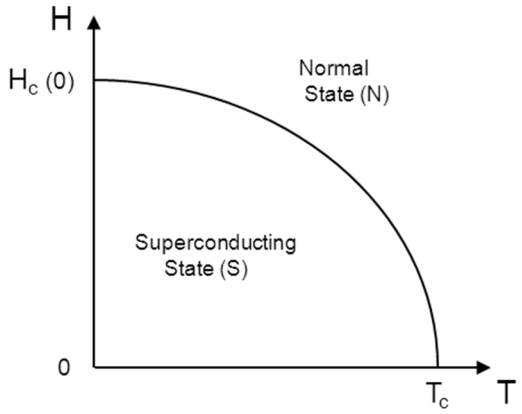


**Figure 3-3:** H-T diagram illustrating the temperature dependence of the critical magnetic field, $H_c$.

### 3.1.2 London Theory

The brothers Fritz and Heinz London [64] tried for many years to find an explanation for the two main properties of superconductivity, zero resistance and perfect diamagnetism. They achieved this by modifying the electrodynamic equations describing the (infinite) conductivity of the material. The London brothers based their hypothesis on the two fluid model.

In classical mechanics, the movement of electrons in a conductor is described by,

$$m\frac{dv}{dt} = eE + \frac{mv}{\tau}, \quad (3\text{-}8)$$

where $\tau$ is the damping time for scattered electrons, $e$ is the electronic charge, $m$ is the electronic mass, $v$ is the electron velocity and $E$ is the electric field.

Following from the first property of superconductivity (zero resistivity), the damping time τ can be neglected and equation 3-8 can be rewritten as,

$$\frac{dv}{dt} = \frac{eE}{m}, \tag{3-9}$$

The supercurrent density $J_s$ is given by,

$$J_s = n_s e v_s , \tag{3-10}$$

where $v_s$ is the superconducting velocity and $n_s$ is the superelectron density. By differentiating equation 3-10 with respect to time and substituting into equation 3-9.

$$\frac{dJ_s}{dt} = \frac{n_s e^2}{m} E . \tag{3-11}$$

Combining equation 3-11 with the third and fourth Maxwell equations leads to,

$$\frac{dB}{dt} = \frac{m}{\mu_0 n_s e^2} \nabla^2 \frac{dB}{dt} \quad \text{or} \quad \frac{dB}{dt} = \lambda_L^2 \nabla^2 \frac{dB}{dt}, \tag{3-12}$$

where, $\lambda_L = \sqrt{\frac{m}{\mu_0 n_s e^2}}$, is a characteristic lengthscale.

Given that the Meissner effect leads to $B$ = 0 the London brothers conjectured that equation 3-12 applies to $B$ as well as $dB/dT$and this leads to the London equation

$$\nabla^2 B = \frac{B}{\lambda_L^2}, \tag{3-13}$$

where $\lambda_L$ is known as magnetic field penetration depth.

The solution to equation 3-13 in one dimension [65] is

$$B(x) = B(0) e^{-x/\lambda_L} , \tag{3-14}$$

where *x* is the depth measured from the surface of the superconductor. The magnetic induction decays to zero over a finite length called the penetration depth, $\lambda_L$, as shown in the sketch in Fig. 3-4. Hence one has the Meissner effect deep within the superconductor where the field has been excluded.

Hence, the London brothers predicted that a static or a low frequency magnetic field is not excluded from a superconductor and penetrates a small distance beyond an N/S boundary. The magnetic field induces supercurrent loops at the

surface of a finite superconductor producing a magnetic field inside which is equal and opposite to the applied field. Also, the penetration of the magnetic field into the superconductor increases with increasing temperature *T*, and complete penetration occurs at $T \geq T_c$ when the superconducting state is destroyed. London theory agreed qualitatively with experiments but did not correctly predict the value of $\lambda_L$ as T→0 [61, 63].

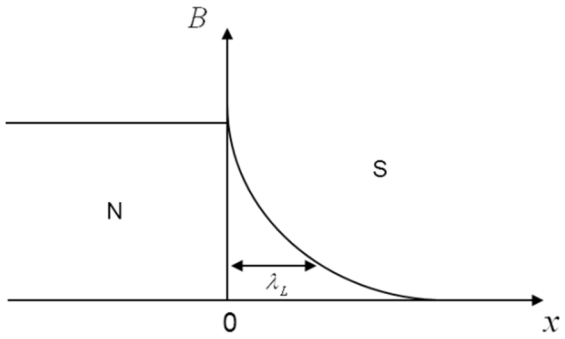


**Figure 3-4:** The decay of the magnetic induction *B* into a superconductor over the scale of the penetration depth, $\lambda_L$, at a normal/superconductor (N/S) interface.

### 3.1.3 Ginzburg-Landau (GL) Theory

In 1957 Ginzburg and Landau [66] developed a theory of superconductivity based on an order parameter or "wave function", $\psi(r)$, that describes the behaviour of the superconducting electrons. The density of objects that are responsible for superconductivity is $n_s^* = |\psi(x)|^2$, $(n_s^* = \frac{n_s}{2})$ .

They proposed that in the case of a homogenous system, when $n_s^*(r) = constant$, the free energy density can be expanded as a power series of $|\psi|^2$,

$$f_s(T) = f_n(T) + \alpha(T)|\psi|^2 + \frac{\beta(T)}{2}|\psi|^4 + \cdots , \tag{3-15}$$

where, $f_s$ is the free energy density in the superconducting state, $f_n$ is the free energy density of the normal metal and $\alpha$, $\beta$ are Ginzburg-Landau (GL) coefficients. By minimizing equation 3-15 with respect to $|\psi|^2$, the following condition can be obtained,

$$|\psi_\infty|^2 = n_s^* = \frac{-\alpha(T)}{\beta(T)} \tag{3-16}$$

where, $\beta(T)$ must be positive. Two situations arise according to the sign of $\alpha$. For $T > T_c$, $\alpha(T) > 0$ (positive value), the system will be in the normal state as the energy minimum is at $|\psi|^2 = 0$. However, at $T < T_c$, $\alpha(T) < 0$, the system will be in the superconducting state as the minimum energy is at $n_s^* = |\psi_\infty|^2$. These two cases are presented in Fig. 3-5 [66].

In an inhomogeneous system with applied fields/currents, another two terms are added to the free energy density equation,

$$f_s = f_n + \alpha|\psi|^2 + \frac{\beta}{2}|\psi|^4 + \frac{1}{2m^*}|(-i\hbar\nabla - e^*A)\psi|^2 + \mu_0\frac{H^2}{2}, \quad (3\text{-}17)$$

where $m^*$ is the mass of the object that is responsible for superconductivity $(m^* = 2m_e)$ and $e^*$ is the charge of the object that is responsible for superconductivity $(e^* = 2e)$.

The pair of well-known GL equations is obtained by minimizing the free energy density expression and has the following form,

$$\alpha\psi + \beta|\psi|^2\psi + \frac{1}{2m^*}(-i\hbar\nabla - e^*A)^2\psi = 0 \quad (3\text{-}18)$$

$$J_s = \frac{-ie^*\hbar}{2m^*}(\psi^*\nabla\psi - \psi\nabla\psi^*) - \frac{e^{*2}}{m^*}|\psi|^2 A, \quad (3\text{-}19)$$

where A is the electromagnetic vector potential.

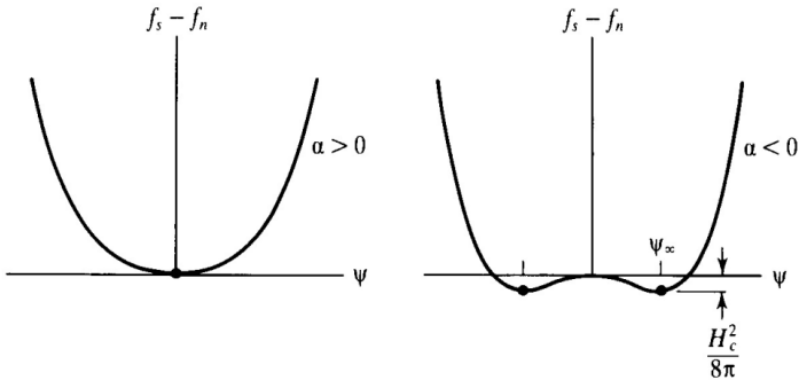


**Figure 3-5:** The two possible energy minima at a) $T > T_c$, $\alpha(T) > 0$ and b) $T < T_c$, $\alpha(T) < 0$ [63].

Assuming that the magnetic field in equation 3-18 is equal to zero (A = 0), and dividing the equation by $\alpha$ we find,

$$\psi + \frac{\beta}{\alpha}|\psi|^2\psi - \frac{\hbar^2}{2m^*\alpha}\nabla^2\psi = 0. \quad (3\text{-}20)$$

Hence the GL equation introduces a new lengthscale which is known as the coherence length, $\xi$,

$$\xi(T) = \sqrt{\frac{\hbar^2}{2m^*|\alpha|}}. \tag{3-21}$$

This is defined as the shortest characteristic lengthscale over which $\psi(r)$ can vary.

Ginzburg - Landau theory also allows one to write the London penetration depth in a new form.

$$n_s^* = \frac{n_s}{2} = \frac{-\alpha}{\beta} \;\&\; \lambda_L = \sqrt{\frac{m}{\mu_0 n_s e^2}}, \qquad \text{or}$$

$$\lambda = \sqrt{\frac{m\beta}{2\mu_0|\alpha|e^2}}. \tag{3-22}$$

One of the successes of GL theory is in being able to deal with the mixed state that arises in type II superconductors. The schematic diagram in Fig. 3-6, illustrates the interface between coexisting superconducting and normal domains [63].

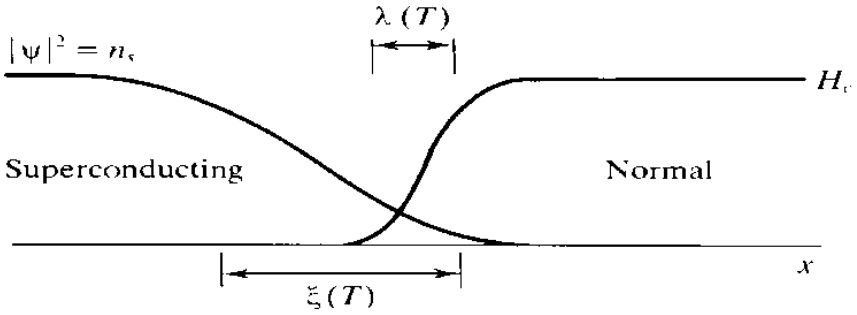


**Figure 3-6:** Sketch of the interface between coexisting normal and superconducting domains [63].

Moreover, Ginzburg and Landau introduced an important parameter that distinguishes between type I & type II superconducting materials. The GL parameter is the ratio between the penetration depth $\lambda$ and the coherence length $\xi$,

$$\kappa = \frac{\lambda}{\xi}. \tag{3-23}$$

For type I materials $\kappa < \frac{1}{\sqrt{2}}$ and for type II materials $\kappa > \frac{1}{\sqrt{2}}$. Figure 3-7 illustrates the difference between type I & type II superconducting materials with strongly different values of $\kappa$.

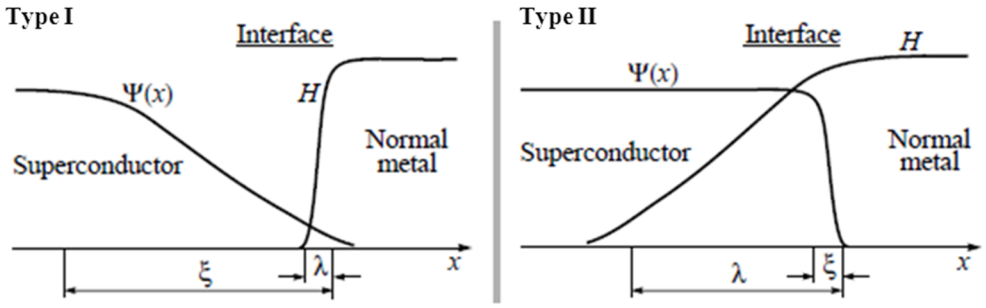


**Figure 3-7:** The value of $\kappa$ distinguishes between type I & type II superconductors [62].

### 3.1.4 BCS Theory

In 1956 Cooper [67] developed the concept that superconductivity was associated with bound pairs of electrons, each having equal but opposite spin and momenta. The pairs are bound together by an electron-phonon interaction. In 1957 Bardeen, Cooper and Schrieffer [68] used a many body microscopic theory to demonstrate that this leads to superconductivity with a finite energy gap for an indefinitely, small attractive interaction, $V$.

The mechanism of attraction between the two electrons in a Cooper pair is explained as follows; the first electron moves through the material and attracts the positively charged nuclei of the surrounding atoms in the lattice via Columbic interactions. These atoms will be displaced towards the electron and once this electron has moved away the resulting cloud of positive charge that formed around it will attract the second electron travelling in the opposite direction. Thus, this indirect attraction can overcome the Coulomb force repulsion between the first and second electron and they become bound. This mechanism of attraction is illustrated in Fig. 3-8.

Electrons in a normal conductor are Fermions and are described by Fermi statistics [69]; they singly occupy the quantum energy levels up to the Fermi energy, $E_F$. In contrast, Cooper pairs of electron can be viewed as Bosons which are governed by Bose-Einstein statics. Therefore, in contrast to ordinary electrons, Cooper pairs can multiply occupy the same quantum states.

BCS theory accounted for many of the previous experimental observations such as the existence of an energy gap, $2\Delta(0)$, in the quasiparticle spectrum which it predicted to have a value of 3.52 $k_B T_c$ in the weak coupling limit.

Another aspect of the BCS theory is that it deals with the metal in terms of quasiparticles rather than electrons; a quasiparticle is a mixture of electron and hole states.

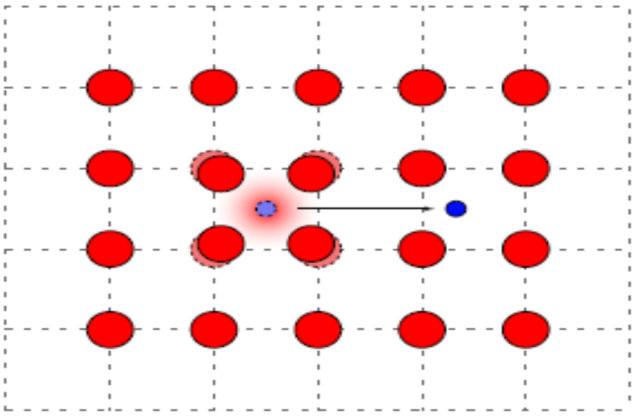

**Figure 3-8:** Illustration of the mechanism Cooper pair formation as a result of lattice polarization. Adapted from [70].

### 3.1.5 Type I and Type II Superconductors

A superconductor in which the magnetic flux is completely expelled for any field less than a critical value $H_c$ is known as a type-I superconductor. Above this critical value, flux penetration occurs and the material turns normal. These superconductors are usually elements or simple alloys. Type-II superconductors are characterized by having a mixed state phase in which there is partial flux penetration, while the bulk of the material remains superconducting. Type-II superconductors can remain superconducting up to relatively large magnetic fields (> 50T). The criterion that determines whether a superconductor is type-I or type-II is the ratio of the magnetic penetration depth, $\lambda$, to the coherence length, $\xi$. This is equivalent to differentiating between type-I and type-II on the basis of the interface energy, $\sigma_{S/N}$, between normal and superconducting domains,

$$\sigma_{S/N} \approx \frac{1}{2}\mu_0 H_c^2 A[\xi(T) - \lambda(T)]\,, \tag{3-24}$$

where, $A$ is area of the interface. The material only exclusively exhibits the Meissner phase when $\xi(T)/\sqrt{2} > \lambda_L(T)$, and $\sigma_{S/N}$ is positive. Also, the sample does not like to form new S/N interfaces and it is called a type-I superconductor. The following sketch (cf., Fig. 3-9) illustrates the Meissner effect and the H-T phase diagram for type-I superconductor [62].

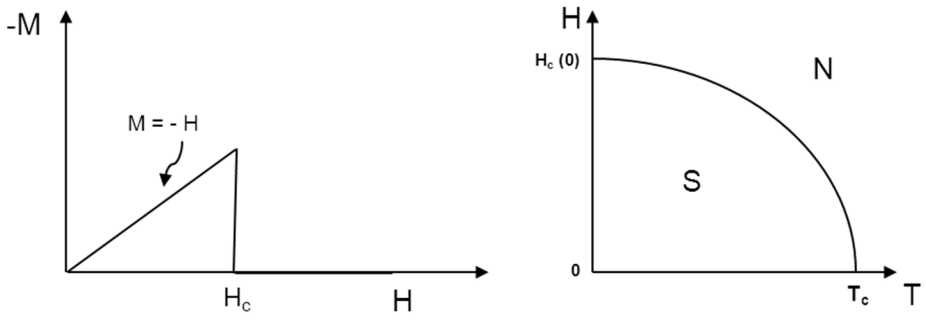


**Figure 3-9:** Illustration of the Meissner effect and H-T phase diagram for a type I superconductor.

On the other hand, when $\lambda(T) > \xi(T)/\sqrt{2}$ and $\sigma_{S/N}$ is negative, the sample favours formation of S/N interfaces and, above its lower critical field $H_{c1}$, magnetic flux enters in the form of quantised cylindrical tubes called vortices. This type of material is called a type-II superconductor. The M-H and H-T phase diagrams for a type-II superconductor are sketched below in Fig. 3-10 [62].

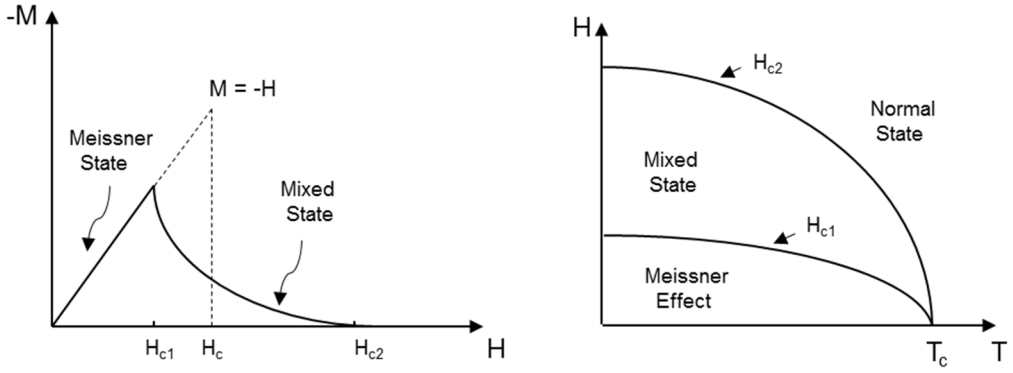


**Figure 3-10:** Illustration of the M-H and H-T phase diagram for a type II superconductor.

### 3.1.6 Vortex Matter

A. A. Abrikosov [71] introduced the concept of vortices to describe the intermediate state of type-II superconductors when the magnetic field exceeds $H_{c1}$. Physically, when a magnetic field is applied to a type-II superconductor it penetrates the material as discrete flux lines, which form tubular regions parallel to the applied field. These tubes form around normal cores and each contain the same amount of flux, equal to one flux quantum $\Phi_0 = \frac{h}{2e} = 2.07 \times 10^{-15}\ \mathrm{Tm}^2$. These normal regions are surrounded by a matrix of superconductor, which can still carry

supercurrent. The magnetic flux in each tube is generated by a vortex of persistent supercurrents circulating around the core. Energetically it is favourable for the flux lines to form a regular periodic array called the vortex lattice in samples with low disorder. For high current/field applications large values of critical current density, $J_c$, are obtained in type-II superconductors by the controlled introduction of crystal defects which pin the flux lines and prevent them from moving and dissipating energy. The structure of vortices in a superconducting slab is sketched in Fig. 3-11.

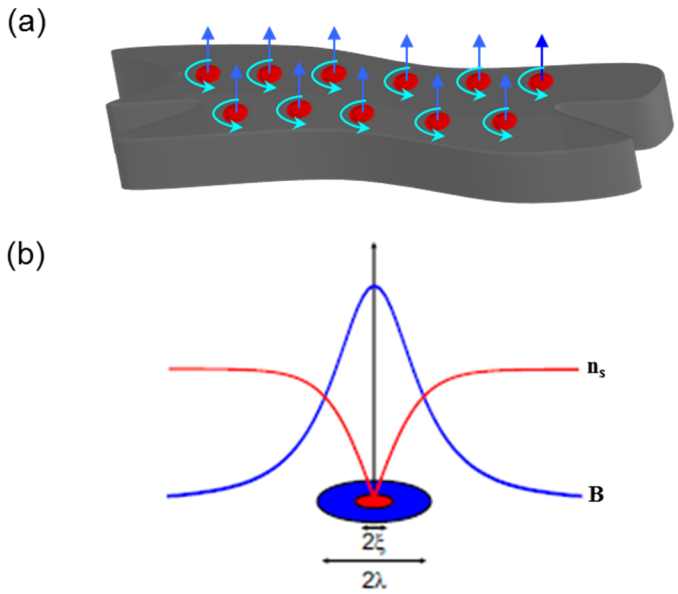


**Figure 3-11:** Sketch showing the structure of vortices. a) Each vortex is formed from two parts, a line of flux (the core) and a supercurrent circulating around the core. b) The field of a vortex drops off over a lengthscale $\lambda$ and the superelectron density falls to zero in the normal core over a lengthscale $\xi$.

### 3.1.7 BKT Theory in the 2D limit

It is well known that true long-range order (LRO) in a 2D system is impossible because the condensate or LRO should be destroyed by long-wavelength excitations. At the same time, the superfluidity of a system is not completely suppressed by these long-wavelength excitations.

It was hypothesised by Berezinskii [72], and independently by Kosterlitz and Thouless [73], that in the low temperature phase in the 2D limit LRO will be replaced by so-called quasi-long range order. They showed that in the absence of an applied magnetic field, a phase transition from a superfluid (superconducting state)

to a normal state occurs at the critical temperature $T_{BKT}$. To develop an understanding of the Berezinskii–Kosterlitz–Thouless (BKT) transition, understanding the distinction between bound vortex-antivortex pairs and free vortices is important. A vortex can be defined as an object that exists in a superfluid which has zero atomic density at its centre and $2\pi$ phase winding around it. In addition, an anti-vortex is an object that possesses the same properties as a vortex, but with $-2\pi$ phase winding. An estimation of the BKT temperature can be obtained as follows. The energy of adding a free vortex into a 2D system increases with, $R$ (the system size) and is described by [73, 74],

$$E_v \backsimeq \frac{\pi\hbar^2}{m} n_{SF,2D} \, log \left(R/\xi\right), \tag{3-25}$$

where, $n_{SF,2D}$ is the 2D superfluid density, $m$ is the particle mass and $\xi$ is the size of a vortex core. The energy cost for inserting this free vortex into the 2D system is large as compared to the energy cost of forming a vortex-antivortex pair. The energy required for creating this pair is given by,

$$E_v \backsimeq \frac{\pi\hbar^2}{m} n_{SF,2D} \, log \left(r_{12}/\xi\right), \tag{3-26}$$

where, $r_{12}$ is the pair separation.

The probability of creating these vortex-antivortex pairs is high at finite temperature (which keeps the 2D system in its superfluid state), since the energy cost is small. Furthermore, it is thermodynamically favourable to introduce a free vortex into a system when

$$F = E_v - T S_v \leq 0, \tag{3-27}$$

where the entropy, $S_v$, is proportional to the log of the number of vortex positions and given by

$$S_v \backsimeq 2 k_B \log \left(R/\xi\right)^2. \tag{3-28}$$

The universal relation between the 2D superfluid density, $n_{SF,2D}$, and the BKT transition temperature, $T_{BKT}$, can be obtained by minimizing the free energy of the 2D system ($F$) [73, 74] giving

$$T_{BKT} = \frac{\pi\hbar^2 n_{SF,2D}}{2mk_B}. \tag{3-29}$$

It was found that this transition is driven by thermally created vortices [73]. At $T < T_{BKT}$, pairs of vortex-antivortex are thermally created and the 2D system is in a superfluid phase. In contrast, at $T \geq T_{BKT}$, the unbinding of these pairs occurs and free vortices proliferate in the system and a transition to a normal state occurs afterwards. Figure 3-12 schematically describes the process of thermally activated proliferation of vortices.

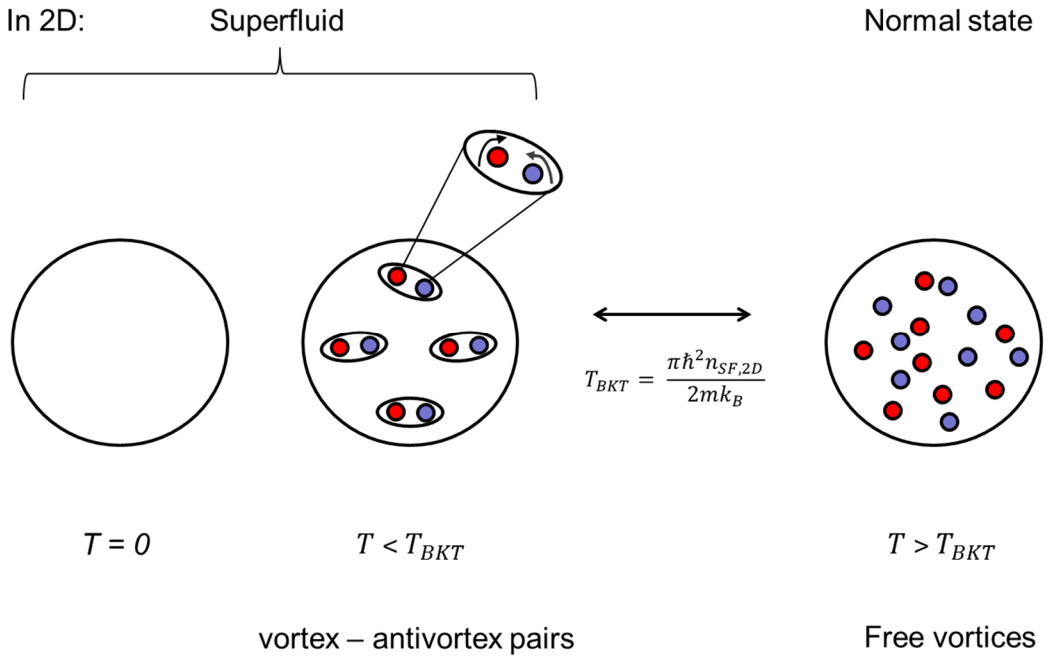


**Figure 3-12:** For $T < T_{BKT}$, bound vortex-antivortex pairs are created. For $T \geq T_{BKT}$, free vortices or free anti-vortices start to proliferate. Adapted from [74].

## 3.2 Josephson Effect

The superconducting proximity effect was first observed by Holm and Meissner in 1932 [75]. In 1962 Josephson [45] succeeded in interpreting this phenomenon when he predicted that a supercurrent (Cooper pairs) could pass coherently through the weak link between two superconductors. The Josephson Effect is interesting from several perspectives. First of all, it is considered to be one of the defining phenomena relating to superconductivity. Secondly, it is the building block for most cryo-electronic devices.

The Proximity effect is a phenomenon whereby Cooper pairs pass from a superconductor into an adjacent normal material. This effect is readily observed by

making a weak link between two pieces of superconductor. This heterostructure (superconductor-weak link-superconductor) forms the well-known Josephson junction. Effectively the junction acts like a weak superconducting link. The non-dissipative current of Cooper pairs through the junction is known as a supercurrent. The weak link material assumes properties reminiscent of a regular superconductor and exhibits a modified DOS as a consequence of the transport of Copper pairs through it.

### 3.2.1 Josephson Junctions

In 1962 Josephson introduced Josephson junctions based on the tunnelling effect. Tunnelling is a powerful probe of the superconducting state as it allows one to determine the energy gap of the superconductor and was important in verifying the BCS theory. Josephson described three types of junctions S-I-S, S-N-S and S-C-S junctions as shown in Fig. 3-13, where S, I, N and C refers to superconductor, insulator, normal metal and constriction respectively. All I, N and C, work as weak links in in these Josephson junctions. The weak link is simply a tunnel barrier for Cooper pair transport with a thickness limited by the length scale of the proximity effect.

Transport in the weak link material must be phase coherent and time reversal symmetry must be preserved. Graphene is a good candidate for the weak link material, as it is capable of satisfying these two conditions. Thus, it can support Cooper pair transport over short distances. The supercurrent in superconductor-graphene-superconductor (SGS) junctions can also be tuned by the gate voltage. In addition, Josephson also introduced two ways in which current can flow from one superconductor to the other through the weak link. The current from the transport of Cooper pairs at zero bias voltage is described by the DC Josephson effect. Above $I_c$ the current results from the tunnelling of individual quasiparticles, maintaining a constant non-zero voltage across the link, and is described as the AC Josephson effect. These Josephson effects exist in all types of weak link Josephson junctions and play an important role in superconducting applications [62]. There are two important equations that describe the behaviour of Josephson junctions.

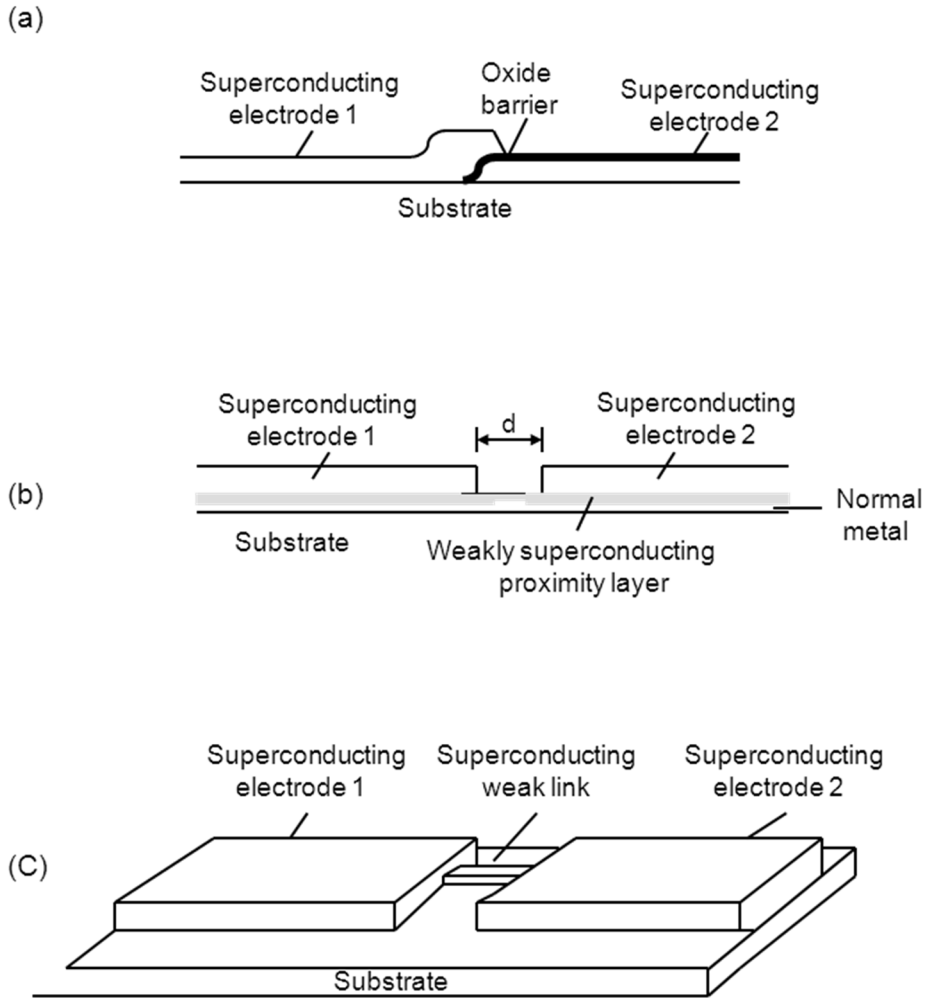


**Figure 3-13:** Different types of Josephson junctions. Adapted from [63].

The first equation describes the DC Josephson effect, in which the current in the junction is proportional to the sine of the difference in phase, $\Delta\Phi$, between the electrodes

$$I_s = I_c \sin \Delta\Phi \,, \tag{3-30}$$

where $I_c$ is the maximum supercurrent that the junction can support and $\Delta\Phi$ is the difference in phase of the GL order parameter in the two superconducting electrodes [63]. Hence in equilibrium (V = 0) the direct current flowing through the junction depends on the phase difference across it $\Delta\Phi = \Phi_2 - \Phi_1$ and arises as a consequence of the tunnelling of Cooper pairs. A DC supercurrent was observed experimentally shortly after Josephson's initial predictions. Figure 3-14 shows a schematic I-V curve for Josephson tunnelling in a junction with two similar electrodes. The maximum Josephson current, $I_c$, is obtained at zero voltage, which

results from the tunnelling of Cooper pairs. Upon increasing the voltage across the junction an abrupt current turn on occurs at $eV = 2|\Delta|$, where $|\Delta|$ is the superconducting energy gap, and the junction becomes Ohmic once the voltage exceeds the gap in the quasiparticle DOS. For two dissimilar superconductor electrodes with gaps $|\Delta_1|$ and $|\Delta_2|$, the abrupt turn on occurs at $eV = |\Delta_1| + |\Delta_2|$ .

The second equation relates the time dependence of the phase difference to the voltage across the Josephson junction and describes the AC Josephson effect.

$$\frac{d\Phi}{dt} = \frac{2eV}{\hbar}, \tag{3-31}$$

where $V$ is the voltage applied across the junction. Applying a constant non-zero voltage across the tunnel barrier produces an alternating current that has angular frequency $\omega = 2eV/\hbar$, which results from the flow of Cooper pairs tunnelling through the barrier. This oscillating current is still flows, but with small amplitude signal, at voltages lower than $2|\Delta|/e$, and it can be recorded either with applying microwaves radiation to the junction or with being on the return branch of an unshunted junction. A photon with energy $\hbar\omega = 2eV$, either emitted or absorbed, accompanies the flow of each Cooper pair through the weak link. The oscillating current of Cooper pairs, which flow through the link under the applied voltage, represents the AC Josephson effect. The microwave frequency range (GHz) is the appropriate one to observe this phenomenon. Applying microwaves to Josephson junctions leads to the observation of equidistant steps (Shapiro steps) in the I-V characteristic. These steps are observed at voltages that depend on the microwave frequency, $\omega$, $V_n = n\hbar\omega/2e$ [62]. Figure 3-15 sketches an experimental I-V curve for a Josephson junction in which the AC Josephson effect leads to steps that occur at harmonics between the DC Josephson frequency and the applied AC frequency [76].

The dependence of the amplitude of the DC Josephson supercurrent on the applied magnetic field is presented in Fig. 3-16, and described by,

$$I_c(\Phi) = I_c(0)\left|\frac{sin(\pi\Phi/\Phi_0)}{\pi\Phi/\Phi_0}\right|, \tag{3-32}$$

where $\Phi$ is the magnetic flux threading through the weak link in the junction and $\Phi_0$ is the flux quantum [62]. The Fraunhofer-like dependence of the critical current on magnetic field is similar to the situation of diffraction of light through a single slit.

The minima in $I_c$ arise at integer multiplies of flux quanta ($\Phi = n\Phi_0, n = 1, 2, 3, \ldots \ldots$) [62].

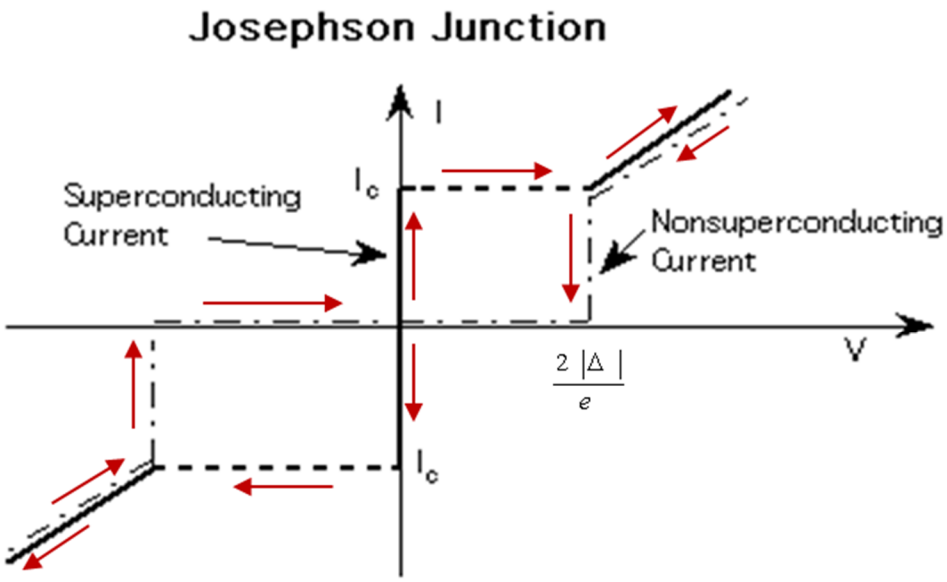


**Figure 3-14:** Typical I-V characteristic for the DC Josephson effect. The maximum Josephson current $I_c$ is obtained at $V = 0$, and an approximately Ohmic I-V characteristic is obtained for $eV > 2|\Delta|$.

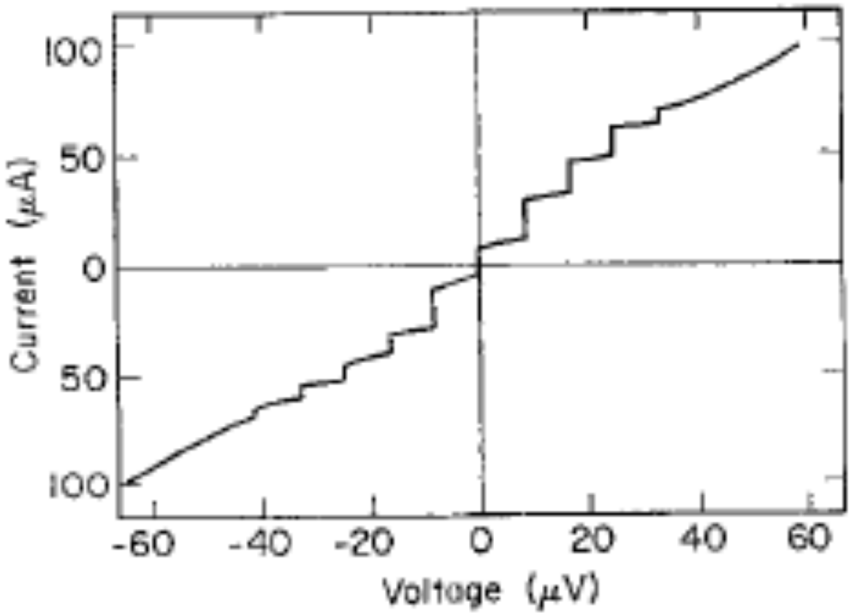


**Figure 3-15:** Constant current steps in the I-V characteristic for a Sn-SnO-Sn junction irradiated with 4 GHz microwaves (Shapiro steps) [76].

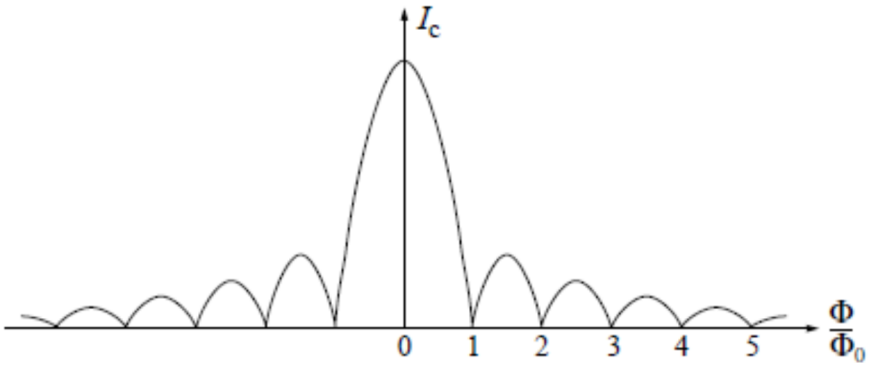


**Figure 3-16:** $I_c - \Phi$ characteristic for a DC Josephson Junction [62].

### 3.2.2 Andreev reflection

An important processes that is central to the proximity effect is Andreev reflection (AR) [77]. AR is a charge-transfer mechanism that converts single electron states incident at normal/superconductor (N/S) interfaces to Cooper pairs in the superconducting layer [78]. In the AR process, an incident electron from the normal metal side with energy $E < \Delta$ (superconducting gap) cannot transfer to the superconducting side. This electron is converted into a reflected hole at the N/S interface. The reflected hole has opposite spin and charge to the incident electron. The retro-reflected hole retraces the same trajectory as the incident electron as shown in Fig. 3-17. A charge $2e$ is lost in the retro-reflection process; this is equivalent to two single electrons with opposite momenta and spin that enter the superconductor as a Cooper pair [79]. To summarise the AR process, it is a mechanism in which the reflection of an electron (hole) and a transfer of a Cooper pair in or out of the superconducting condensate are equivalent [78].

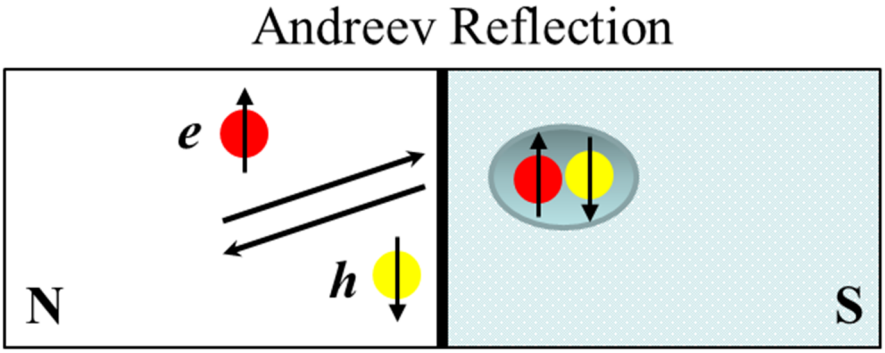


**Figure 3-17:** Illustration of the AR process.

The AR process in the case where the normal metal is replaced by graphene is shown in Fig. 3-18 [79]. In this illustration the Fermi energy lies in the conduction band and both electron and hole come from the conduction band. The electron excitation is shown as a filled state at energy $\epsilon$ above $E_F$, whilst the empty state at energy $\epsilon$ below $E_F$ represents a hole excitation. AR in graphene is achieved for the situation where the Cooper pair carries zero total momentum. This is realised by taking both electron and hole from opposite valleys $(\pm K)$ of the Brillouin zone [79]. The AR process presented in Fig. 3-18 shows the case of intra-band Andreev reflection which occurs in the case of doped graphene.

In undoped graphene, when the Fermi energy, $E_F$, lies at the Dirac point, an unusual electron-hole conversion occurs which is known as specular Andreev reflection (SAR). SAR represents the case of inter-band Andreev reflection in which an electron excitation in the conduction band will be scattered into a hole excitation in the valence band. In normal AR, the retro-reflected hole travels along the same trajectory as the incident electron, and a change in sign of all components of the velocity $(v_x \text{ and } v_y)$ of the charge carrier occurs. In SAR the hole is reflected with an inverted reflection angle, and one component of the velocity $(v_x \text{ or } v_y)$ which is perpendicular to the interface changes its sign, whilst the other component $(v_x \text{ or } v_y)$ is the same as that of the incident electron. The sketches shown in Fig. 3-19 distinguish between the usual AR and the SAR processes.

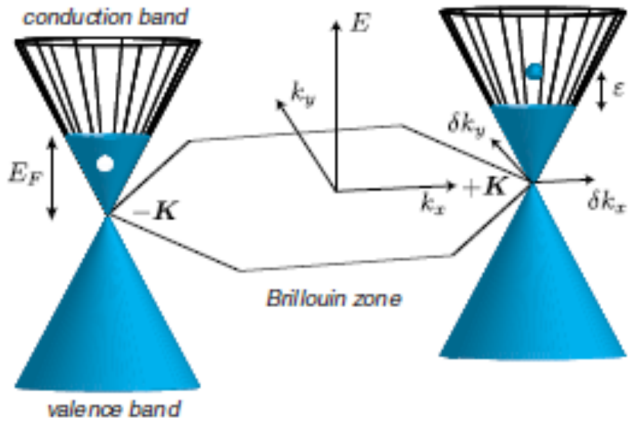


**Figure 3-18:** The AR process in the conical band structure found in graphene. Electron (filled circle) and hole (empty circle) excitations lie at energies $E_F + \epsilon$ and $E_F - \epsilon$ respectively [79].

Another feature which has been observed in SGS Josephson junctions is multiple Andreev reflection (MAR). In a voltage-biased SGS junction, a few local minima in the differential resistance occur at specific voltage values where the bias voltage is twice the superconducting gap, Δ, divided by an integer. MAR is shown in Fig. 3-19. Three dips are observed at $V = \frac{2\Delta}{3}$ , $V = \frac{2\Delta}{2}$ and $V = 2\Delta$ , where $\Delta = 0.125\, meV$ for the Ti/Al superconducting electrodes used in this device [80].

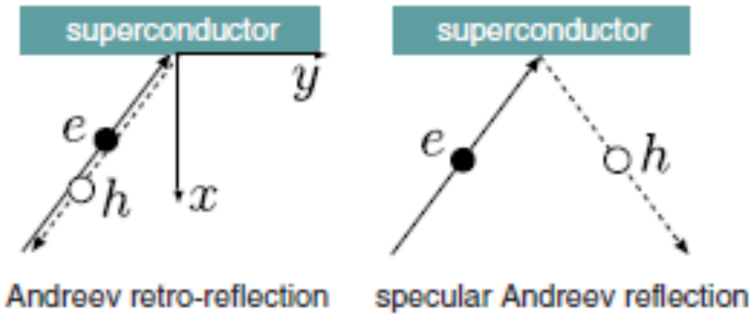


**Figure 3-19:** AR (left) and SAR (right) processes. Solid arrows present the incident electron, whilst the dotted arrows represent the reflected holes in both cases [79].

The MAR process occurs in the following way. An electron moving in a normal region towards the second N/S interface, may be Andreev reflected into a moving hole towards the first N/S interface, which may then in turn have a probability of creating an Andreev reflected electron that moves again towards the second N/S interface. When a voltage bias is applied to the junction, the Andreev reflected hole and electron both gain energy $eV$ per transit, regardless of whether they traverse the junction from left to right or vice versa. Thus, a twice Andreev reflected electron gains energy $2\,eV$ [81]. Since, this process is associated with creating extra charge carriers through Andreev retro-reflection it leads to increases and decreases in the conductivity. Where an increase in the number of extra charge carriers occurs at the allowed reflection, a sharp increase in conductivity is obtained, followed by a decrease in conductivity until the energy is large enough to satisfy another allowed MAR transition. Andreev reflection dips in differential resistance in Fig. 3-20 illustrate this cycle of increasing and decreasing conductance.

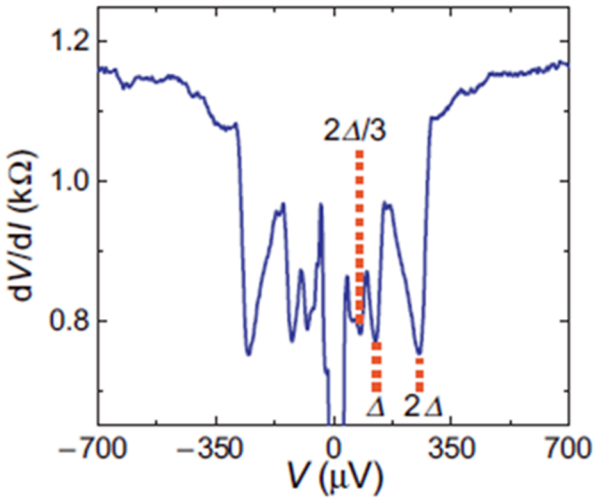


**Figure 3-20:** MAR in a SGS junction. Andreev reflection dips in the differential resistance occur at energies below the superconducting gap, Δ [80].

## 3.3 Superconductivity in graphene and prior work on the proximity effect in graphene Josephson junctions GJJs

Graphene is not normally a superconducting material. However placing it between two superconductors creates SGS proximity junctions in which graphene takes on superconducting characteristics. SGS junctions have attracted significant attention due to the remarkable tuneable electronic properties of graphene with gate voltage [82]. In addition, the charge carriers in graphene behave as massless Dirac Fermions as a result of the linear relationship between energy and momentum and exhibit non-zero minimum conductivity, $\sigma_{min} \approx 4e^2/h$, at the point where the valence and conduction bands touch each other (Dirac point), and the free carrier concentration vanishes [83].

A systematic investigation of induced superconductivity in an S-graphene-S Josephson junction is described by Hubert *et al.* [80]. Experimental preparation of low resistance electrical contacts on the graphene surface is achieved by depositing metals using a standard thermal evaporation technique. A back gate can then be used to sweep the Fermi level from the conduction band to control the carrier type and concentration. This is of great interest as it allows investigation of the proximity effect mediated by both electrons and holes. It also allows the behaviour close to the Dirac point (the charge neutrality point) to be studied [84].

Both phase coherence and time reversal symmetry (TRS) should be preserved in the normal conductor (graphene) which links two closely spaced superconducting electrodes. The Josephson effect in graphene allows the supercurrent carried by Dirac electrons in the relativistic regime to be investigated [80].

From the point of view of Cooper pair transfer in graphene, a non-zero critical supercurrent at the DP was predicted theoretically in a S-graphene-S Josephson junction and this has been verified experimentally [83].

**Prior work on the proximity effect in graphene JJs**

This section gives an overview of past and current research on the proximity-induced superconductivity in graphene.

Heerche *et al*. investigated devices with Ti/Al bilayer (10/70 nm) superconducting contacts as illustrated in Fig. 3-21 [69]. Proximity-induced superconductivity in graphene was observed after cooling the devices below the critical temperature of the Al electrodes ($T_c$ ~ 1.3 K). The existence of a Josephson supercurrent was clear evidence for the induced superconductivity [80].

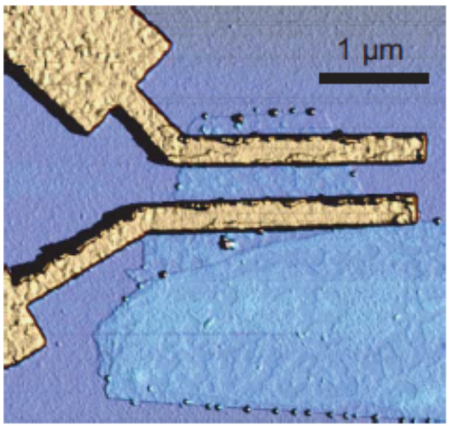


**Figure 3-21:** AFM image of two Ti/Al superconducting electrodes on top of a single graphene layer [80].

I-V characteristics for single layer devices at different values of $V_g$ are shown in Fig. 3-22. It was demonstrated that these devices work as bipolar supercurrent transistors whereby the supercurrent is transported in both hole and electron carrier regimes with the Fermi level in the valence band and conduction bands respectively. These studies were made possible by varying $V_g$, allowing the Fermi level to be swept from the valence band ($V_g < V_D$) to the conduction band ($V_g > V_D$). The Fermi

level crosses the Dirac point during these investigations where a finite supercurrent was recorded regardless of the fact that the density of states is expected to vanish here. All single layer samples exhibited this behaviour regardless of the value of the gate voltage at the DP, illustrating that the electronic transport in graphene is phase coherent even when the Fermi level is placed at the charge neutrality point [80]. The value of the critical current, $I_c$, was found to vary from 10 nA to more than 800 nA depending on $V_g$. The width of the graphene layer, the spacing between the contacts and the gate voltage , $V_g$, are the three parameters that control this value [84].

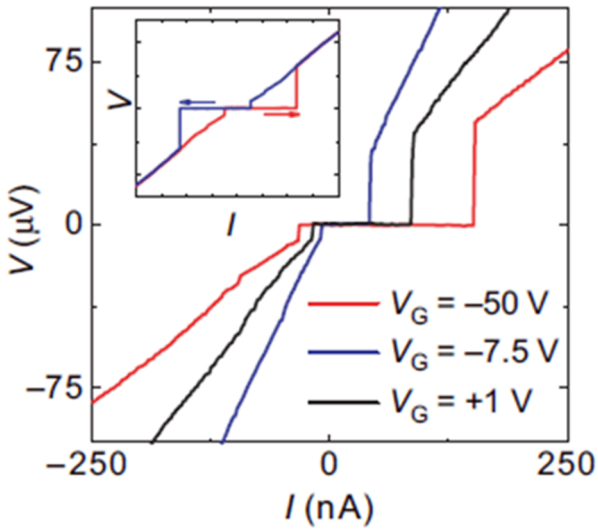


**Figure 3-22:** I-V characteristics at different gate voltages (T = 30 mK). The result of sweeping the current bias from negative to positive values and vice versa is shown in the inset [80].

Figures 3-23, 3-24 illustrate the temperature and magnetic field dependence of the critical current. The oscillations in the Fraunhofer pattern in Fig. 3-24 exhibit a good relationship between the periodicity (2.5 ± 0.5 mT) and the expected ratio of $\Phi_0$ divided by the area of the junction (0.7 ± 0.2 μm$^2$). Furthermore, this interference pattern confirms that the supercurrent density distribution is spatially uniform [84].

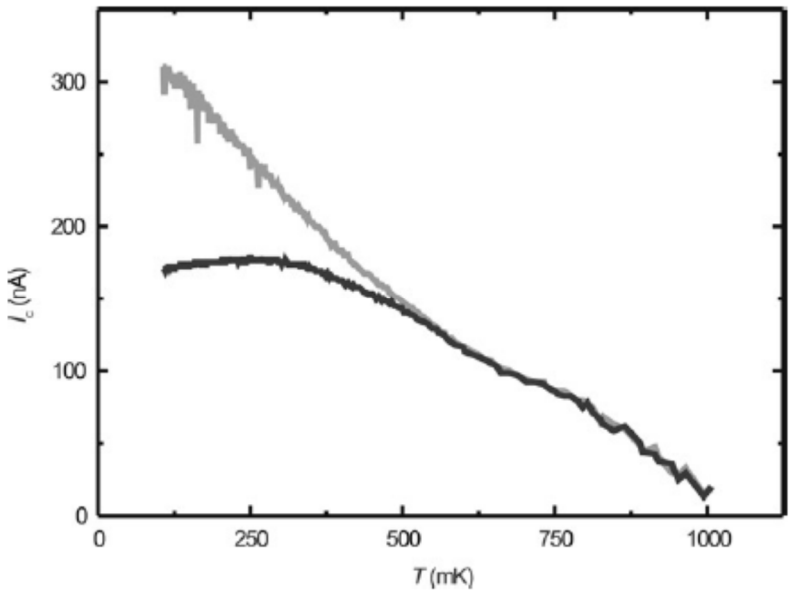


**Figure 3-23:** Dependence of the critical current on temperature ($V_g$ = 0 V). The retrapping and switching currents are described by the black and the grey curves respectively [84].

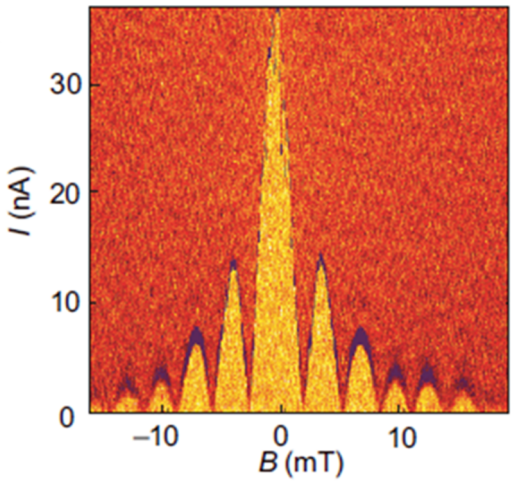


**Figure 3-24:** Fraunhofer-like dependence of the critical current on magnetic field. The supercurrent and the normal current regimes are indicated by the yellow and the red colours respectively [84].

Figure 3-25 shows the subgap structure in the form of a series of minima at certain source-drain voltages. The subgap structure is another direct proof of induced superconductivity in graphene. The superconducting gap can be determined using the equation $V = 2\Delta/en, (n = 1, 2, \dots)$, where $\Delta$ is the superconducting energy gap of the electrodes. There is good agreement between the expected and the experimental value of the superconducting gap, $\Delta = 125\ \mu eV$ for Ti/Al bilayers [84].

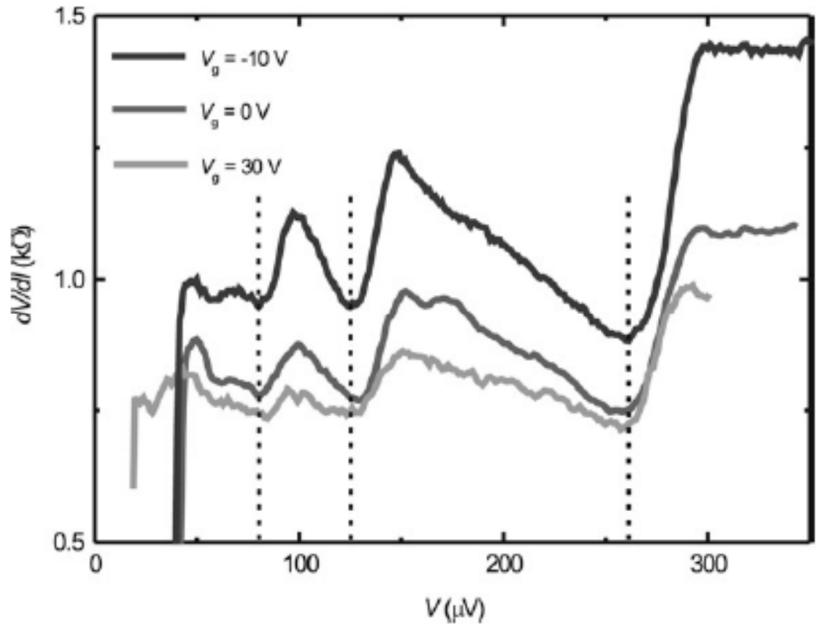


**Figure 3-25:** The differential resistance dV/dI as a function of bias voltage. Andreev reflection dips can be seen at positions where the voltage $V < 2\Delta$ (T=30mK) [84].

Sato *et al.* investigated a thick graphene flake containing around 30 layers with a thickness of ~ 10 nm. In their design they used it to link two superconducting electrodes (Pd (5 nm)/ Al (100 nm)) with a spacing of 0.4 μm. Figure 3-26 shows a scanning electron micrograph and a schematic diagram of their sample [83].

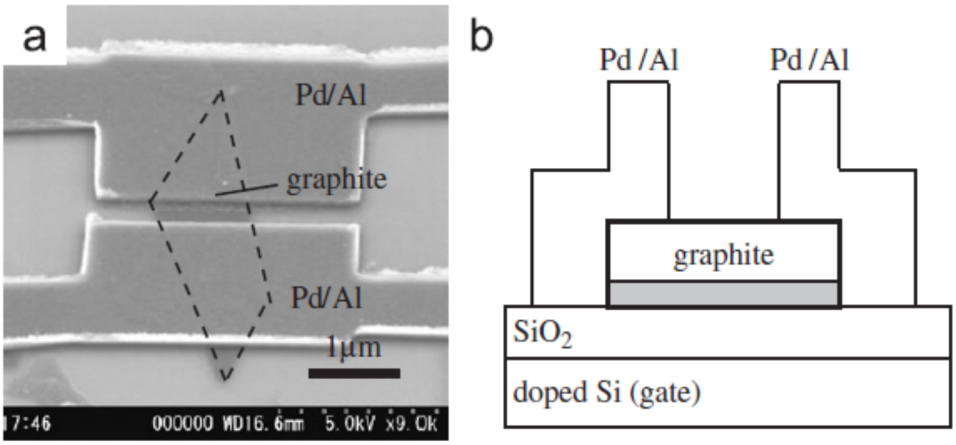


**Figure 3-26:** a) Scanning electron micrograph of the sample prepared by Sato *et al.* b) A schematic diagram of this device [83].

Sato *et al.* used a lock-in measurement method with an excitation current of 10 nA to measure the zero-bias resistance (ZBR) and numerically differentiated I-V

characteristics to obtain the differential conductance. A doped Si substrate back gate was used. The dependence of the ZBR of their (A) sample on the temperature at different $V_g$ values is shown in Fig. 3-27. The Pd/Al electrodes used have a superconducting transition temperature of 1.1 K. Thus, the normal state resistance, $R_n$, of the S-G-S junction is the value shown above 1.1 K. The maximum value of the ZBR occurs at gate voltage $V_g^p$. Below 1.1 K, two resistance drops are observed, one around 1.1 K and the other at lower temperatures. Around 1.1 K the superconducting transition of the Pd/Al electrodes occurs and there is no dependence of this resistive transition on the gate voltage. The second drop is related to the proximity induced superconducting transition of the graphene film [83].

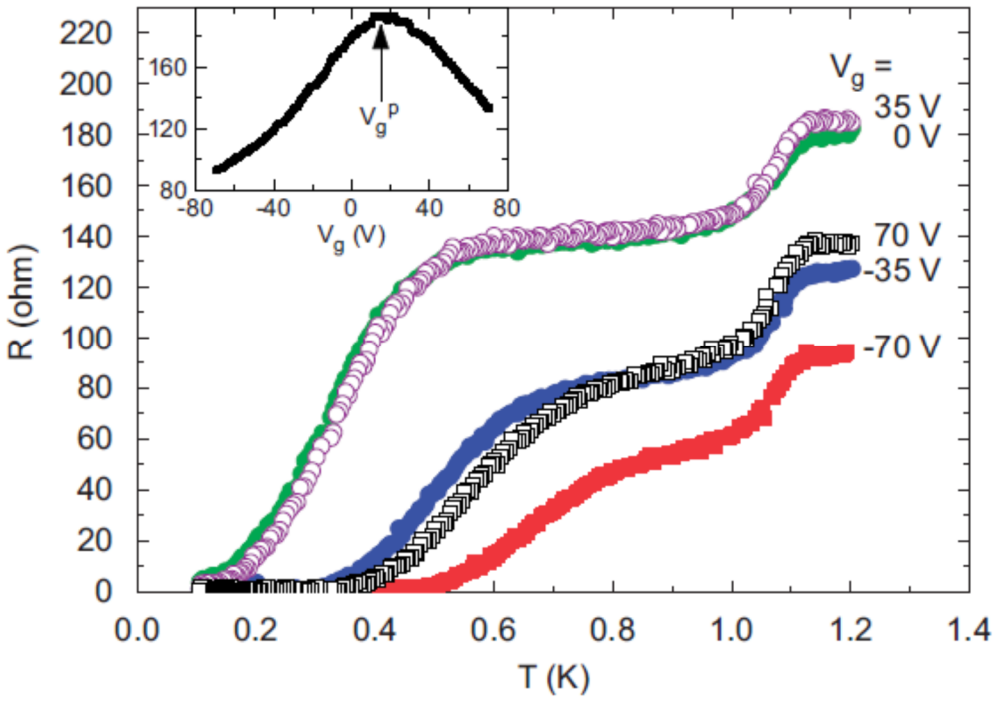


**Figure 3-27:** The relation between the zero-bias resistance and temperature of sample (A). The solid symbols refer to the resistance values taken at $V_g$ =-70, -35, 0V, whereas the open symbols indicate the values taken at $V_g$ = 35, 70V. The gate-voltage dependence of the normal-state resistance is shown in the inset. The maximum value of the normal-state resistance is obtained at $V_g = V_g^p \approx 15$ V [83].

The differential resistance of their (A) sample at 0.06 K is presented in greyscale in Fig. 3-28 (a), where the current has been swept from negative to positive values. The retrapping current, $I_r$, and the critical current, $I_c$, caused two switches in the junction from the resistive to zero-voltage states and vice versa. Figure 3-28 (c) reveals a strong dependence of $I_c$ & $I_r$ on $V_g$. It was deduced that the base graphene layers were responsible for carrying the supercurrent and that the supercurrent totally vanishes at $V_g^P$ (c.f., Fig. 3-28 (b)) [83]. Sato *et al.* concluded that just a few layers of graphene carry the supercurrent. They found that the effective normal resistance for their films, which consists of 30 layers of graphene, would be about 10 times larger than the observed value. This conclusion was confirmed by the data shown in the inset of Fig. 3-28 (c). The calculated value of $I_c R_n \approx \left(\frac{\pi\Delta}{2e}\right) \approx 260\ \mu V$ was nearly equal to the observed value multiplied by 10, confirming their prediction [83].

Ojeda-Aristizabal *et al.* fabricated SGS junctions using a Pt/Ta/Pt trilayer of thicknesses 3/70/3 nm where Ta is the superconducting lead. The spacing between the superconducting leads was 330 nm in their device and the width of the junction was 2.7 µm. They found that the quality of the graphene/electrode interface was considerably improved by current annealing their samples [85].

Even though W and Pt/Ta represent alternative choices for the superconducting electrodes, a long annealing step is found to be needed to clearly observe the supercurrent in these devices [85, 86]. Using a higher energy gap material helps to overcome problems associated with the external noise affecting measurements of Al-based SGS junction devices below 1 K. Thus, Jeong *et al.* introduced new SGS junctions using PbIn alloy superconducting electrodes [87]. Jeong *et al.* fabricated their devices using $Pb_{0.39}In_{0.07}$/Au (200/10 nm) as superconducting electrodes with widths of 900 nm and spacings of 300 nm [87].

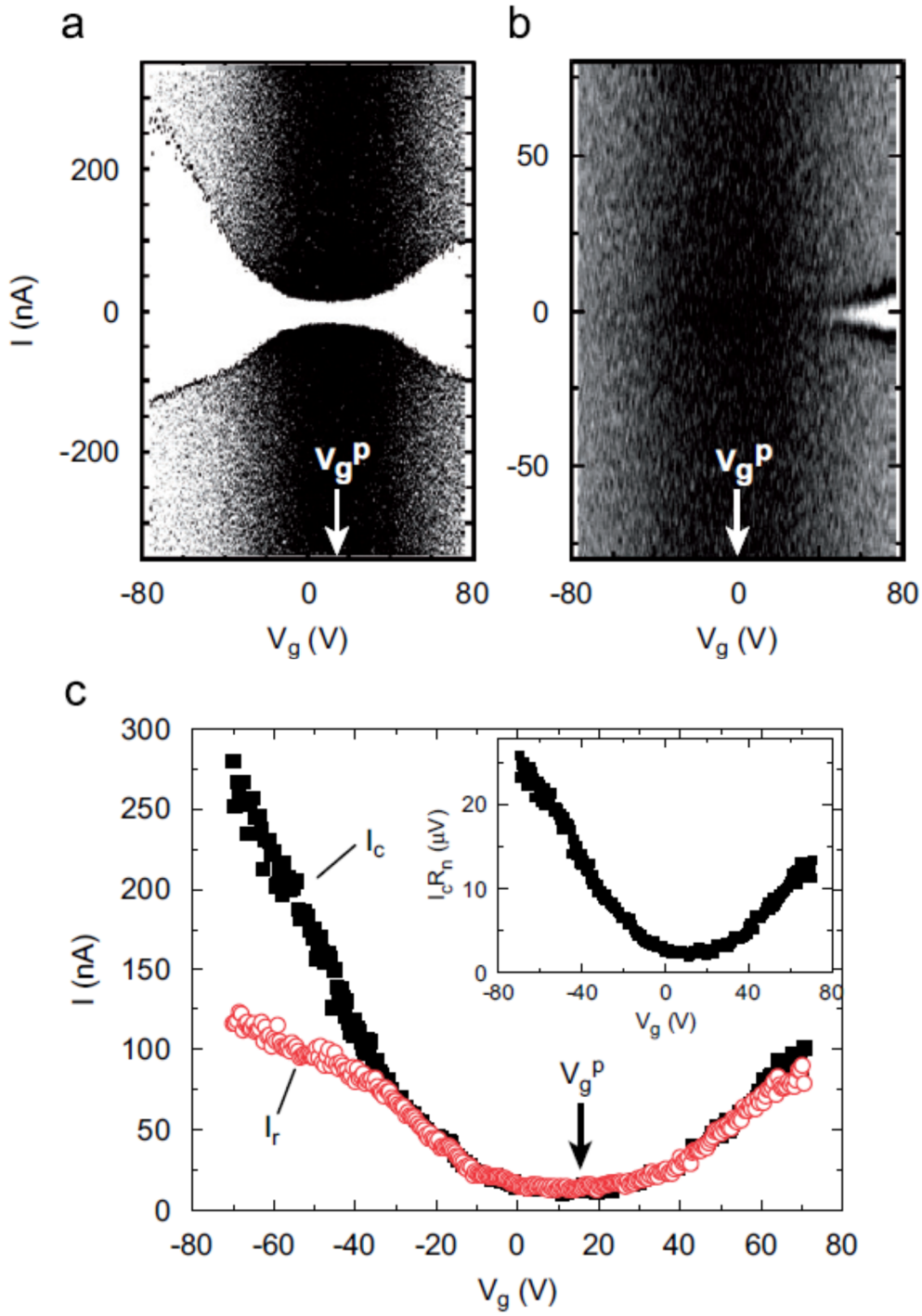


**Figure 3-28:** a) A greyscale plot of the differential resistance in the I-$V_g$ plane for sample (A) at 0.06 K. The white region shows the zero resistance supercurrent and the black region represents the resistive current at $250\,\Omega$. b) The same plot as (a) but for sample (B). c) The critical current, $I_c$, and the retrapping current, $I_r$, of sample (A) at 60 mK plotted as a function of $V_g$. The inset displays the gate-voltage dependence of the $I_cR_n$ product of sample (A) [83].

The microwave response of the junction was investigated by exposing it to microwave radiation with frequencies varying from 6 to 21 GHz. This allowed them to study the AC Josephson effect and to observe quantized voltage plateaus (or Shapiro steps) in the I-V curves. The Shapiro steps in Fig. 3-29 (a), were recorded at bias voltages of $V_n = nhf/2e$ [63]. The interval between neighbouring steps, $\Delta V$, was found to be $12.4\ \mu V$. The dependence of $\Delta V$ on microwave frequency is plotted in Figs. 3-29 (c) and 3-29 (d), where a good agreement with the AC Josephson relation $\Delta V = hf/2e$ is found as reflected by the solid line in Fig. 3-29 (d). The modulation of $\Delta V$ with the microwave power $\left(P^{1/2}\right)$ is presented in the inset of Fig. 3-29 (a). The effect of varying temperature on the I-V curve for the irradiated junction with $f = 6\ \mathrm{GHz}$ and at gate voltage of $V_g = 60\ \mathrm{V}$ is illustrated in Fig. 3-29 (b). Normalising the voltage by $hf/2e$ for $T = 4.2, 4.8$ and $5.4\ \mathrm{K}$, helps to determine the specific temperature, at which the quantized voltage plateaus disappear. This is shown in the inset of Fig. 3-29 (b) [87].

Another approach has been introduced by Kessler *et al*. [88]. The difficulties accompanied with fabricating narrow-spaced superconducting electrodes in SGS junctions were avoided by "decorating" graphene sheets with a non-percolating network of nano-scale tin clusters. This technique allows one to dope the graphene sheet efficiently, as well as to induce long-range superconducting correlations in it. Figure 3-30 (a) shows a scanning electron micrograph of a graphene sheet decorated with Sn islands, as well as an optical image of the four terminal device. Figure 3-30 (b) illustrates the influence of gate voltage on the resistance at 300 K before and after Sn deposition. It was found that for a 10 nm average deposition thickness led to the creation of Sn islands with $80 \pm 5\ \mathrm{nm}$ diameters and $25 \pm 10\ \mathrm{nm}$ spacings between them [88].

Even though the deposited Sn islands represent an inhomogeneous Sn layer, they behave as a weakly disordered two-dimensional superconductor. Figure 3-31(a) shows a partial drop in the sheet resistance at $T_c^{bulk} = 3.72\ \mathrm{K}$, when the condensation of Cooper pairs in the Sn islands occurs. Good agreement between the experimental data and a fit using Aslamazov-Larkin formalism [89] is obtained. The main pairing temperature $T_{c0}$ of $3.54 \pm 0.02\ \mathrm{K}$ has been estimated by fitting the equation in the temperature range 3.8-4.5 K.

Kessler *et al.* extracted values for the vortex-antivortex unbinding temperature, $T_{BKT}$ [88] using the universal form of the flux flow resistance [90] at different gate voltages as shown in Fig. 3-31 (b). This new self-assembling approach represents significant progress in producing a 2D graphene-based superconductor and is an attractive approach for investigating other forms of electronic order such as magnetism in two dimensions [88].

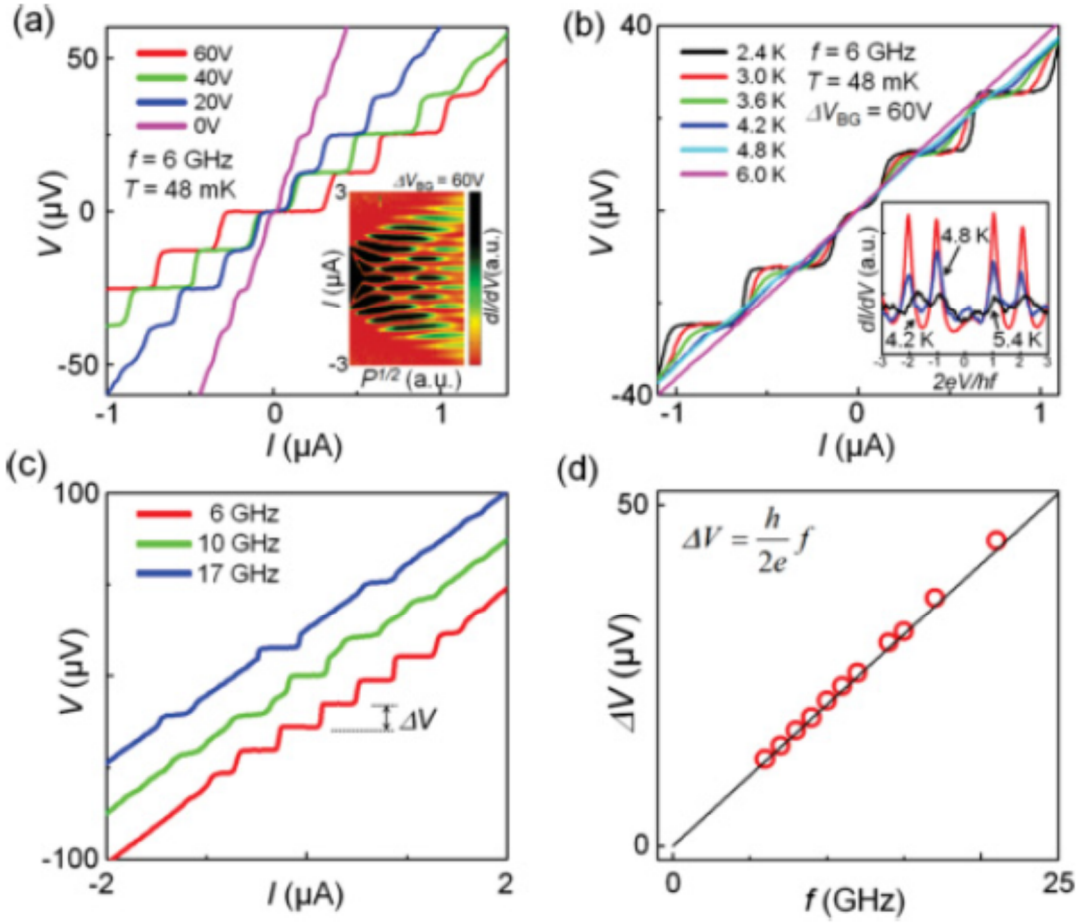


**Figure 3-29:** a) I-V characteristics for an irradiated PbIn-G-PbIn junction ($f = 6\,\text{GHz}$) at $T = 48\,\text{mK}$. The inset shows the relation between *dI/dV*, *I*, and $P^{1/2}$ at $V_g = 60\,\text{V}$. b) Influence of changing temperature on the I-V curves of the irradiated junction at $f = 6\,\text{GHz}$ and $V_g = 60\,\text{V}$. The inset plots *dI/dV* versus $2eV/hf$ at $T = 4.2, 4.8 \text{ and } 5.4\,\text{K}$. c) The influence of varying the microwave frequency on the appearance of Shapiro steps in the I-V characteristics. d) The dependence of $\Delta V$ on the microwave frequency in the range $f = 6 - 21\,\text{GHz}$ [87].

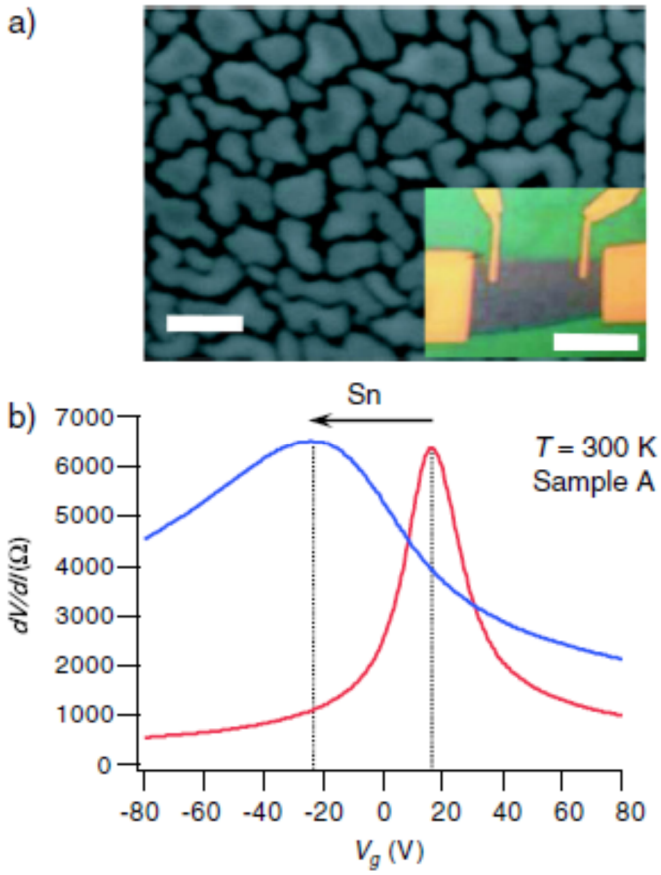


**Figure 3-30:** a) SEM image of Sn islands on the graphene sheet. The inset displays an optical image of the four terminal device. b) The effect of the deposited Sn islands on the graphene sheet resistance [88].

Allain *et al*. fabricated several devices, varying both the thickness of Sn layer (8-20 nm) as well as the number of graphene layers in each device. No significant correlation was found between behaviour of their devices and the values of these two parameters [91].

Girit *et al*. succeeded in fabricating the first working DC superconducting quantum interference device (SQUID). In their device, the SQUID loop consists of two SGS junctions formed from a graphene monolayer with Pd/Al superconducting electrodes. Two control parameters can be used to modulate the supercurrent in this device; the electrostatic gate and the applied magnetic field. These properties make graphene-based structures powerful potential future platforms for nano-scale SQUID applications [92].

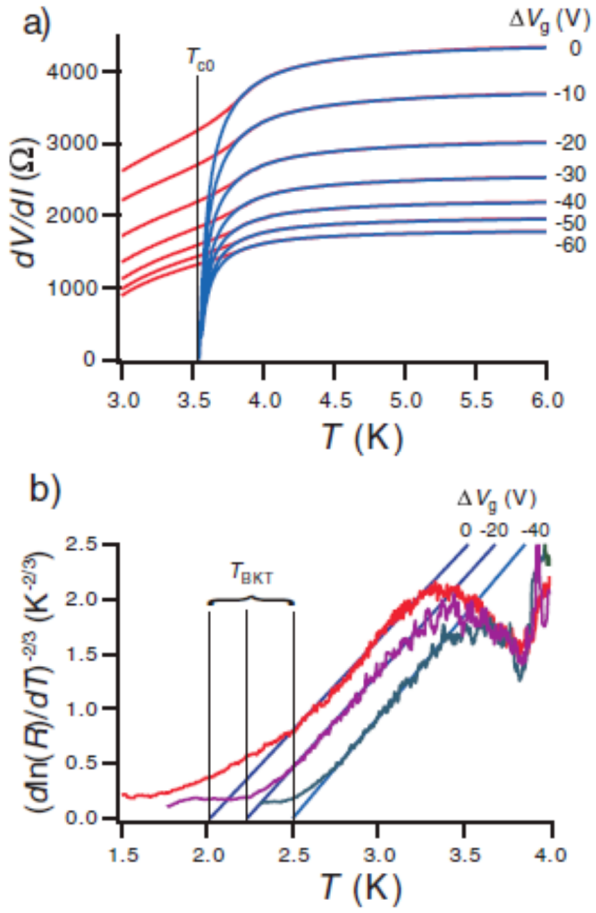


**Figure 3-31:** a) Fits to the Aslamazov-Larkin formalism (blue lines) to extract the value of $T_{c0}$. Red lines show the experimental data. b) Values of $T_{BKT}$ extracted at different gate voltages from plots of the rescaled sheet resistance versus temperature [88].

## 3.4 Prior work on superconductivity in few unit cell $NbSe_2$

This section presents an overview of past and current research in the area of superconductivity in few unit cell $NbSe_2$.

In 1972, Frindt [32] succeeded in exfoliating thin crystals of $NbSe_2$ from a bulk single crystal. Sticking a $NbSe_2$ single crystal onto various substrates such as mica, epoxy and fused quartz and repeatedly peeling off layers many times, allowed him to obtain a wide range of thicknesses of $NbSe_2$ films. He found that the critical temperature $T_c$ decreased with reduction in the number of molecular layers in the cleaved crystal. Also, the decrease in $T_c$ only became pronounced in crystals that were below six $NbSe_2$ molecular layers thick. The $T_c$ value for single layer $NbSe_2$ was estimated to be 3.8 K, whereas it is 7.2 K in a bulk 2H-$NbSe_2$ crystal [32].

Figure 3-32 shows the superconducting resistive transitions in the $NbSe_2$ films of different average thicknesses. Curve (a) was obtained by sticking the $NbSe_2$ crystal on an epoxy substrate, while curves (b), (c), and (d) have been obtained from exfoliated $NbSe_2$ crystals on mica substrates. The steps in curves (a) and (c) were proposed to be related to lateral (in-plane) inhomogeneity in the thickness of these $NbSe_2$ crystals. A reduction in the number of $NbSe_2$ molecular layers in these crystals did not appear to have any significant effect on the resistive transition width [32].

There has been renewed interest in 2D atomic crystals since the first isolation of graphene by the Manchester group in 2004 [1]. Single atomic/molecular layer films have been obtained by mechanically exfoliating bulk graphite, $MoS_2$ and $NbSe_2$. Figure 3-33 shows the change of conductivity of single layer of graphene, $MoS_2$ and $NbSe_2$ as a function of gate voltage at 300 K. These curves have been measured in field effect transistor-like devices as shown in the inset of Fig. 3-33. The mobility of a graphene monolayer was found to vary between 2,000 and 5,000 $cm^2/Vs$, whereas it was determined to be 0.5 and 3 $cm^2/Vs$ for 2D $NbSe_2$ and 2D $MoS_2$ respectively. Novoselov *et al*. suggested that the existence of significant changes in the electronic energy spectrum of 2D $NbSe_2$ makes it a semimetal, while it is a normal metal in 3D [1].

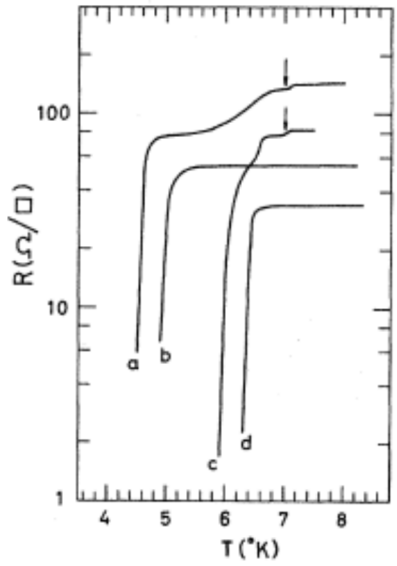


**Figure 3-32:** The resistive superconducting transition for $NbSe_2$ flakes exfoliated on various substrates, epoxy substrate for curve a and mica substrate for curves b, c and d [32].

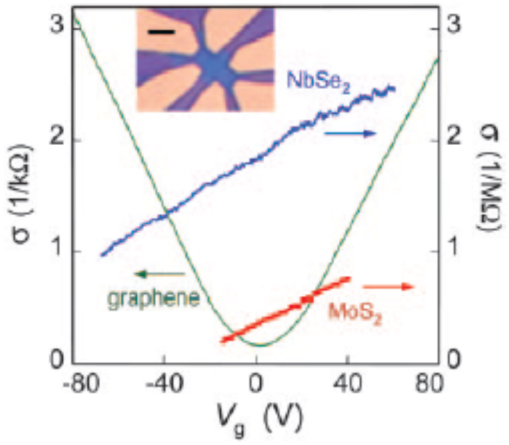


**Figure 3-33:** The influence of an applied gate voltage on the conductivity of single atomic/molecular layer crystals of graphene, $MoS_2$ and $NbSe_2$ [1].

Investigations of the effect of a transverse electric field on superconductivity in atomically thin flakes of $NbSe_2$ have been made by Staley *et al*. [31]. Their samples were fabricated using micromechanical exfoliation techniques. Their $NbSe_2$ flakes exhibited superconductivity at thicknesses down to a single unit cell. The critical temperature for a single $NbSe_2$ unit cell was estimated to be as high as 2.5 K. Staley *et al*. observed a clear modulation of $T_c$ with gate voltage in their thinnest flakes as can be seen in Fig. 3-34. The importance of cleaning samples by high-current annealing at low temperatures was highlighted. The behaviour of their thinnest flakes changed from non-superconducting to superconducting with an onset $T_c$ of to 2.5 K after annealing. Magnetoresistance measurements for two of their samples with 2-3 molecular layers of $NbSe_2$ are shown in Fig. 3-35. These data were obtained after current annealing and yielded a $\mu_0 H_{c2\perp}$ of ~ 1 $T$ [31].

2D TMDs are promising candidates for the fabrication of field effect transistors, and Zhang *et al*. [93] have succeeded in fabricating ambipolar $MoS_2$ thin flake transistors with a high on/off ratio $> 10^2$, using an electric double layer structure in their transistors. In this new electric double layer transistor (EDLT), the conventional dielectric (300 nm $SiO_2$) is replaced by higher dielectric gate oxides such as $HfO_2$ for improved EDLT performance. This new approach could play an important role in accessing hitherto unexplored properties in other layered metal chalcogenides [93].

Ayari *et al.* [94] exfoliated ultrathin crystals of two of the layered TMD material: $MoS_2$ (semiconducting) and $TaS_2$ (metallic) by mechanical peeling and chemical exfoliation respectively, and Cr/Au leads were deposited to form transistors. An on/off ratio greater than $10^5$ as well as a high field effect mobility (10's of $cm^2/Vs$) were observed in $MoS_2$ transistors. In addition, $TaS_2$ nano-patch devices remained metallic despite the existence of disorder due to the exfoliation process, and exhibited superconducting behaviour at low temperature [94].

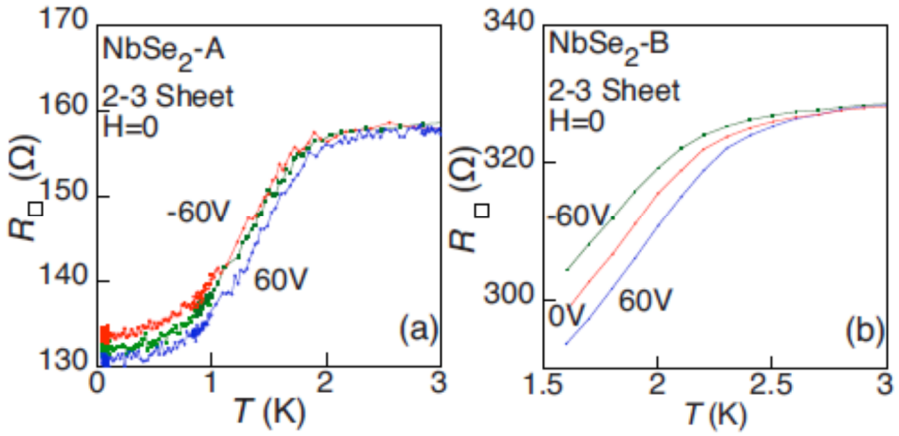


**Figure 3-34:** The effect of an applied gate voltage on the resistance of samples A and B (2-3 molecular layer $NbSe_2$ flakes) after cleaning by current annealing [31].

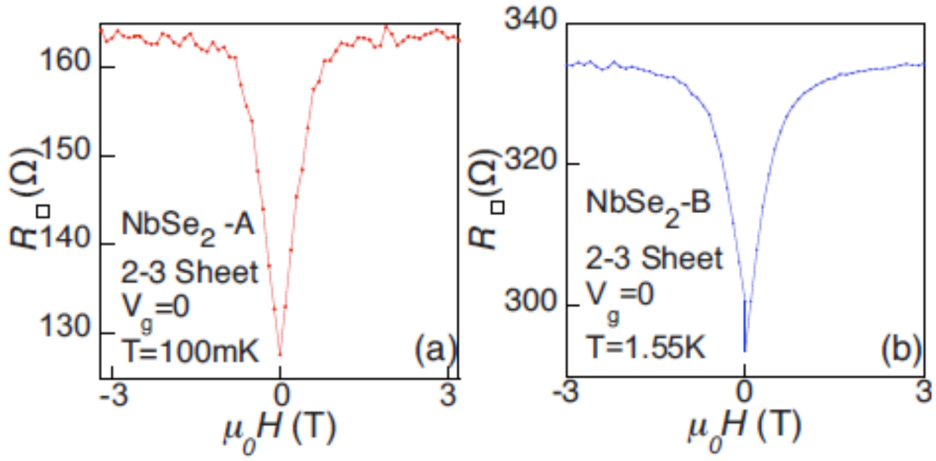


**Figure 3-35:** The effect of applying magnetic field on the resistance of samples A and B (2-3 molecular layer $NbSe_2$ flakes) after cleaning by current annealing [31].

# Chapter 4

# Experimental methods

## 4.1 FET device fabrication

This section is dedicated to a description of the methods that are used to fabricate FETs with both graphene and $NbSe_2$ flakes. One must take into account the fact that the transport properties of each sample depend on several factors that relate to the fabrication procedures. Some of these factors can either be controlled or avoided during fabrication, whilst the origin of other factors is not yet clearly established. Difficulties in establishing a reliable fabrication process for making low resistance Ohmic contacts to both graphene and $NbSe_2$ flakes motivated research within this project to establish reliable key technological steps to overcome this obstacle. The workflow chart in Fig. 4-1 presents a brief summary of the main procedures within this fabrication process route. Using these procedures yields a number of advantages as compared to some well-established techniques that have been reported in earlier publications [83, 84, 95]. These advantages can be summarised in the following points. Firstly, a registration marker pattern was printed on the $Si/SiO_2$ wafers to be able to search for flakes more easily. The advantage of adding registration marks before exfoliation is that graphene/$NbSe_2$ is subjected to one less lithographic step. Secondly, exfoliating graphene/$NbSe_2$ onto a clean wafer that has an array of registration marks helps to reduce possible contamination under the flake. Thirdly, coating the wafer ($Si/SiO_2$) surface immediately with PMMA (Poly methyl methacrylate) after flake deposition reduces the quantity of adsorbed material on top of the flake. Finally, protecting the flake from exposure to the environment during most of the fabrication process with a protective PMMA layer eliminates several factors that affect the quality of such devices. Flakes are only exposed to room air for a few minutes during the metallization and lift-off processes, followed by being exposed to the environment just immediately prior to inserting them into the measurement system after the packaging and bonding. The established

process from the initial wafer cutting to the final bonding stage will be discussed in further detail in this section.

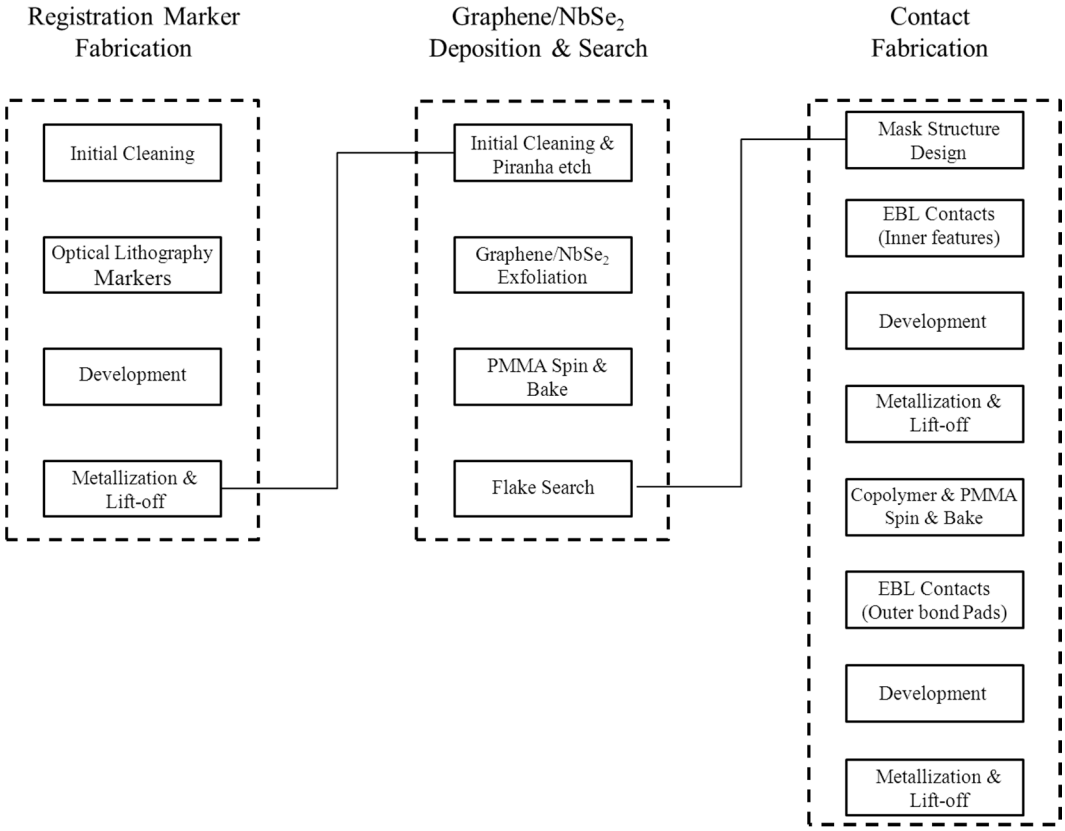


**Figure 4-1:** Workflow for FET device fabrication.

## 4.2 Description of $Si/SiO_2$ wafers

In view of the fact that measurements of the FET devices would occur at low temperatures down to mK temperatures, highly doped wafers ($Si/SiO_2$) were required to avoid carrier freeze out. Furthermore, choosing the right thickness of $SiO_2$ layer plays a key role in the optical identification of both graphene and $NbSe_2$ flakes [96, 97]. In the light of these requirements the following parameters were chosen in the $Si/SiO_2$ wafers used as substrates for fabricated FET devices. Wafers were specified as the following: 100 mm N‹100› CZ Si wafers with resistivity of 0.01-0.02 Ω.cm, thickness of 525 µm and single side polish with SEMI std flats. Wafers had 297.4 (+/- 1.5 %) nm of thermal oxide grown on both sides. The wafers were doped with Sb with density in the range of $4 - 6 \times 10^{18}$ atoms/$cm^3$.

### 4.2.1 Cutting Si wafers

Initially, $Si/SiO_2$ wafers were diced up into $1\,cm \times 1\,cm$ squares using a diamond scriber. The cuts followed the crystallographic axes of the wafer. The chosen size was considered suitable in order to obtain uniform thumb pressure during the exfoliation process, as described later in the chapter.

Once the devices were fabricated, the $Si/SiO_2$ substrate $(1\,cm \times 1\,cm)$ squares were scribed into smaller $3.75\,mm \times 3.75\,mm$ or $3.75\,mm \times 5.75\,mm$ chips with graphene or $NbSe_2$ flakes at the centre. These sizes were chosen to fit the chips into commercial ceramic packages for measurements.

### 4.2.2 Sample cleaning

Three cleaning methods were used throughout the entire fabrication process depending upon the requirements at each step. These methods were used to avoid any potential contamination to the flakes and are presented in the workflow in Fig. 4-2.

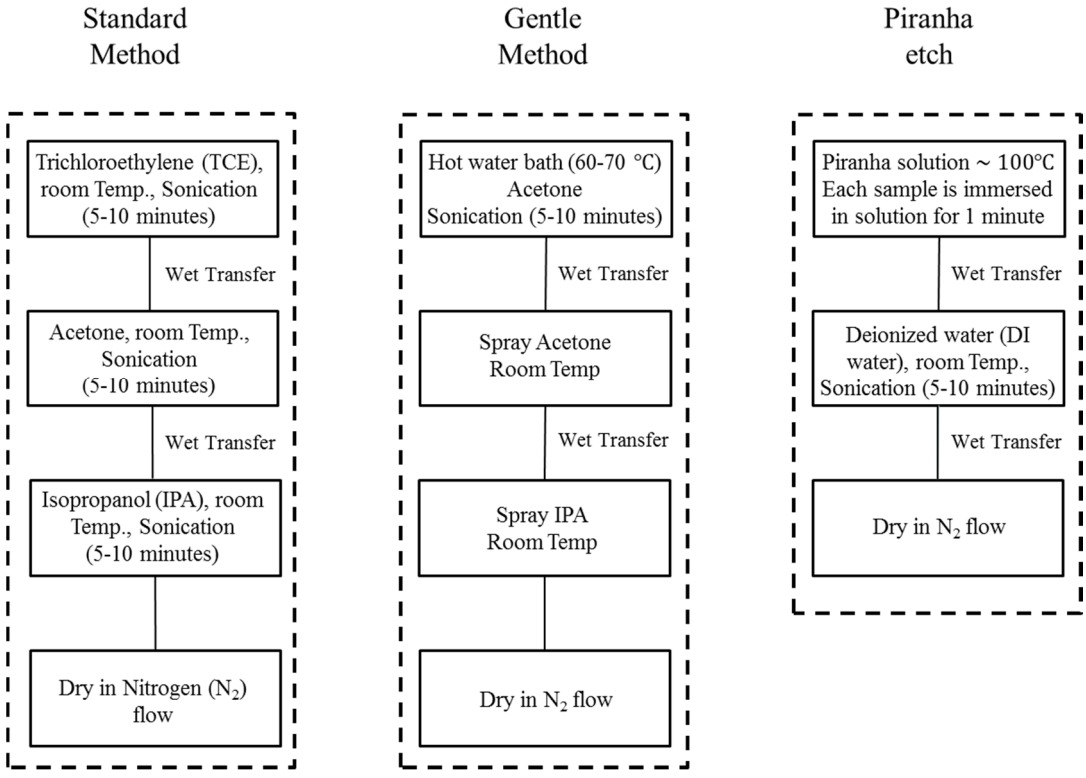


**Figure 4-2:** Workflow of cleaning methods used in the fabrication route.

The standard method was generally used on samples for all steps, with variation of both the power of the ultrasonic bath and the sonication time. For instance, when cleaning samples before flake deposition, a higher power of the ultrasonic bath coupled with a longer sonication time (50-70 % for 5-10 minutes) proved most satisfactory, while less power and time were chosen to clean samples after flake deposition (20-50 % for 2-5 minutes). The standard method was also used to clean the deposition materials and tungsten boats that were used in the metallization processes. The gentle method was used to remove the protective PMMA layer on top of the patterned design on the flake prior to measurement. The piranha etch was used to remove any organic residues from the substrate surface before flake deposition. Piranha solution is a mixture of sulphuric acid (concentrated) and hydrogen peroxide (30 % aqueous solutions) in a volume ratio of 3 : 1. Piranha is a strong oxidizer, and hydroxylates most surfaces (adds OH groups) producing a hydrophilic surface (water compatible). To form such a mixture hydrogen peroxide is slowly added to sulphuric acid. This order of mixing is important since sulphuric acid is a weaker oxidising agent than hydrogen peroxide. Hydrogen peroxide reacts exothermically with sulphuric acid and typically increases the solution temperature to ~ 100 ℃.

## 4.3 Registration Marks

### 4.3.1 Registration Mark Mask

An optical mask (a glass or quartz plate coated with a thin layer of chrome) was designed using Wave Maker software (5.004 Basic). On this mask an array of $45 \times 45$ numbered cross-shaped registration marks was made with a pitch of 200 µm. These marks were used for aligning the e-beam writer when contacts were made to the graphene/$NbSe_2$ flakes by electron beam lithography (EBL). The advantage of having registration marks before exfoliation was that the graphene/$NbSe_2$ flake was subjected to one less lithographic step. Figure 4-3 illustrates a small section of the registration mark mask.

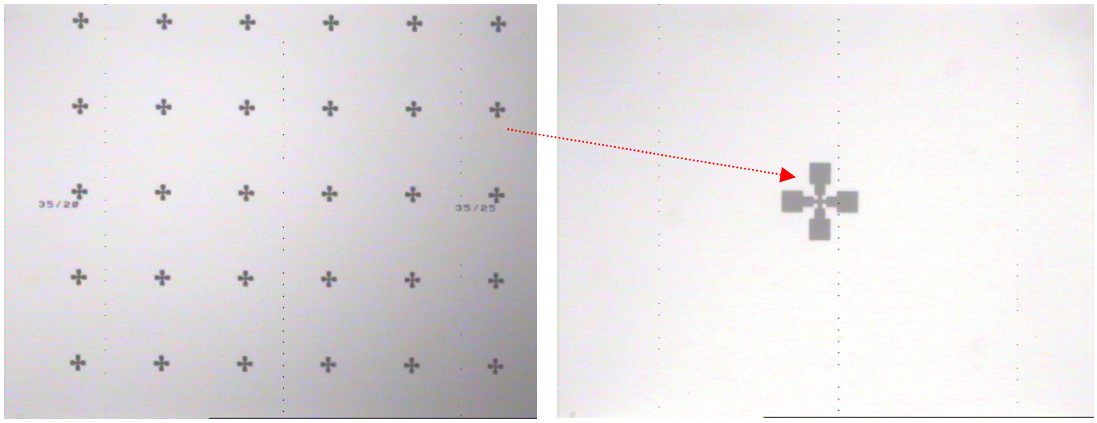

**Figure 4-3:** A small section of the registration mark mask plus a zoom of one of the marks in it.

### 4.3.2 UV lithography and evaporation

Photolithography is one of the basic means for transferring patterns to a substrate in nanofabrication technology. This process consists of two main steps, the spin coating of the photoresist onto the substrate surface using a spinner, and printing or transferring the pattern required from the mask to the substrate using a mask aligner. A brief description of photoresist materials is provided below, followed by a more thorough description of these two main steps.

A photoresist is typically a photon sensitive macromolecular polymer that it is usually sensitive to ultraviolet (UV) radiation. The photoresist is applied to the substrate by applying drops onto the surface, followed by a specific recipe in the spinner. A uniform thin film of resist is formed upon the substrate with a thickness dependent on the chosen spin speed and recipe. Samples are then baked to remove solvents, and exposed through the mask to UV light for a specific time using a mask aligner. After exposure, the resist is developed, leaving resist matching the pattern on the mask in the case of a positive resist.

Photoresists are classified into two tones, “positive” or “negative” depending on the chain length of the molecules. After exposure to UV light a positive resist becomes soluble and a negative resist becomes insoluble.

In the spin coating process, a spin coater is used to apply uniformly thin films of material onto the surface of the substrate. These materials are in liquid form after dissolution in a solvent, with the concentration determining its viscosity. A syringe

or pipette is used to dispense the liquid onto the substrate surface. Once on the spinner, a centrifugal force causes the liquid to spread out radially over the surface until it achieves the desired thickness. Hardening of the film and elimination of solvents is achieved by baking samples in an oven at 90º C for 30-60 minutes [98].

Shipley 1813 photoresist was used to pattern the registration marks on the $Si/SiO_2$ substrates. The recipe that was used in this case was as follows: (500 RPM (5 s) + 5000 RPM (30 s)). Samples were then baked in an oven at 90º C for 15 minutes, followed by soaking in chlorobenzene for 5 minutes to harden the top layer of the resist in order to leave an overhang profile post development. Finally, samples were baked again for 15 minutes at 90º C before using a mask aligner to pattern the registration marks. This last step made use of a mask aligner, a tool for transferring the pattern from a mask to a photoresist through UV exposure. A mercury vapour discharge lamp is generally the source of ultraviolet light. There are three common types of mask aligner (contact, proximity and projection) [98]. A contact mask aligner was used here whereby a direct contact between the optical mask and the sample occurs causing the effects of diffraction at the periphery of the mask features to be minimised. Frequent cleaning of the mask is required as residual resist is often deposited on it.

After UV illumination each sample was developed for ~ 30-45 seconds in a mixture of DI water: 351 Developer in a ratio of 3.5 : 1. The sample was then rinsed in DI water for ~ 15-30 seconds to terminate the development process at which point the photoresist had been removed from the exposed areas. Finally, Cr/Au (10/50 nm) was deposited using thermal evaporation, and the unwanted deposited gold "lifted off" around the registration marks. The deposition techniques as well as the lift-off process will be discussed in detail in sections (4.5.3) and (4.5.4).

## 4.4 Mechanical Exfoliation

Utilising a newly developed mechanical exfoliation protocol assisted in exfoliating high quality, large sized flakes of both graphene and $NbSe_2$. In the developed technique, magnetic disks were used to apply a well-controlled force to flakes. A 'mechanical exfoliation' method similar to "drawing by chalk on a blackboard" was used to create 2D graphene flakes. [1]. The sticky side of a piece of Nitto tape was pressed onto small pieces of natural graphite (NGS nature graphite

GmbH, graphenium flakes 1.0 – 1.8 mm) stuck on the other end of the tape. Pulling the tape away from the graphite and repeating this step several times resulted in multiple cleaving of the graphite. The freshly cleaved surface on the tape was then pressed strongly onto the $Si/SiO_2$ substrate. The process took approximately one to two minutes, creating several flakes on the surface, with a variety of thicknesses varying from a monolayer to a few microns, held by van der Waals bonds. Most were multilayer flakes which could be readily seen in an optical microscope.

For the following reasons it is challenging to obtain 2D graphene flakes from a 3D crystalline solid [1]. Firstly, the majority of the layers obtained with the mechanical exfoliation method described above contained more than one layer and it was difficult to obtain monolayers. Secondly, the glue left behind by the tape could complicate further device processing. Thirdly, 2D crystals do not have a clear signature in transmission electron microscopy and monolayer flakes are transparent to visible light so cannot be easily seen in an optical microscope on most substrates, e.g., glass and metals. It is possible for the atomic force microscope (AFM) to be used to find and identify monolayers, but it is known that the step height can vary considerably on a $Si/SiO_2$ wafer.

To overcome some of these problems, small changes were made to the process. Rather than using one piece of scotch tape in the peeling off process, multiple pieces were used, where each piece of the tape is used for only one peeling off step, and the final used piece is utilized to transfer the exfoliated flakes to $Si/SiO_2$ substrate. This approach helped to increase the number of monolayer flakes. In practice the best results were obtained with an applied perpendicular force to the surface (thumb force) and an increase in the total flake density resulted from an increase in vertical pressure. This may, however, have caused damage to the oxide layer left unwanted surface debris. Hence it was necessary to evolve a system to apply uniform force as well as the correct magnitude of vertical pressure. To achieve this, small magnets were used to stick the cleaved flakes onto the substrate surface as opposed to employing a poorly calibrated thumb force.

Using these techniques there were significant improvements in the flakes obtained in comparison to the conventional exfoliation process and a clear step forward in terms of both the number and size of monolayer flakes was achieved, especially in case of $NbSe_2$ flakes. A monolayer graphene flake with size ~ 120 μm

and a single unit cell $NbSe_2$ flake of length ~ 70 μm were obtained this way as shown in Fig. 4-4.

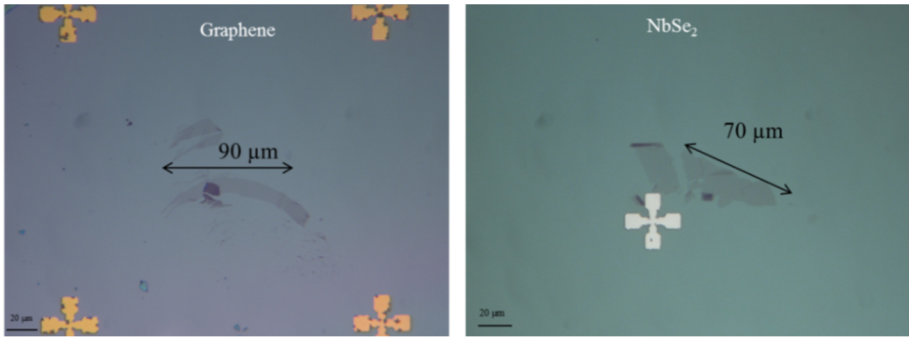


**Figure 4-4:** Exfoliated monolayer graphene and $NbSe_2$ flakes.

### 4.4.1 Annealing process

During the fabrication procedure a number of chemical compounds such as: PMMA, acetone, and IPA come in contact with the graphene surface. The contamination from these compounds can be reduced by a high temperature annealing process. The high temperature reaction between hydrogen and unsaturated hydrocarbons is utilised in this annealing process. It was found that contamination can be removed efficiently by heating samples up to 400 ℃ in a hydrogen/argon ($H_2$/Ar) mixture [99]. The forming gas mixture used here had a percentage ratio $H_2$/Ar 10 : 90 %. The annealing process was run for two hours at 400 ℃. The annealing furnace was purged with forming gas for half an hour and then took ~ 50 minutes to reach the required target temperature (400 ℃) with the heating rate set to 8 ℃ / minute. The furnace took around three hours to cool down in a medium of pure argon gas, helping to avoid any adsorption of hydrogen by the graphene flakes. The annealing process takes place immediately after exfoliating the graphene flakes which are then immediately capped with a PMMA protective layer. To avoid any oxidization or degradation of the flakes, the high temperature annealing process was not used with $NbSe_2$ flakes.

### 4.4.2 Optical Microscopy

The visibility of graphene [96] and $NbSe_2$ [97] has been studied both experimentally and theoretically and it was found that it depends on the choice of substrate and the correct light filters for the microscope. There are four types of media with different optical properties in each fabricated device; the order from the

bottom to the top is the Si substrate, the $SiO_2$ layer, the flake (graphene/$NbSe_2$) and air. The interference effects of light scattered at the interfaces between these four media, especially at the $SiO_2$/flake interface, plays an important role in the visualisation of monolayer flakes using optical microscopy. It was also found that this was the cause of an oscillation in flake contrast as a function of the oxide thickness. A standard choice for the oxide layer thickness is 300 nm, which gives maximum contrast when using a green filter, and good contrast under a white light. The use of appropriate filters has been reported to help maximize the contrast of graphene flakes for any $SiO_2$ thickness [96].

The use of a thin PMMA protective layer on top of the graphene flake was found to increase the graphene visibility by a few percent. A Leitz optical microscope with attached DS digital camera head (colour camera-High resolution-Digital camera head DS-Fi1, 5 Mega pixels) plus a DIS camera control unit (DS-L1) was used to search for flakes over the $45 \times 45$ cell array of registration marks in each sample. Single and few-layer flakes were readily recognized, with some usually found attached to thicker ones. The selection of homogenous flakes was generally preferred for devices. A multiple-step graphene flake consisting of monolayer, bilayer and multilayer graphene is shown in Fig. 4-5.

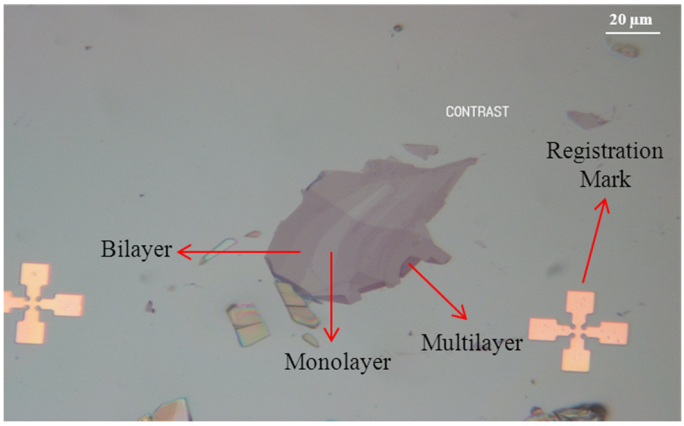


**Figure 4-5:** A multiple-step graphene flake containing monolayer, bilayer and multilayer graphene.

## 4.5 Contact Fabrication

### 4.5.1 Electron Beam Lithography (EBL)

The technique whereby a pattern is transferred from computer memory to a surface using electron beam irradiation is known as electron beam lithography

(EBL). Some macromolecular polymers are sensitive to electrons irradiation; thus electron beam lithography can be used like optical lithography to pattern nanoscale features using electron exposure instead of UV exposure [100]. E-beam lithography has a much higher spatial resolution than optical lithography. There are several factors such as electron lens aberrations and electron scattering in resists that limit the resolution of e-beam lithography [100].

A brief description of an electron beam writer will be given in the following paragraph, which will be followed by more specific considerations about the details of using this system to pattern our device designs. Figure 4-6 shows a schematic diagram of the electron optical system in our e-beam lithography machine. This system uses a combination of a SEM (HITACHI S-4300SE) and a lithography system (ELPHY plus software accompanied with nanolithography hardware system made by Raith). The SEM is necessary to provide an electron beam to write the desired structure into the resist.

In the electron beam system, an acceleration voltage is applied to the electron gun to accelerate the electron beam to a specified kinetic energy, which was typically 30 keV. The electron gun is followed by gun alignment to collimate the electron beam. A condenser lens allows one to focus the maximum number of emitted electrons from the cathode onto the exposure surface. The beam blanker functions as an automated on/off switch for the beam, and it enables the beam to reach the substrate when an exposure is needed. The zoom lens can be used to adjust the dynamic focusing of the electron beam and a stigmator helps avoid astigmatism resulting from aberrations in the beam focusing in *x* and *y* directions. Several apertures were used to control the required resolution resulting in a trade-off between the angle of the electron beam spread and the incident beam current. Higher resolution was obtained with a smaller aperture, whilst high beam currents at a low resolution were obtained with a larger aperture. The final beam spot at the exposure surface was formed by focusing the electron beam emerging from the aperture using the projection lens. The back scatter detector was used to detect the reflected electrons from the sample after the beam had hit the surface. Hence SEM images can be acquired by scanning the surface and reading the detector response for each point sequentially.

### a) Electron Beam Resists and Processes

Electron beam resists can also be classified into the same two groups as photoresists: positive and negative. One of the most common positive resists used in EBL is PMMA and was used in the fabrication processes described here [100].

#### i) PMMA

The most important features of this resist are high resolution, high contrast and low sensitivity. It is commonly used as a high resolution positive resist for direct write e-beam lithography. Its sensitivity depends upon two main parameters; the relative molecular mass (to which it is inversely proportional) and the concentration of the developer [100].

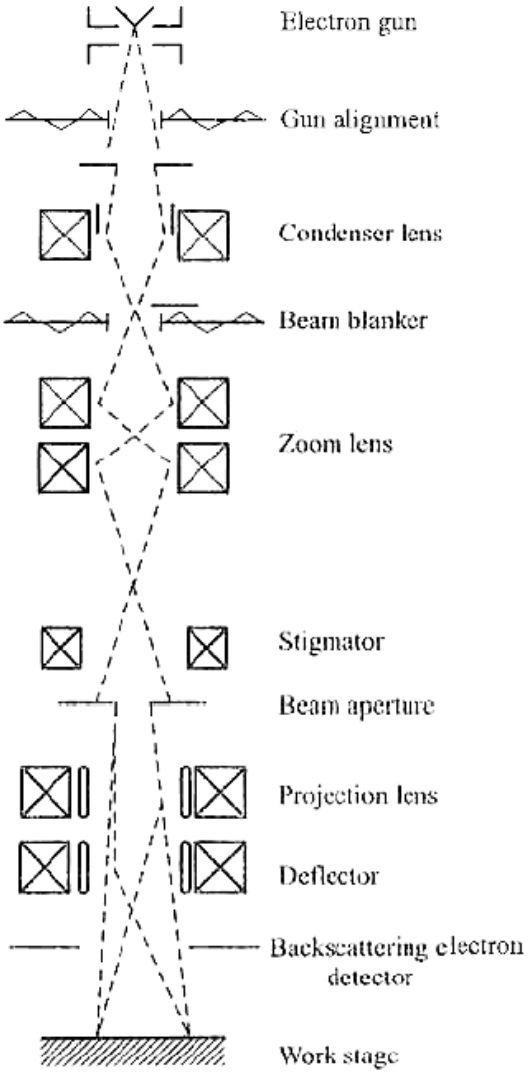


**Figure 4-6:** A sketch of a typical electron optical system in an electron beam writer [100].

ii) **Copolymer (MMA (8.5) MAA)**

The second type of resist used was copolymer, a polymer derived from PMMA and methacrylic acid (MAA). This hetero-polymer has a lower molecular weight than PMMA and hence has a higher dissolution rate in developers as compared to PMMA [100].

**b) Developer**

The standard developer used was a mixture of methyl isobutyl ketone (MIBK) and isopropanol (IPA) with a volume ratio of 1: 3 respectively. Samples were soaked in this mixture in an ultrasonic bath for a specified time period and power. Finally, samples were rinsed in IPA to terminate the development process.

**c) Multilayer Resists Process**

The advantages of multilayer resists rest in the ability to obtain a suitable resist profile to facilitate the lift-off process and to achieve high resolution lithography [100]. Figure 4-7 shows both the undercut profile which was formed as a result of using this process and the steps of the metal lift-off process. Double layer resists were used in the final step of fabrication to realise the outer bond pads. The bottom layer was copolymer while the upper layer was PMMA. The recipe that was used will be detailed later.

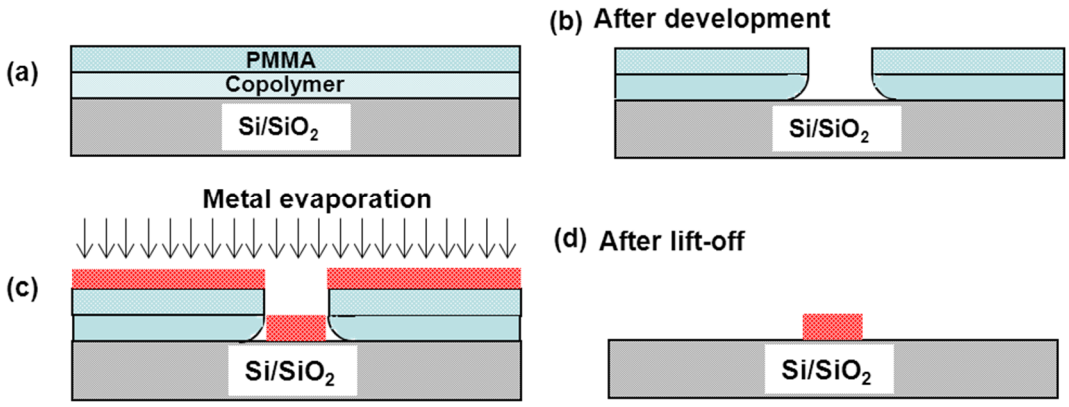


**Figure 4-7:** Deposition and lift-off processes using double layer resist.

### 4.5.2 EBL: Flake contact formation

Fabricating electrical contacts to exfoliated flakes takes place after mapping its exact position relative to the registration marker pattern, and follows the fabrication steps shown in the workflow chart in Fig. 4-1. ELPHY plus software (Software Suite 5.0) was used to write the electrode designs, which were custom designed for each individual flake. The entire design was written in two steps, the inner electrodes and the outer bond pads. The sample-stage was locked throughout exposure to minimise its movement and to maximise the required writing accuracy. Before the initial writing phase (inner features) the sample was coated with a PMMA layer using a spinner recipe (500 RPM (5 sec) + 2000 RPM (45 sec)) that resulted in a thickness of approximately 150 nm. The sample was then baked in a fan oven for 35 minutes at $150\ ^{\circ}C$. The writing process began by using the nearest registration marks to align the electron beam and the electrode layout was then written into the resist. The electron dose used for writing each contact on the flake was typically $400\ \mu C/cm^2$.

Chains in the positive resist (PMMA) were broken after exposure to the electron beam and could be developed away using the standard developer (MIBK: IPA (1:3)). For closely spaced contacts on graphene samples (~ 100's nm), the resist was developed for 30 sec - 1 min at $\sim 35\ \%$ ultrasonic power, and samples were continuously stirred. They were then removed and rinsed in IPA for $\sim 50\ s$ and blown dry with nitrogen gas. For all $NbSe_2$ devices and graphene devices with widely-spaced electrodes (a few $\mu m$), the developing time was increased to $2-6$ minutes in the developer at $\sim 40\ \%$ power of the ultrasonic bath, stirring continuously. Samples were then removed and rinsed in IPA for $\sim 3$ minutes and blown dry with $N_2$ gas. Subsequently, the required metal layers were evaporated and lifted-off in warm acetone. This resulted in only the written areas being covered with metal. The contact materials used for graphene samples were either Cr/Al (10/50 nm) or Pd/Al (10/50 nm), while Cr/Au (10/50 nm) was used for all $NbSe_2$ samples. The details of both the deposition process as well as the lift-off process will be discussed in the next sections.

A few changes to the procedure for the first writing step were made for the second writing step (the outer bond pads). Double resist layers were used, the bottom

layer being copolymer and the upper layer PMMA resist. The spinner recipe used for both of them was (500 RPM (5 s) + 2000 RPM (45 s)). The samples were baked in a fan oven for 25 minutes at $125\,^{\circ}\mathrm{C}$ for the copolymer, and were baked in the same oven for 35 minutes at $150\,^{\circ}\mathrm{C}$ for the PMMA layer. The electron beam dose used at this stage was $300\,\mu\mathrm{C/cm^2}$. The sample was again developed in the standard developer post exposure. Both graphene and $NbSe_2$ were soaked in the developer for $2-6$ minutes at $\sim 40\,\%$ ultrasonic power. Further cleaning took place by rinsing the samples in IPA whilst continuously stirring; they were then blown dry with $N_2$ gas. The bonding contacts in all devices were made from Cr/Au (20/250 nm). The lift-off process took place in warm acetone so that only exposed regions of the chip were contacted by metal. Figure 4-8 shows images that illustrate the two steps of e-beam lithography in a graphene device.

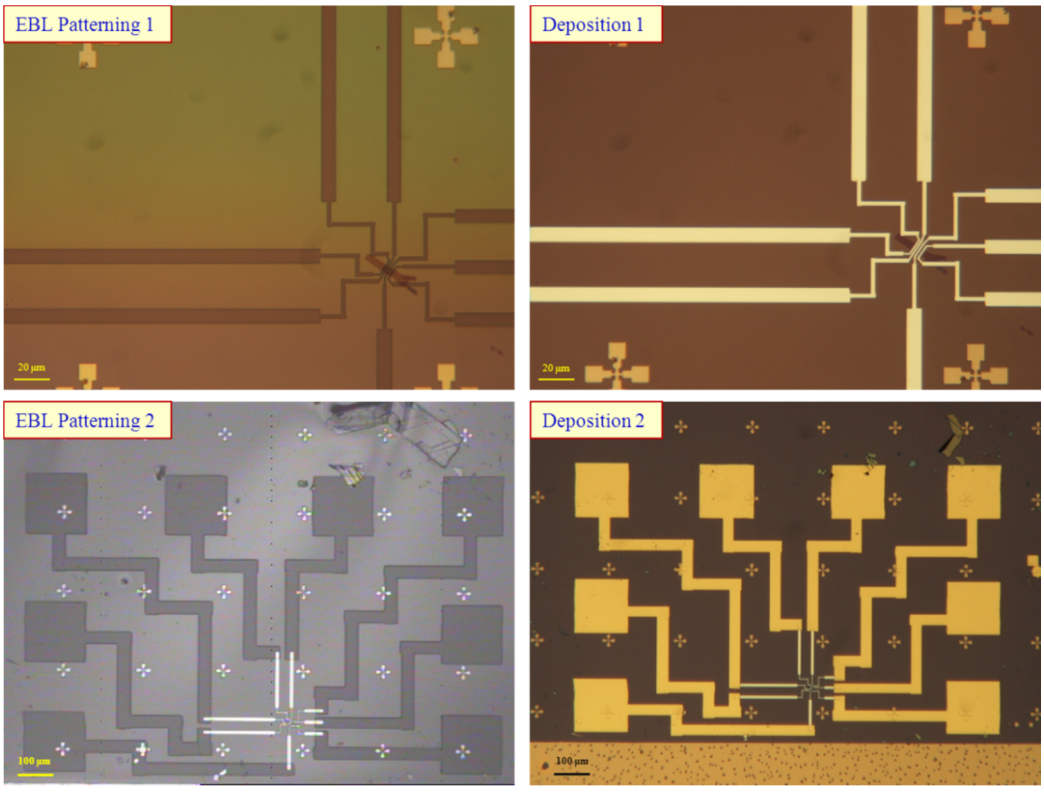


**Figure 4-8:** Images of a graphene device illustrating the different steps of electrode fabrication.

### 4.5.3 Deposition of contacts

Contact metallization was deposited using two different vapour deposition systems, thermal evaporation and electron beam (e-beam) evaporation. In both cases, to minimize contamination by background gases, the system was maintained at a low

pressure $(1.5 - 3 \times 10^{-6}\ \text{mbar})$. This also leads to an increase in the mean free path of the metal particles which helps avoid contamination of the film and prevents evaporated metal from coating the sidewalls of vertical features. To prevent oil back flowing from the diffusion pump to the main chamber, a liquid nitrogen trap is used.

The simplest method to deposit a metal film is by thermal evaporation. Metal sources were placed in tungsten boats that were resistively heated in an Edwards Auto 306 thermal evaporator. The current flowing through tungsten boats determines its temperature and thus the rate of evaporation. Both the film deposition rate and the total film thickness were monitored using a quartz crystal oscillator [101].

In an e-beam evaporator (Edwards Auto 306), a tungsten filament is heated via a high current that is in turn held at high DC voltage with respect to ground. The filament emits electrons through thermionic emission; these electrons are then accelerated and focussed by means of bending magnets onto the source in an inert crucible. In both techniques the source material heats up and transformed into a vapour phase. The gaseous atoms then travel ballistically through the vacuum and condense back to a solid state on the substrate.

Thermal evaporation was used for graphene devices whereas e-beam evaporation was used for $NbSe_2$ devices. The thermal evaporator used in this project was equipped with an Argon (Ar) plasma cleaning tool, a process that was found to be valuable for producing graphene devices with low contact resistances. This process was not available on the e-beam evaporator system.

E-beam evaporation has two advantages compared with thermal evaporation. Since the electron beam is only focused on the source material in the crucible, the latter can receive a large quantity of energy. Hence higher deposition rates for the film with greater adhesion to the substrate can be obtained. There is also a lower degree of contamination from the crucible compared with the hot W boats used for thermal evaporation.

Figure 4-9 shows schematic diagrams of both evaporation systems. The working chamber located on top of the pumping system relates to the thermal evaporator, whereas the other head represents the working chamber for the e-beam evaporator. The pumping system is very similar for both systems.

More than one deposition was made during the full device fabrication process. For each deposition it was necessary to clean both the materials and the boats using the same process used to clean the actual substrates but with higher ultrasonic power. Graphite crucibles used in e-beam evaporation are only cleaned once before use and stored in a clean box afterwards.

The first deposition made was Cr/Au (10 nm/50 nm) in order to form the registration marks in the thermal evaporator. Subsequently, Ti/Al, Cr/Al or Pd/Al (10/50 nm) and Cr/Au (10/50 nm) were deposited to obtain the inner electrode contacts of the device after EBL, using a thermal evaporator or an e-beam evaporator respectively. The final deposition was made using Cr/Au (20 nm/250 nm) to create the outer bond pads of the electrode mask after EBL pattering. The thermal evaporator was again used for graphene devices, while the e-beam evaporator was used for $NbSe_2$ devices.

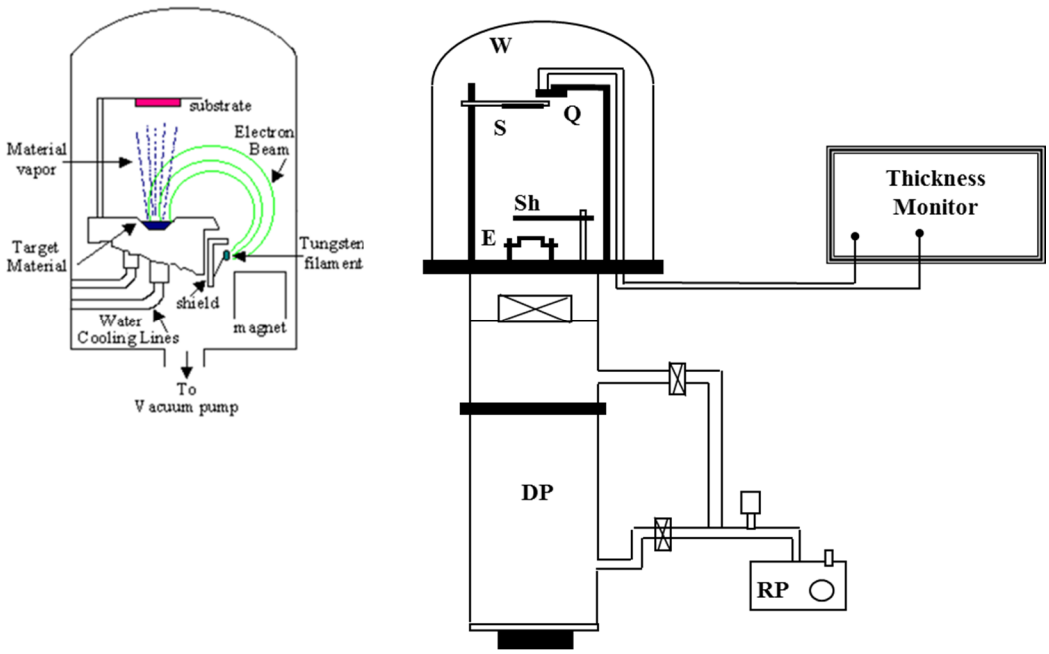


**Figure 4-9:** Sketches of e-beam and thermal evaporation systems. The two different work chambers operate with very similar pumping systems.

### 4.5.4 Lift-off process

The samples were soaked in acetone after metallization in order to remove the resist and enable lift-off of the metal film. Acetone dissolves resist layers causing the metal film to float off where it is not in direct contact with the substrate. The lift-off process can be sped up by using hot acetone which facilitates PMMA removal.

The lift-off process was performed as follows: samples were removed from the glass slides they were mounted on by placing each individually in acetone at room temperature while agitating the sample for 1-2 minutes. The sample was then readily detached from the slide. The isolated sample was left in a beaker containing hot acetone $(\sim 60\,℃)$ in a hot water bath $(\sim 60-70\,℃)$ for 15 minutes. The sample was then sprayed with acetone while still wet. A wet transfer to a beaker of clean hot acetone $(\sim 60\,℃)$ was then performed. The sample was sonicated for 2-5 minutes in the ultrasonic bath at power $\sim 20-35\,\%$ and then sprayed again with acetone whilst still wet in the acetone beaker. Finally, the sample was removed from the acetone and sprayed with acetone followed by IPA and dried with $N_2$ gas. These procedures were used with all devices with good results.

### 4.5.5 Deposition Materials

Producing low resistance Ohmic contacts to graphene/$NbSe_2$ flakes is crucially important as it is one of the major factors that limits the performance of fabricated FET devices [102, 103]. Several studies have tried to determine the main factors which influence the metal/graphene contact resistance; metal type, metal work function and number of layers in the graphene flake [102].

Russo *et al*. reported that the contact resistance, $R_c$, is independent of both the number of graphene layers in the flake and the applied gate voltage [104]. The key factor in achieving stable and low $R_c$ was to increase the density of states in the graphene layer which is in contact with the metal. This can be achieved by highly doping the contact region. Metals with high work function are the best choices to realise good graphene/metal contacts. These metals have lower reactivity with graphene, and transfer a large amount of charge to the graphene layer (graphene doping) [103, 105].

The most commonly used electrodes for graphene flakes are Ti/Au or Cr/Au bilayers [104]. Following reports by Heersche *et al*. [84] that highly transmissive contacts were obtained using Ti/graphene interfaces in their SGS junctions [104], Ti/Al electrodes were selected for the first SGS devices fabricated within this project. However, high two-point connection resistances $(\geq 60\,k\Omega)$ were encountered in these devices. In contrast, Nagareddy *et al*. [106] reported that Cr/Au electrodes exhibited lower $R_c$ values than Ti/Au at high temperatures. Knowledge of the work

function for graphene, Ti, Cr, and Au (4.50, 4.33, 4.60, and 5.31 eV respectively) [106], in addition to the fact that Ti is chemisorbed and Cr is physisorbed by graphene, allows one to understand the low contact resistance of Cr/Au electrodes. Firstly, less charge transfer from the Au layer to graphene is obtained when using Ti as a contact material in contrast with Cr, since the work function difference at the Ti/graphene interface (-0.17 eV) is less than at the Au/graphene interface (+0.81 eV) [107]. Secondly, as Ti is chemisorbed to graphene, the formation of a continuous uniform layer of Ti covering graphene was expected with a greater of binding energy of 1.75 eV [108]. This strong chemical interaction could cause degradation of the hopping conduction, which results from a damage in the region of graphene in contact with Ti. Furthermore, an additional carrier scattering mechanism was expected to be introduced in the contact area. These factors led Nagareddy *et al*. to conclude that the lowest $R_c$ could be obtained by selecting non-reactive metals with higher work function.

Cr/Au electrodes were used in the second generation of fabricated FET devices within this project. The two-point connection resistances obtained with these devices were ~ 5 – 10 kΩ. Later the protocol was altered again to use palladium (Pd) as a contact material instead of Cr, but only for graphene devices, whereas Cr/Au electrodes were always used with $NbSe_2$ FET devices.

For graphene SGS devices superconducting electrodes are required, thus Cr/Al bilayer electrodes were used. Palladium (Pd) also has a high work function (5.67 eV) and was found to make superior Pd/Al electrodes in the third generation of SGS graphene FET devices fabricated. Very low values for Pd/Al-graphene two-point resistances in the range ~ 60 Ω - 2 kΩ were obtained in all 3$^{rd}$ generation devices fabricated.

## 4.6 Packaging & wire bonding

Packaging was performed after the EBL definition of the bonding contacts. Initially the sample was diced up to fit the required package as in section 4.2.1. A diamond scriber was then used to scratch through the oxide layer on the reverse side of the chip to ensure that a reliable back gate contact was obtained. The sample was then cleaned in the standard way to remove any debris.

The chip carriers used to hold graphene and $NbSe_2$ FETs are shown in Fig. 4-10. Both packages were made of a ceramic material with Ni/Au plated contacts and either a square or a rectangular cavity where the sample was mounted. Packages had two sets of contacts, one on the inside and one on the outside, which were connected with vias. Initially the chip carrier was mounted on a glass microscope slide with double-sided tape and a wire bond was created between one pin of the package and the cavity into which the sample was mounted. Ag epoxy (EPO-TEK H20E) was mixed by a weight ratio of A: B (1: 1). A small amount of this epoxy was spread on the chip carrier base covering the ends of the wire bonds prepared for the back-gate connections. Alumina spacers were added under the chip to elevate the sample and make it accessible to the AFM tip for imaging. The package was then baked in an oven at 85 ℃ for one and a half hours in order to cure the epoxy. Another small amount of Ag epoxy was spread on the alumina plate to glue it to the sample. The package was again cured at 85 ℃ for one and a half hours. If the chip had any gold film around the edges resulting from the edge bead mask used during the lithography of registration marks, these were covered by GE varnish to avoid electrical shorts between bond wires. Finally, 25 μm diameter Au wire bonds were made to the device using a commercial wire bonder.

Wire bonding is a method of making interconnections between the pads on a fabricated device and the chip carrier. A combination of heat, pressure and ultrasonic energy is used to connect the wires to the bond pads without any need for solder. “Wedge” bonding and “ball” bonding are the two most common methods of wire bonding. Here wedge bonding was used. Firstly, the wedge was positioned over one contact of the chip carrier. The wire was pressed between the wedge foot and the contact, ultrasonic energy was applied to the wedge to weld the bond. The wedge was then moved to the first bond pad whilst feeding out the wire to make the second bond, at which point a clamp closes and the wire is broken at the tail. These steps were repeated for each connection. The ultrasonic power and the duration of the ultrasonic pulse were the most important parameters for wedge bonding, both of which could be controlled independently.

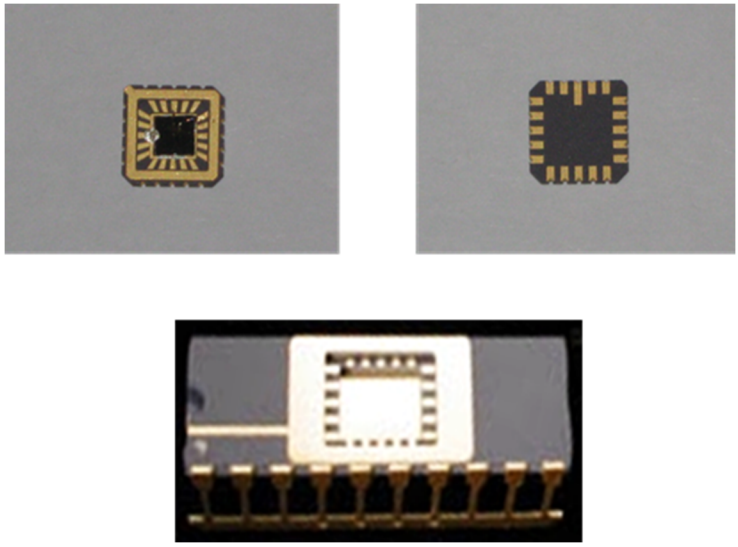

**Figure 4-10:** (Top) the front and back side of the leadless chip carrier used for graphene devices. (Bottom) An optical image of the leaded package used for $NbSe_2$ devices.

## 4.7 AFM imaging of flakes

The AFM has emerged to be a powerful tool for imaging nanoscale sample details and for studying surface topography. Compared to STM (scanning tunnelling microscopy) which usually requires a high vacuum environment, AFM is a simpler imaging method that can be performed under ambient conditions [109, 110].

Figure 4-11 shows a sketch of our AFM system which will be described briefly below. AFM is a surface scanning technique in which the deflection of a microscopic cantilever is recorded as its tip scans over the sample surface. The deflection of the cantilever arises due to the force between the sample atoms and those located at the apex of its sharp tip. This deflection is detected by a feedback mechanism and a constant force (for topographic information) or a constant height (for force information) is maintained between the tip surface and the sample by a piezoelectric actuator.

There are three modes of AFM operation: contact, non-contact and tapping mode. Tapping mode is often the preferred choice to avoid damaging samples during scanning and it is generally used for studying soft materials. This mode was chosen for studying both graphene and $NbSe_2$ flakes in this project. In this mode, there is only intermittent contact between the tip and the sample surface. The cantilever tip is excited to vibrate close to its resonant frequency. On approach to the surface,

changes of the oscillation parameters when the tip is attracted or repelled by features on the sample surface provides the feedback signal. These occur because the resonance frequency is shifted by the interaction force between the cantilever tip and the sample surface. A feedback circuit controls the piezoelectric scanner to keep the frequency shift constant. This process generates height information for the surface under study. The cantilever probes used were fabricated from micromachined Si and have a reflective Al layer on the back side for improved optical detection (Asylum Research, silicon probe, Al reflex coated, type- Ac mode soft (Air)).

Monolayer graphene has been reported [96] to have a step height in the range 0.3-0.4 nm, either from the substrate to the first graphene layer or from one graphene layer to the next. Different types of force such as van der Waals, adhesion and capillary forces can be sensed by the cantilever tip, and this must be taken into consideration when scanning a graphene flake on a $SiO_2$ surface. Other studies showed that the thickness of monolayer graphene is $\sim 0.33$ nm. This value is expected in the absence of water, either on the $SiO_2$ surface below the graphene flake or as a hydration layer on top of it.

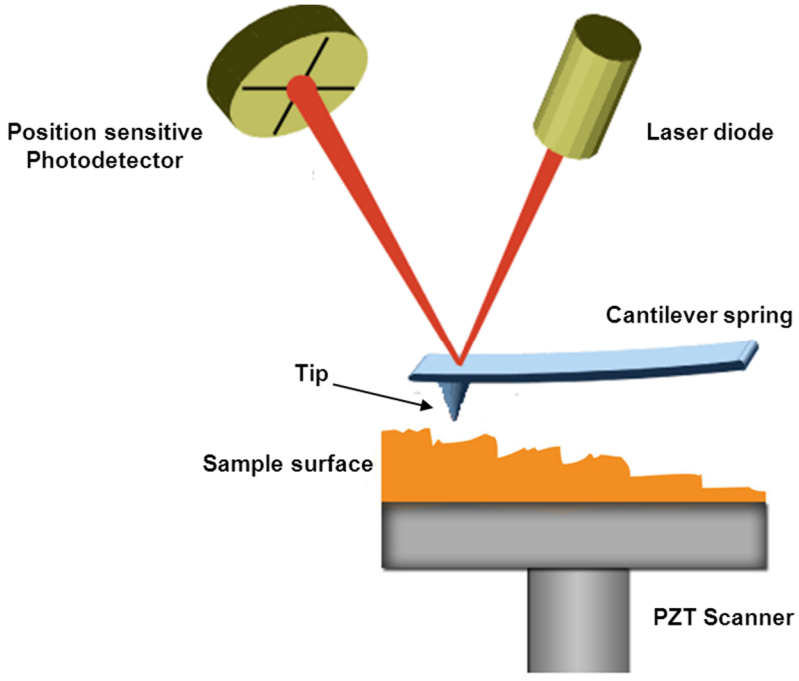


**Figure 4-11:** Sketch of an AFM system showing its key components.

During the fabrication process the $SiO_2$ surface of the chip was cleaned with piranha solution to make it hydrophilic and wettable. An approximate thickness of $\sim 0.15$ nm of water on an $SiO_2$ surface was reported by Wo *et al.* [111]. The

possibility of a hydration layer forming on the graphene surface was also likely. The existence of two water layers, above and below graphene flake, would make it difficult to distinguish monolayer graphene from multi-layers. The substrate roughness could also affect the accuracy of the measured thickness.

To conclusively confirm the number of layers in a measured flake Raman spectroscopy was used. A brief description of Raman spectroscopy will be given in the next section.

## 4.8 Raman spectroscopy of flakes

When light interacts with matter the process can be inelastic corresponding to Raman scattering. During this process an exchange of energy occurs between the incident photons and the sample, which results for example in the generation of red-shifted light at energies lower than that of the incident radiation. This is known as Stokes scattering. Another process called anti-Stokes Raman scattering is possible where the exchange of energy results in the generation of blue-shifted (higher energy) photons.

Due to the low intensity of Raman scattered light it is usual to use monochromatic high intensity light sources, or lasers. In most cases the molecules relax directly back to the lowest vibrational energy level by emission of light at the same wavelength as the exciting light, which is known as elastic or Rayleigh scattering. High quality optical components are required to filter out Rayleigh light and sensitive detectors are needed to record information from a Raman experiment in a reasonable length of time. Finally, as with absorption, the Raman effect can be observed for incident light frequencies in the UV, visible and NIR regions [112].

The Raman spectrum is depicted as a plot of the Raman shift (difference in wavelength of the scattered and incident light in wavenumbers) versus the intensity of Raman scattering. The main features of a Raman spectrum (number of Raman bands, their position, intensities and shape) are related directly to the molecular structure of the sample. The interpretation of Raman spectra is based on band positions, shapes and intensities [112].

Raman spectrometers are used to analyse light scattered inelastically by molecules. A major benefit of Raman spectroscopy is the high spatial resolution that can be achieved, typically on the order of 1 μm. This means that Raman

spectrometers are often coupled to light microscopes in order to take advantage of their superior spatial resolution. A Raman spectrometer has to combine intense sources of monochromatic (usually laser) light, with efficient filters for Rayleigh scattering and highly sensitive detectors for observing the very weakest Raman bands. The Raman scattering intensity scales inversely with the fourth power of the excitation wavelength, which means that detected intensities increase strongly as the incident light moves to shorter wavelengths [113].

Raman spectroscopy is a powerful tool for studying graphene as it can distinguish between single layer and few-layer graphene, and quantify both the doping level and the quality of the graphene flake [114]. In all graphene flakes, two characteristics Raman peaks, the G band and the 2D band, are observed in the spectra at $\sim 1580\ \mathrm{cm}^{-1}$ and $\sim 2700\ \mathrm{cm}^{-1}$ respectively [114].

The G band arises from the doubly degenerate iTO (in-plane Transverse optical mode) and LO (Longitudinal optical phonon mode) phonon modes ($E_{2g}$ in-plane vibration) at the Brillouin zone centre. This represents the normal case of first order Raman scattering. The second order Raman scattering processes gives rise to the 2D band in which two iTO phonons near the K point are involved. This band is used to determine the number of layers in the graphene flake. In contrast to monolayer graphene, few layer graphene and graphite show a broad 2D peak, whereas monolayer graphene shows a single sharp 2D peak (FWHM $\sim 30\ \mathrm{cm}^{-1}$) [114]. The number of layers in a graphene flake can be estimated from the intensity ratio between the 2D and G peaks $\left(I(2D)/I(G)\right)$.

Another feature at $\sim 1350\ \mathrm{cm}^{-1}$ (the so-called disorder-induced D band), which appears in some spectra, is taken as an indication of the defect level in the graphene flake or the quality of the flake, as it is generated by the defect-mediated zone-edge phonons. Thus, its absence from the spectrum is an indication of the relatively good quality of the measured graphene flake.

John *et al*. [115] captured Raman spectra that clarified the differences between 1LG, 2LG, 3LG, few layered graphene and graphite. On the left hand side of their graph (cf., Fig. 4-12) the D band is found at $1347\ \mathrm{cm}^{-1}$, and the appearance of this band quantifies the density of defects in their flakes. Increasing the number of layers in graphene did not show any significant change to the G band

at ~ $1578\ cm^{-1}$. On the right hand side of the graph, both the position and the shape of the 2D band changed upon increasing the number of layers in the graphene flake. This band exhibits a blue shift from $2686\ cm^{-1}$ for 1LG to $2703\ cm^{-1}$ for multilayer graphene. The FWHM also increased from $32\ cm^{-1}$ for 1LG to $64\ cm^{-1}$ for multilayer graphene [115].

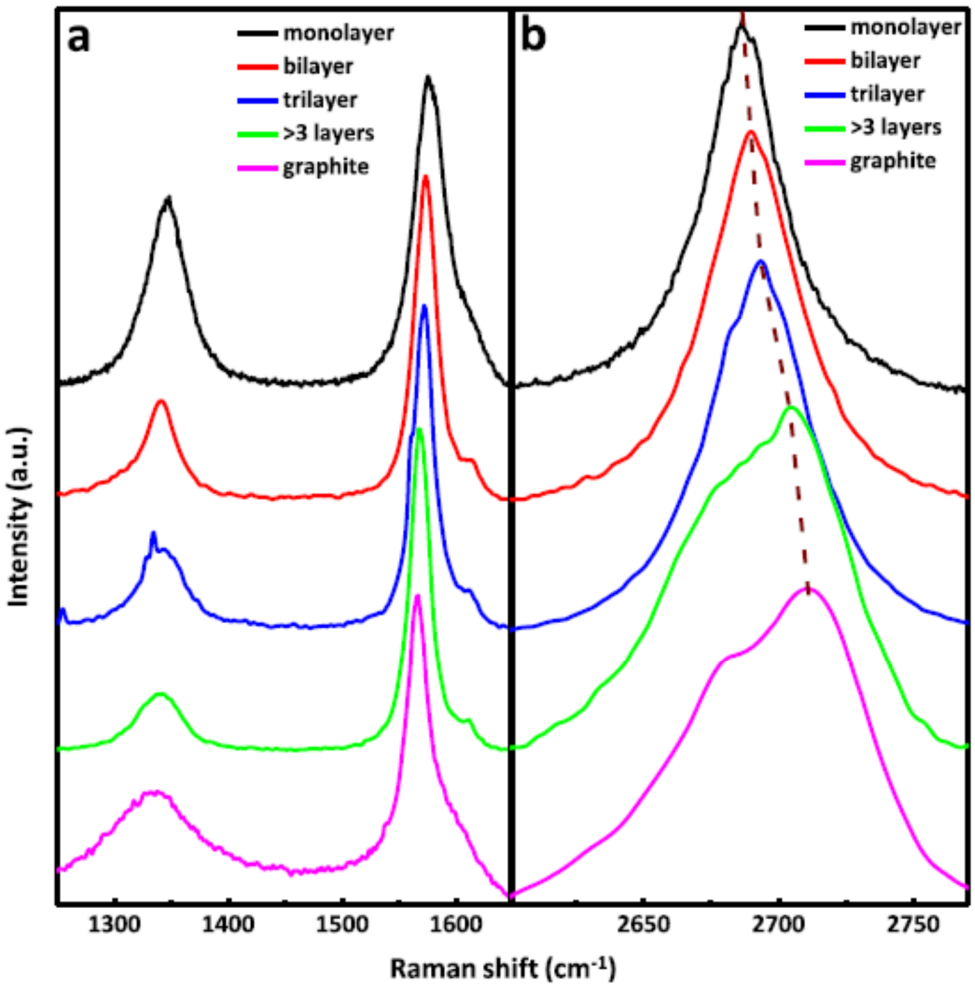


**Figure 4-12:** Raman spectra for 1LG, 2LG, 3LG, few-layer graphene and graphite. The strength of the D band (1347 $cm^{-1}$) is an indication of the flake quality. The G band (1578 $cm^{-1}$) has nearly the same position for all flakes. A significant change in both the position and shape of the 2D band is observed allowing different flake thicknesses to be distinguished [115].

## 4.9 FET device characterisation

### 4.9.1 Sample Holders

To ensure measurements could be made on the fabricated devices at low temperatures a custom sample holder was built. Three vacuum tight feedthroughs were fixed at the end of a sample rod and 14 twisted pairs of copper wires were connected to them. The wires were fed through the inside of the tube and attached to two separate strips of copper contacts that were fixed to the tube using a low temperature varnish (GE Varnish). This varnish was also used to glue a heater and a temperature sensor. The heater is made of a high resistance wire and is used to control the temperature from a commercial controller. The temperature sensor was a carbon glass resistance sensor (CGR) that is very accurate in moderate magnetic fields over a wide range of temperatures. The sensor was placed in the middle of the heater spool. At the end of the sample holder a spring-loaded plastic socket was attached to hold the leadless chip carriers that contained the fabricated devices. Figure 4-13 shows the steps followed to make this sample holder which was only used with graphene devices.

Figure 4-14 shows the second sample holder that was used with $NbSe_2$ samples, both FET devices and $NbSe_2$ flakes placed on top of a Hall probe array. This holder was constructed by a colleague (André Müller) following similar steps to those illustrated in Fig. 4-13. Two modifications were however included. Firstly, stainless steel (SS) wires, which have a very low thermal conductivity, were used instead of twisted Cu pairs. Secondly, an infrared light emitting diode (IR LED) was glued to one side of the sample holder to allow in situ illumination. The LED can reduce the Hall probe resistance at low temperature by exciting electrons from deep donor states in the AlGaAs barrier layer into the conduction band [116]. A good thermal contact between the chip carrier and the copper body of the sample holder was achieved by spreading a small amount of Apiezon Grease N between them.

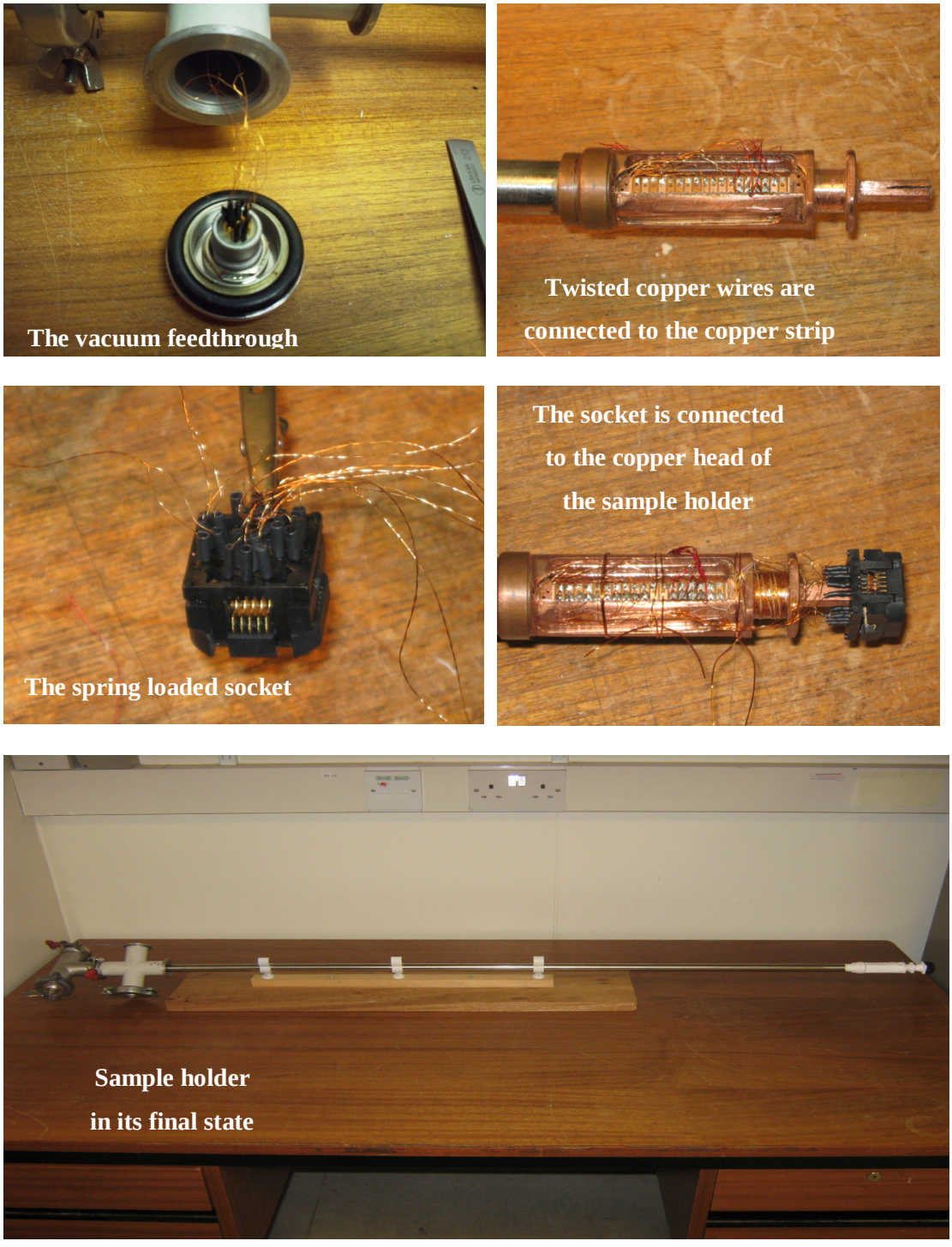


**Figure 4-13:** Illustration of the steps followed to make the sample holder for leadless packages.

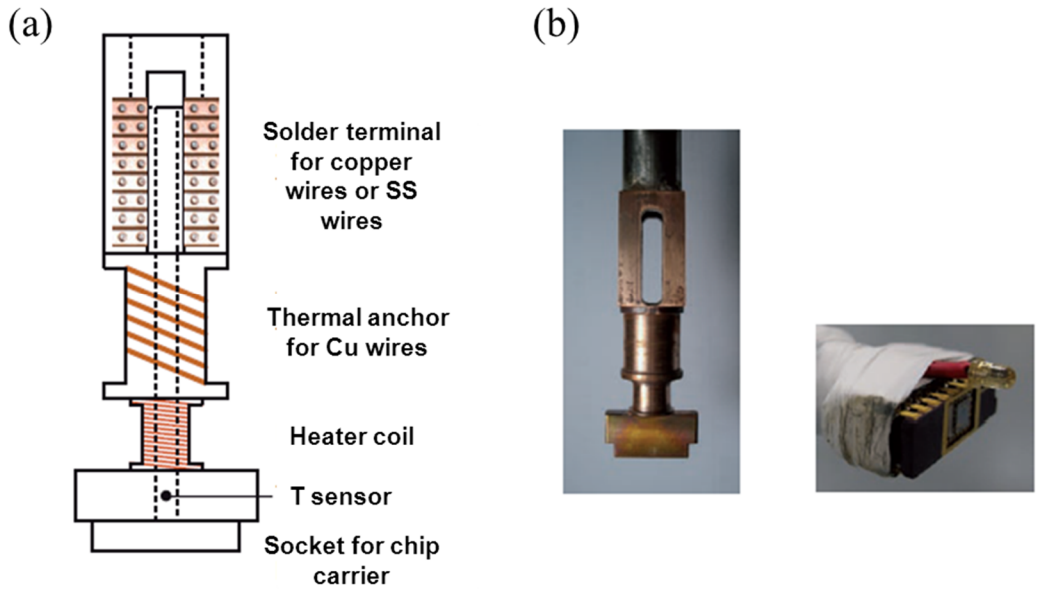


**Figure 4-14:** a) Sketch of both sample holders. b) Two photos of the head of the sample holder for DIL packages showing the inner copper body, and a close up of the IR LED and an inserted chip carrier. Adapted from [70].

### 4.9.2 LabVIEW programs

One of the goals of this project was to design a set of labVIEW programs to characterise the fabricated devices as a function of temperature, back-gate voltage and magnetic field. This section will present the four labVIEW programs that were developed to achieve this goal. Three of them were designed for this project while the fourth was written by a colleague.

Measuring the critical temperature, $T_c$, of the sample is clearly vital for the verification of the existence of superconductivity. The first labVIEW program was designed to control the experiment and plot a resistance-temperature curve for the sample from room temperature to ~ 8K. This program was also designed to control a lakeshore DRC-91CA temperature controller which was used to record the sample temperature and the sample voltage from a Stanford Research SR830 digital lock-in amplifier. The program then calculated the sample resistance by dividing the voltage reading by the constant applied current.

The second program was designed to acquire more accurate data for the R-T dependence in the temperature range 1.5 - 8 K. This program allowed one to monitor

an abrupt resistance drop in small time intervals. The major change in the labVIEW code involved adding a temperature ramping loop. A smooth continuous change in the set point was tracked by the sample temperature and an increasing or decreasing set point was controlled at a chosen ramp rate. The ramp rate could be varied in the range 0.1 -1 K/min. One of the greatest advantages of this approach was the minimisation of temperature over and undershoots. Figure 4-15 depicts the front panel for this program.

The third labVIEW program was designed to record the dependence of the resistance of a graphene device as a function of gate voltage. This program was initially designed to control the gate voltage source (Keithley 230 programmable voltage source) to sweep the voltage using a Boolean switch and record the sample voltage with the SR830 lock-in. Later, a small modification was made to the program whereby another control parameter was added to allow one to choose a different stopping point to the set point in the main program menu.

The fourth program was a custom-designed labVIEW program, in which the external magnetic field at the sample was swept either to study the behaviour of flakes as a function of applied magnetic field (R-B relation), or to record the Hall voltage of individual Hall probes (micro-magnetometry measurements of thicker $NbSe_2$ flakes). This program controls both the Lakeshore temperature controller and a Kepco bipolar power supply that drives the superconducting solenoid as well as the lock-ins which measure the sample voltage. The Kepco bipolar power supply could be run in both constant voltage and constant current modes depending on the range and stability required for magnetic field sweeps. The constant voltage mode was used for small sweep ranges ($\pm 2500$ G) with a resistance of 22.5 Ω, 50 Ω or 200 Ω connected in series with the superconducting coil and the current measured independently with a Keithley multimeter. When in constant current mode the Kepco power supply sends current directly to the superconducting coil allowing larger magnetic field ranges to be achieved ($\pm 8500$ G).

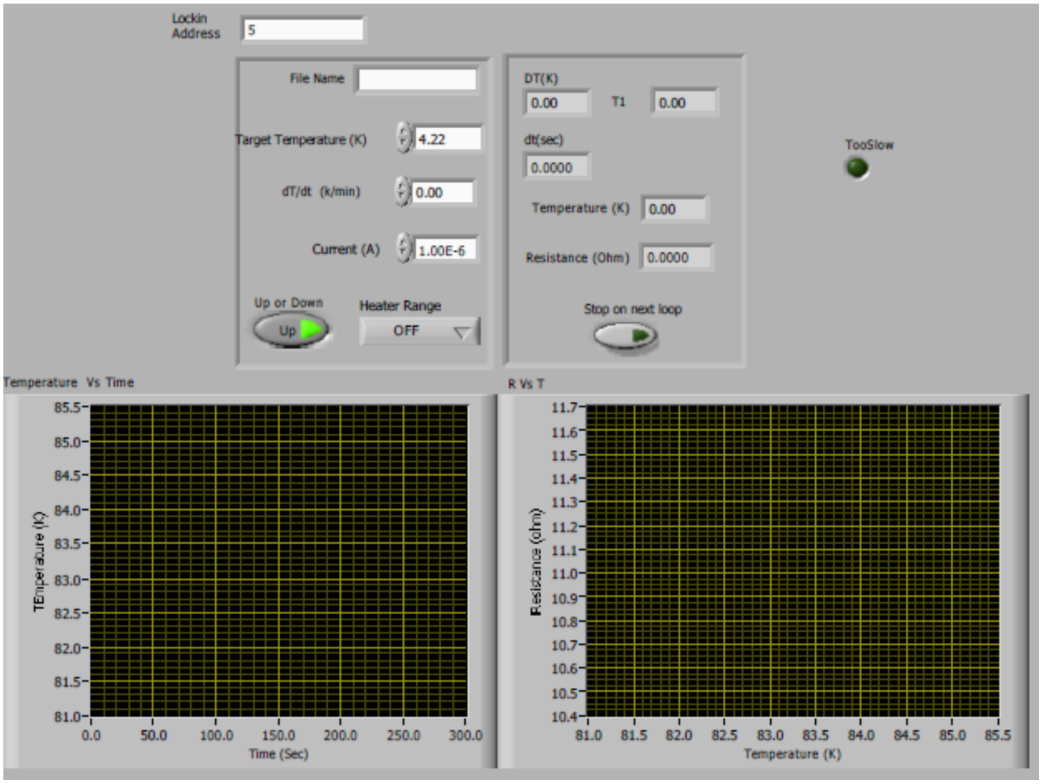


**Figure 4-15:** The front panel of the R-T measurement program.

### 4.9.3 Cryogenic system

After the fabricated device had been glued into the chip package and wire bonded it was mounted on the sample holder and inserted into the cryostat. A glass cryostat was used which composed of two dewars; the outer one for liquid Nitrogen ($LN_2$) and the inner one for liquid Helium (LHe). The outer Dewar has a permanently sealed insulating vacuum whereas the inner one was evacuated before every cool down.

In some measurements it was not necessary to use liquid Helium in the inner Dewar. Initially only the contact resistances of the superconducting electrodes on the graphene flakes were checked which simply required the temperature to be near to the boiling point of liquid Nitrogen 77 K. Regardless of which liquid was used to fill the inner Dewar ($LN_2$ or LHe), filling the outer Dewar with $LN_2$ was important as it ensured much lower boil-off rates and the whole system remained cold for longer. A viton o-ring seal was used to make a vacuum-tight fit to the top of the inner Dewar at a brass flange. The vacuum jacket, sample space and the inner Dewar were pumped down using a rotary pump. Helium gas was filled into the sample space using the same pipework connected to the vacuum pump. To lower the temperature

below 4.2 K the LHe could be pumped down to ~ 2 K. The superconducting coil was attached to the end of the sample tube and both were directly immersed in the LHe in the inner Dewar.

Cables inside the sample tube were connected to two breakout boxes through three vacuum feedthroughs. These were then connected to the measurement instruments with BNC cables. To have a homogeneous magnetic field at the device being measured, the sample was placed exactly in the middle of the coil. A small pressure of Helium exchange gas in the sample space was used to cool down the sample holder itself. Figure 4-16 shows a diagram of the whole cryostat system [70].

### 4.9.4 Measurement setup

Electrical and magneto-transport measurements on all samples were performed using the electrical set-up shown in Fig. 4-16. In general, four probe configurations of the device contacts were used, where the outer contacts one and four ($I^+$ and $I^-$) were used to send current through the flake whilst the voltage drop was measured between the middle contacts numbered two and three ($V^+$ and $V^-$). In this way resistance contributions from the metal leads and any contact resistances were avoided. All samples were checked for continuity at room temperature by measuring the two-point lead-to-lead resistances. A Philips PM5109 low distortion AC generator with a 32 Hz output of 1 V or 10 V in series with a (1-10) MΩ resistor was used as a current source. This series resistor was chosen to be much greater than the 2-point resistance of the current leads. The AC generator also provided a reference frequency for the digital lock-in amplifiers used to measure the voltage drop between contacts 2 and 3. Two lock-ins were needed in some experiments such as Hall magnetometry measurements. Signals from the lock-ins were sent to the computer via a GPIB bus.

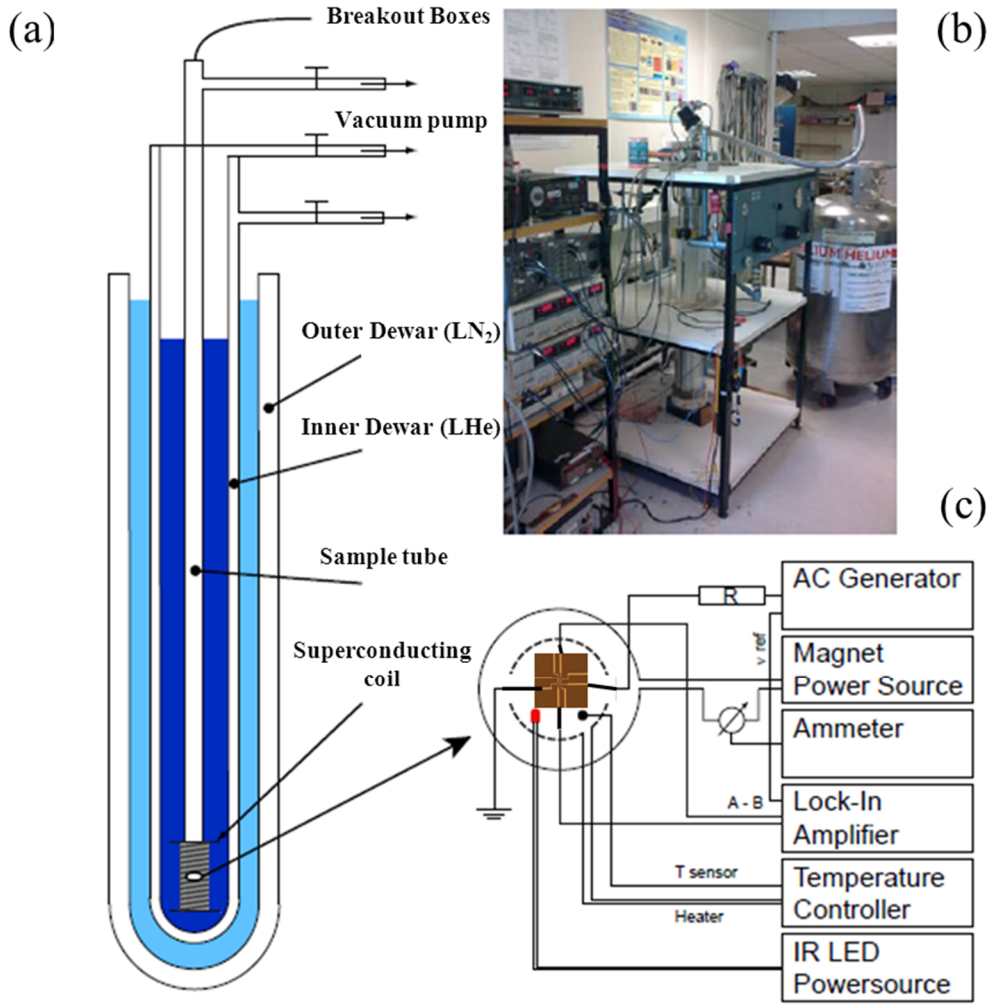


**Figure 4-16:** a) A schematic diagram of the cryostat. b) Photo of the measurement setup during LHe transfer to the cryostat. c) A sketch of the electrical measurement system. Adapted from [70].

The electrical setup shown in Fig. 4-16 (c) illustrates the situation when a Kepco bipolar power supply was used in constant voltage mode. The ammeter (Keithley 199 system DMM/scanner) was not used in this case. All current lines, voltage connections and back-gate connection were filtered using LCR low pass filters consisting of two capacitors (22 nF), one inductor (1 mH), and one resistor (10 kΩ) as shown in Fig. 4-17. These filters cut out the high frequency (spike) components of the signal but allowed the low frequency components to pass. The calculated cut-off frequency for this filter was 100 Hz. The lifetime of fabricated devices was greatly extended after starting to use these filters due to their ability to

suppress high amplitude voltage spikes arising from the mains ring circuit. They also reduced the pick-up noise.

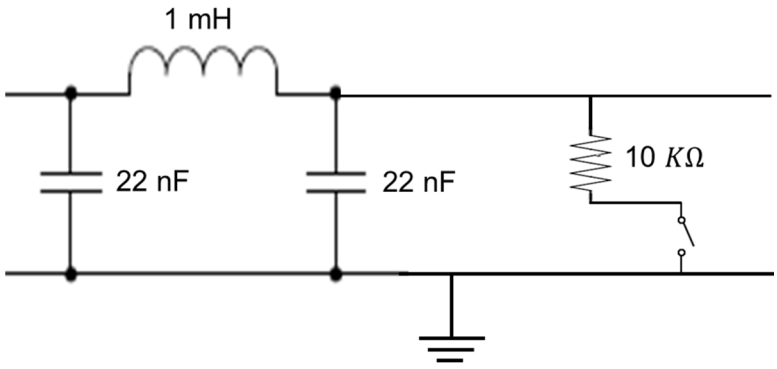


**Figure 4-17:** Circuit diagram of the LCR filters.

## 4.10 Hall Magnetometry– 2DEG

### 4.10.1 Hall Effect

Magnetisation studies of few-layer $NbSe_2$ flakes were based on the Hall effect. The Hall effect was discovered by Edwin Hall in 1879 [117] and is analogous to the transverse deflection of an electron beam by a magnetic field in free space, resulting in the generation of a voltage difference between opposing edges of the conductor. The sketch in Fig. 4-18 helps to understand this effect. Assuming that the applied classical current flows in the $+x$ direction, electrons travel at the drift velocity, $v_d$, in the $-x$ direction. Applying a perpendicular magnetic field, generates a Lorentz force $(F_z = ev_dB_y)$ on the charge carriers which is perpendicular to both the magnetic field and the current, and a moving charge is driven towards one side of the sample. Thus, an accumulation of negative charges will occur at the upper edge of the sample, leaving an excess positive charge at the lower edge of sample, generating an electric field, $E_H$. This field in turn causes a force, $F_H$, on electrons that opposes the Lorentz force, $F_z$. In the steady state these two forces, $F_z$ & $F_H$, are balanced and there is no longer any net transverse force to deflect the moving charges. Hence, the charge carriers start to move parallel to the initial current direction. This results in a constant Hall voltage between the two opposing sides of the sample, $V_H$, which is proportional to the product of the magnetic induction, $B$, and the transport current $I$.

$$V_H = R_H I B \,, \tag{4-1}$$

where $R_H$ is Hall coefficient and is given by

$$R_H = \frac{1}{n.ed} \,. \tag{4-2}$$

Here $n$ is the concentration of charge carriers, $e$ is the electronic charge, and $d$ is the sample thickness. To measure the magnetisation of $NbSe_2$ samples, Hall probes were used in which the charge carriers were confined in a two dimensional electron gas (2DEG). In this case the product $n.d$ in equation 4-2 can be replaced by $n_{2D}$ (the 2D carrier density) and the Hall coefficient becomes $R_H = (n_{2D}.e)^{-1}$.

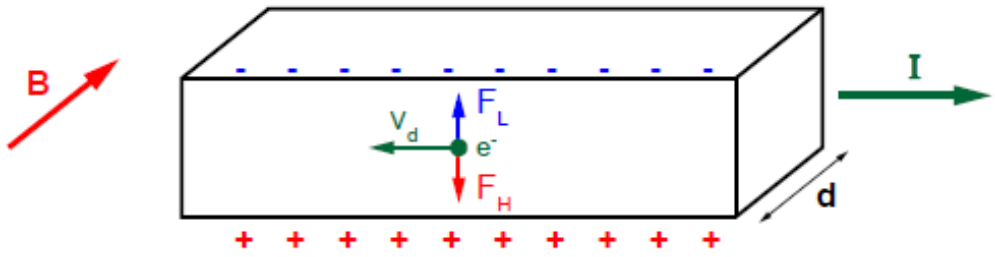


**Figure 4-18:** Schematic diagram illustrating the Hall effect in a block of semiconductor [118].

### 4.10.2 Two dimensional electron gas (2DEG)

A two dimensional electron gas (2DEG) corresponds to the confinement of carriers in a 1D potential well, allowing them to move freely in the other two dimensions (2D). Acquiring a good signal-to-noise ratio (SNR) for measurements at low temperatures can be achieved using micrometer-sized probes, fabricated from the 2DEG in a GaAs/AlGaAs heterostructure. The band structure of the multilayer 2DEG Hall probes used is sketched in Fig. 4-19. GaAs/AlGaAs heterostructures are good candidates for high quality 2DEGs, since the two components have very similar lattice constants but different band gaps [119]. Thus, a modulation of both the conduction and valence bands is achieved across the structure. The Fermi energy is set so that it lies in a V-shaped potential well at the GaAs/AlGaAs interface (cf., Fig. 4-19). The V-shaped well confines electrons in a layer of width ~ 10 nm. The semiconductor Hall probes used here have a very high sensitivity because they contain a very low charge carrier concentration (large Hall coefficient, $R_H$). At low temperatures the conductivity of the sensors is also high due to the spatial separation

of ionised dopant atoms and carriers. This gives rise to very low Johnson noise levels [120].

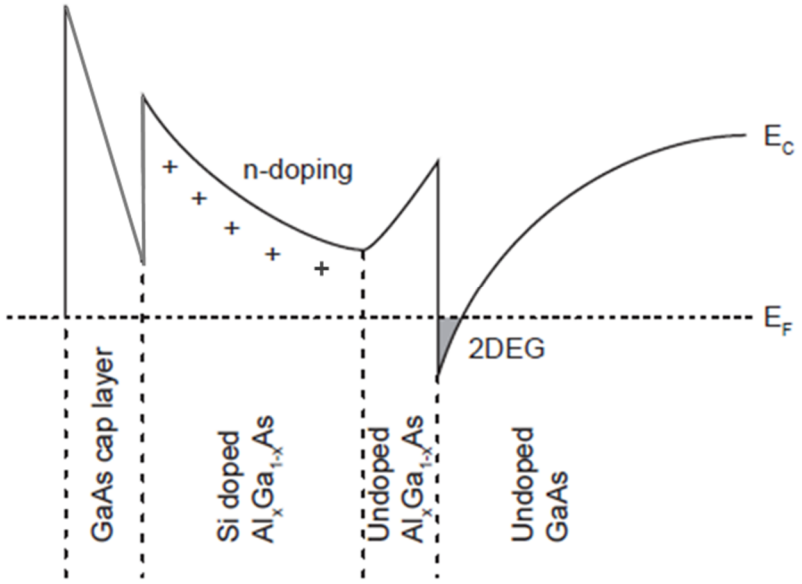


**Figure 4-19:** Schematic structure of the conduction band edge of the GaAs/AlGaAs 2DEG Hall probes used [70].

### 4.10.3 Hall array design

Nine active Hall crosses were patterned in a linear array as can be seen in Fig. 4-20. The Hall voltage was measured at pairs of Hall voltage contacts while one shared current line was used to supply the current. The active area of each Hall probe was $2\ \mu m \times 2\ \mu m$ as shown in Fig. 4-20.

MBE grown GaAs/AlGaAs wafers (C2276 and A3542) were used to fabricate the Hall probes employed. The layer structure of the GaAs/AlGaAs heterostructures had the following order from bottom to top. Firstly, the undoped GaAs substrate followed by an undoped spacer AlGaAs layer $(20\ nm)$ which separates ionised impurities from free carriers. Next a $40\ nm$ Si-doped AlGaAs layer provides the free electrons for the 2DEG with a doping density of $N_D = 1.1 \times 10^{18}\ m^{-3}$. Finally, a GaAs cap layer of thickness $10\ nm$, was added to protect the surface from oxidation. The 2DEG layer formed $\sim 70\ nm$ below the surface. The Hall probe arrays used in this work were fabricated by a colleague (André Müller). The fabrication procedures for these Hall probes are similar to those followed to fabricate FET devices. A detailed description of both the Hall probe

design and the fabrication procedures can be found in the PhD theses of Engbarth [118] and Müller [70].

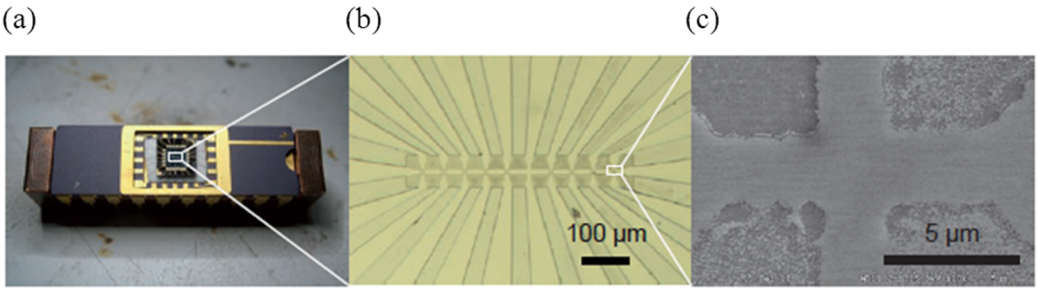


**Figure 4-20:** a) Optical image of the chip carrier package used in the micromagnetic measurements. b) A photograph of the Hall probe array with, c) a close up electron micrograph of a 2 µm Hall cross [70].

### 4.10.4 Magnetometry measurements

For the micromagnetic measurements of $NbSe_2$ flakes, a 20 pin ceramic DIL chip carrier package was used to mount the fabricated Hall probe array as shown in Fig. 4-20 (a). A single crystal of 2H-$NbSe_2$ was cleaved using the mechanical exfoliation technique. The cleaved flakes needed to be positioned on top of one of the Hall crosses using a nanomanipulator as shown in Fig. 4-21. A tungsten needle attached to a 3-axis piezoelectric positioner could be moved in steps of about 200 nm to push samples around. If required a nylon hair could be attached to the needle to more gently align a flake at the centre of a Hall cross.

The transfer of exfoliated flakes from the scotch tape was performed by sticking the tape containing the flakes on top of the Hall probe array, spraying it with acetone to separate the flakes from the tape and removal of the tape. The piezo positioner and the nylon hair were then used to move the flakes into the correct location. Positioning was performed under a drop of IPA, which enabled free movement of the flakes. Care was taken to avoid the needle carrying the nylon hair touching the surface of the Hall array in order that the capping layer was not damaged leading to depletion of the 2DEG.

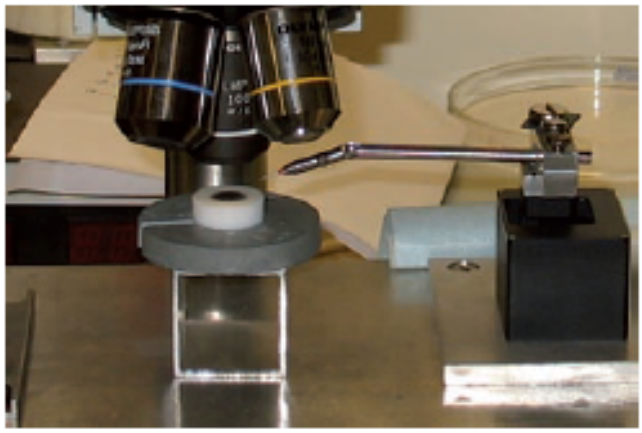

**Figure 4-21:** Photograph of the piezoelectric manipulator [118].

After the flake positioning, the DIL package was plugged into the sample holder for measurements. The electrical setup for the micromagnetic measurements is shown in Fig. 4-22. Two lock-ins were used, one connected to the Hall probe which held the flake and the other connected to an empty reference Hall probe [70].

A detailed description of both the electrical setup and the labVIEW program used to determine the relationship between sample magnetisation, $M$, and the applied magnetic field, $H$, can be found in sections 4.9.4 and 4.9.2 respectively. The key problems encountered with this method were that only thick $NbSe_2$ flakes could be obtained and characterised. Thus, we were not able to characterise very thin, few-layer flakes with this approach.

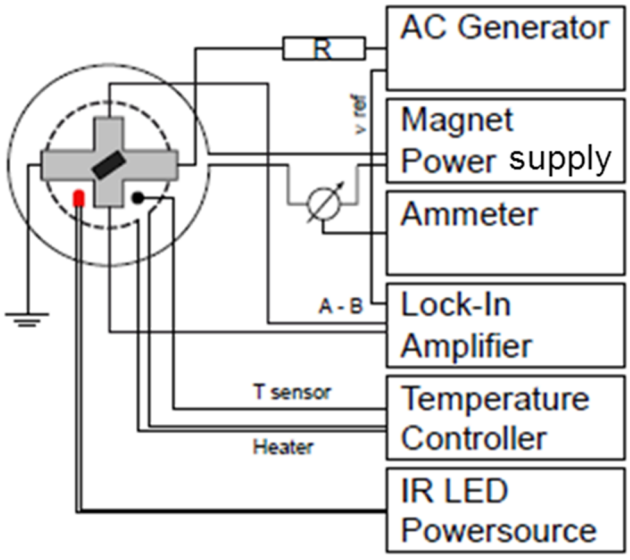


**Figure 4-22:** Sketch of the electrical set-up used for micromagnetic measurements [70].

# Chapter 5

# Graphene Results and Discussion

## 5.1 Basic Characterization of Flake Quality

Graphene flakes can be characterised using several different techniques, each of which provides complementary information. A focus on utilising both AFM and Raman spectroscopy to identify single and few-layer graphene, and to determine the quality of graphene flakes, will be introduced in this section. Both the doping level and the mobility of carriers in graphene flakes are used as indicators of the quality. These two quantities are probed by a quantitative investigation of the flake resistance as a function of applied gate voltage. This will be described in detail in the next section.

The first technique used for identifying single and few-layer graphene is atomic force microscopy (AFM). A brief description of the AFM system is given in section 4.7. AFM scanning is performed at room temperature with a commercial atomic force microscope (MFP-3D, Asylum Research). The AFM is a valuable tool for surface studies of graphene as it provides very high spatial resolution which enables the observation of graphene flake edges, flake corrugation and interplanar distances [99]. The AFM was used in tapping mode to quantitatively measure the thickness of the graphene sheets on $Si/SiO_2$ substrates. A selection of some of the graphene flakes studied in this project is presented in Fig. 5-1. Different flakes have distinct interference colours when viewed under an optical microscope corresponding to the number of layers present. AFM images for these flakes were obtained by scanning the devices after measuring them electrically. The different contrast of these flakes is associated with different step-heights obtained by AFM scanning. Both the AFM images for the flake devices and their associated step-height profiles are illustrated in Figs. 5-2 and 5-3, for two selected devices.

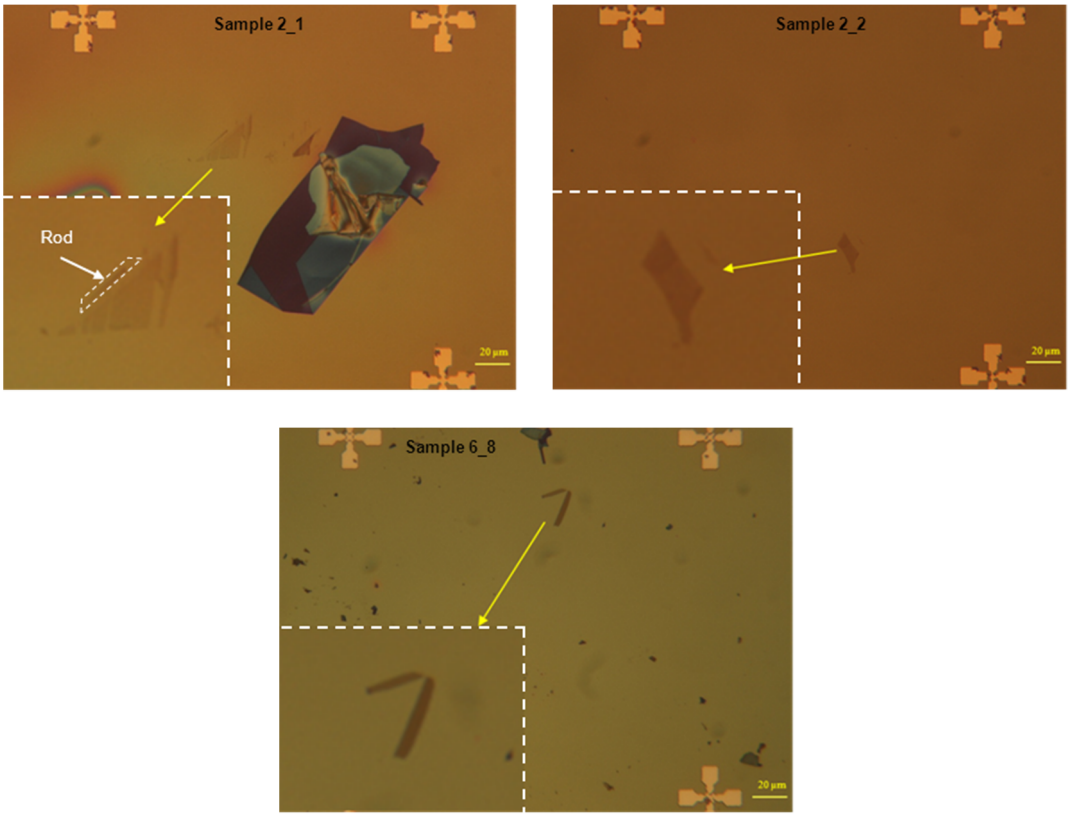


**Figure 5-1:** Optical micrographs of a selection of three of the graphene flakes studied in this experiment. Inset in sample (2-1) image shows the 2LG rod flake.

AFM scanning could not be done for device (2-1) since the chip had not been raised to a height that makes it accessible to the AFM tip. Both 2D and 3D AFM images and the step-height profile for the measured device (2-2) are shown in Fig. 5-2. Theoretically, the thickness of monolayer graphene is ~ 0.34 nm. However some authors report that the step height could be closer to 0.4-0.45 nm [111]. The AFM topography of the graphene flake indicates both the homogeneity of the flake and its thickness of 0.88±0.17 nm, which is close to the value expected for 3LG as indicated by the Raman spectra in the next section. A thick graphene flake device that was also scanned by AFM is shown in the 2D and 3D AFM images of Fig. 5-3 along with the relevant step-height profile. The estimated number of graphene layers was 12 for this flake based on the measured thickness of 4±0.37 nm.

The AFM technique has some limitations which make it inappropriate for determining the actual flake thickness accurately. Such limitations arise from the possibility of the existence of one or two water layers either above or below the graphene flake [111]. Also, an incorrect estimate of the flake thickness can result

from the chemical contrast between graphene and the substrate, which shifts the measured thickness about 0.5 – 1 nm from the expected thickness of the interlayer graphene spacing [114].

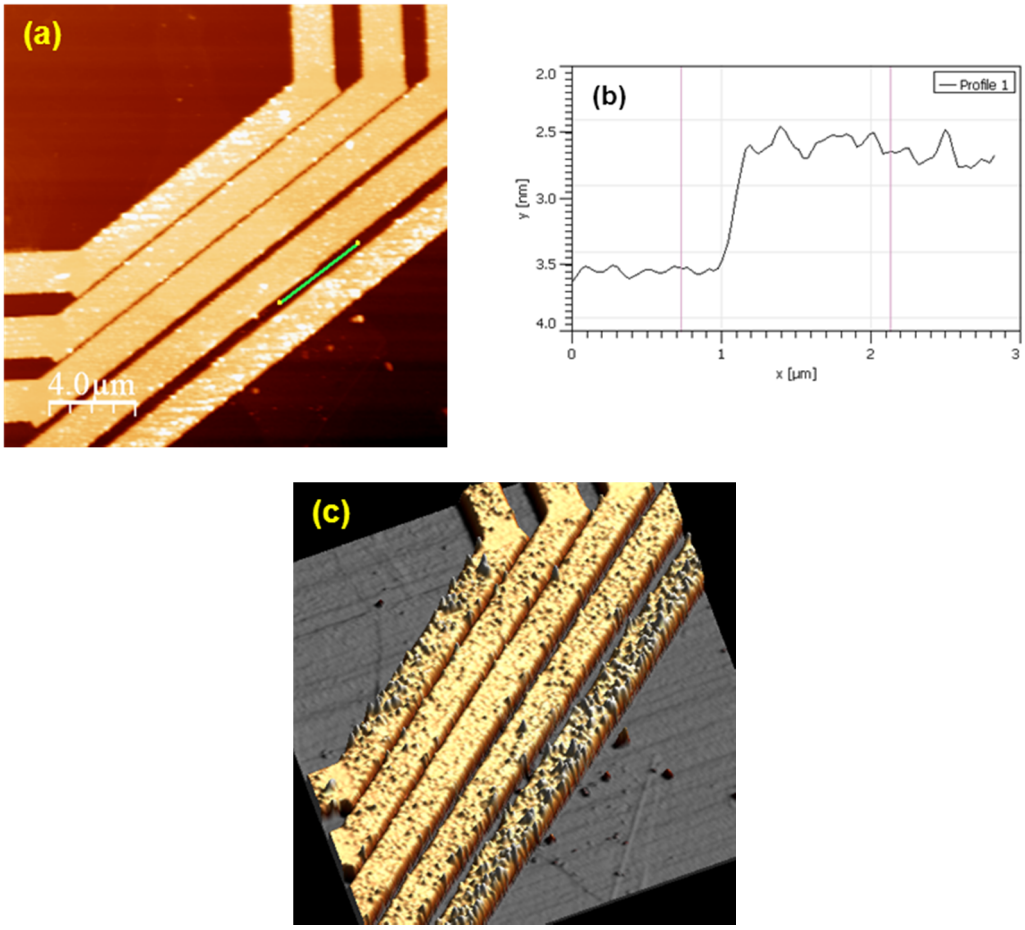


**Figure 5-2:** a) 2D AFM image of device (2-2). b) Step-height profile for the flake along the line shown in a). c) 3D image of the same device.

To overcome these limitations, Raman spectroscopy was used to determine the number of graphene layers, since it represents an unambiguous, high-throughput, and non-destructive method to characterise graphene flakes [114]. Flakes were scanned at room temperature using a Renishaw inVia Raman microscope at an illumination wavelength of 514 nm. A piezoelectric stage and a short working distance 50x objective lens were used to capture Raman spectra from the graphene flake with integration times varied between 100 and 400 seconds.

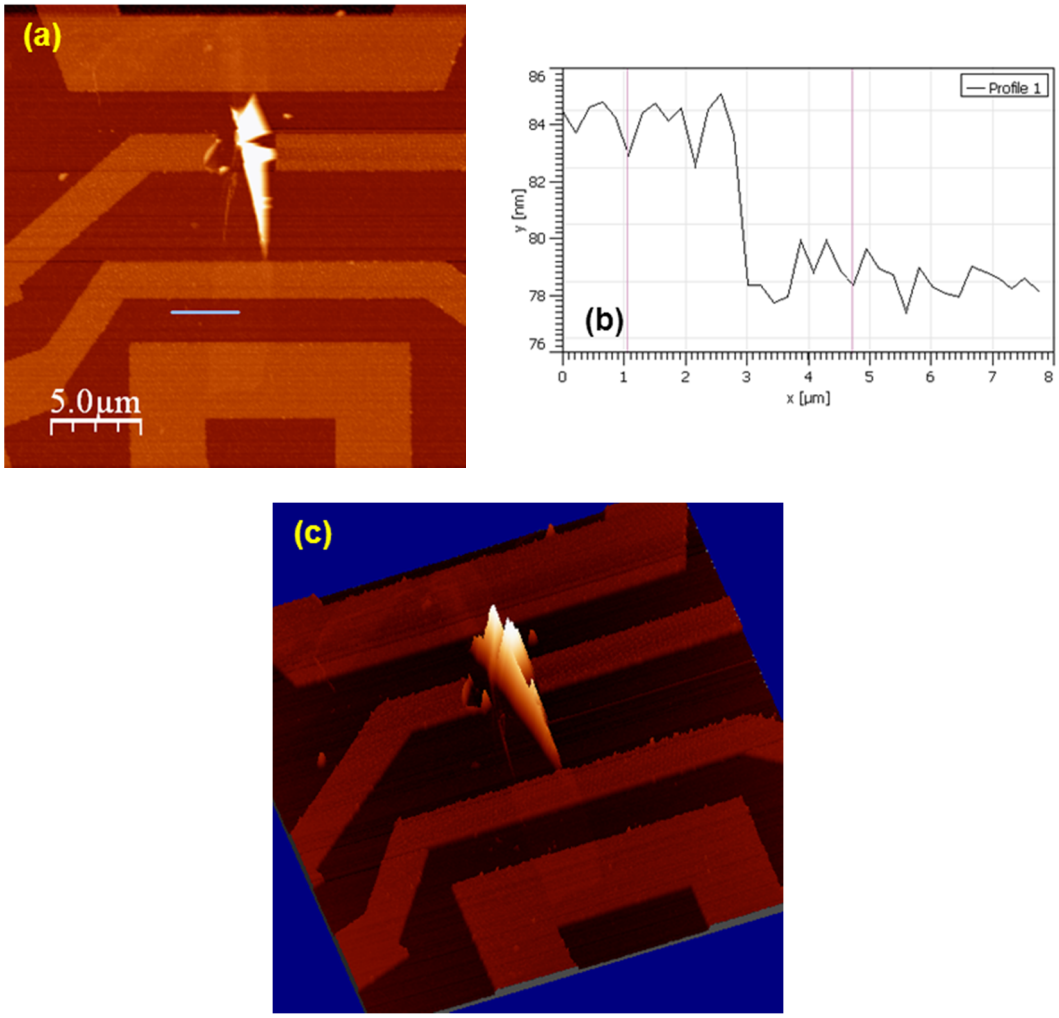


**Figure 5-3:** a) 2D AFM image of device (8-6). b) Step-height profile for the flake along the line shown in (a). c) 3D image of the same device.

Figures 5-4 and 5-5 show the Raman spectra of four selected graphene flakes of different thickness. In all cases both the characteristic G band and 2D band Raman peaks as well as the G* band peak were observed, while the D-band peak was observed in sample (2-1) and was absent in samples (2-2) and (8-6). The physical origin of these different peaks in the Raman spectra was described in section 4.8, and further details can be found in Ferrari *et al.* [114] and Malard *et al.* [121]. Information about both the layer number and structure of the graphene flake can be extracted from analysis of the relative height and shape of these peaks.

The appearance of the D-peak in sample (2-1) is an indication of high levels of disorder or defects in the sample, which could arise from the presence of adsorbates, impurities or $sp^3$ carbon bonds. In contrast, the absence of the D-band in samples (2-2) and (8-6) suggests these flakes are of a rather higher quality. Adding

more layers to monolayer graphene does not effect the shape of the G-peak, while its height increases with increasing number of layers. This is clearly seen in Fig. 5-4, which shows Raman spectra for several flakes, ranging from monolayer up to 12-layer graphene. All of the studied flakes have the same FWHM of ~ 13.13 $cm^{-1}$ for the G-peak.

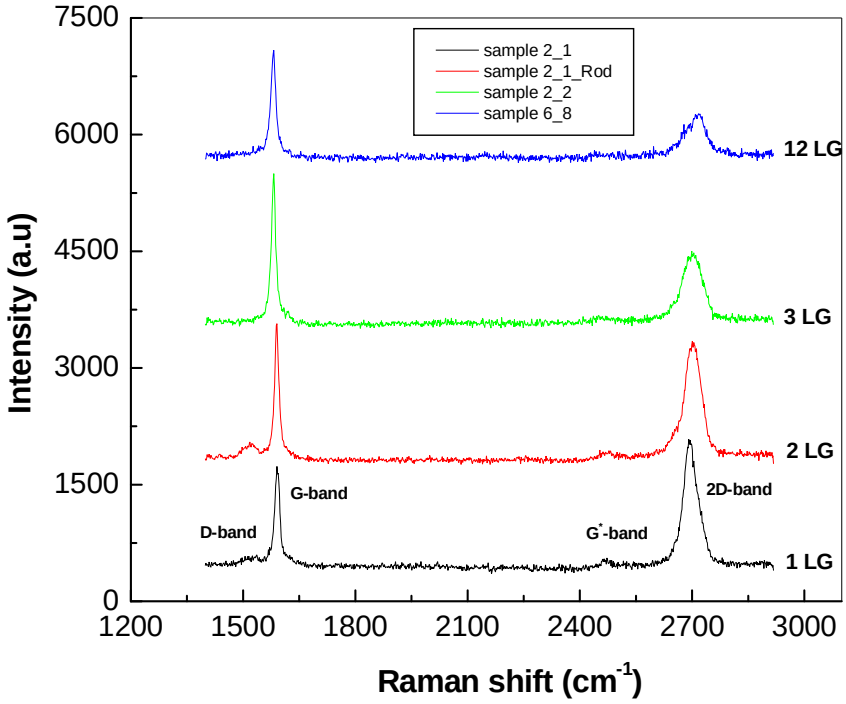


**Figure 5-4:** Raman spectra for 1LG, 2LG, 3LG and 12LG flakes.

The shape of the 2D peak is very sensitive to the number of layers in the graphene flake, and changes from a single uniform peak in monolayer graphene (sample 2-1) to a non-uniform one that begins to resemble bulk graphite in the 12 layer flake (sample 8-6), as can be seen in Fig. 5-5. Hence, around 10-15 layers is traditionally considered to be the crossover between graphene and graphite. In addition, both the structure of the 2D peak (width, and the fit to one or more Lorentzian components) and the peak position hold important information which provides more details about the layer number and structure of samples. A single Lorentzian fit is used for the 2D-peak for 1LG (sample 2-1) (c.f., Fig. 5-5), while fitting the 2D-peak in the other flakes requires multiple Lorentzian components to match the peak shape. The FWHM was increased from ~ 45 $cm^{-1}$ for 1LG to 75 $cm^{-1}$ for 12 LG. The intensity ratio $I(2D)/I(G)$ can be used to estimate the number of

layers in graphene flakes. This ratio is greater than one for 1LG, nearly equal to one for 2LG and less than one for NLG where N> 2.

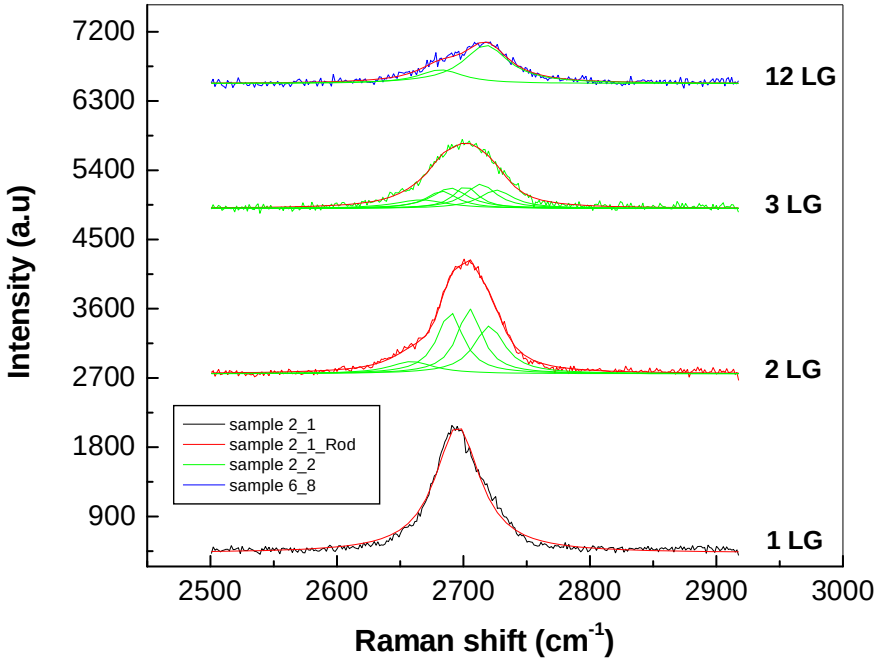


**Figure 5-5:** Raman spectra in the vicinity of the 2D-band peak showing the changes in the peak position, structure and number of fitted Lorentzian peaks as a function of the number of graphene layers.

## 5.2 Gate Sweep and Charge neutrality point

The electric field effect in graphene was reviewed in section 2.3. The gating effect has been studied using a voltage source (Keithley 230 programmable voltage source) connected to the Sb-doped Si substrate which operates as a back gate. Both the two-point resistances and their dependence on the back gate voltage were measured at room temperature, and samples were then measured down to 4.2 K after cooling in the He cryostat described in section 4.9.3.

Unintentional doping affects the graphene flake resistance because charge carriers can be introduced via impurities both in the graphene and on the surface of the flake itself. The maximum resistivity of graphene is observed at the charge neutrality point (CNP or Dirac point) which is at zero gate voltage in ideal "undoped" graphene, and is shifted to positive or negative gate voltages in real graphene samples depending on the type of charge carriers (negative or positive)

introduced by unintentional doping. Hence the concentration of impurities in and on the graphene can be inferred from the position of the Dirac point. Applying a gate voltage to the device modulates the charge carrier density and carrier type, and can compensate the unintentional doping present in the system.

Almost, all our measured graphene devices showed the CNP at positive gate voltages as can be seen in Fig. 5-6 for sample (8-6) and Figs. 5-7, 5-8, for samples (2-1) and (2-2). Therefore, a positive gate voltage is required to induce electrons into graphene to compensate the hole doping and achieve charge neutrality. Water molecules can act as charge acceptors and so the possible presence of a layer of water molecules, either above or below the graphene flake, could explain the hole doping observed at $V_g$ = 0 in these samples.

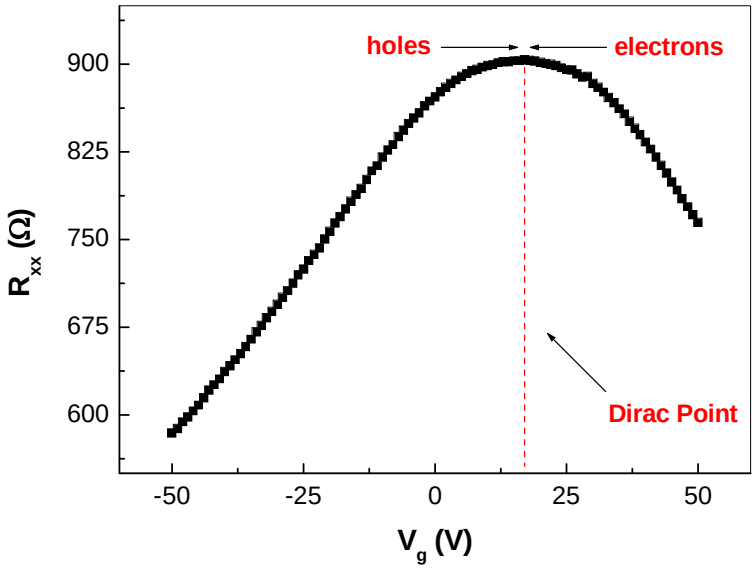


**Figure 5-6:** Graphene flake resistance as a function of gate voltage at 300 K for device (8-6).

The dependence of the resistance of three selected graphene devices on the gate voltage is shown in Figs. 5-6, 5-7 and 5-8, corresponding to the flakes characterised with AFM and Raman spectroscopy in the previous section. The first device (8-6) had a large spacing (~ 4.7 µm) of the contact electrodes and undesirably high contact resistances. Figure 5-6 shows the influence of gate voltage on the resistance at 300K for this device. The position of the Dirac point, as well as the symmetry of the electron and hole branches, are influenced by extrinsic doping

effects, whether from the unintentional doping by absorbed water [22] or from electrostatic doping caused by impurities [122].

Figures 5-7 and 5-8 display R versus $V_g$ for samples (2-1) and (2-2). These devices, with Pd/Al electrodes, show very low contact resistances (~100 Ω) arising from chemisorption of Pd at the graphene surface. Junctions in these devices had contact spacings of 250 nm (x2), 500 nm and 750 nm, and the 4-point resistances scaled very well with lithographic dimensions. All junctions were functioning properly in device (2-1), whilst only two 250 nm gap junctions worked in device (2-2). Figure 5-7 shows the influence of gate voltage on resistance for all the functional junctions at 4.2 K, while Fig. 5-8 shows R versus $V_g$ for the selected junctions in both devices at 300 K, 77 K and 4.2 K.

In Fig. 5-8 (b), the resistance drops at low temperatures due to an increase in mobility, μ(T), while at high temperature μ(T) should be approximately constant and the resistance drops again due to an increasing number of thermally excited free carriers. Every voltage sweep consists of trace and retrace, where the gate voltage is swept from $-V_M$ to $+V_M$ and from $+V_M$ to $-V_M$ respectively and $V_M$ is the maximum voltage magnitude for the sweep. Irreversibility (hysteresis) between trace and retrace curves is observed at T = 4.2 K and is more pronounced at T = 77 K. This hysteresis is probably due to the slow redistribution of charges in the $SiO_2$ substrate or the migration of water molecules that might be trapped below and/or above the graphene flake. These devices show very strong proximity hole doping by the Pd contacts leading to a shift of the Dirac point to very large positive gate voltages, above the maximum $V_M$ that could be applied to the back gate. Strong proximity doping suggests the presence of a clean interface between electrode and graphene flake.

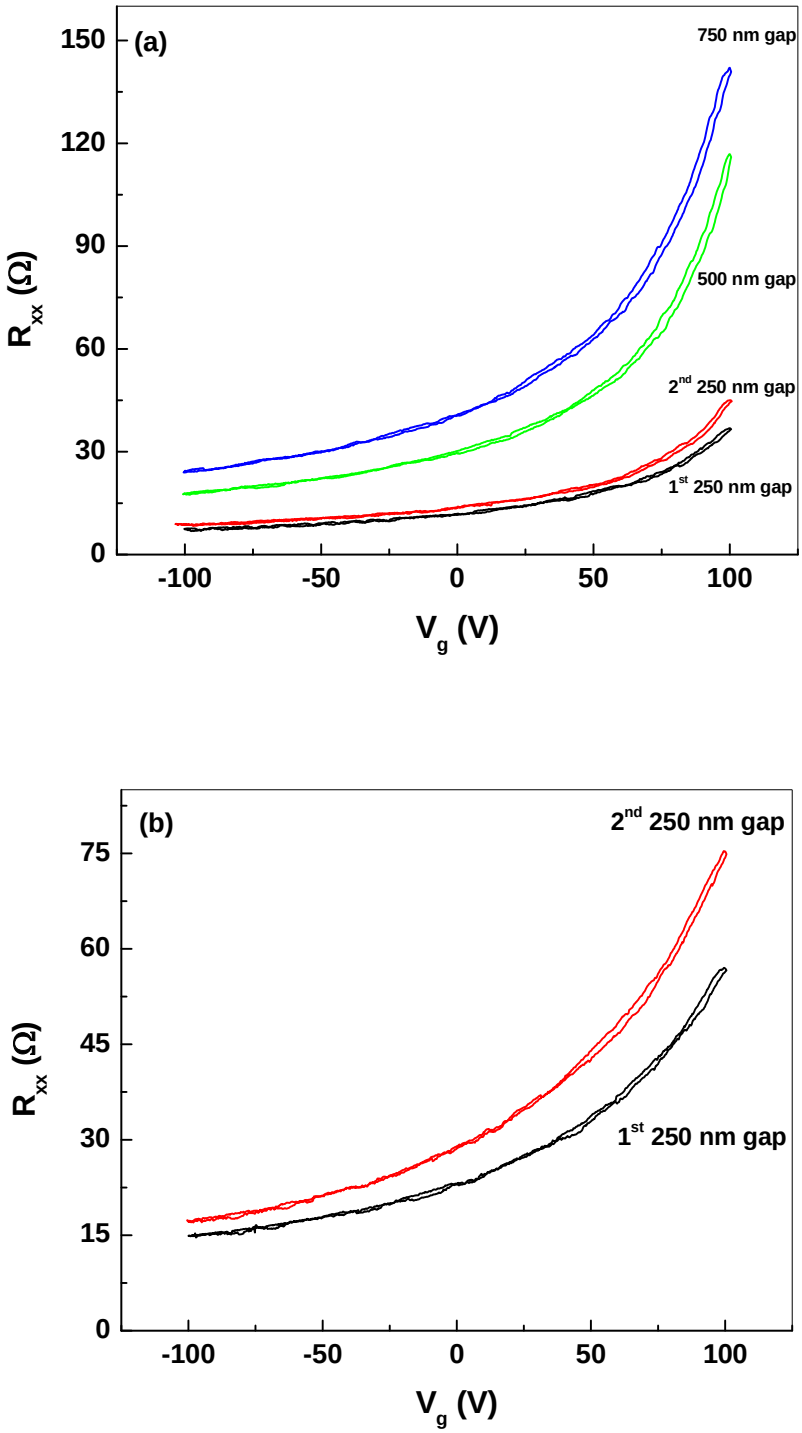


**Figure 5-7:** Plots of $R_{xx}$ versus $V_g$ at T = 4.2 K showing a pronounced shift of the Dirac point due to strong proximity hole doping by the Pd contacts. a) All junctions on sample (2-1) and b) the two working 250 nm junctions on sample (2-2).

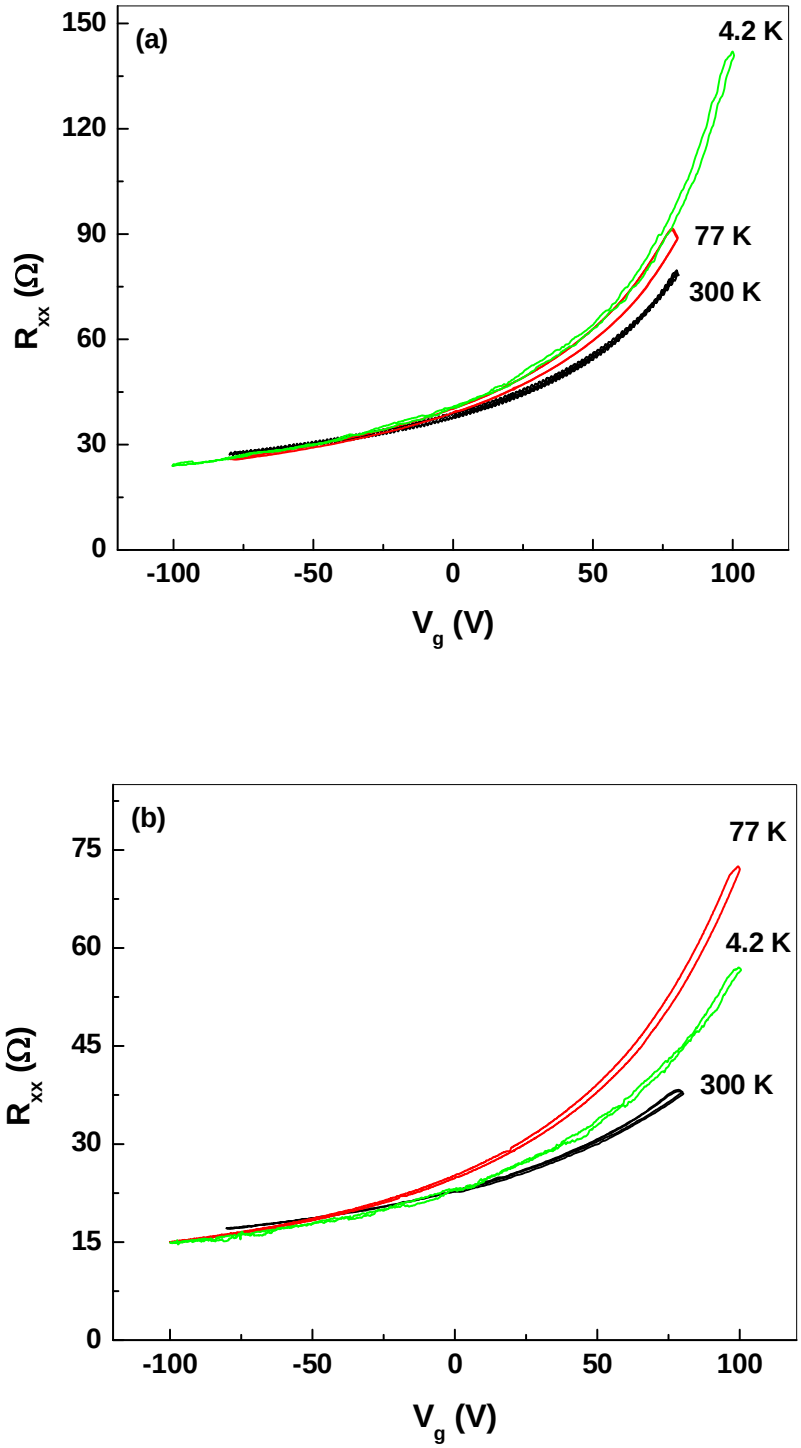


**Figure 5-8:** Plots of $R_{xx}$ versus $V_g$ at three different temperatures. a) 750 nm gap on sample (2-1), and b) 1st 250 junction on sample (2-2).

A charge-transfer model was introduced by Nouchi *et. al.* [123] to describe the doping effect of metal contacts in the adjacent graphene sheet and to investigate the causes of the electron-hole asymmetry. A schematic diagram of the device described by this model is shown in Fig. 5-9 (a), where $L$ is the graphene channel length between the source and drain electrodes, and $L_d$ is the length over which the graphene is doped by the metal contact. The overall graphene channel resistance is assumed to be modelled by a sequence of local resistances connected in series. The overall resistance, R, of the graphene sheet of length $L$ between the metal electrodes can be expressed by equation 5-1, where homogeneity of the graphene channel along the direction parallel to the contact edge is assumed [123].

$$R = \frac{1}{W}\int_0^L \rho(x)dx = \frac{1}{W}\int_0^L \frac{1}{\sigma(x)}dx \ , \tag{5-1}$$

where $W$ is the channel width and $\rho(x)$ ($\sigma(x)$) are the local resistivity (conductivity) at distance $x$ respectively.

Taking into account the fact that the charge carrier density dependence on the gate voltage can be modelled as a parallel-plate capacitor, a phenomenological expression for the conductivity as a function of distance can be derived [123]:

$$\sigma(x) = \sqrt{\left\{\mu\frac{\varepsilon_0\varepsilon_r}{d}[V_g - V_{DP}(x)]\right\}^2 + \sigma_{min}^2} \ , \tag{5-2}$$

where $V_g$, is the gate voltage, $V_{DP}(x)$ is the Dirac voltage at a distance $x$, $\sigma_{min}$ is the local conductivity at the charge neutrality point ($V_g = V_{DP}(x)$), and $\left[V_g - V_{DP}(x)\right]$ is the "local" gate voltage with respect to the Dirac voltage. Using expressions 5-1 and 5-2, the overall resistance can be rewritten as [123]

$$R = \frac{1}{W}\int_0^L \left(\left\{\mu\frac{\varepsilon_0\varepsilon_r}{d}[V_g - V_{DP}(x)]\right\}^2 + \sigma_{min}^2\right)^{-1/2} dx \ . \tag{5-3}$$

To solve this equation, the doping profile must be known. Nouchi *et. al.* [123] introduced two types of doping profile to model the effects of the charge transfer from the metal contacts, as can be seen in Figs. 5-9 (b) and (c). The first profile (Fig. 5-9 (b)), represents the assumed gate voltage dependence in the case of pinned charge density at the metal contacts. Here, the doping potential is pinned at both contacts and is varied linearly until it reaches the gate voltage $V_g$ over a length $L_d$ from the contact edges. Varying the gate potential, $V_g$, does not change the length $L_d$

on both sides of the contacts while it does change the doping level within the channel. The second doping profile (Fig. 5-9 (c)) represents the case of no-pinning of the charge density at the metal contacts. As a result of contact-induced doping linear offsets at the edges are obtained, while the doping of the entire channel is modulated by the gate potential $V_g$.

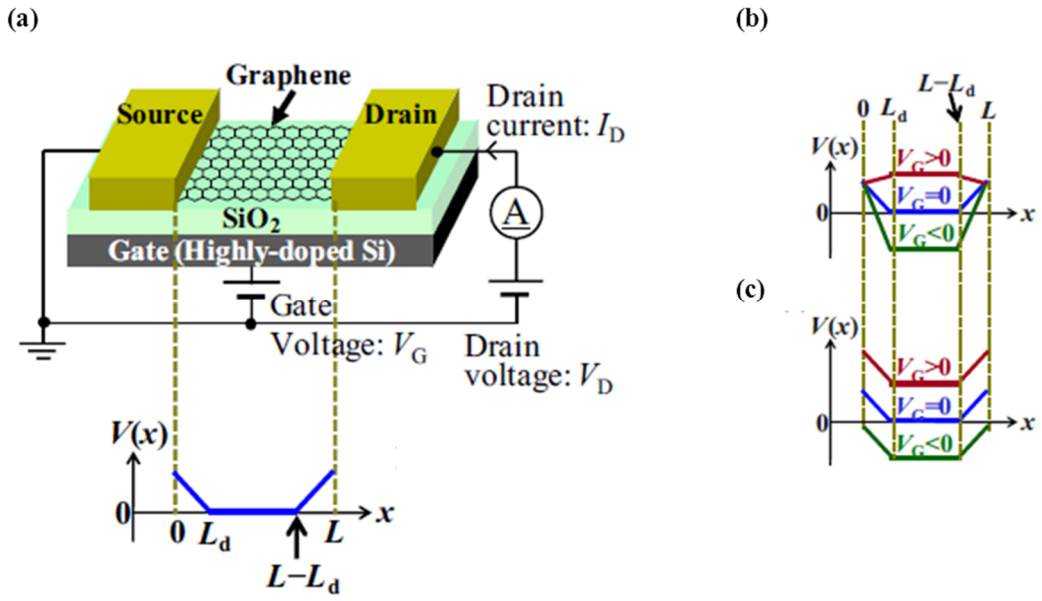


**Figure 5-9:** a) Sketch of the device described in the charge transfer model illustrating the doping profile along a graphene channel of length $L$ between source and drain electrodes. b) and c) represent the assumed doping profiles for the cases of pinned and unpinned charge density beneath the contacts, respectively [123].

In every device two contacts are involved in the doping process, thus the influence of both of them must be included. The transfer characteristics of graphene FETs with different channel lengths have been simulated by Nouchi *et. al.* [123] using the two assumed doping profiles. One of the most interesting findings of their study was the possibility of superposition of the doping profiles arising from two adjacent contacts. This scenario appears to be in agreement with the results obtained for devices (2-1) and (2-2). As a consequence of the superimposed doping profiles the effective gate potential of the device does not correspond to $V_g$, and the Dirac point is shifted to a high positive gate voltage. It is also important to note that in a real measurement, a shift in $V_{DP}$ away from zero voltage not only originates from the

doping by both the gate voltage and the metal contacts but also any additional doping caused by contaminants or charge centres present.

Linear fits to the conductivity have been made for all junctions on device (2-1) at 4.2 K. These fits are achieved using an automated procedure to fit a cubic polynomial to the whole curve and then differentiating the fit function to find the local slope at the point of interest. The expected trend that $V_{DP}$ falls as the gap gets wider is broadly obtained and illustrated in Table 5-1. The presence of conductance fluctuations (CFs) in the devices with 250 nm gaps strongly perturbs the local slopes, and the $V_{DP}$ values obtained from these junctions are somewhat less reliable. Figure 5-10 shows an example of the fits made for these junctions.

| **At V(0) = 25 V** | 1st 250 nm gap | 2nd 250 nm gap | 500 nm gap | 750 nm gap |
|---|---|---|---|---|
| $\boldsymbol{V_{DP}}$ **(V)** | 144.7 | 153.3 | 135.4 | 135.6 |

**Table 5-1:** The extracted $V_{DP}$ values for all junctions in device (2-1) at 4.2 K.

Similar fits have been generated for each junction at 300 K, 77 K and 4.2 K. The fit procedure was particularly helpful for the 300 K data as the conductance has a strongly non-linear behaviour at negative voltages. Fits reveal that the Dirac point shifts slightly to lower voltages as the temperature is reduced, and this shift is more pronounced in the case of the 750 nm gap junction in device (2-1), as compared to the 500 nm junction in same device. The extracted $V_{DP}$ values for both junctions are presented in Table 5-2.

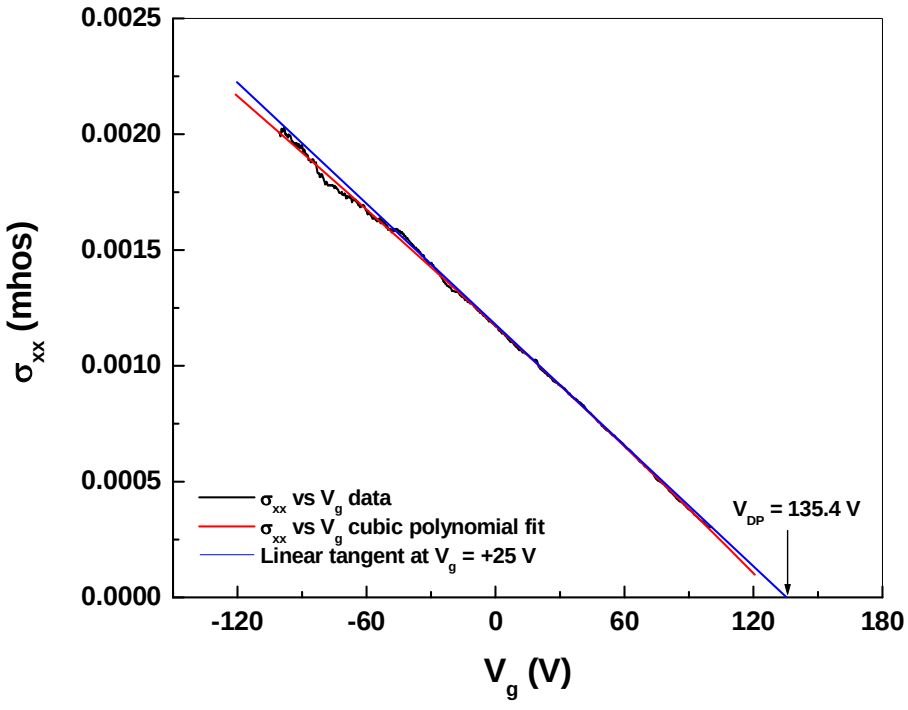


**Figure 5-10:** Fits to the conductance data for the 500 nm gap in sample (2-1) at 4.2 K and its intercept with the x-axis yielding $V_{DP}$.

| Extrapolated from $V_g$ = 70 V | $V_{DP}$ (V) | | |
|---|---|---|---|
| | **300 K** | **77 K** | **4.2 K** |
| 500 nm gap | 158 | 124 | 133 |
| 750 nm gap | 147 | 140 | 138 |

**Table 5-2:** The extracted $V_{DP}$ values for 500 nm , and 750 nm junctions in device (2-1) at 300 K, 77 K and 4.2 K.

All the characterisation data from these junctions suggests that they should be optimised for investigating proximity supercurrents and we have made extensive measurements of them in a $^3$He refrigerator down to 300 mK. For reasons we do not currently understand we have not observed any sign of proximity supercurrents in any of the junctions. Neither were we able to find any signatures of superconductivity in the Al electrodes.

From measurements of the R($V_g$) curves for samples (8-6) at 2 K and (2-2) at 4.2 K, mobilities for each sample were calculated using the Drude formula 2-9. In addition, the carrier concentration of each sample was estimated theoretically as a function of applied gate voltage using equation 2-15. Both the charge carrier concentrations and the mobilities as a function of the applied gate voltage are shown in Fig. 5-11 (a) for sample (8-6) and in Fig. 5-11 (b) for sample (2-2). The main point of interest in these graphs is the Dirac point (CNP), at which the carrier concentration theoretically drops to zero and hence an anomalously high mobility is calculated. On both sides of this point, an increase in the carrier concentration and a decrease in mobility are obtained over the range of applied back gate voltages used.

Since, sample (2-2) is strongly p-doped due to proximity doping from Pd in the Pd/Al contacts we were unable to reach the Dirac point with the maximum back gate voltage that could be applied. From the gate dependant conductivity, the Dirac point is estimated to be at about $V_g \approx +$ 140 V (cf., Fig. 5-12). This enables one to estimate the charge carrier concentrations for this sample at arbitrary gate voltages. The carrier concentration is found to reach as high as $10^{16}$ $m^{-2}$ for sample (8-6) and $10^{17}$ $m^{-2}$ for sample (2-2) over the available range of gate voltages. The mobilities are in the range 0.3 – 7.4 $m^2$/Vs for sample (8-6), and 0.0758 - 0.1034 $m^2$/Vs for sample (2-2). These values are in good agreement with those obtained on similar devices in the literature [2, 22, 122].

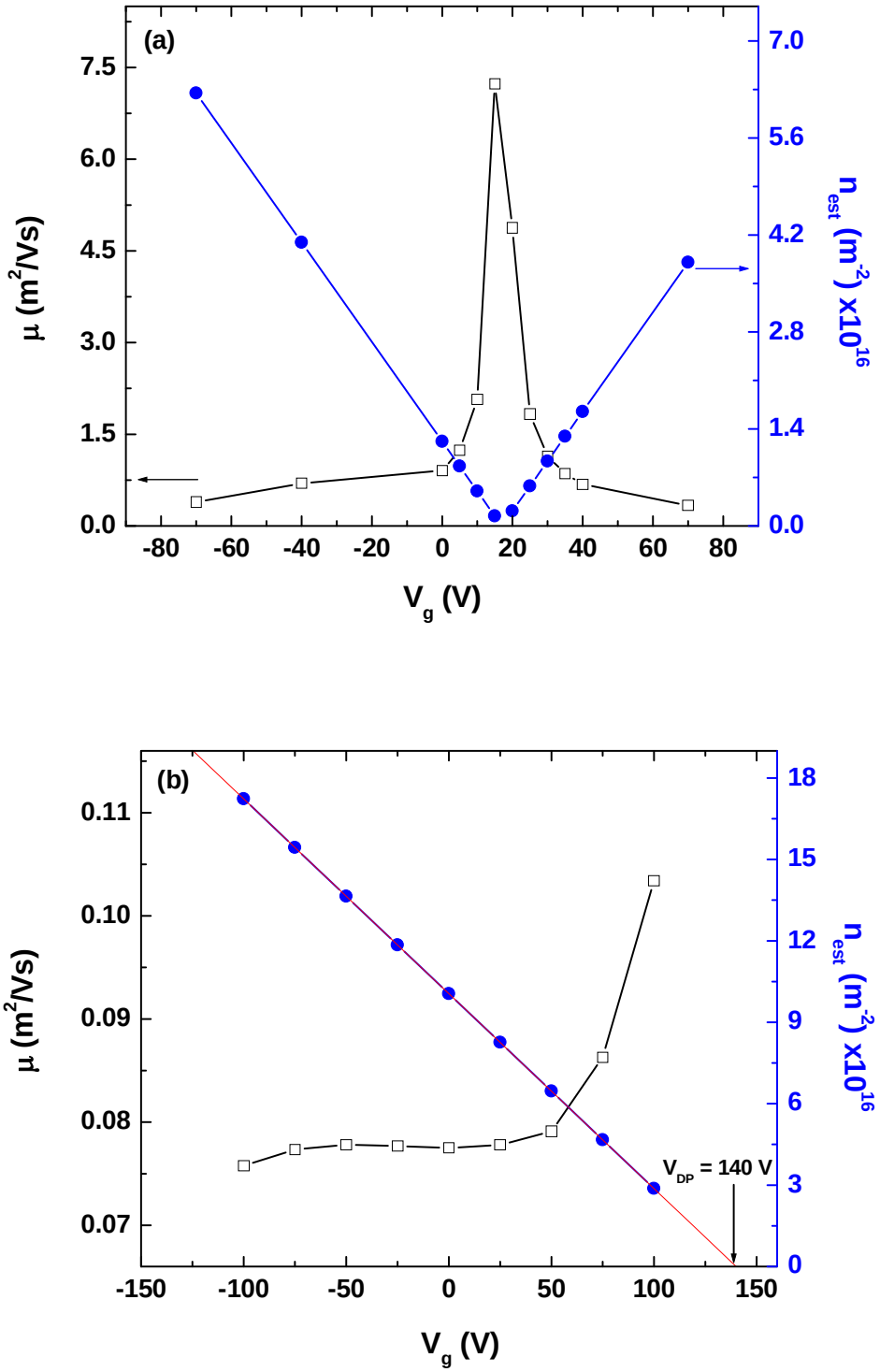


**Figure 5-11:** Carrier mobility and charge carrier concentration as a function of back gate voltage for a) sample (8-6) at 2 K and b) sample (2-2) at 4.2 K.

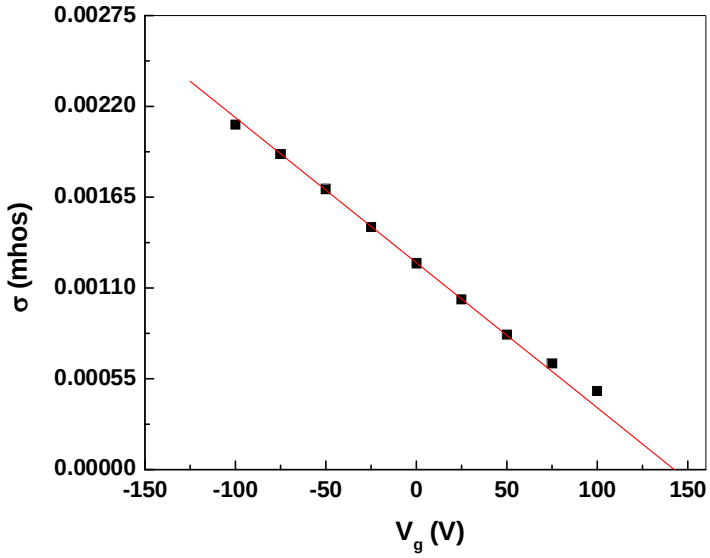


**Figure 5-12:** The conductivity of sample (2-2) as a function of gate voltage is used to estimate that the voltage at the Dirac point is + 140 V.

## 5.3 Resistance measurements in a transverse magnetic field: comparison with weak localisation/anti-localisation theory

### 5.3.1 Weak localisation/anti-localisation effects

Magnetoresistance is defined as the change of longitudinal resistance, $R_{xx}$, as a function of the applied magnetic induction, $B$, and shows an interesting behaviour in graphene.

Weak localisation and weak anti-localisation are two phenomena that play an important role in describing the behaviour of the magnetoresistance in graphene. Electron waves can be coherent over long distances, even when the Fermi wavelength is comparable to or longer than the mean free path ($k_F l \leq 1$). Weak localisation corrections need to be added to the classical Drude expression for conductivity as a consequence of both quantum interference and electron coherence. The constructive interference between time-reversed electron paths along a closed loop, as shown in Fig. 5-13, is the origin of these corrections. At the point of intersection the interference will be constructive if the phase change of the waves is the same along the two paths. Consequently, one gets constructive back scattering and the probability of the electron remaining at the intersection increases (i.e., the

electron is weakly localised) and the overall electrical resistance increases as well (constructive back scattering).

This interference can be suppressed in two situations; firstly, when the dephasing length (the length over which coherence is destroyed) becomes shorter than the length of the electron path and secondly, when an applied magnetic field adds a random relative phase to the electron wavefunction, and destroys the time reversal symmetry. Thus, negative magnetoresistance appears in most metals at low temperatures and applying a small magnetic field decreases their resistivity.

Graphene has two interesting characteristics which are related to the nature of its charge carriers. These are chiral and their wavefunctions have an associated Berry phase of $\pi$ [124]. As a consequence weak anti-localisation is expected with a reduction in resistance due to interference effects. This phenomenon is the opposite of the one that appears in metals. Again, the anti-localisation effect can be suppressed by applying a magnetic field which randomises the carrier phase. Consequently, an increase of the resistivity (positive magnetoresistance) is expected to occur.

The band structure of graphene has two valleys with opposite chirality $(\mathrm{k}, \mathrm{k}')$. Localisation effects are expected when electrons are scattered between the valleys (inter-valley scattering), while anti-localisation is expected when electrons are scattered within the valley (intra-valley scattering). Depending on the experimental conditions, graphene can exhibit both localisation and anti-localisation effects [125].

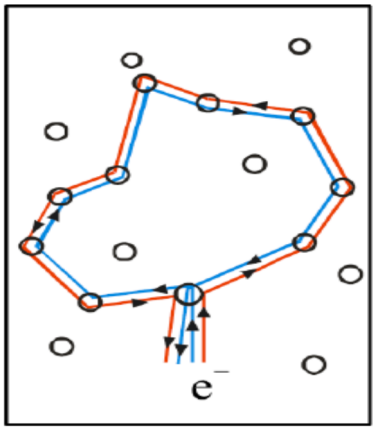


**Figure 5-13:** A quantum correction to the conductance arises due to interference of time-reversed electron trajectories which have been multiply scattered by impurities [125].

### 5.3.2 Magnetoresistance measurements in a transverse field

The characterization of the electronic properties of thin-films or 2DEG systems frequently involves the application of a magnetic field (usually perpendicular to the sample plane). The application of a field to graphene produces some behaviours that are unique to graphene and others that are shared with other 2DEG systems. The longitudinal resistance, $R_{xx}$ (B), as a function of field at different gate voltages is plotted in Fig. 5-14 (a) for sample (8-6). The applied gate voltage has a clear effect on the changes of $R_{xx}$ with magnetic field. Two features can be noted from this dependence. The strongest positive magnetoresistance is found at the charge neutrality point (CNP) while, in contrast far from the Dirac point the longitudinal resistance $R_{xx}$ is nearly independent of the applied magnetic field [125]. The observed positive magnetoresistance could be due to the suppression of WAL in our system, arising from the suppression of backscattering due to the Berry phase of $\pi$.

Figure 5-14 (b) plots the positive longitudinal magnetoresistance $R_{xx}$ (B) as a function of field at temperatures 2.5 K, 3.5 K and 4.2 K over the range $B$ = ± 100 mT A clear WAL minimum can be seen at zero magnetic field. Both the value of the minimum and its sharpness are temperature dependant, becoming shallower and more rounded at higher temperatures. This behaviour is in agreement with data obtained by Morozov *et.al.* [126]. The increase of $R_{xx}$ with T is due to increased phonon scattering of carriers.

Further magnetoresistance characterization of sample (8-6) was not possible as the contacts were destroyed during an electrostatic discharge (ESD) damage event.

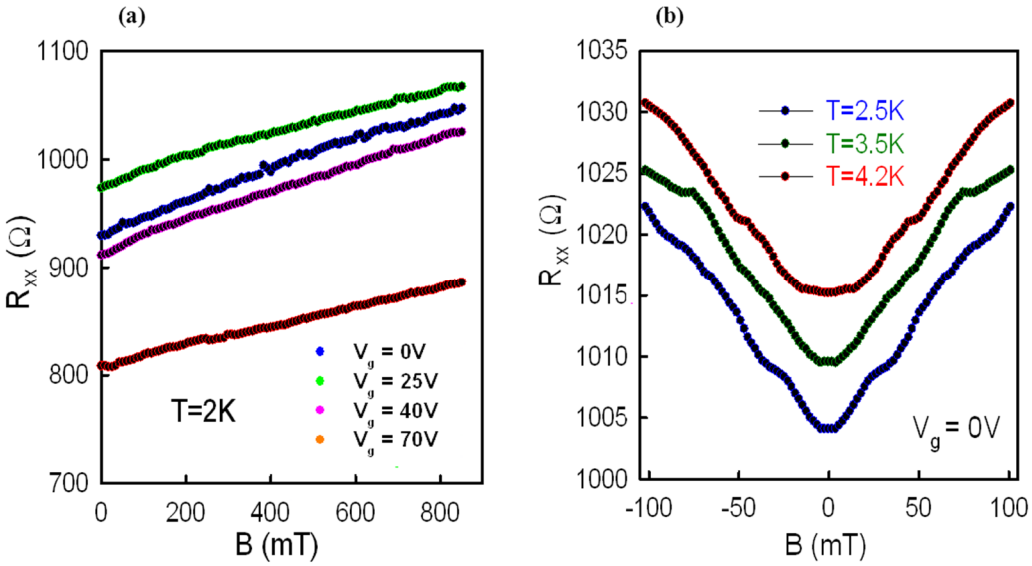


**Figure 5-14:** a) $R_{xx}$ as a function of B and $V_g$ at 2 K for sample (8-6). b) $R_{xx}$ for the same sample as a function of B at 2.5 K, 3.5 K and 4.2 K.

### 5.3.3 Magnetoresistance trends with temperature

The dependence of the phase coherence length on temperature is the origin of the temperature dependence of the magnetoresistance observed in all samples. In sample (2-2) the magnetoresistance data contain more than one component as can be seen in Fig. 5-15 for both 250 nm junctions. At B = 0 a sharp WL peak indicates a relatively long phase coherence length. With increasing temperature, a reduction in the amplitude of the WL peak is observed, while its width increases due to the reduction of the phase coherence length [127, 128]. The half width of the MR peak ($\Delta B = {}^{\varphi_0}/_{L_\varphi^2}$ where $L_\varphi = \sqrt{D\tau_\varphi}$) is a measure of the sample quality as sharper peaks are obtained with more ordered samples. For each curve in Fig. 5-15 increasing the applied field leads to a suppression of WL and negative magnetoresistance. However, above a certain field a positive magnetoresistance component from WAL is obtained, which appears to be more pronounced at low temperatures. At high fields, the WAL is suppressed again as the applied field randomises the carrier phases. Consequently, an additional increase of the resistivity (positive magnetoresistance) is obtained. These observations are in agreement with data published in the literature for both epitaxial [129] and exfoliated graphene [125]. WAL can be suppressed at low fields due to corrugations of the graphene sheet [126] and trigonal warping [130]. At the same time the breaking of chirality conservation

and restoration of WL can be caused by elastic scattering within the valley and between valleys [130]. This is the expected result of the presence of short range scattering.

For the analysis of our results an equation that was derived specifically for graphene [130] is used which expresses the conductance as a function of inelastic ($\tau_\varphi^{-1}$) and elastic ($\tau_i^{-1}$, $\tau_z^{-1}$, $\tau_w^{-1}$) scattering rates [128].

$$\frac{\pi h}{e^2}\,\Delta\sigma(B) = F\left(\frac{\tau_B^{-1}}{\tau_\varphi^{-1}}\right) - F\left(\frac{\tau_B^{-1}}{\tau_\varphi^{-1}+2\tau_i^{-1}}\right) \pm 2F\left(\frac{\tau_B^{-1}}{\tau_\varphi^{-1}+\tau_i^{-1}+\tau_*^{-1}}\right), \qquad (5\text{-}4)$$

where $F(z) = \ln z + \psi(0.5 + z^{-1})$, $\psi(z)$ is the digamma function, $\tau_B^{-1} = (4eDB)/\hbar$, $D$ is the diffusion constant, $\tau_\varphi^{-1}$ is the phase-breaking rate, $\tau_i^{-1}$ is the inter-valley scattering rate and $\tau_*^{-1}$ is the intra-valley scattering rate, where $\tau_*^{-1} = \tau_w^{-1} + \tau_z^{-1}$, and $\tau_w^{-1}$, $\tau_z^{-1}$ are the trigonal warping rate and the single valley chirality-breaking rate respectively. This equation was derived to describe data for ML and BL graphene, as represented by the negative or positive sign of the third term respectively.

The correction to the conductivity is defined as $\Delta\sigma(B) = \sigma(B) - \sigma(0)$. WL in equation 5-4 is described by the 1st positive term while WAL is described by the 2nd and 3rd terms. The data for sample (2-2) (3L graphene) were fitted well by the theory for ML flakes (- sign), with $\tau_\varphi^{-1}$, $\tau_i^{-1}$ and $\tau_*^{-1}$ as three free parameters. Using this formula is not technically correct for 3LG in practice; however it seems to describe our data rather precisely. Certainly, the BL form (+ sign) does not even come close to being a reasonable description of our data. Moreover, the correct expression for 3LG has not been calculated yet to the best of our knowledge.

Figure 5-16 shows representative examples of the fits to equation 5-4 for the 1st 250 nm junction of sample (2-2) at 2.16 K, 8 K and 15 K. The thin solid curves represent fits obtained from an automated routine. An excellent description is obtained for the entire MC behaviour at both low (WL) and high (WAL) fields. Similar results have been obtained at other temperatures in both 250 nm junctions.

The interplay between the scattering rates dominates the shape of the MC curves. According to equation 5-4 the two most obvious features in the MC curves, the width of the dip at low B and the bending of the curve at large B, are dominated by the scattering rates $\tau_\varphi^{-1}$ and both $\tau_i^{-1}, \tau_*^{-1}$ respectively [125]. At low fields the

rapid decrease in MC is more pronounced at 2.16 K than at higher temperatures. This effect is due to a reduction in $\tau_{\varphi}^{-1}$, while smaller values of $\tau_i^{-1}$ lead to a stronger downturn of the curves at high fields. However, no downturn is observed in MC data at 15 K, due to a much larger inter-valley scattering rate $\tau_i^{-1}$ [128].

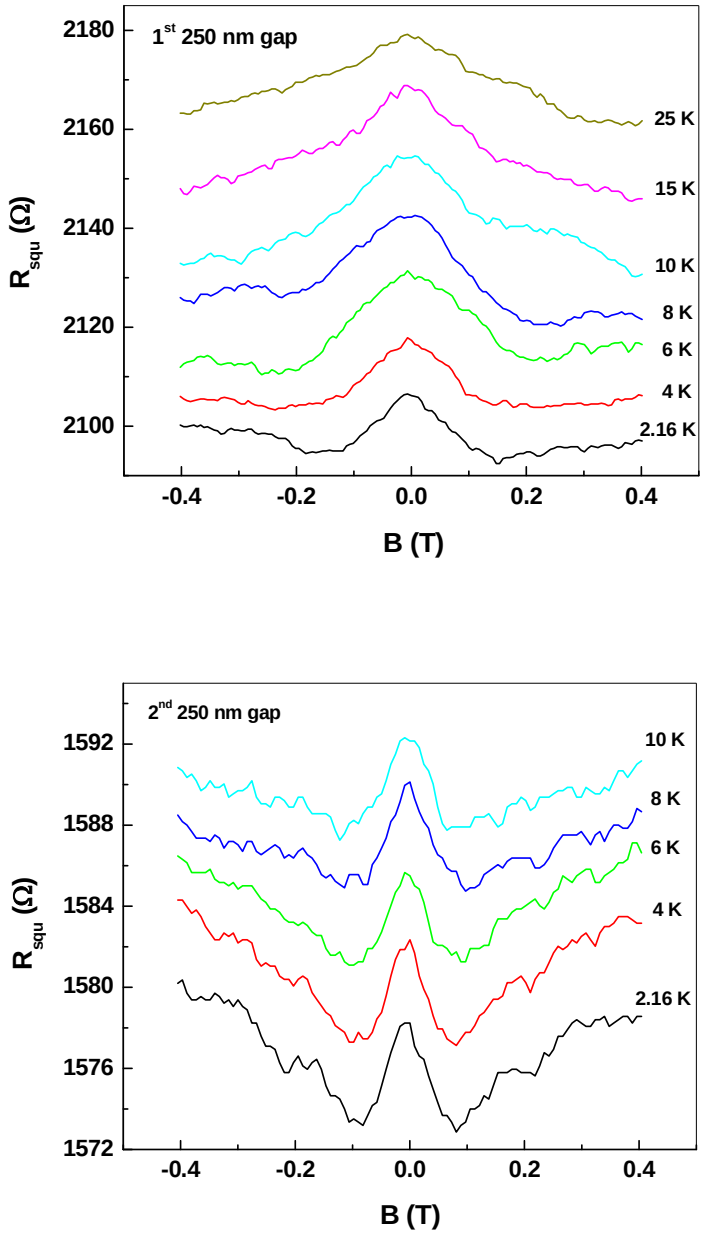


**Figure 5-15:** Magnetic field dependence of the sheet resistance of the two 250 nm junctions of sample (2-2) at different temperatures. Curves are shifted vertically for clarity.

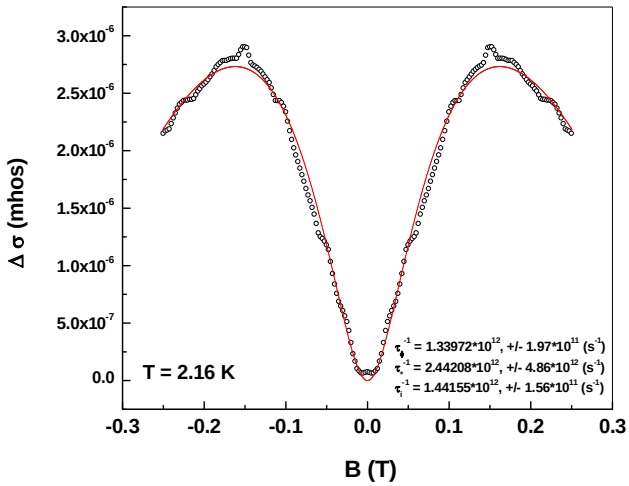


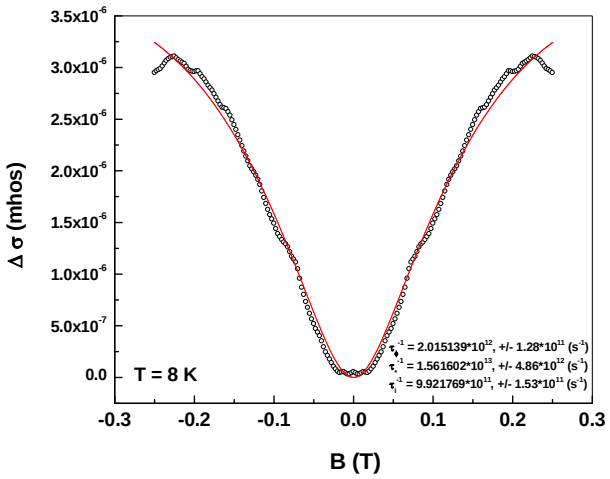


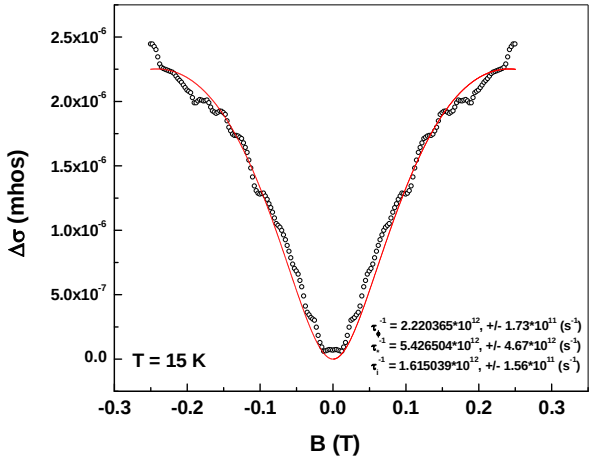


**Figure 5-16:** Evolution of the magnetoconductivity of the 1st 250 nm junction at T = 2.16 K, 8 K and 15 K.

The three scattering rates $\tau_{\varphi}^{-1}$, $\tau_{i}^{-1}$ and $\tau_{*}^{-1}$ are extracted from fits of equation 5-4 to the MC data for the two 250 nm junctions of sample (2-2) at different temperatures. Figures 5-17 and 5-18 show plots of these rates as a function of temperature. Both $\tau_{i}^{-1}$ and $\tau_{*}^{-1}$ are found to be weakly temperature dependent, while $\tau_{\varphi}^{-1}$ is strongly temperature dependent. The approximate linear dependence of $\tau_{\varphi}^{-1}$ on T is taken as an indication that electron-electron scattering is the dominant phase-breaking mechanism in this 2D system [129, 131]. A saturation of the coherence lifetime could be the cause behind the deviation from linearity at the lowest temperatures [131].

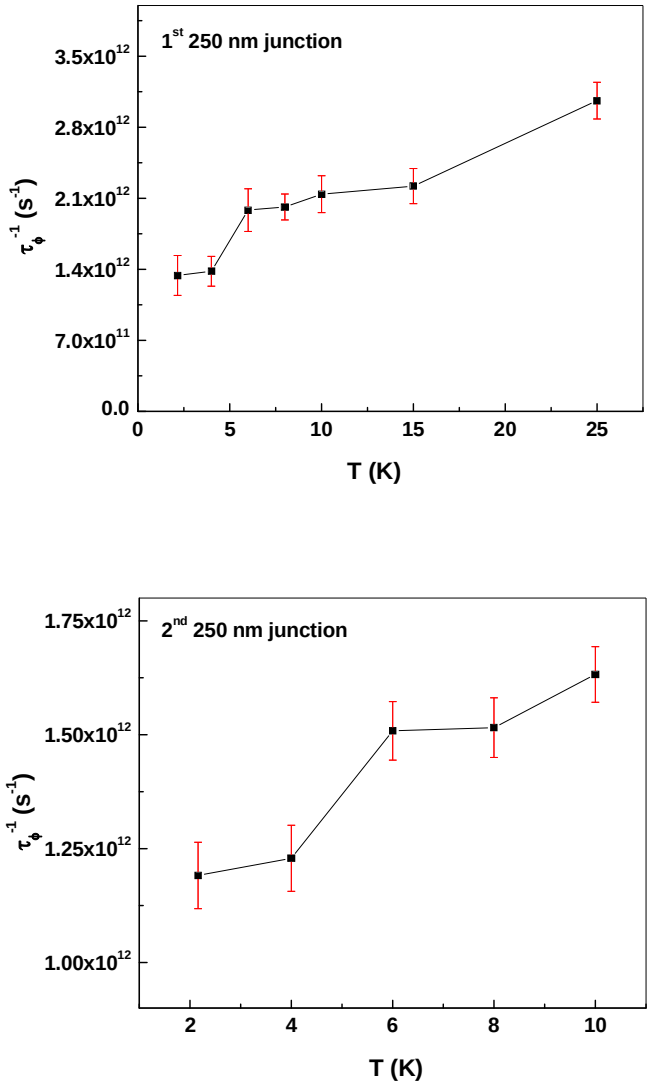


**Figure 5-17:** Phase coherence scattering rate, $\tau_{\varphi}^{-1}$, as a function of T for both 250 nm junctions.

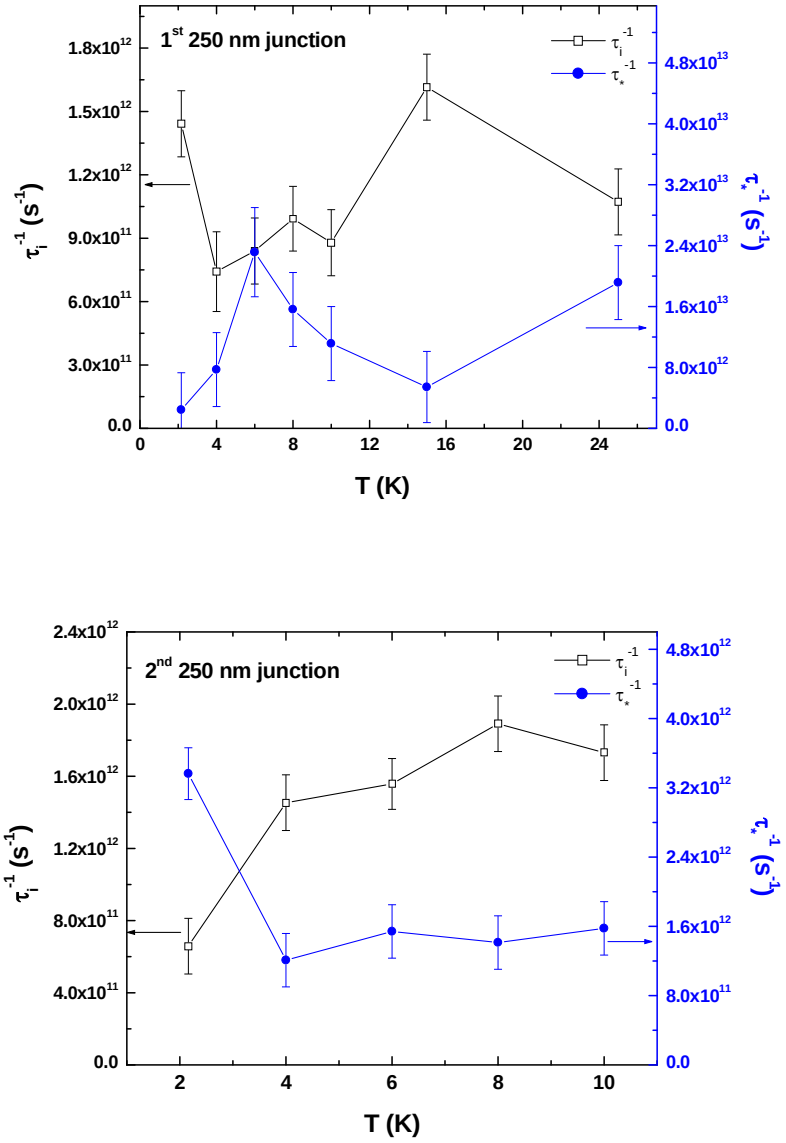


**Figure 5-18:** Scattering rates $\tau_i^{-1}$ and $\tau_*^{-1}$ as a function of T for both 250 nm junctions.

### 5.3.4 Universal Conductance Fluctuations

To obtain a complete picture of the magnetoresistance phenomena of sample (2-2) investigations of the WL magnetroresistance and Universal Conductance Fluctuations (UCF) are required. In addition to the fits to WL (WAL) theory that were presented in the previous section we have focussed on changes in the UCF with varying charge density (gate voltage). The mesoscopic magnetoresistance fluctuations in graphene can be explained by the standard theory of UCFs [132]. The complex interference of multiple electron (or hole) trajectories in phase-coherent

samples accumulates a random phase in an applied external magnetic field or gate voltage, and this is the origin of the UCF observed in our mesoscopic samples. Tuning either the magnetic field or the gate voltage in a disordered mesoscopic sample will lead to fluctuations in the conductance with the dimensionality of the sample playing a key role in the amplitude of the fluctuations [133].

As a result of the mesoscopic nature of device (2-2), UCFs are superimposed on top of WL corrections and observed in the magnetoconductance data as a function of both $V_g$ and B. Fluctuations of the conductance are generally aperiodic in gate voltage and have an amplitude of the order of $e^2/h$. A third order polynomial background subtraction has been made to the conductance, G, versus $V_g$ data in order to quantify UCFs as a function of $V_g$. Figure 5-19 shows the large and reproducible conductance fluctuations obtained after this subtraction for both 250 nm junctions in device (2-2) at 300 K, 77 K and 4.2 K. The 4.2 K data shows by far the strongest aperiodic CFs with a magnitude of the order of $e^2/h$ far from the Dirac point, while it decreases close to the charge neutrality point.

A sixth-order polynomial fit has been used to achieve the background subtraction of G (B). This can be clearly seen in Fig. 5-20, where the UCFs for device (2-2) are plotted as a function of B for different values of $V_g$ at 4.2 K. Magnetoconductance fluctuation graphs at different $V_g$ have been offset vertically for clarity. At more negative gate voltages a very complex evolution of the magnetoconductance, with very strong oscillations as a function of magnetic field, is observed. This can be taken as an indication that the device is entering the conductance fluctuation (CF) regime when the phase coherence length, $L_\varphi$, is comparable to the length of the device.

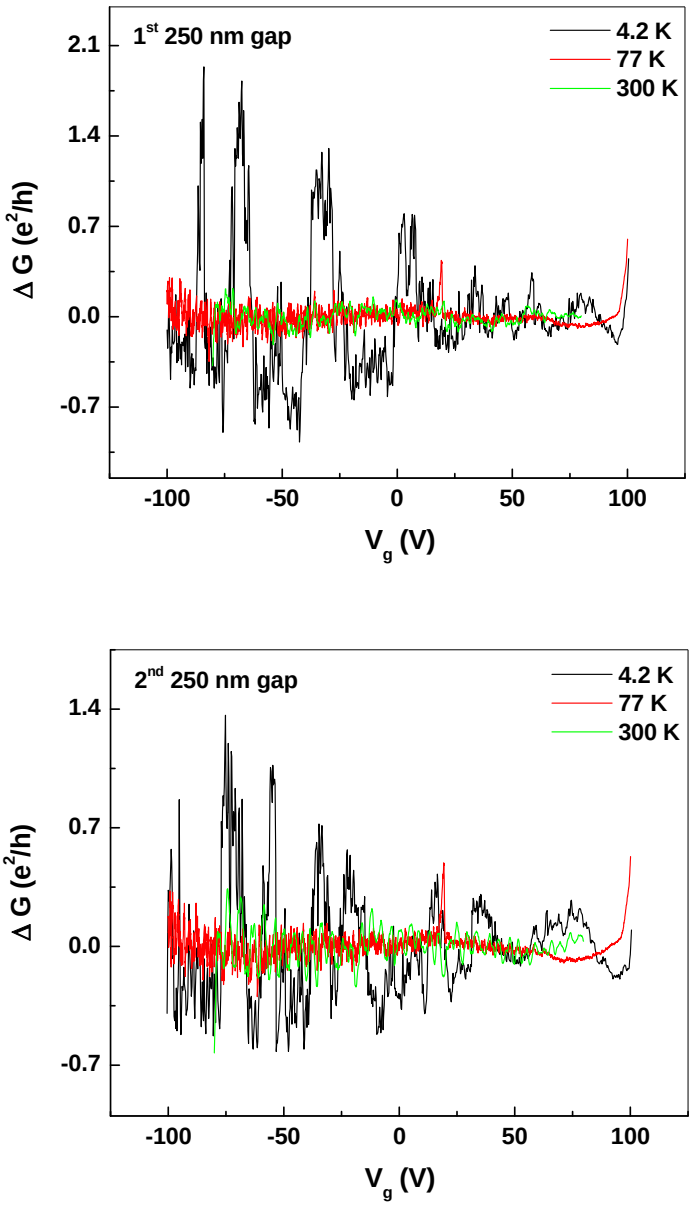


**Figure 5-19:** ΔG versus $V_g$ for both 250 nm junctions of device (2-2) at 4.2 K, 77 K and 300 K.

The amplitude of the UCFs is strongly dependent of the value of applied $V_g$. A suppression of fluctuation amplitude is observed as $V_g$ is increased towards the charge neutrality point. Staley *et al.* [134] have observed the same phenomenon in both 2LG and 3LG devices. A decrease of $L_\varphi$ near the CNP (cf., Fig. 5-21) could be the origin of this suppression. Decreasing carrier density is correlated with a loss of phase coherence giving rise to decreasing amplitude of the UCFs. This suppression could also be due to the formation of electron-hole puddles at low carrier densities (near the CNP) as a result of sample inhomogeneities. In this case an effective

decrease of the phase coherence length results from several scattering events experienced by the carriers at the boundaries of puddles.

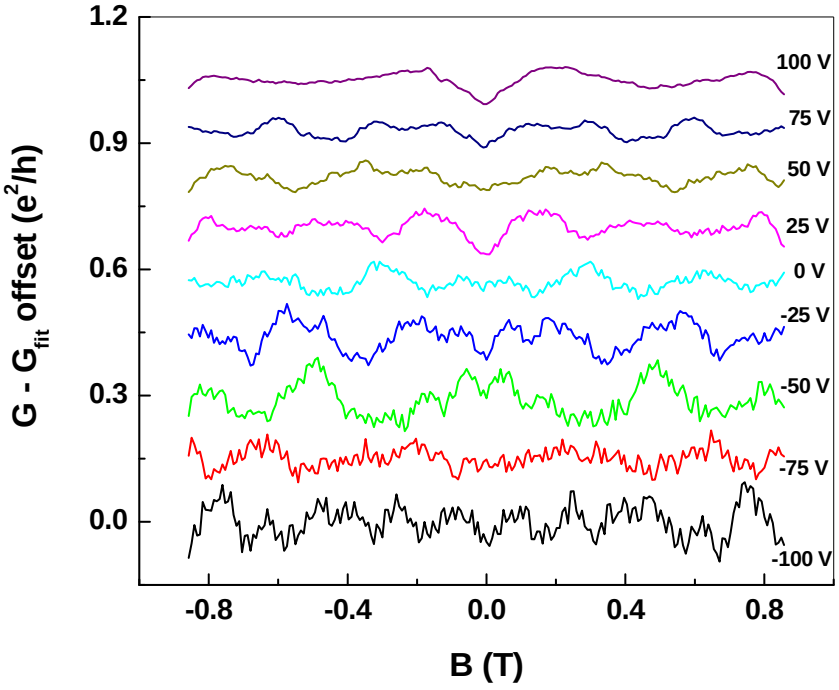


**Figure 5-20:** Magnetoconductance fluctuations after background subtraction at different values of $V_g$ for the 1st 250 nm junction in device (2-2).

Fits of WL using equation 5-4 were not possible in all sets of data due to the absence of a strong WL/WAL signature at low fields. Hence we were not able to determine $L_\varphi$ experimentally as a function of $V_g$. Thus a theoretical equation introduced by Gorbachev *et al*. [135] is used to extrapolate the coherence length, $L_\varphi$, from WL-based estimates at $V_g$ = +100 V. The experimental temperature dependence of the dephasing rate, $\tau_\varphi^{-1}$, has been approximated for T > 1K by [135]

$$\tau_\varphi^{-1} = \beta K_B T \, lng/\hbar g \ , \qquad (5\text{-}5)$$

where $\beta$ is an empirical coefficient that lies between 1 and 2 [128] and $g = \sigma h/e^2$, where $\sigma$ is the conductivity at B = 0. The magnetic field periodicity, $\Delta B$, of UCF depends on the phase coherence length, $L_\varphi$, through $\Delta B \sim \varphi_0/L_\varphi^2$, where $\varphi_0 = h/e$ is the electronic flux quantum [134]. This period is expected to increase with decreasing charge density due to reduction in the phase coherence length, $L_\varphi$ (cf., Fig. 5-21).

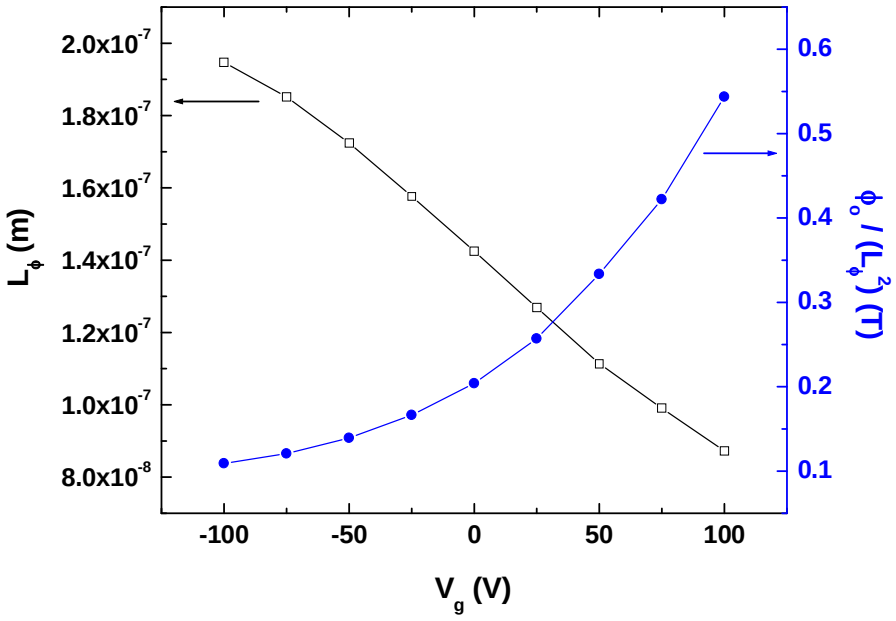


**Figure 5-21:** Estimations of the phase coherence length and ΔB as a function of $V_g$ for the 1st 250 nm junction of device (2-2).

The UCF data have been analysed using Fast Fourier Transforms (FFTs). This identified more than one period in the UCF signals giving important clues about their origin. Two periods can be clearly seen in Fig. 5-22 (a) for fits of data taken at $V_g$ = -50 V for the 1st 250 nm junction of device (2-2). Figure 5-22 (a) plots $F_n$, the Fourier component, as a function of an integer, $n$, which is related to the spatial frequency of the signal by $f_n = 2\pi n/(B_{max} - B_{min})$. Figure 5-22 (b) shows a fit to the raw CF data using the two identified periods, and makes a compelling case that there is a short and a long period in the data with a ratio of roughly 3 between them. An excellent comparison to the data is obtained by adding the two periods together with optimised phases and amplitudes as shown in Fig. 5-22 (c).

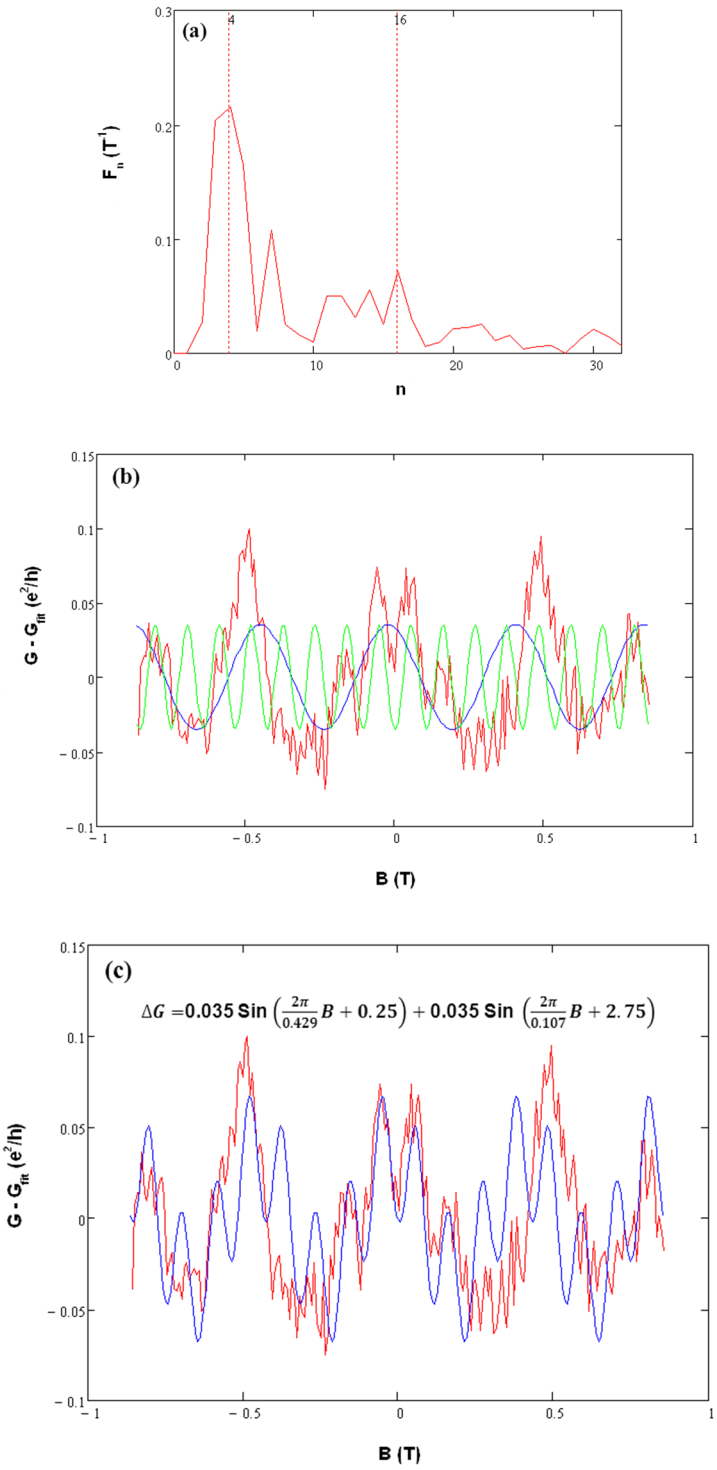


**Figure 5-22:** FFT analysis for the UCF observed in the conductance of the 1st 250 nm junction at $V_g$ = - 50 V. a) $F_n$ as a function of $n$ allows identification of two intrinsic periods in the signal. b) The two intrinsic periods in the raw data at this value of gate voltage. c) Fits of the raw data to two sinusoidal signals with optimised amplitude and phase.

Similar results have been obtained at other values of $V_g$ and a clear dependence of both the frequency and amplitude of the two periods on the gate voltage $V_g$ (hole density) established. This can be seen in Fig. 5-23, which plots the extracted fit values for the period and amplitude of the two sinusoidal signals obtained at each value of $V_g$. A decrease in UCF amplitude, $A_n$, and a weak increase in the UCF periodicity, $\tau_n$, are observed as $V_g$ is increased. These results are consistent with the results of equation 5-5 (cf., Fig. 5-21). While some of the two-frequency fits look very convincing, e.g., $V_g$ = -25 V and 25 V (cf., Fig. 5-24), at other gate voltages this is not really the case (cf., Fig. 5-25). These observations highlight the role of the gate voltage in determining whether the dominant effect is either the superposition of the two intrinsic periods or a UCF signal with only one of the two periods.

The electronic dispersion of ABA trilayer graphene near the Fermi energy consists of the overlap of a linear MLG-like dispersion and a quadratic BLG-like dispersion (cf., Fig. 2-7 (g)). This could be the reason for the presence of two intrinsic periods in the UCF signal, whereby each period reflects fluctuations in one of these sub-systems. Hence we would argue that the following scenario applies to this device. The ML WL equation describes our weak localisation data at $V_g$ = +100 V rather precisely. This suggests that this WL signature near the CNP is dominated by the ML-like dispersion, while the UCF signature at lower value of $V_g$ arises from a complex combination of signals from both ML-like and BLG-like dispersions in our trilayer device.

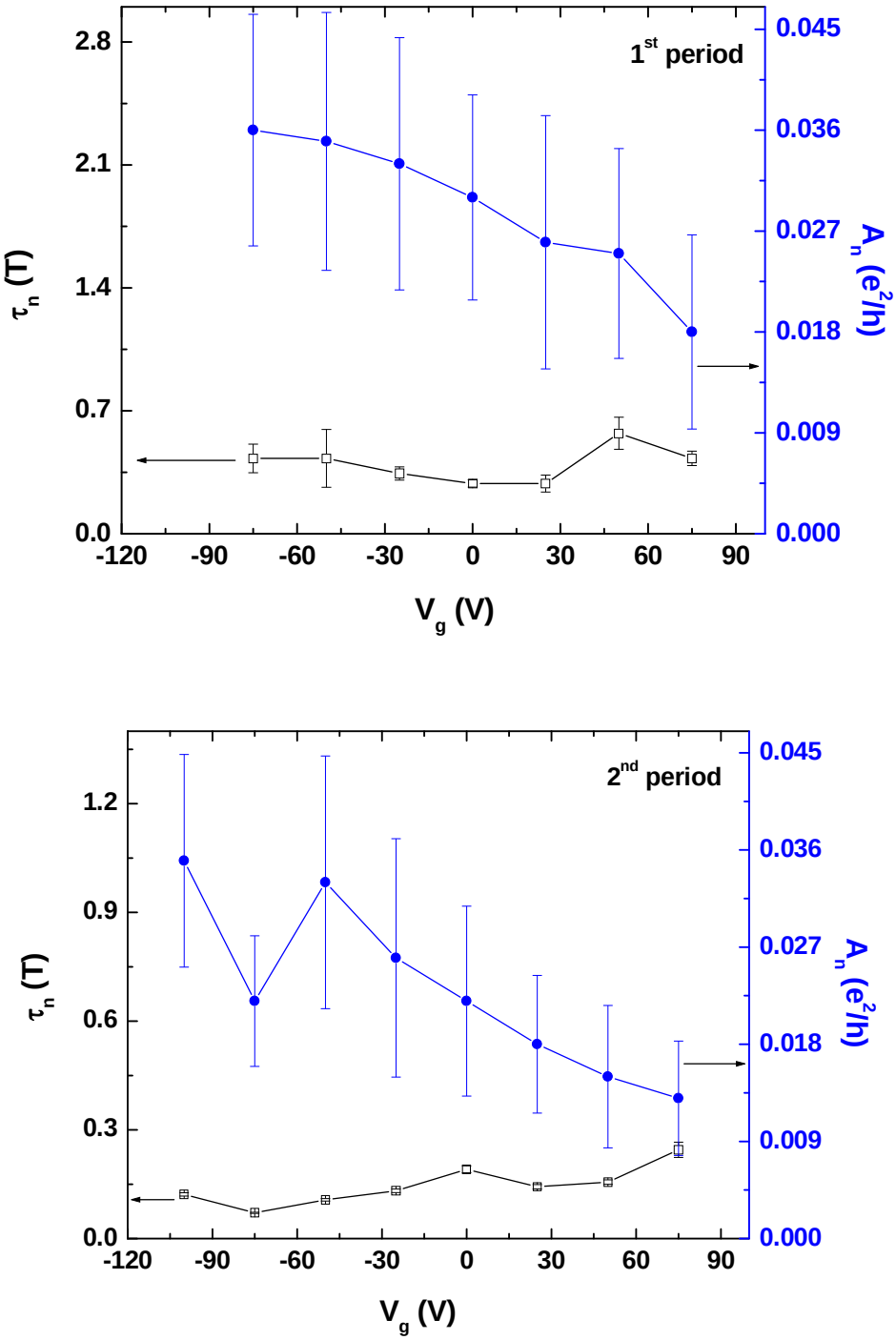


**Figure 5-23:** UCF period, $\tau_n$, and amplitude, $A_n$, as a function of $V_g$ for both fluctuation periods.

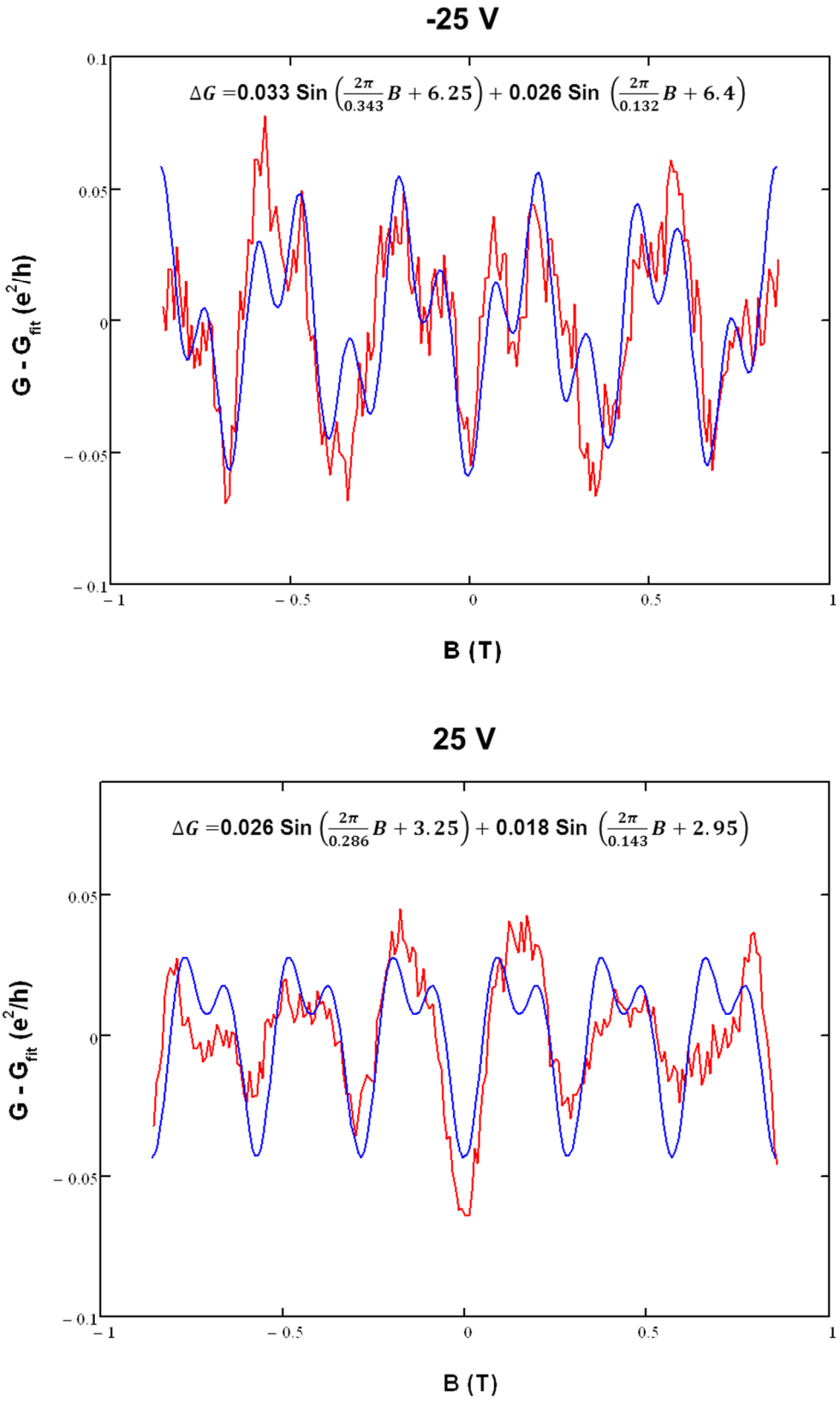


**Figure 5-24:** Fits to UCF data as a function of B at 4.2 K at $V_g$ = -25 V and 25 V.

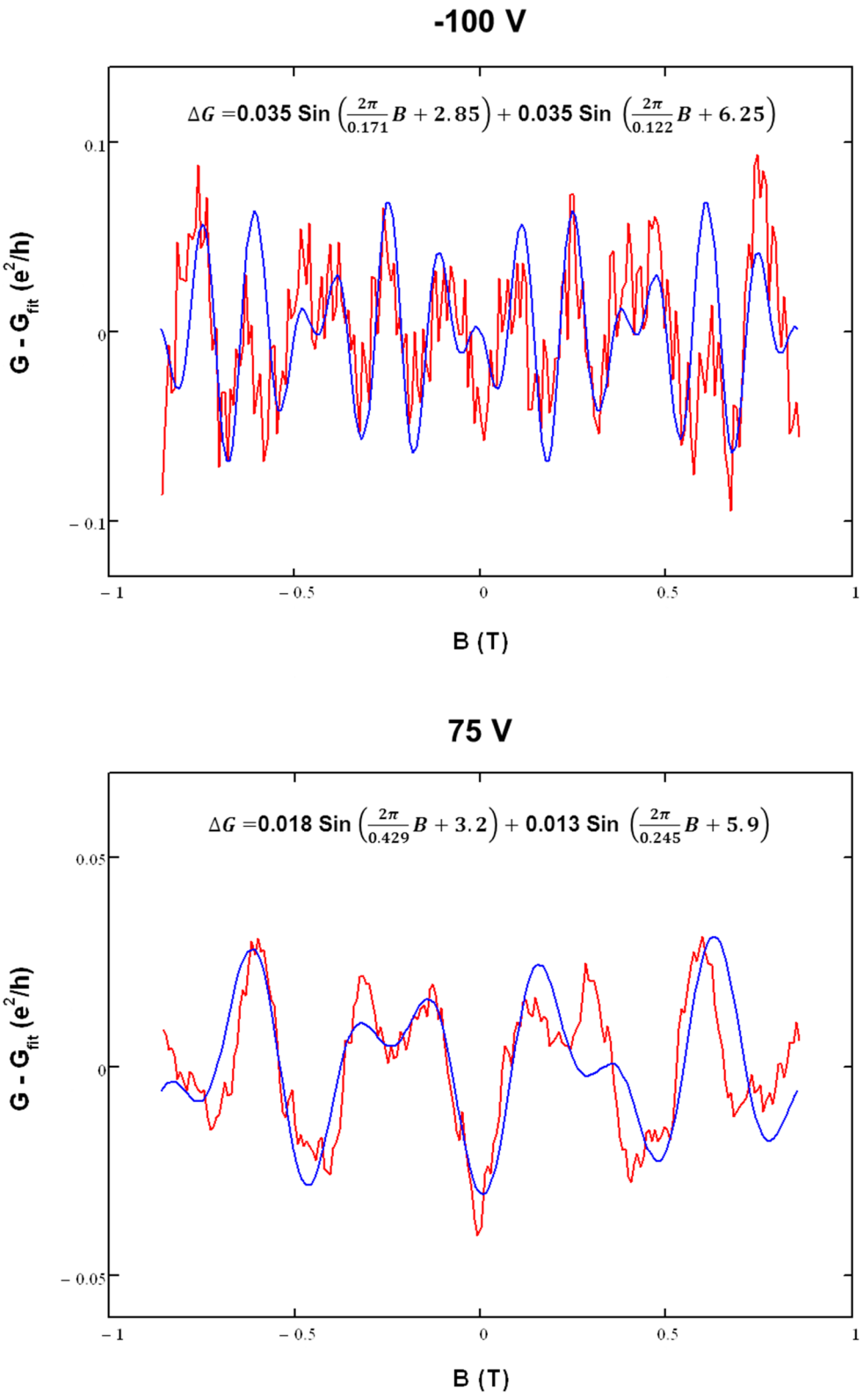


**Figure 5-25:** Fits to UCF data at $V_g$ = -100 V and 75 V as a function of B at 4.2 K illustrating the relatively poor agreement at these densities.

## 5.4 Further Trials

Further attempts have been made to observe the superconducting proximity effect in monolayer and few-layer graphene using both higher $T_c$ PbBi alloy electrodes and by the decoration of flakes with discontinuous nanoscale Sn films.

The use of a higher energy gap (higher $T_c$) material helps to overcome problems associated with the external noise and low operation temperature of Al-based SGS junction devices. This was overcome by Jeong *et al*. [87] who developed a new type of SGS junction with PbIn alloy superconducting electrodes. This new approach motivated our use of $Pb_{82}Bi_{12}$ alloy superconducting electrodes in place of the earlier Pd/Al electrodes. These PbBi alloy contacts with higher critical temperatures allowed measurements to be made using the existing $He^4$ cryostat that was described earlier in section 4.9.3.

Figure 5-26 (a) presents some optical images of a typical device fabricated using this approach. Some devices had junctions with contact spacings of 250 nm (x3) and 500 nm, while others had junctions with spacings of 250 nm (x2), 500 nm and 750 nm. During the fabrication process several difficulties were experienced such as problems during lift-off and the existence of large PbBi grains in the evaporated films as is evident in the granular morphology revealed by AFM images (cf., Fig. 5-26 (b)). Indeed, the lift-off process only worked successfully for junctions with electrode spacings of 500 nm and above.

Several measurements have been performed on PbBi devices at both room temperature and 4.2 K. Two-point resistances confirmed the discontinuous nature of PbBi electrodes resulting in the failure of these devices. In addition, the PbBi electrodes did not show any of the usual signatures of superconductivity.

Another trial has been made using an alternative approach pioneered by Kessler *et. al.* [88] whereby a very thin layer of Sn is evaporated onto the surface of a large graphene transistor. The deposited Sn self-organises into arrays of unconnected nanoscale islands, and proximity supercurrents between these islands have been observed and characterized [88]. Figure 5-27 (a) shows a scanning electron micrograph of a graphene sheet decorated with Sn islands, as well as optical images of the entire device that contains it (cf., Fig. 5-27 (b)). It was found that a 10 nm

deposited Sn film formed islands with ~ 79 nm diameter and ~ 26 nm spacings between them.

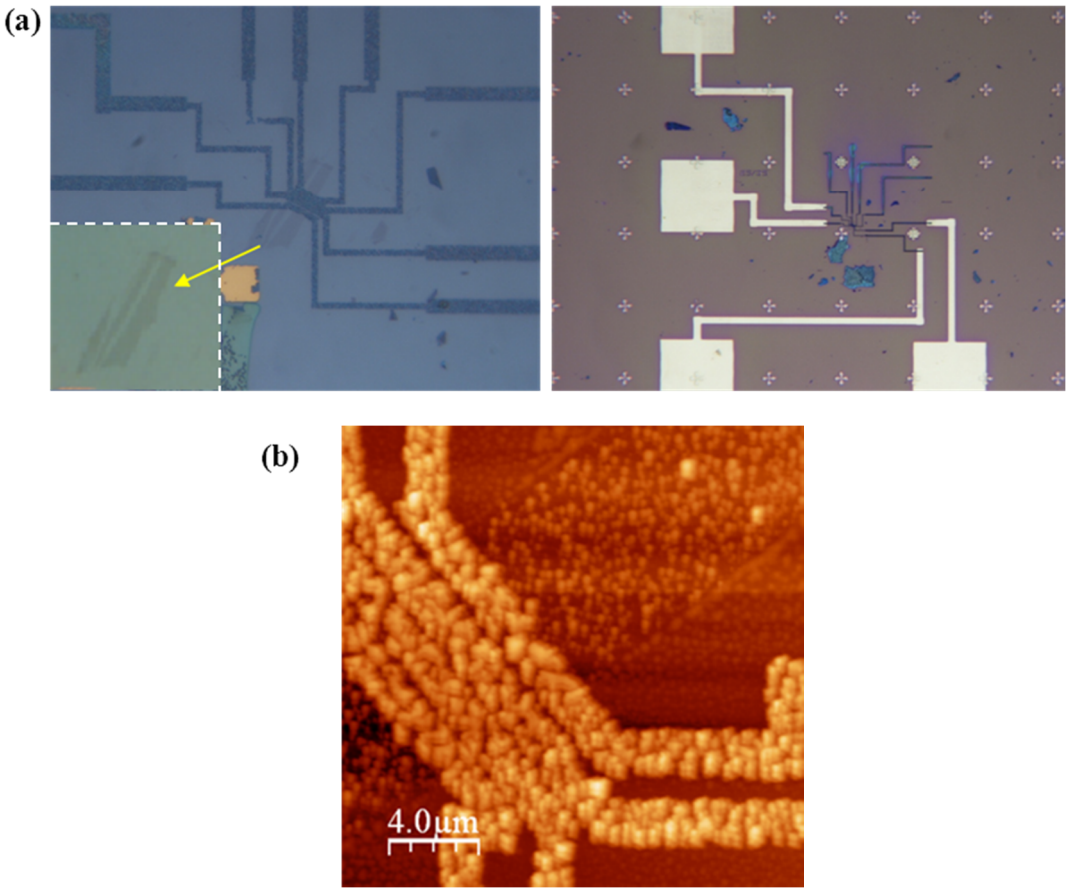


**Figure 5-26:** a) Optical micrographs of a graphene device with PbBi alloy electrodes. b) AFM image of the electrodes of this device.

Again, we were unable to observe any sign of superconductivity in samples of this type at temperatures down to 2K, as can be seen in the R versus T plot shown in Fig. 5-28. We speculate that this is either due to the low transparency of the Sn/graphene interface or inadvertent oxidation of the Sn nanostructures during transfer into cryostat. Unfortunately, the back gate for this device became leaky at ± 2 V at 4.2 K, which did not allow full characterisation of the back gate dependency of resistance to be performed. Since there was no obvious damage in the contact regions, the high gate leakage is presumed to be due to tunnelling between Sn particles coating the entire chip leading to a very large effective device area. The back gate worked slightly better at 2 K when it became leaky at ± 10 V allowing measurements of the graphene resistance as a function of transverse magnetic field at constant values of gate voltage in the range ± 10 V.

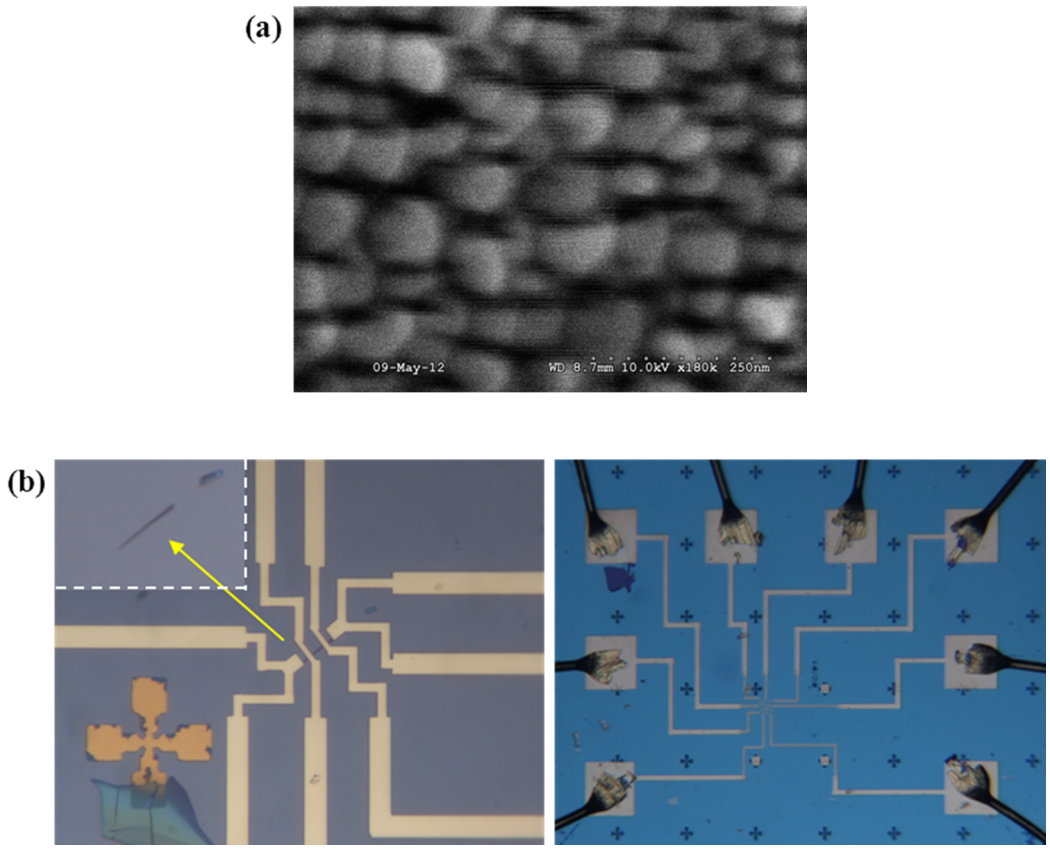


**Figure 5-27:** a) SEM image of Sn islands on a graphene flake formed after deposition of a 10 nm Sn film. b) Optical images of the measured device after coating with an 8 nm Sn film.

Figure 5-29 (a) shows the positive magnetoresistance observed in this device over a range of temperatures from 2.2 K to 10 K. Both the WAL (at lower temperature) [129] and the classical "Lorentz force" magneto-conductance (which persists to higher temperature) could be responsible for the observed behaviour. Another test of the integrity of the back gate was performed at the end of the measurement sequence, and surprisingly the earlier gate leakage had disappeared. The gate voltage could then be swept to ± 100 V without any sign of a leakage current (cf., Fig. 5-29 (b)). This device showed similar behaviour to device (2-2), where a strong proximity hole doping by the Pd contacts was observed causing a shift of the Dirac point to large positive gate voltages.

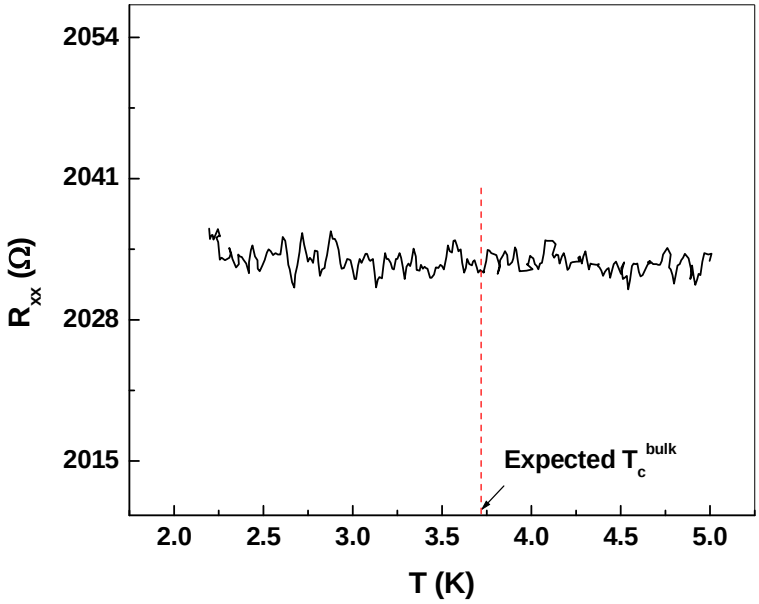


**Figure 5-28:** R versus T for the device shown in Fig. 5-27.

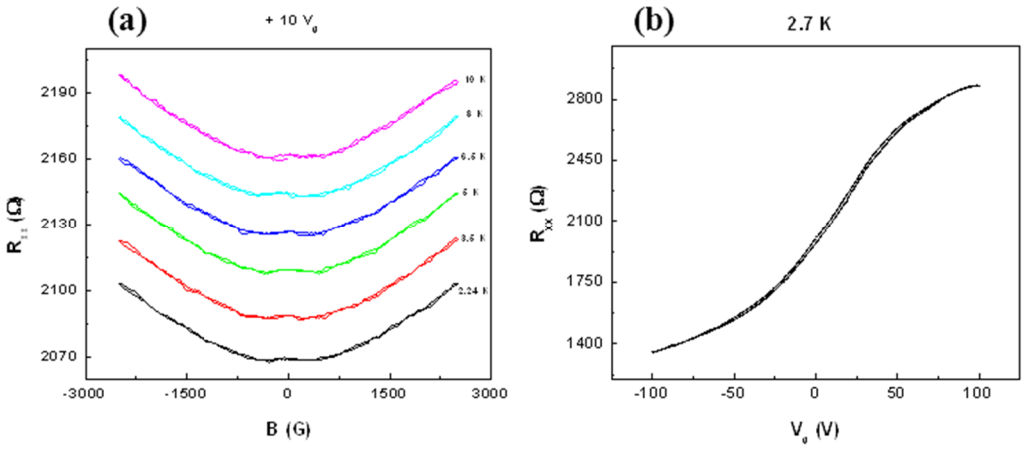


**Figure 5-29:** a) Magnetoresistance of a graphene flake coated with an 8 nm Sn film at $V_g$ = + 10 V. b) The effect of a back gate voltage on the flake resistance at 2.7 K.

## 5.5 Discussion of Graphene results

The present study was targeted at investigations of the superconducting proximity effect in superconductor/graphene structures (Graphene Josephson Junctions GJJ). Graphene structures with superconducting Al electrodes have been realised by micromechanical cleavage techniques on $Si/SiO_2$ substrates. A range of surface science techniques has been used to characterise the studied flakes. Devices show good normal state transport characteristics, efficient back-gating of the longitudinal resistivity, and low contact resistances. Several trials have been made to investigate proximity-induced critical currents in devices with junction lengths in the range 250-750 nm. In addition, further attempts have been made to observe the superconducting proximity effect in monolayer and few-layer graphene using both higher $T_c$ PbBi alloy electrodes and the decoration of flakes with discontinues nanoscale Sn films. For reasons we do not understand, supercurrents were not observed either at temperatures down to 300 mK in high quality GJJ devices with low resistance Pd/Al contacts, or at temperatures down to 2 K in devices decorated with discontinues nanoscale Sn films.

Having failed to observe proximity-induced superconductivity in graphene devices, the attention of the research project was refocused onto the analysis of low field magnetoresistance data on graphene devices. The most interesting findings to emerge from this study are summarised in the following points. A shift of the Dirac point to very large positive gate voltages has been observed and primarily attributed to strong proximity hole doping by the Pd contacts. Molecular adsorption on the graphene surface and ionized charge traps in the $Si/SiO_2$ substrate [122] could be the reasons why such relatively low mobilities are observed in the devices studied.

The analysis of low field data on trilayer graphene devices, e.g., (device 2-2) yields key information about the source of weak localisation or anti-localisation corrections to the conductivity, as well as universal conductance fluctuations. These investigations have given us a much deeper understanding of the underlying physics in our mesoscopic samples. Both WL and UCF in the 3LG device have been investigated as a function of temperature and gate voltage and several theories have been used to analyse the data. The theory of WL/WAL in monolayer graphene has been used to fit the magnetoconductance data near the CNP. The nature of defects

responsible for inter-valley scattering and chirality breaking can be inferred from the interplay of inelastic and elastic scattering mechanisms. A decrease in UCF amplitude is obtained with increasing temperature and/or decreasing carrier density when $V_g$ approaches the charge neutral point due to a reduction of the phase coherence length.

Finally, Fast Fourier Transforms (FFTs) have been used to analyse the field-dependence of the UCF data obtained from the 3LG device. This has identified more than one period in the UCF signals, making a compelling case that a short and a long period is present in the data. The situation is not precisely the same at all gate voltages and our observations have highlighted the role of the gate voltage in determining whether the dominant effect is the superposition of two intrinsic periods or a UCF signal with only one period. We speculate that the WL signature is dominated by the ML-like dispersion near the CNP, while the UCF signature arises from a complex combination of signals from both ML-like and BLG-like dispersions at lower gate voltages in our trilayer device.

# Chapter 6

# $NbSe_2$ Results and Discussion

## 6.1 Micromagnetic Measurements of $NbSe_2$ Flakes

The micromagnetic measurements of $NbSe_2$ were based on the Hall effect. The method used to cleave several thick flakes and mount them on the top of Hall effect sensors was described in section 4.10.4. One of the ways to investigate the behaviour of a thin flake in a magnetic field is to study its magnetisation as a function of the applied field. A perpendicular dc magnetic field (parallel to the crystalline c-axis) was applied to $NbSe_2$ flakes and the plane of the sensor. The magnetic field was produced using a superconducting solenoid with calibration, $= 0.0112\ T/A$ .

The solenoid current and Hall voltage were recorded using a Keithley ammeter and a lock-in amplifier and were converted to magnetisation in the following steps. Since no two Hall probes are exactly identical, a small difference in the Hall coefficient, $R_H$, of the loaded and reference (empty) probes is expected. Hence, after subtraction of the empty reference Hall probe data from the loaded Hall probe a correction was applied. A linear fit $(f(x) = ax + b)$ was made to the difference signal. The magnetisation, M, was then calculated using the following expression, $M = \frac{\left[\left(U_H^{loaded\ HP} - U_H^{empty\ HP}\right) - f(x)\right]}{I \times R_H}$, where $R_H$ is the Hall coefficient of the loaded probe. Figure 6-1, illustrates the magnetisation data analysed in this way for one of the $NbSe_2$ flakes [70].

In a type II superconductor the lower critical field, $H_{c1}$, separates the Meissner phase and the mixed state. A gradual reduction of the magnetisation occurs above $H_{c1}$ due to the penetration of flux in the form of quantized vortices, which is energetically favourable for type II superconductors. However, penetration of the first vortex into the bulk of the superconductor usually occurs at a higher field than the lower critical field, due to the presence of surface and geometric barriers. This is

known as the penetration field, $H_p$, which can be defined as the field at which the first Abrikosov vortex enters the sample [136].

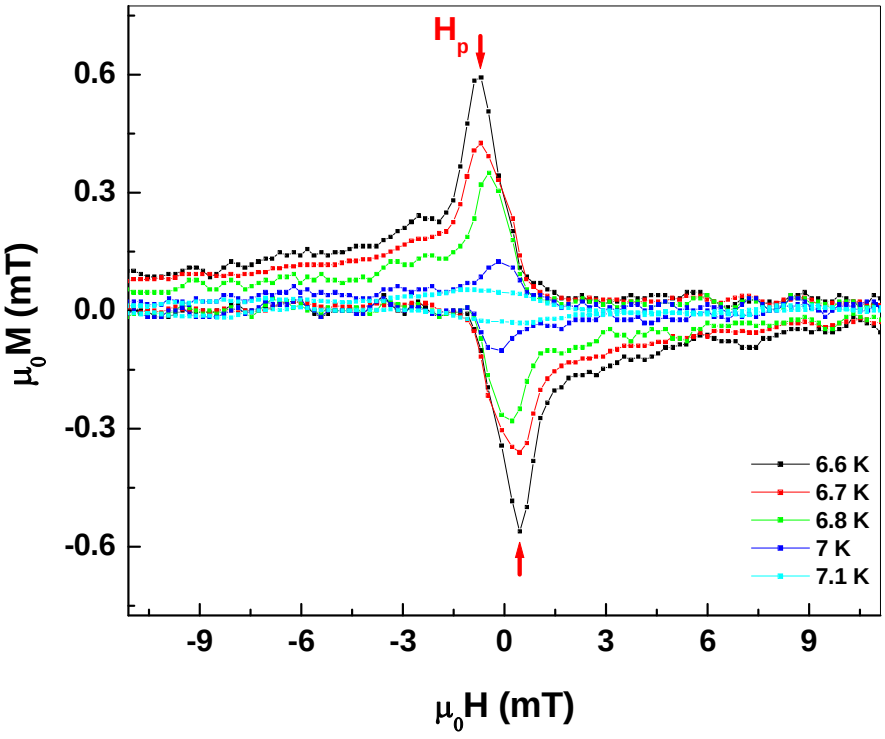


**Figure 6-1:** Magnetisation loops for one of the $NbSe_2$ flakes studied at several different temperatures.

$H_p$ lies between the lower critical field and the thermodynamic critical field, $H_c$, and its value depends on several factors such as the surface quality, sample shape, pairing symmetry and material anisotropy [136]. The value of the penetration field depends on various energy barriers that delay vortex penetration due to the presence of abrupt "edge" boundaries [137, 138].

Several types of energy barrier, such as a surface and geometrical barrier (SB), Bean-Livingston barrier (BLB), and Bean bulk pinning barrier, can control the penetration of flux into a sample [139-142]. In general, in strong pinning superconductors the main source of hysteresis in the magnetisation curves is expected to be the bulk pinning barrier [143], whereas other theoretical [144] and experimental [143] studies have shown that surface barriers are the dominant mechanism in materials with lower bulk pinning. In addition, the local field at the sample edge can be enhanced by the presence of large demagnetisation factors that

depend on the size and shape of the flake and lead to a reduction of the first penetration field. Further investigations using flakes of different shapes and sizes would be required to develop a complete understanding of the importance of these enhancement factors, and this is outside the scope of this thesis.

Asymmetry with respect to vortex entry and exit is observed in that there appear to be no barriers for flux exit. This behaviour can be understood in terms of the details of barrier formation, e.g., the attraction to image vortices in the BLB barrier which break the symmetry [143]. Magnetisation curves have been recorded at different temperatures in the range 6.6-7.2 K.

Plotting the $H_p$ values obtained as a function of temperature allows one to estimate the onset transition temperature for each of the studied flakes (cf., Fig. 6-2). As expected $H_p$ has approximately the same functional parabolic form as $H_{c1}$, being systematically scaled by demagnetisation effects related to the shape and size of the flake.

The key problem encountered with making such measurements systematically as a function of thicknesses was that only relatively thick $NbSe_2$ flakes could be mounted and characterised. It also tended to be difficult to estimate the thickness of the flakes. Therefore, this approach is not very useful for characterising very thin, few-layer flakes, which is one of the main goals of this project.

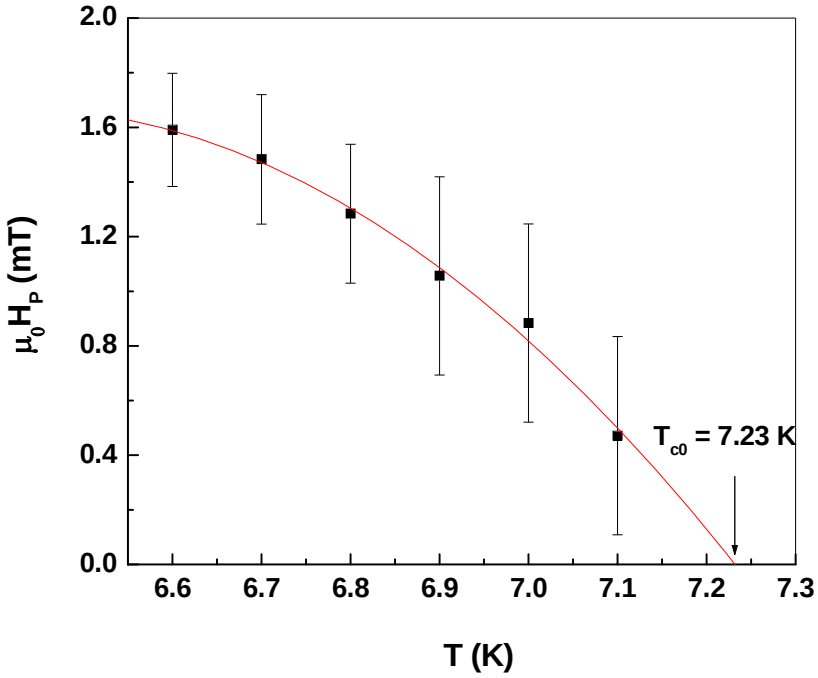


**Figure 6-2:** Dependence of penetration field on temperature for a thick $NbSe_2$ flake.

## 6.2 Results for $NbSe_2$-FETs

Four-terminal field-effect devices were realised by micromechanical cleavage from a high quality 2H-$NbSe_2$ single crystal onto $Si/SiO_2$ substrates. Optimisation of this process using pairs of permanent magnets to apply a controlled pressure allowed flakes up to ~70 μm in size to be exfoliated. A selection of the $NbSe_2$ flakes studied in this thesis is presented in Fig. 6-3. The lateral width of the electrodes varied from 1-1.5 μm, and various electrode spacings were used (typically 1-3 μm). A schematic diagram of a completed $NbSe_2$ field effect transistor has been presented earlier in Fig. 2-18.

The completed devices were wire-bonded in a DIL ceramic package and mounted on a temperature-controlled sample holder which was coupled to a liquid Helium bath via exchange gas. Small signal magnetotransport measurements were performed in a variable temperature Helium cryostat with a base temperature of 2 K. Great care was taken to avoid damage to the devices arising from electrostatic shock, and all leads down to the sample were protected with custom-designed pi filters (see section 4.9.4). Four-point measurements were performed with a constant

0.1-10 μA 32Hz ac current, and voltages were detected using a digital lock-in amplifier. Magnetic fields up to 1T could be applied perpendicular to the $NbSe_2$ flakes with a small superconducting solenoid in the liquid Helium Bath.

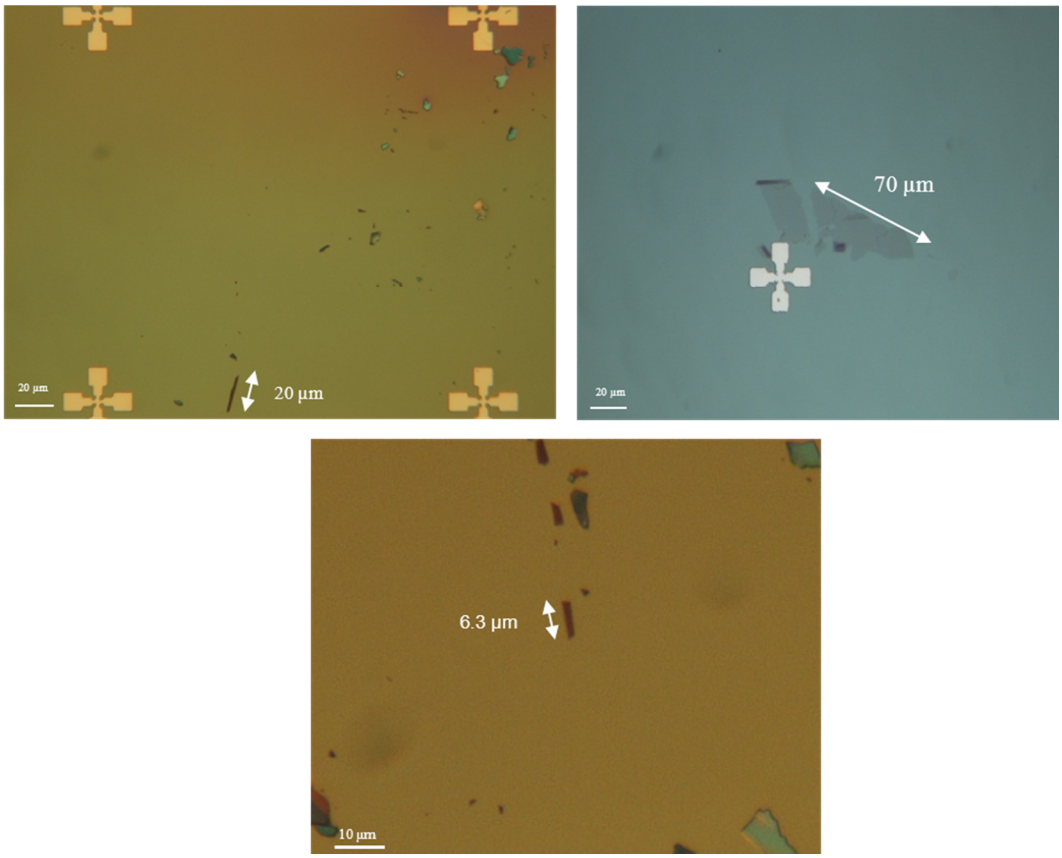


**Figure 6-3:** Optical micrographs of a selection of three of the $NbSe_2$ flakes studied.

## 6.2.1 Flake Characterisation

This subsection describes the methods that have been used to characterise $NbSe_2$-FETs. Single and few-layer flakes were readily characterised using an optical microscope, with some thin flakes frequently found attached to thicker ones. Appropriate flakes (homogeneous ones) were chosen for device fabrication to avoid issues with thickness inhomogeneity.

Atomic Force Microscopy (AFM) was used in tapping mode to quantitively measure the thickness of the $NbSe_2$ flakes on $Si/SiO_2$ substrates. Samples will henceforth be referred to by their nominal AFM thicknesses. Different flakes have distinct interference colors when viewed under an optical microscope corresponding to the number of layers present. The AFM images for these flakes were obtained by

scanning the devices after measuring them electrically. AFM images of two typical devices are reproduced in Fig. 6-4. The measured thicknesses obtained using AFM are listed in Table 6-1.

Raman spectroscopy was used to further characterize all of the $NbSe_2$ flakes studied. A Renishaw inVia Raman Microscope was used to scan the $NbSe_2$ flakes at room temperature at an illumination wavelength of 514 nm. A piezoelectric stage and a short working distance 50x objective lens were used to capture Raman spectra from the $NbSe_2$ flakes with integration times varied between 100-400 seconds. Figure 6-5 shows Raman spectra for selected flakes of different thickness captured under the same conditions.

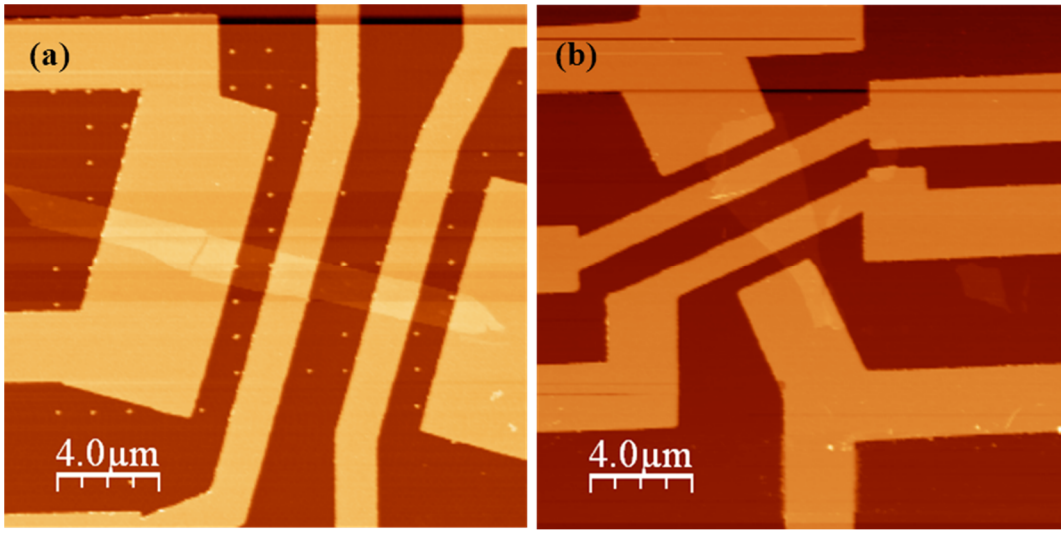


**Figure 6-4:** Topographic AFM images of a) the 7.92 nm flake device and b) the 9.21 nm flake device.

Spectra obtained with high laser intensity or long laser exposures were found to evolve with time. We found that the flakes actually became thicker after laser exposure suggesting that structural changes have occurred and probably also Oxygen incorporation (possibly the formation of Selenates). This could also be happening naturally in the very thin flakes which did not conduct which had possibly reacted with Oxygen during device processing. The series of Raman spectra illustrated in Fig. 6-6 shows the appearance of a new peak near 300 $cm^{-1}$ at high powers/times in the 6.56 nm flake. The origin of this peak is not yet established, however we speculate that it could possibly be due to selenate formation. The new peak is not observed in thicker flakes suggesting the reaction may be with the $SiO_2$ substrate. These observations seem to imply that the physical damage to an $NbSe_2$ flake due to

laser exposure is more pronounced in the case of ultrathin flakes as compared to thicker ones.

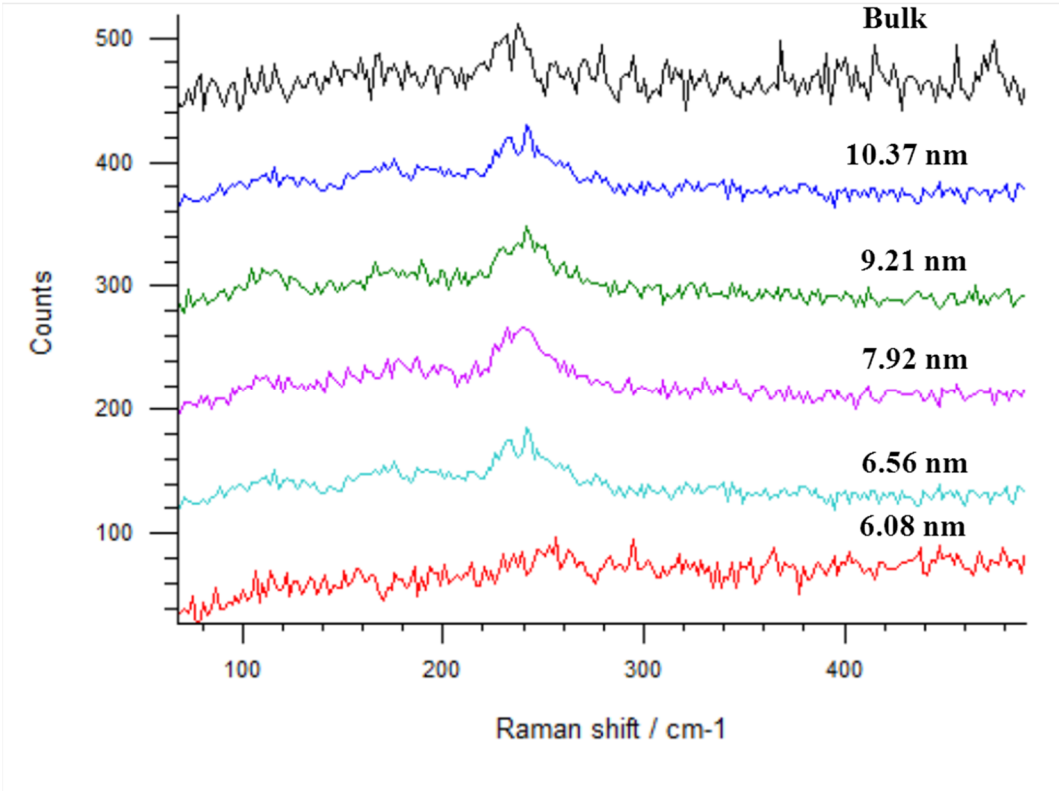


**Figure 6-5:** Raman spectra as a function of flake thickness captured with an integration time of 100 s and employing a laser power of 0.05 mW.

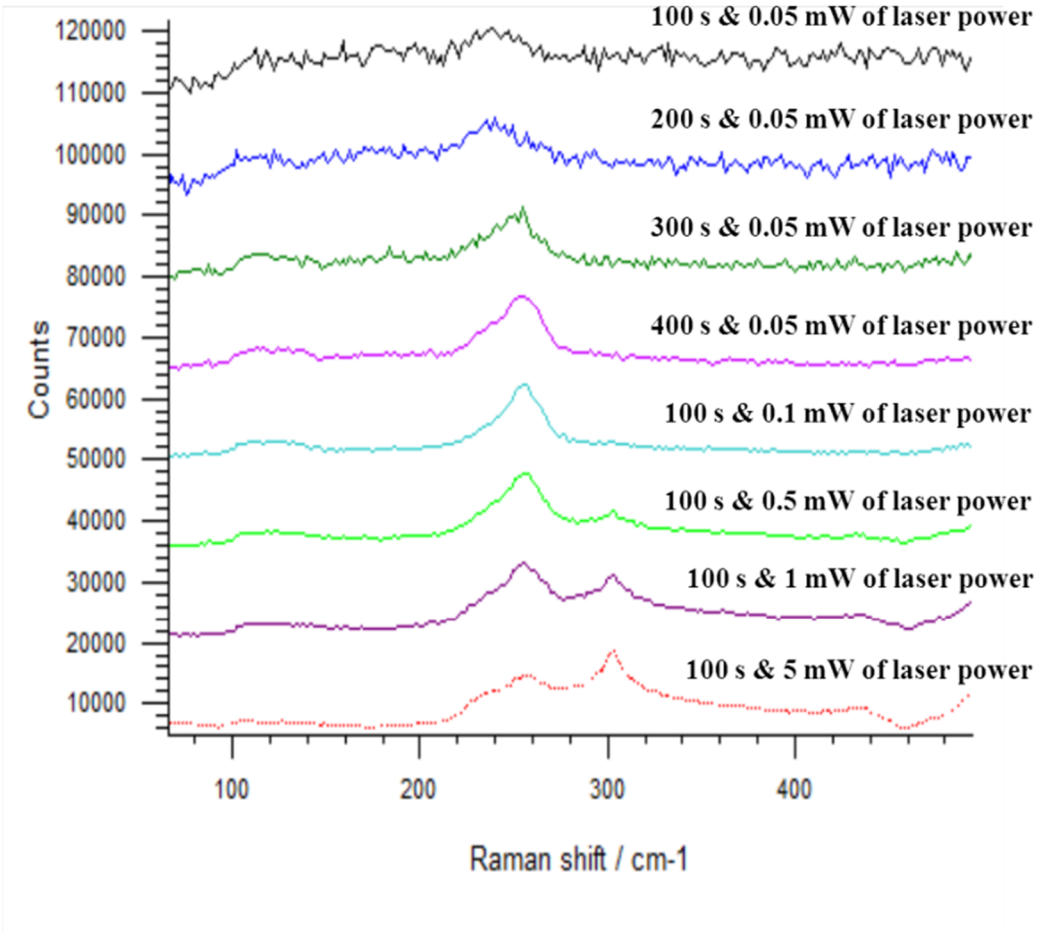


**Figure 6-6:** Series of Raman spectra for the 6.56 nm flake as a function of integration time and laser power.

## 6.3 Electrical and magnetotransport measurements

Systematic electrical and magnetotransport measurements were made on four of the $NbSe_2$-FETs. A detailed investigation of these flakes has been made as a function of temperature, applied field, and back-gate voltage. Figure 6-7 shows one of the four $NbSe_2$-FETs studied. The room temperature sheet resistance, $R_{squ}$, has been estimated using equation 2-8. Multiplication of the flake thickness by the sheet resistance has allowed an estimation of the bulk resistivity, $\rho_{Bulk}$, for the studied flakes, where $\rho_{Bulk} = R_{squ} \times d$. In addition, the residual resistance ratio, *RRR*, has been determined using the expression $R(300\ K)/R(T > T_c)$. These $R_{squ}$, $\rho_{Bulk}$, and $RRR$ values are summarized in Table 6-1 for the four samples of interest. The 300 K sheet resistances for three devices are quite consistent, but the fourth falls well out of line with the rest (cf., Fig. 6-8). It is noteworthy the trend line represents a much

higher bulk resistivity than was assumed earlier by Frindt to calculate flake thicknesses [32].

| **Device thickness, ($d$ nm)** | **$R_{squ}$ (Ω) at 300 K** | **$\rho_{Bulk}$ (Ω.cm) at 300 K $\times 10^{-4}$** | ***RRR*** |
|---|---|---|---|
| 6.56±0.38 | 1400 | 9.20 | --- |
| 7.92±0.32 | 690 | 5.44 | 5.27 |
| 9.21±0.35 | 1330 | 12.2 | 5.08 |
| 10.37±0.34 | 1170 | 12.1 | 4.62 |

**Table 6-1:** Values of flake thickness, sheet resistance, $R_{squ}$, bulk resistivity, $\rho_{Bulk}$, and reduced resistance ratio, $RRR$, for the four devices studied.

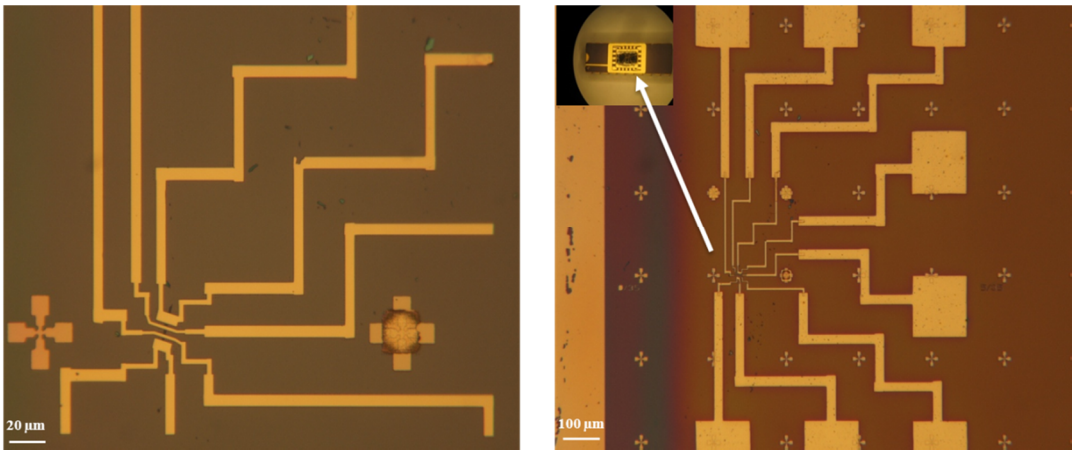


**Figure 6-7:** Optical images of the 6.65 nm flake FET.

It was found that very thin $NbSe_2$ flakes (1-2 unit cell flakes) exhibited insulating behaviour, even though the end-to-end electrode resistances were less than 100 Ω (i.e., were continuous). This insulating state may arise due to the oxidation of $NbSe_2$ during processing resulting in one or more "dead" molecular layers in each flake. Hence in all cases the number of "active" layers may be somewhat less than the apparent number. In contrast, slightly thicker flakes exhibit a true R = 0 state in measurements down to T ~ 1.5 K, as can be seen in Fig. 6-9.

The first derivative of the temperature dependent longitudinal resistance was investigated to look for a signature of the charge density wave (CDW) transition in

one of the flakes. The inset of Fig. 6-9 shows a smooth temperature dependence of the longitudinal resistance of the 9.21 nm device in the vicinity of $T \sim 32\,K$, indicating suppression of the CDW transition as expected. Since a very high sample quality is needed to see the CDW [145-147] with a high value of $RRR$ (~ 30 or higher) [148], this is consistent with the relatively low mobility of our devices.

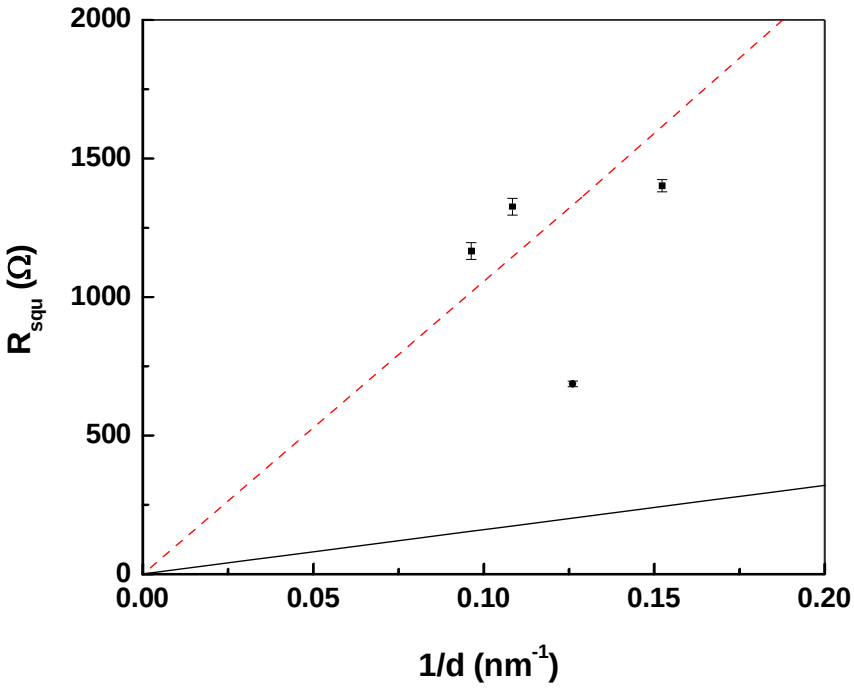


**Figure 6-8:** Sheet resistance as a function of inverse flake thickness for several devices. The solid black line represents values estimated from the bulk resistivity of large single crystals ($\rho_{Bulk}$ = 160 μΩcm) [32].

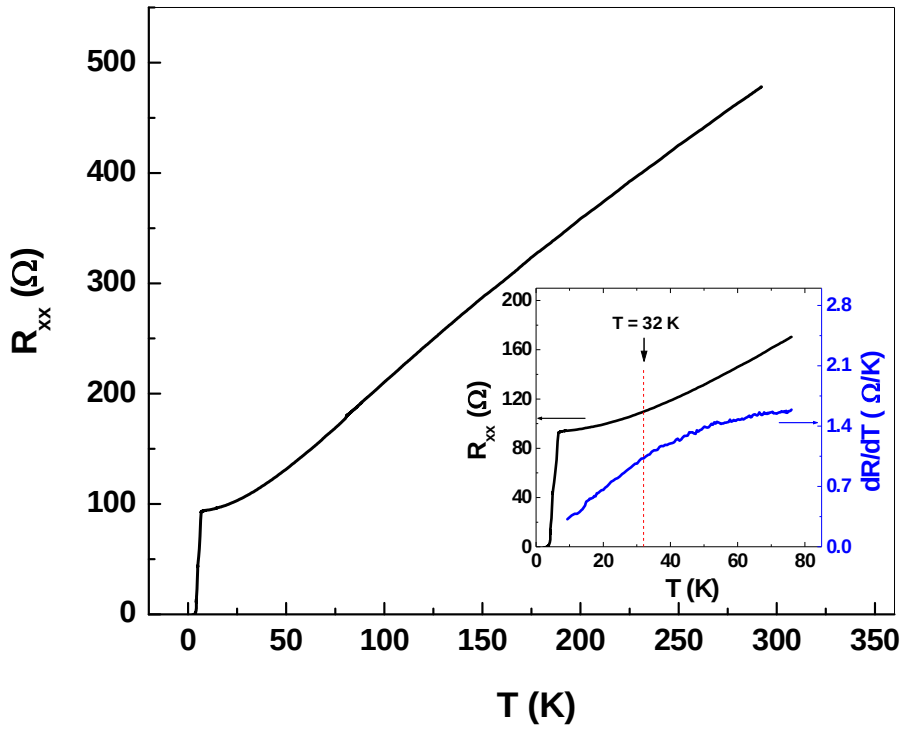


**Figure 6-9:** $R_{xx}$ as a function of temperature for the 9.21 nm sample. The inset shows an expanded view of the low temperature data and its first derivative confirming the absence of a resistive signature of the CDW transition in this sample.

### 6.3.1 Temperature dependence of flake resistivity

A careful analysis of the temperature dependent resistance, R (T), of the 9.21 nm device was performed by making power law fits ($T^n$), in the temperature ranges 10-40 K and 100-300 K. A linear fit was obtained in range 100-300 K with $R_{squ} \sim T$, whilst this changed to $R_{squ} \sim T^2$ in the range 10-40 K. In the high temperature range (100-300 K), the $R_{squ} \sim T$ dependence is consistent with that of a normal metal at temperatures above the Debye temperature Θ, where $R_{squ} = AT$, and Θ was calculated theoretically to be ~ 190 K in $NbSe_2$ [149]. In the low temperature range (10-40 K), the $R_{squ} \sim T^2$ dependence can be attributed to electron-electron scattering according to Matthiessen's rule [150]. These fits are presented in Fig. 6-10.

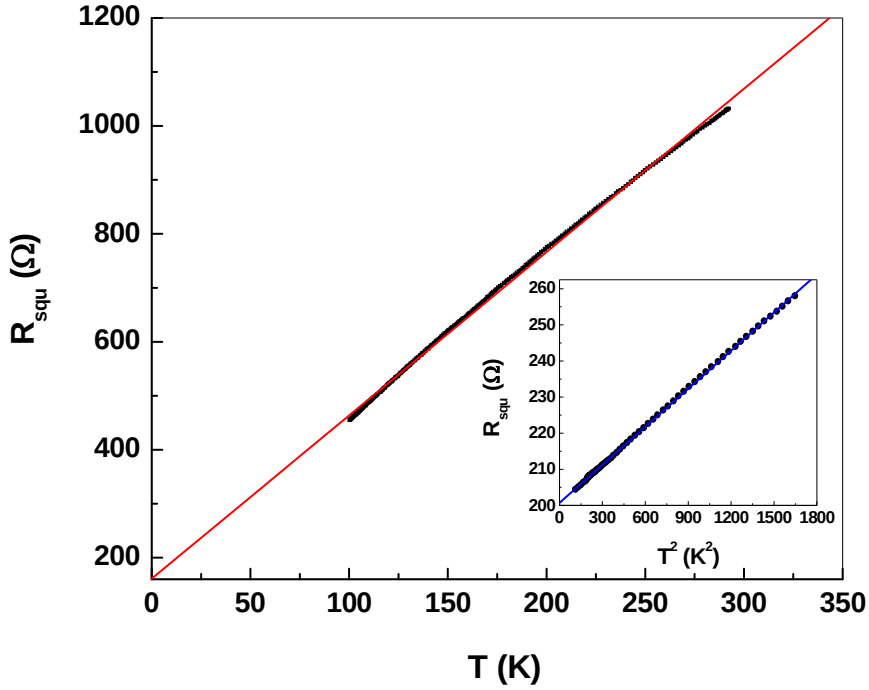


**Figure 6-10:** Linear fit obtained assuming $R_{squ} \sim T$ in the 100-300 K temperature range. Inset shows fit to $R_{squ} \sim T^2$ in the 10-40 K temperature range.

Figure 6-11 shows a typical resistive transition. Multiple superconducting transitions were observed in all flakes and all the samples appear to show at least two transitions (some three). Note that AFM scans indicate that the flakes have a uniform thickness throughout the current-carrying region. Thus, we speculate that these multiple resistive transitions are related to disorder in the layer stacking rather than lateral inhomogeneity as was proposed by Frindt [32]. Table 6-2 lists the estimated critical temperatures associated with these multiple transitions for all samples. The highest temperature transition seems to reduce systematically with reduced thickness, but the low temperature transitions do not appear to vary particularly systematically. This can be clearly seen in Fig. 6-12, which plots $T_{c1}$ and $T_{c2}$ values for the highest two resistive transitions for all samples as a function of thickness. The suppression of $T_{c1}$ can be attributed to enhancement in the Coulomb interaction, and a reduction in electron screening, which arises from reduced flake thickness as well as increasing disorder and stronger interaction effects. The complete suppression of

superconductivity leading to an insulating state is seen in highly disordered flakes [31, 32].

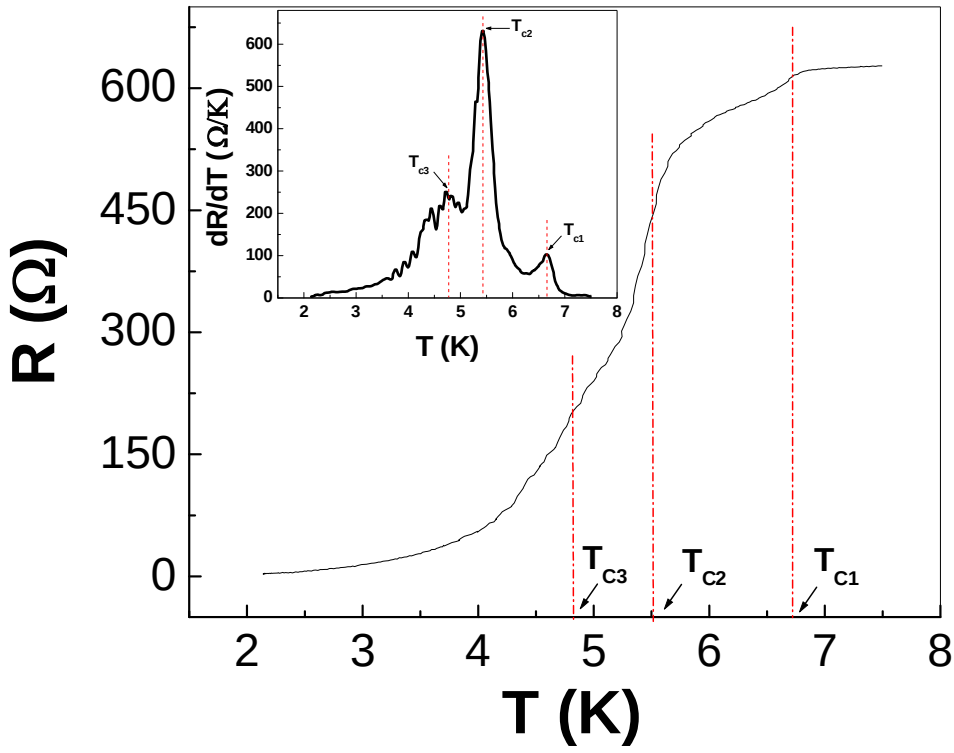


**Figure 6-11:** $R_{xx}$ plotted as a function of temperature revealing three distinct resistive transitions in the 10.37 nm device. Inset shows expanded view of the changes in dR/dT which aids to determine the $T_c$s values.

| FET flake thickness (nm) | $T_{c1}$(K) | $T_{c2}$(K) | $T_{c3}$(K) | $T_{c0}$(K) |
|---|---|---|---|---|
| 6.56±0.38 | 6.14±0.04 | 5.27±0.06 | --- | 6.40±0.01 |
| 7.92±0.32 | 6.35±0.09 | 5.40±0.06 | 4.99±0.03 | 6.47±0.01 |
| 9.21±0.35 | 6.50±0.07 | 5.06±0.08 | --- | 6.55±0.02 |
| 10.37±0.34 | 6.65±0.06 | 5.43±0.09 | 4.79±0.12 | 6.67±0.01 |

**Table 6-2:** A list of the resistive transitions $T_{c1}$, $T_{c2}$, and $T_{c3}$, and the onset temperature $T_{c0}$ values estimated from fits to the fluctuation conductivity.

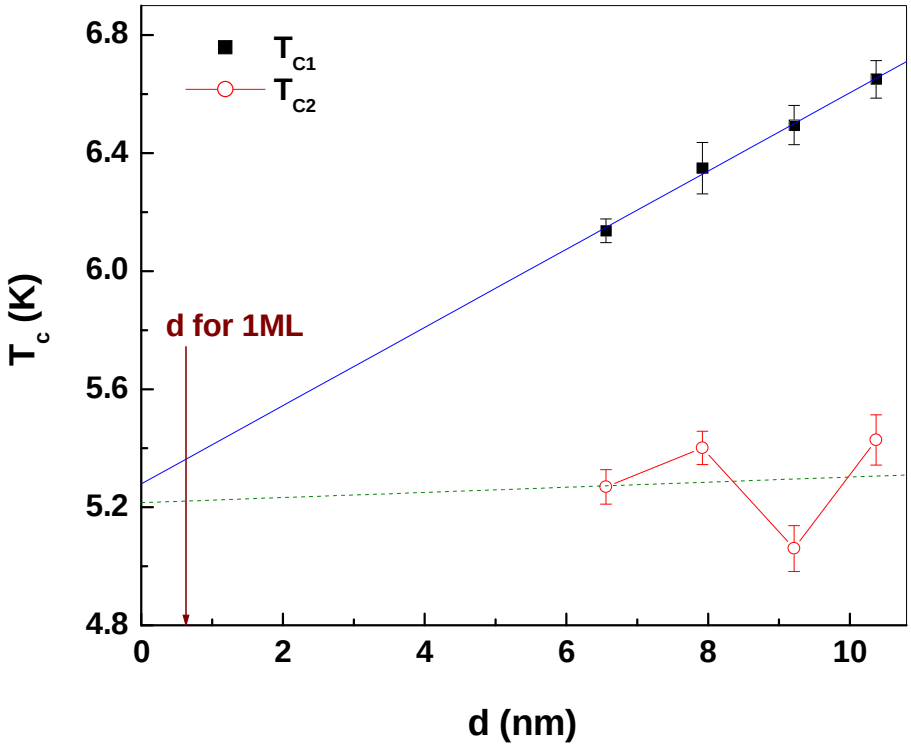


**Figure 6-12:** Values of $T_{c1}$ and $T_{c2}$ as a function of flake thickness.

### 6.3.2 Analysis of the H=0 resistive transition

Analysis of the H=0 resistive transition was made for all samples to extract both the mean-field pairing temperature, $T_{c0}$, and where possible the Brezinskii-Kosterlitz-Thouless critical vortex-antivortex unbinding temperature, $T_{BKT}$. The onset $T_{c0}$ values were estimated by fitting the highest temperature transition data to the Aslamazov-Larkin equation that describes fluctuation-enhanced conductivity in 2D samples, $\Delta\sigma(T) \propto ln(T/T_{c0})^{-1}$ [89]. Figure 6-13 illustrates the fit used to extract $T_{c0}$ for the 7.92 nm sample. Estimated $T_{c0}$ values for all samples are listed in Table 6-2.

It is well known that below the pairing temperature, $T_{c0}$, a loss of global phase coherence and dissipation due to a finite flux resistance occurs as a result of the penetration of vortices. In addition, a finite supercurrent can flow below $T_{BKT}$ owing to the formation of the bound vortex-antivortex pairs which result from the attractive interaction between oppositely oriented vortices. The universal form of the flux flow resistance, $R_{squ}(T) \propto exp[b(T - T_{BKT})^{-1/2}]$, has been used to identify

the vortex-antivortex unbinding temperature, $T_{BKT}$. Here, the strength of the vortex-antivortex interaction is governed by the constant b [88, 90]. $T_{BKT}$ values have been extracted by plotting the low temperature tail of $[1/R_{squ} \cdot dR_{squ}/dT]^{-2/3}$ versus T, and associating the x-axis intercept with $T_{BKT}$, as shown in Fig. 6-14 for the 9.21 nm and 10.37 nm samples.

It is noteworthy that one of these samples shows quite a long BKT tail and the other does not. It suggests that apparently similar samples can have very different properties related to the dependence of 2D layered materials on their degree of stacking order [33]. The different behaviour seen in the two samples can be attributed to qualitatively different stacking disorder, whereby one is somehow much more 2D-like than the other.

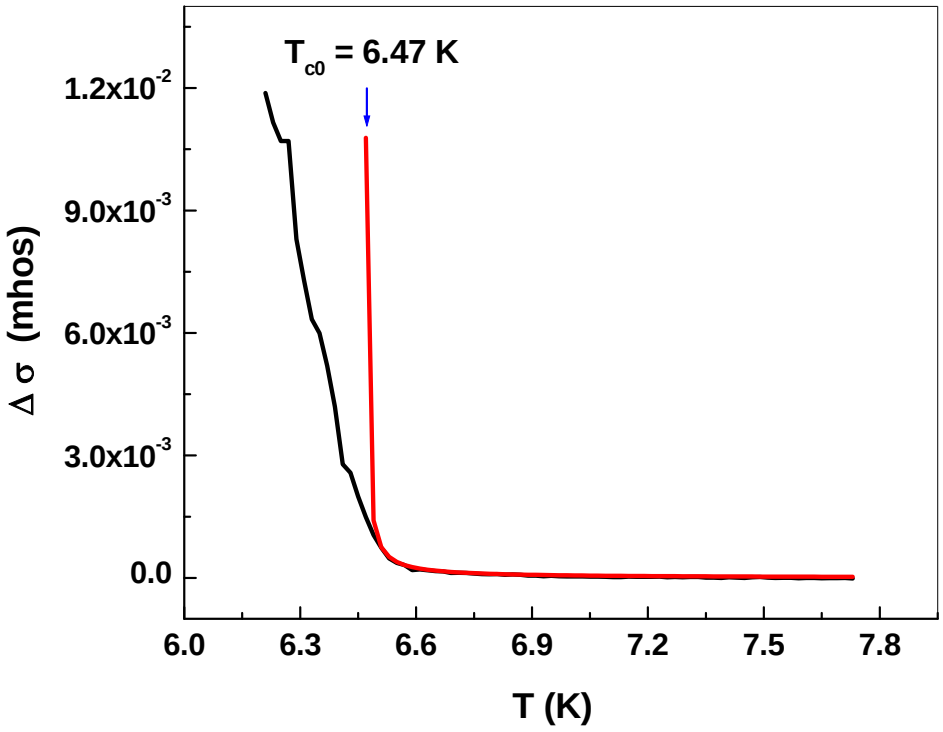


**Figure 6-13:** The solid red curve represents the fit made to the temperature-dependent conductivity data (black curve) for the 7.92 nm device.

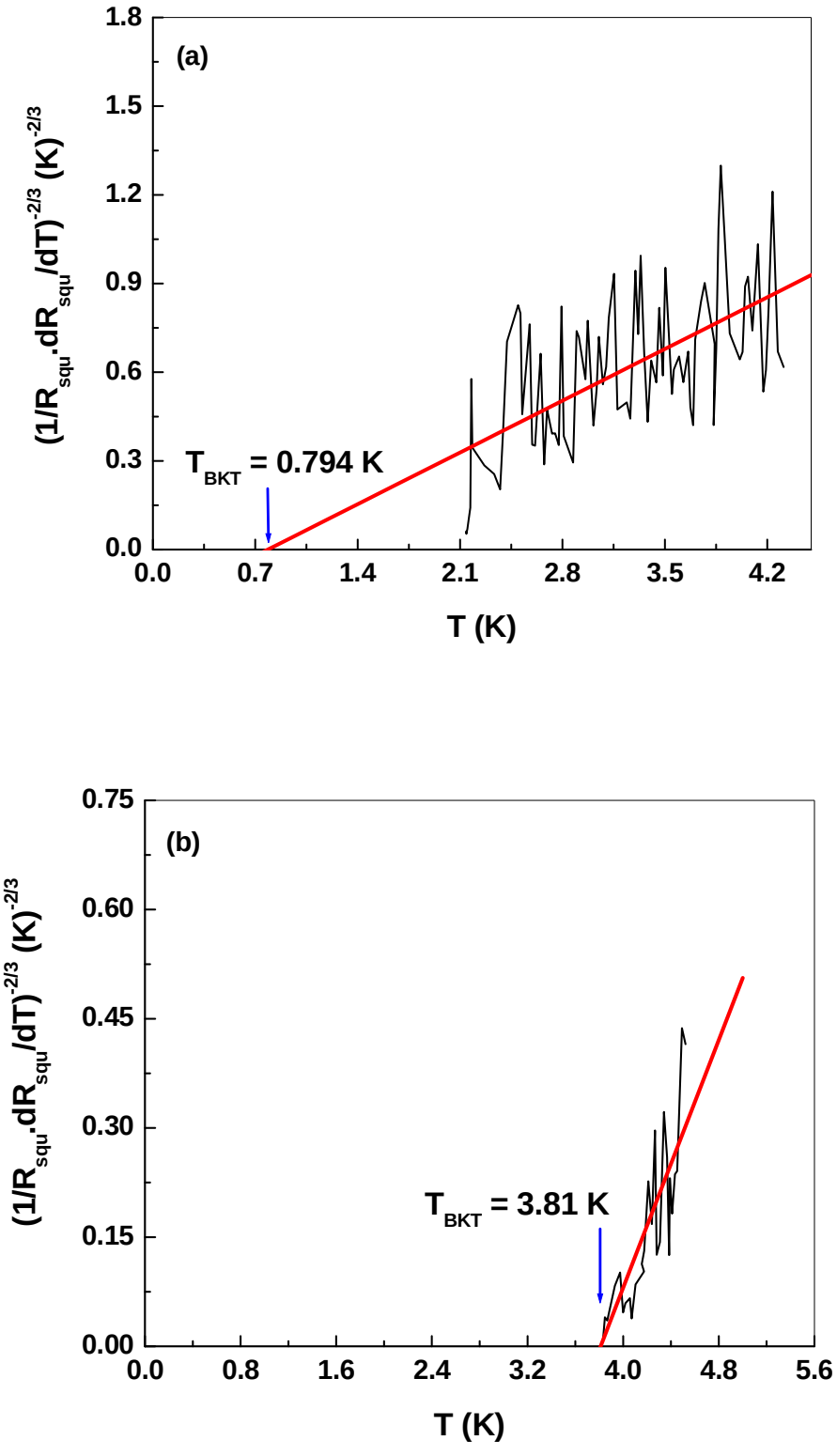


**Figure 6-14:** The universal form of the flux flow resistance has been used to extract the vortex-antivortex unbinding transition temperature, $T_{BKT}$, for the 10.37 nm (a) and 9.21 nm (b) samples, respectively.

### 6.3.3 Resistive transition as a function of applied magnetic field B

The temperature dependence of the resistance for the 9.21 nm sample at various values of magnetic field, B, and the resistance of the 10.37 nm sample as a function of magnetic field at various values of temperatures, T, are shown in Figs. 6-15 (a) and (b), respectively. These data appear to show how the separate resistive transitions all seem to smear together combined with a weak downwards shift as a function of increasing magnetic field.

We assume that the upper critical field of the individual superconducting grains (uncoupled pockets of superconductivity) controls the observed onset transition shift, whereas the shift in the tails near R ~ 0 can be attributed to vortex flow and the field dependence of the vortex-antivortex unbinding transition [151]. The resistive transition temperatures were determined from the first derivative of R (T), being associated with the point of maximum slope in each transition. Using dR/dT in this way greatly aids tracking the evolution of $T_{c1}$ and $T_{c2}$ as a function of applied magnetic field as illustrated in Fig. 6-16 (a) for the 9.21 nm sample.

Tracking the main peaks/shoulders ($T_{c1}$ and $T_{c2}$ values) of dR/dT as a function of B allows the determination of the upper critical field, $H_{c2}$ (T), in these samples. The zero-temperature upper critical field, $H_{c2}$ (0), has been determined using the Werthamer-Helfand-Hohenberg (WHH) formula [152],

$$H_{c2}(0) = -0.69\, T_c \left(\frac{dH_{c2}}{dT}\right)_{T=T_c}, \tag{6-1}$$

where $T_c$ is the resistive transition temperature and $H_{c2}(T)$ is the upper critical field.

A different estimation of $H_{c2}(0)$ can also be made using a phenomenological formula based on the Ginzburg-Landau (GL) equation for multiband superconductors [153],

$$H_{c2}(T) = H_{c2}(0)[1 - (T/T_c)^a]^b . \tag{6-2}$$

When a = 1.45 and b = 1 equations 6-1 and 6-2 become consistent, and a good match between $H_{c2}(0)$ values could be obtained. Taking into account the fact that $NbSe_2$ is a multiband superconductor and $H_{c2}(T)$ values are expected to be influenced by this, it is not clear *a priori* which of the two approaches is more appropriate. Figure 6-16 (b) shows the fits to equation 6-2 for both transitions observed in the

9.21 nm sample. Accurate estimation of $H_{c2}(0)$ allows the calculation of the zero temperature GL coherence length $\xi(0)$ in these samples from [63],

$$H_{c2}(0) = \Phi_0/2\pi\xi(0)^2 , \quad (6\text{-}3)$$

where $\Phi_0$ is the flux quantum $(2.07 \times 10^{-15}\ \mathrm{Tm}^2)$. $H_{c2}(0)$ values obtained using equations 6-1 and 6-2, as well as the calculated coherence length $\xi(0)$ values are listed in Table 6-3, and these values are in good agreement with those obtained in the literature [153, 154].

| **FET flake thickness (nm)** | $H_{c2}(0)$ (T) Equation 1 | | $\xi(0)$ (Å) Equation 1 | | $H_{c2}(0)$ (T) Equation 2 | | $\xi(0)$ (Å) Equation 2 | |
|---|---|---|---|---|---|---|---|---|
| | $T_{c1}$ | $T_{c2}$ | $T_{c1}$ | $T_{c2}$ | $T_{c1}$ | $T_{c2}$ | $T_{c1}$ | $T_{c2}$ |
| **7.92±0.32** | **3.04±0.01** | **2.67±0.16** | **102±0.01** | **109±0.08** | **3.30±0.19** | **2.67±0.18** | **98.2±0.09** | **109±0.09** |
| **9.21±0.35** | **2.94±0.04** | **4.19±0.02** | **104±0.02** | **87.2±0.01** | **2.94±0.14** | **4.2±0.22** | **104±0.07** | **87.1±0.11** |
| **10.37±0.34** | **3.93±0.05** | **3.70±0.03** | **90±0.03** | **92.8±0.02** | **3.93±0.23** | **3.94±0.26** | **90.0±0.12** | **89.9±0.13** |

**Table 6-3:** Table of the zero-temperature upper critical field, $H_{c2}(0)$, and the coherence length, $\xi(0)$, estimated values for three of the devices.

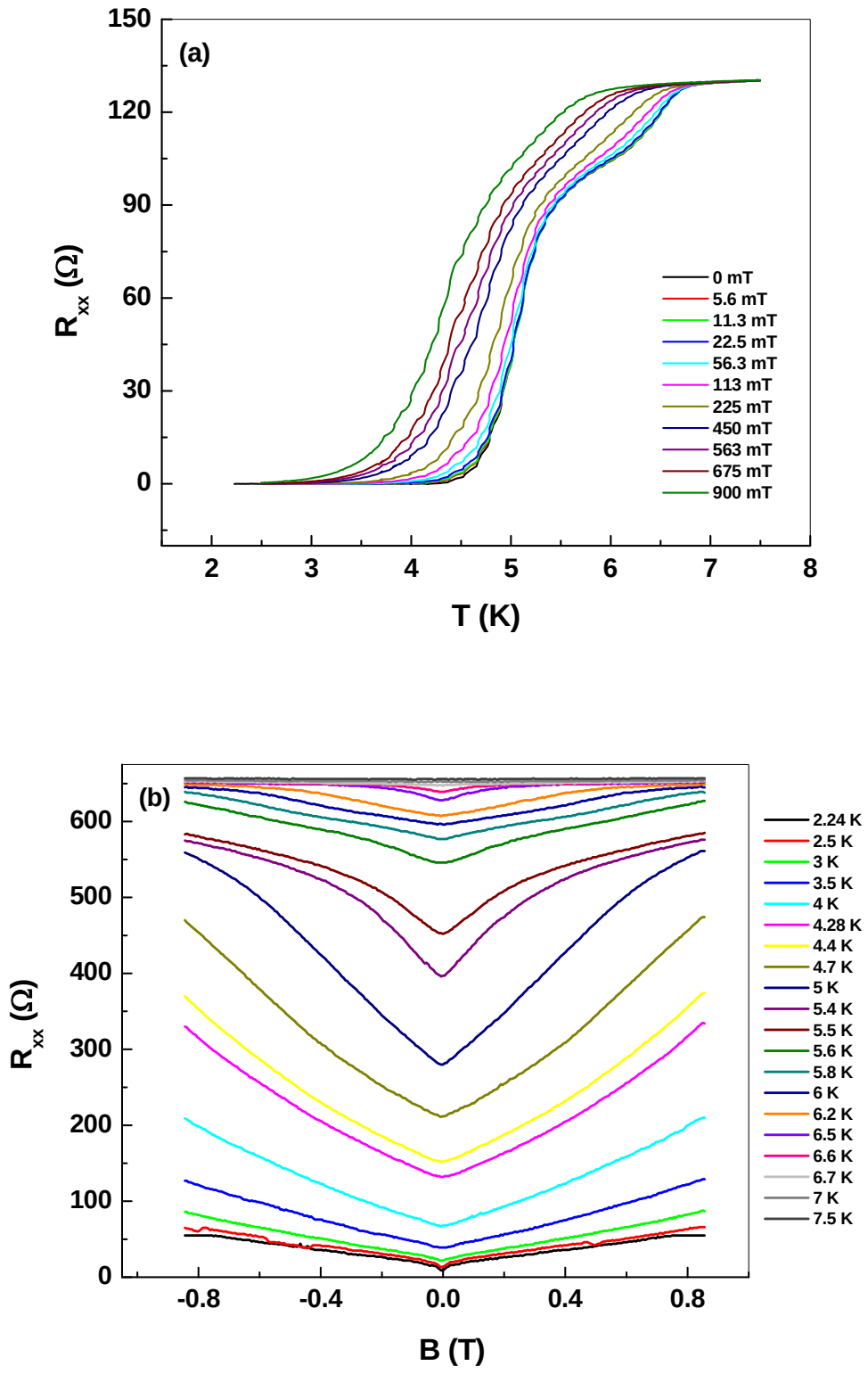


**Figure 6-15:** a) $R_{xx}$ as a function of temperature for the 9.21 nm sample. b) $R_{xx}$ as a function of magnetic field for the 10.37 nm sample.

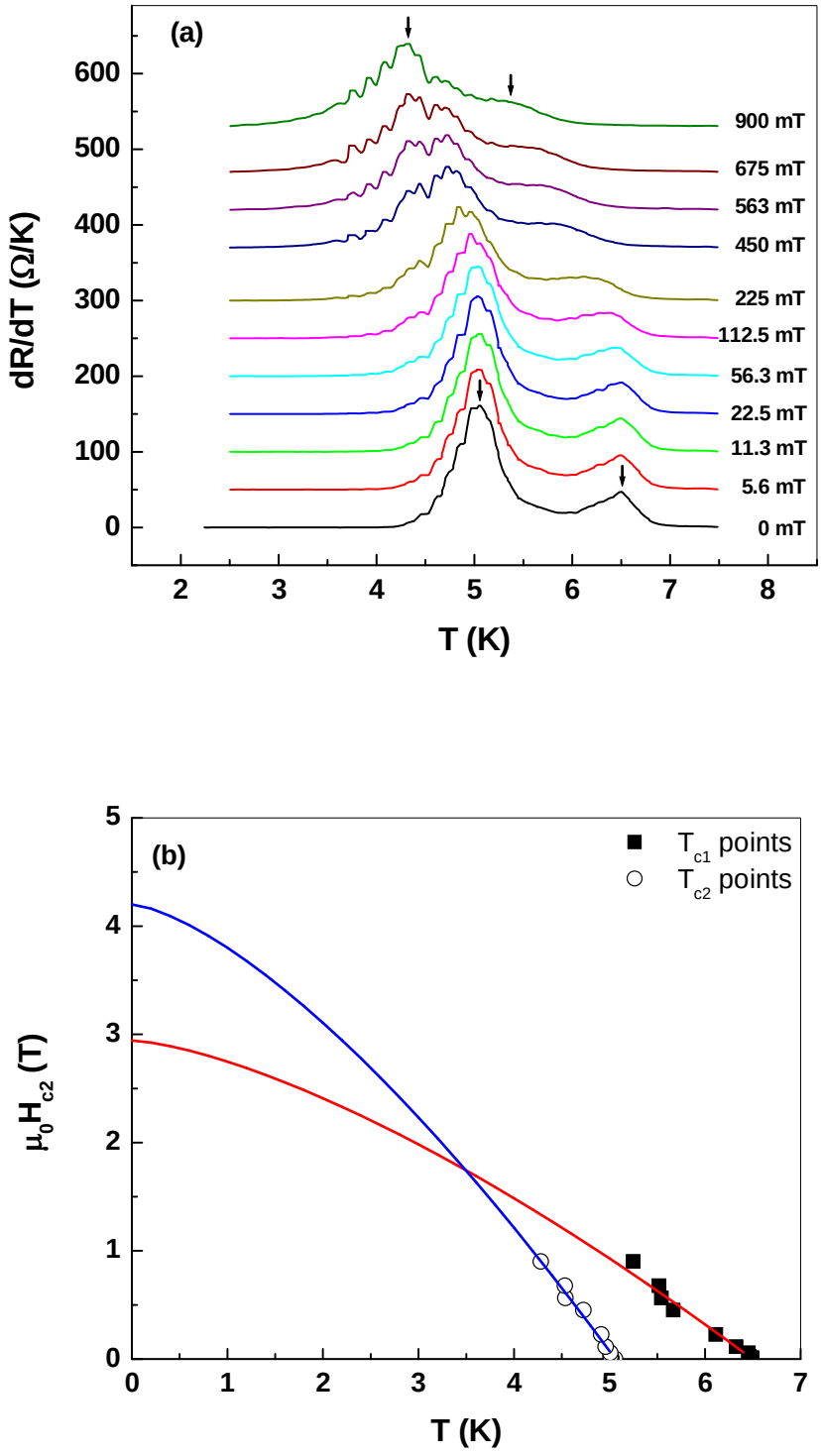


**Figure 6-16:** a) Digital derivative of R (T, B) for the 9.21 nm sample. Arrows show estimated positions of $T_{c1}$ and $T_{c2}$. b) Fits to equation 6-2 for the first two resistive transitions in the same sample.

### 6.3.4 Influence of a back-gate voltage

The electrical conductivity, σ, of all the samples in the normal state at 7 K was measured as a function of $V_g$. Figure 6-17 shows the longitudinal conductivity of the 10.37 nm sample as a function of $V_g$. The extracted slope, $\Delta\sigma_{2D}/\Delta V_g$, of the observed linear dependence allows the calculation of the dynamic field effect mobility [134],

$$\mu_{FE} = \frac{d}{\epsilon\epsilon_0}\frac{\Delta\sigma_{2D}}{\Delta V_g}, \tag{6-4}$$

where d is the $SiO_2$ layer thickness, $\epsilon$ is the dielectric constant of $SiO_2$ (3.9), and $\epsilon_0$ is the permittivity of free space. The motivation for using this indirect way to estimate the mobility of our samples arises from the design of our devices that have not been patterned in a Hall bar configuration. It was found that the calculated dynamic mobilities, $\mu_{FE}$, lay in the range 7-64 $cm^2/Vs$, in agreement with the findings of Staley *et al.* [31], and were very much higher than the values reported by Novoselov *et al.* [1]. Moreover, it was observed that, the conductivity *decreases* at positive gate voltages as can be seen in Fig. 6-17.

The effect of an applied gate voltage on the resistive transition of the 10.37 nm sample is shown in Fig. 6-18. A very weak shift in the resistive transition with gate voltage is observed. Interestingly, the resistive $T_c$s are very slightly reduced by positive gate voltages (enhanced electron densities). The change in critical temperature due to electric field modulation was estimated to be 10 mK and 45 mK for $T_{c1}$ and $T_{c2}$, respectively. This shift can be clearly seen in the insets of Fig. 6-18, which show expanded views of dR/dT versus T. The observed gate dependencies of both the $T_c$ values and the conductivity could possibly arise from sharp structure in the electronic density of states near the Fermi level. However a more careful analysis of the realistic band structure of our flakes must be made to confirm this speculation.

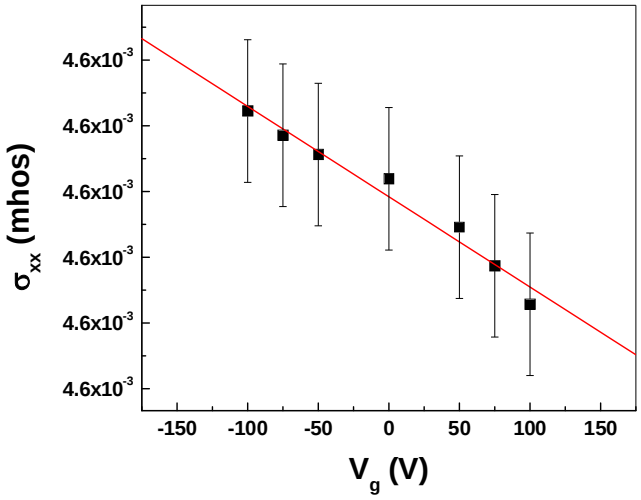


**Figure 6-17:** Plot of the longitudinal conductivity as a function of applied gate voltage, $V_g$, for the 10.37 nm sample at T = 7 K.

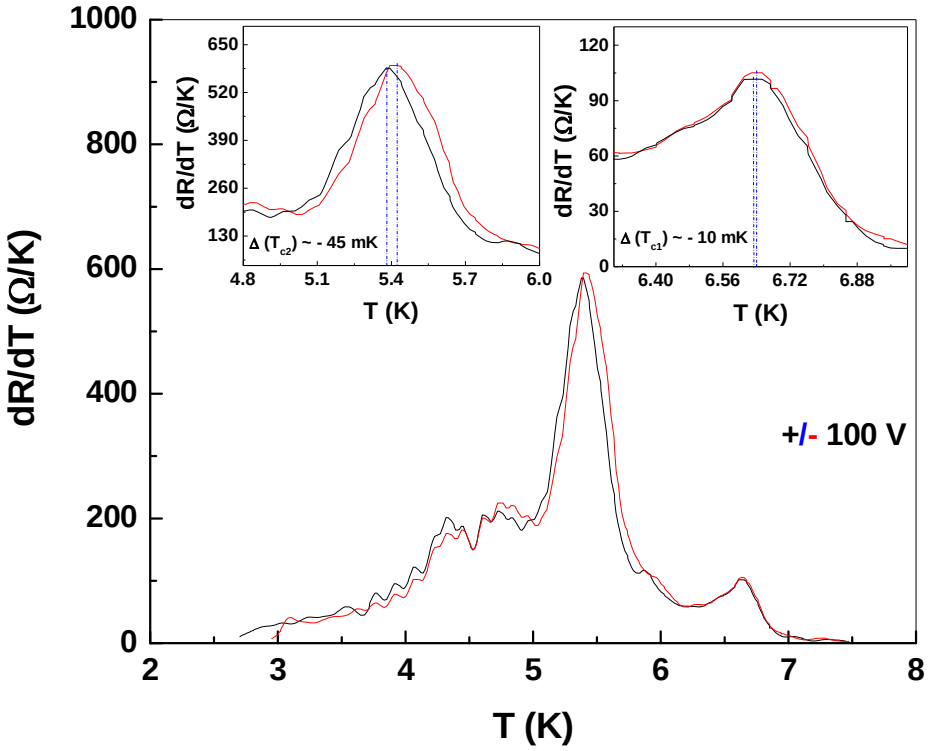


**Figure 6-18:** The effect of the back gate on the resistive transition of the 10.37 nm sample. Insets show expanded views around $T_{c1}$ and $T_{c2}$ of the changes in dR/dT with gate voltage.

### 6.3.5 Discussion of the superconducting transition in few layer $NbSe_2$ flakes

Patterning 4-terminal transport structures allows "ideal" measurements in which the influence of contact resistances is almost entirely eliminated. This distinguishes our results from those obtained by Staley *et al.* [31], who only made 2-terminal measurements, while Frindt [32] did not actually state how his measurements were made in his paper. Frindt [32] was not able to measure flake thickness directly but inferred it from the 300 K resistance assuming a bulk resistivity of 160 μΩ.cm. However, we have measured the flake thicknesses directly and can correlate this with the 4-point device resistance. We measure a much higher effective 300 K resistivity for our samples suggesting that Frindt's values for flake thicknesses and resistivity may have been grossly underestimated.

The resistive superconducting transitions as a function of $NbSe_2$ flake thickness, the influence of a magnetic field perpendicular to the flake and the effect of a back-gate voltage on the conductivity of these flakes, has been studied to extend our current understanding of the underlying physics. $T_c$ values decreased in thinner flakes. We speculate that this is due to stacking disorder, whereby neighbouring planes in the flake could be shifted slightly relative to one another. In addition, it was found that the conductance in the normal state, as well as the resistive transition temperatures, depend weakly on the gate voltage with both conductivity and $T_c$ decreasing as the electron concentration is increased. The observed gate dependencies of both the $T_c$ values and the conductivity could possibly arise from sharp structure in the electronic density of states near the Fermi level. However a more careful analysis of the realistic band structure of our flakes must be made to confirm this speculation.

The resistance typically showed a small, sharp high temperature transition followed by one or more broader transitions which ended in a wide tail to zero resistance at low temperatures. The origin of the sharp high temperature transition could be attributed to the presence of uncoupled pockets of superconductivity in a normal matrix (cf., Fig. 6-19). Such "puddles" could naturally arise from stacking disorder or fluctuations due to extrinsic charges (c.f., the formation of electron/hole

puddles in graphene) [91]. Also, large fluctuations from sample to sample suggest non-systematic process-dependent factors.

The lowest temperature transitions seem to be 2D in nature and dominated by the BKT vortex-antivortex unbinding transition (cf., Fig. 6-19). Normally highly disordered films with very short mean free paths are needed to see a clearly separated BKT transition. In dirty 2D superconductors, the material dependent screening of the attractive vortex-antivortex interaction through a dielectric constant, $\in_v$, is known to directly reduce $T_{BKT}$ ($T_{BKT} \propto 1/\in_v$) [88]. Thus, the low value of $T_{BKT}$ observed in some of our flakes suggests a relatively large screening parameter, $\in_v$, leading to weakly bound vortices and antivortices. We attribute the multiple resistive superconducting transitions to the inhomogeneous superconductivity arising from layer stacking disorder in our devices. It would be natural to assume that the layer coupling strength in the perpendicular direction plays a key role in determining specific transition temperatures. That is, the strongest layer coupling represents the highest temperature transition, etc. This is also consistent with $T_{c1}$ reduces with number of layers. In addition all $T_c$s seem to extrapolate to the same value at the thickness of one molecular layer of $NbSe_2$ ($d$ = 1ML)). Thus, we speculate that some of these low $T_c$s could almost be attributed to uncoupled monolayers which could be referred to band structure calculations with/without interlayer coupling.

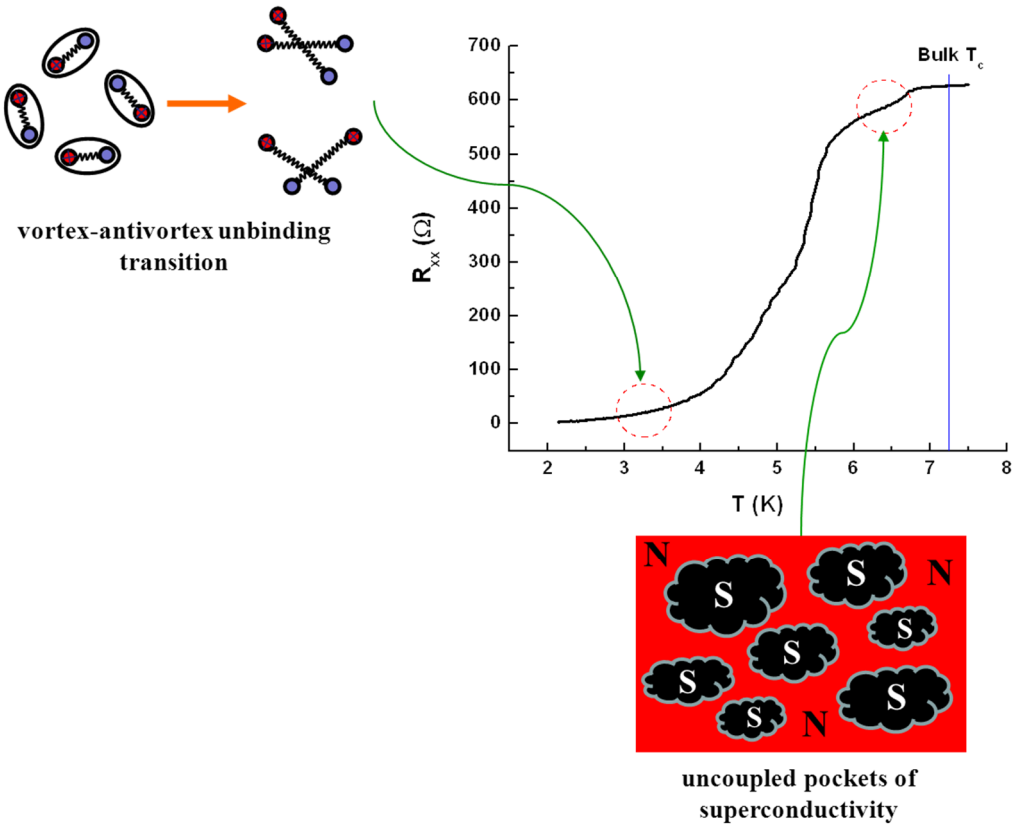


**Figure 6-19:** Cartoon depicting the possible existence of uncoupled superconducting pockets near the high temperature onset transition, whereas the low temperature resistive tail is controlled by vortex-antivortex unbinding.

# Chapter 7

# Conclusions and Outlook for Future Work

## 7.1 Conclusions

The discovery of graphene (single layer graphite) in 2004 demonstrated for the first time that truly two-dimensional crystals can be stable on $Si/SiO_2$ substrates and as free-standing membranes, opening up the possibility of new and exciting physics for a new class of materials. It was subsequently shown that single layer graphene can carry significant proximity supercurrents, even when the Fermi energy is at the Dirac point and there are theoretically no free carriers. This research project has extended this work to investigations of two-dimensional superconducting crystals of the layered chalcogenide $NbSe_2$. Thin flakes of this material have been prepared on $Si/SiO_2$ substrates using the same micromechanical cleavage techniques developed for graphene, and the number of layers present in different regions determined by both AFM and optical spectroscopy. The exploration of new material parameters and new phenomena in such 2D systems is expected to lead to wide ranging industrial applications [1].

Lithographic techniques have been used to make electrical contacts to several samples enabling measurements of magnetoresistance and superconductivity in 4-point graphene and $NbSe_2$ devices. The same techniques could be widely applied to other layered superconducting materials paving the way for the exploration of new physics and potential device applications for 2D superconducting materials.

### 7.1.1 Graphene

The unusual properties of graphene charge carriers make it one of the most interesting materials in mesoscopic physics. Graphene provides an opportunity to produce nanoscale devices of a type not possible in conventional silicon-based electronics. The possibility to produce high quality graphene flakes using the

mechanical exfoliation technique has been a major advantage for research in the field. The present study was targeted at investigations of the superconducting proximity effect in superconductor/graphene structures (Graphene Josephson Junctions-GJJ).

Modulation of both the graphene charge carrier type and its density with an applied back-gate voltage has allowed studies of the influence of external electric fields on the induced superconducting state in graphene. Several high quality proximity-effect graphene devices with low resistance Pd/Al contacts were fabricated. However, for reasons we do not understand supercurrents were not observed in these devices at temperatures down to 300mK.

Realising sufficiently high quality metal/graphene interfaces to observe proximity-induced superconductivity in graphene devices is a major challenge. Consequently, an alternative approach pioneered by Allain *et al.* was trialled [91] whereby a very thin layer of Sn was evaporated onto the surface of a large graphene transistor. The deposited Sn self-assembles into arrays of unconnected nanoscale islands, and proximity supercurrents between these islands have been observed and characterised [91]. Once again, there was no sign of superconductivity in the samples we fabricated of this type at temperatures down to 2K. Having failed to observe proximity-induced superconductivity in graphene devices, the attention of the project was refocused onto an analysis of low field magnetoresistance data in trilayer graphene devices. In particular, low field data yielded key information about the source of weak localisation or anti-localisation corrections to the conductivity, as well as universal conductance fluctuations.

The following conclusions can be drawn from this study of our graphene devices. A shift of the Dirac point to very large positive gate voltages has been observed and was primarily attributed to strong proximity hole doping by the Pd contacts, with a lesser contribution due to transferred charges from the flake environment. We obtain rather low mobility graphene devices, a fact attributable to both molecular adsorption on the graphene surface and ionized charge traps in the $Si/SiO_2$ substrate [122].

Both WL and UCF have been investigated in trilayer flake as a function of temperature and gate voltage, and data analysed using several theoretical descriptions. The theory of WL/WAL in monolayer graphene has been used to fit the

magnetoconductance data near the CNP and estimate several characteristic scattering rates. A rapid decrease in UCF amplitude was obtained with increasing temperature and/or decreasing hole density, as $V_g$ approaches the Dirac point from below. Both these effects are probably due to a corresponding reduction of the phase coherence length.

Fast Fourier Transforms (FFTs) have been used to analyse magnetic field-dependent UCF data. This identified more than one period in the UCF signals and makes a compelling case for the presence of a short and a long period in the data. This situation is not precisely the same at all gate voltages values and our measurements highlight the role of the gate voltage in determining whether the dominant effect is either the superposition of the two intrinsic periods or a UCF signal with one of the two periods. We speculate that the WL signature near the CNP is dominated by the ML-like dispersion of trilayer graphene, while the UCF signature arises from a complex combination of signals from both ML-like and BLG-like dispersions in our device.

### 7.1.2 $NbSe_2$

The physical understanding of 2D materials obtained from working with graphene as well as the experience gained of preparing and manipulating 2D flakes, have led to a renewed interest in studies of atomically thin 2D forms of the transition metal dichalcogenides. These systems are expected to find many exciting applications in nanoelectronics, logic transistors and optoelectronics. Investigations of superconductivity in few molecular layer $NbSe_2$-FETs have been performed in carefully characterised 4-terminal devices. A newly developed mechanical exfoliation protocol enabled the production of large, high quality flakes of $NbSe_2$ from a single crystal. Patterning 4-terminal transport structures in this way allows "ideal" measurements in which the influence of contact resistances is almost entirely eliminated. While devices fabricated from extremely thin $NbSe_2$ flakes did not appear to conduct, slightly thicker flakes were superconducting with an onset $T_c$ that was only slightly depressed from the bulk value (7.2K). The resistance typically showed a small, sharp high temperature transition followed by one or more broader transitions which ended in a wide tail to zero resistance at low temperatures. These multiple resistive transitions are speculated to be related to disorder in the stacking of molecular layers.

The behaviour of several flakes has been characterized as a function of temperature, applied field and back-gate voltage. It was found that the conductance in the normal state and resistive transition temperatures depend weakly on the gate voltage, with both conductivity and $T_c$ decreasing as the electron concentration is increased. Finally, the application of a perpendicular magnetic field allowed the evolution of different resistive transitions to be tracked and values of the T = 0 upper critical field, $H_{c2}$ (0), and GL coherence length, $\xi(0)$, to be independently estimated. This work was complemented by 'contactless' measurements of the magnetisation of $NbSe_2$ few layer flakes using Hall array micromagnetometry.

## 7.2 Outlook for future work

### 7.2.1 Graphene

In the final section of this thesis, a review of several directions for future work in the field of GJJs and graphene transistor structures is outlined. Fabricating better quality graphene devices with higher mobility that operate in the ballistic transport regime would be an important step forward for these experiments. The ability to observe the Josephson effect in the I-V characteristics or multiple Andreev reflection processes, depends intimately upon whether transport is ballistic or diffusive. This will demand further improvements in the fabricated devices. Hence, some modifications in the fabrication process are suggested such as depositing graphene in a controlled glove box environment and experimenting with different substrates in order to avoid limitations in current devices. Recently, hexagonal boron nitride (h-BN) was used as an alternative substrate to $SiO_2$ and was shown to result in much higher quality graphene devices. This relates to the interesting properties of h-BN which is an insulator with a large band gap and a similar lattice constant to that of graphene. It presents an atomically smooth (almost) lattice matched surface for graphene deposition resulting in a surface that is free of dangling bonds and charge traps [155]. An alternative approach for studying the proximity effect would be to fabricate suspended graphene Josephson junctions as this is one of the best ways to get high mobility devices.

In addition, the possibility to change the transport properties of graphene through various chemical modifications at its surface could be an important new direction for fabricating GJJs. In this regard our collaborators at Exeter University

have recently succeeded in intercalating few-layer graphene with ferric chloride, greatly enhancing the electrical conductivity. Proximity-induced critical currents have recently been observed in this material and full characterisation of these devices as a function of temperature, back gate voltage, magnetic field and contact spacing is now required.

Other extensions to graphene transistor structures could be realised by fabricating electrodes with different physical properties (superconductors, ferromagnets), and by gating the flakes with both top and back-gates. Finally, studying the WL/WAL and UCF in chemically modified mesoscopic graphene samples could reveal surprising new phenomena.

### 7.2.2 $NbSe_2$ and other 2D superconducting materials

Our research on superconductivity in $NbSe_2$ flakes has thrown up many questions that require further investigation. At present more systematic measurements are needed of 4-terminal $NbSe_2$ superconducting devices containing flakes with a range of different thicknesses, with a focus on studies of the resistive critical temperature as well as the upper critical field and their dependence on back gate voltage. More comprehensive measurements will be required to confirm our current interpretation in terms of phase coupling of superconducting "pockets" followed by a BKT vortex-antivortex binding/unbinding transition.

Further improvements are recommended aimed at enhancing the quality of these samples. In particular, it seems that the act of patterning contacts is enough to strain the flakes and disorder the layer coupling somehow. Hence, it would be interesting to use a lithography-free technique, such as shadow masking as reported by Staley *et al.* [31], to pattern these contacts as this could yield higher mobility less strained samples. Moreover, using higher permittivity gate dielectrics like $HfO_2$ instead of $SiO_2$, could enhance FET performance as demonstrated by Zhang *et al.* [93] in their ambipolar $MoS_2$-FETs.

Our results on $NbSe_2$-FETs are encouraging and naturally suggest a number of extensions to the work. Observing a shift in $T_c$ with gate voltage as well as attributing the presence of multiple resistive transitions to the lateral disorder in the studied samples, suggests the possibility of the presence of sharp structure in the electronic density of states near the Fermi level. Also, account must be taken of the

band structure of $NbSe_2$ near the Fermi energy which is quite complicated; electrons are the majority carrier in determining the conductivity but holes do contribute as well. Therefore, a more careful analysis of the realistic band structure of 2D $NbSe_2$ flakes must be made to confirm these speculations. Enhancing our understanding of these issues would be the first step in accomplishing the ultimate goal of this project to investigate 2D-superconducting crystals in common layered materials, e.g., $NbSe_2$ and $Bi_2Sr_2CaCu_2O_{8+\delta}$ using the new fabrication protocols we have developed. In addition, magnetotransport and magnetisation data should be measured in devices fabricated from these common layered materials in applied perpendicular magnetic fields when pancake vortices (or short stacks of pancake vortices) are expected to be present.

Further information on the ordering and dynamics of vortices in these structures could possibly be obtained using Scanning Hall probe microscopy if the signal: noise ratio was high enough. Finally, more work is required to fully understand superconductivity in $NbSe_2$ and other layered two dimensional superconductors and could play an important role in exploring new physics and device applications.

## 7.3 Publications

**Superconductivity in two-dimensional $NbSe_2$ Field Effect Transistors**
(in preparation for *Superconductor Science and Technology*)

**WL/WAL and UCF in mesoscopic trilayer graphene FETs**
(in preparation for *Semiconductor Science and Technology*)

# Bibliography


1. Novoselov, K.S., et al., *Two-dimensional atomic crystals.* Proceedings of the National Academy of Sciences of the United States of America, 2005. **102**(30): p. 10451-10453.
2. Geim, A.K. and K.S. Novoselov, *The rise of graphene.* Nature materials, 2007. **6**(3): p. 183-191.
3. Peres, N.M.R., F. Guinea, and A.H.C. Neto, *Electronic properties of disordered two-dimensional carbon.* Physical Review B, 2006. **73**(12).
4. Pierson, H.O., *Handbook of carbon, graphite, diamond and fullerenes.* 1993: Noyes publications.
5. Yacoby, A., *GRAPHENE Tri and tri again.* Nature Physics, 2011. **7**(12): p. 925-926.
6. Lui, C.H., et al., *Observation of an electrically tunable band gap in trilayer graphene.* Nature Physics, 2011. **7**(12): p. 944-947.
7. Partoens, B. and F. Peeters, *From graphene to graphite: Electronic structure around the K point.* Physical Review B, 2006. **74**(7): p. 075404.
8. Aoki, M. and H. Amawashi, *Dependence of band structures on stacking and field in layered graphene.* Solid State Communications, 2007. **142**(3): p. 123-127.
9. Yan, J.A., W. Ruan, and M. Chou, *Phonon dispersions and vibrational properties of monolayer, bilayer, and trilayer graphene: Density-functional perturbation theory.* Physical Review B, 2008. **77**(12): p. 125401.
10. Craciun, M.F., et al., *Tuneable electronic properties in graphene.* Nano Today, 2011. **6**(1): p. 42-60.
11. Xia, F.N., et al., *Graphene Field-Effect Transistors with High On/Off Current Ratio and Large Transport Band Gap at Room Temperature.* Nano Letters, 2010. **10**(2): p. 715-718.
12. Jhang, S.H., et al., *Stacking-order dependent transport properties of trilayer graphene.* Physical Review B, 2011. **84**(16): p. 161408.
13. Saito, R., G. Dresselhaus, and M.S. Dresselhaus, *Physical properties of carbon nanotubes.* Vol. 35. 1998: World Scientific.

14. Wallace, P., *The band theory of graphite.* Physical Review, 1947. **71**(9): p. 622.
15. Charlier, J.C., et al., *Electron and phonon properties of graphene: Their relationship with carbon nanotubes.* Carbon nanotubes, 2008: p. 673-709.
16. Avouris, P., Z. Chen, and V. Perebeinos, *Carbon-based electronics.* Nature Nanotechnology, 2007. **2**(10): p. 605-615.
17. Ando, T., *Screening effect and impurity scattering in monolayer graphene.* Journal of the Physical Society of Japan, 2006. **75**(7).
18. Kittel, C. and P. McEuen, *Introduction to solid state physics.* Vol. 7. 1996: Wiley New York.
19. Ando, T., T. Nakanishi, and R. Saito, *Berry's phase and absence of back scattering in carbon nanotubes.* Journal of the Physical Society of Japan, 1998. **67**(8): p. 2857-2862.
20. Adam, S., et al., *A self-consistent theory for graphene transport.* Proceedings of the National Academy of Sciences of the United States of America, 2007. **104**(47): p. 18392-18397.
21. Coleman, J.N., et al., *Two-Dimensional Nanosheets Produced by Liquid Exfoliation of Layered Materials.* Science, 2011. **331**(6017): p. 568-571.
22. Novoselov, K.S., et al., *Electric field effect in atomically thin carbon films.* Science, 2004. **306**(5696): p. 666-669.
23. Frindt, R.F., *Single crystals of $MoS_2$ several molecular layers thick.* Journal of Applied Physics, 1966. **37**(4): p. 1928.
24. Benameur, M., et al., *Visibility of dichalcogenide nanolayers.* Nanotechnology, 2011. **22**(12): p. 125706.
25. Wilson, J.A. and A.D. Yoffe, *Transition metal dichalcogenides discussion and interpretation of observed optical, electrical and structural properties.* Advances in Physics, 1969. **18**(73): p. 193.
26. Yoffe, A.D., *Low-dimensional systems: quantum size effects and electronic properties of semiconductor microcrystallites (zero-dimensional systems) and some quasi-two-dimensional systems.* Advances in Physics, 2002. **51**(2): p. 799-890.
27. Meerschaut, A. and C. Deudon, *Crystal structure studies of the 3R-$Nb_{1.09}S_2$ and the 2H-$NbSe_2$ compounds: correlation between nonstoichiometry and*

*stacking type (=polytypism).* Materials Research Bulletin, 2001. **36**(9): p. 1721-1727.

28. Radisavljevic, B., et al., *Single-layer $MoS_2$ transistors.* Nature Nanotechnology, 2011. **6**(3): p. 147-150.
29. Yoon, Y., K. Ganapathi, and S. Salahuddin, *How good can monolayer $MoS_2$ transistors be?* Nano Letters, 2011. **11**(9): p. 3768-3773.
30. Wang, Q.H., et al., *Electronics and optoelectronics of two-dimensional transition metal dichalcogenides.* Nature Nanotechnology, 2012. **7**(11): p. 699-712.
31. Staley, N.E., et al., *Electric field effect on superconductivity in atomically thin flakes of $NbSe_2$.* Physical Review B, 2009. **80**(18).
32. Frindt, R.F., *Superconductivity in Ultrathin $NbSe_2$ layers.* Physical Review Letters, 1972. **28**(5): p. 299-301.
33. Mattheis.Lf, *Band structures of transition-metal-dichalcogenide layer compounds.* Physical Review B, 1973. **8**(8): p. 3719-3740.
34. Wang, H., *Low temperature scanning tunneling microscopy and spectroscopy: A study on charge density waves and vortex dynamics.* 2009.
35. Bulaevskii, L.N., *Superconductivity and electronic properties of layer compounds.* Uspekhi Fizicheskikh Nauk, 1975. **116**(3): p. 449-483.
36. Borisenko, S.V., et al., *Pseudogap and charge density waves in two dimensions.* Physical Review Letters, 2008. **100**(19).
37. Takita, K., et al., *Fermi-surface of 2H-$NbSe_2$ studied by Dehaas-Vanalphen oscillation and positron-annihilation.* . Physica C, 1991. **185**: p. 2717-2718.
38. Lebègue, S. and O. Eriksson, *Electronic structure of two-dimensional crystals from ab initio theory.* Physical Review B, 2009. **79**(11).
39. Calandra, M., I. Mazin, and F. Mauri, *Effect of dimensionality on the charge-density wave in few-layer 2H-$NbSe_2$.* Physical Review B, 2009. **80**(24): p. 241108.
40. Liu, W., et al. *Understanding the contact characteristics in single or multi-layer graphene devices: The impact of defects (carbon vacancies) and the asymmetric transportation behavior*. in *Electron Devices Meeting (IEDM), 2010 IEEE International*. 2010. IEEE.
41. Onnes, H.K. *Further experiments with liquid helium. C. On the change of electric resistance of pure metals at very low temperatures etc. IV. The*

*resistance of pure mercury at helium temperatures.* in *KNAW, Proceedings*. 1911.

42. Onnes, H.K., *Communications from the Physical Laboratory of the University of Leiden Supplement.* 1913. **34 b**: p. 64–71.
43. London, F. and H. London, *The Electromagnetic Equations of the Supraconductor*. Proceedings of the Royal Society of London. Series A, Mathematical and Physical Sciences, 1935. **149**(866): p. 71-88.
44. Bardeen, J., L.N. Cooper, and J.R. Schrieffer, *Theory of superconductivity.* Physical Review, 1957. **108**(5): p. 1175.
45. Josephson, B.D., *Possible new effects in superconductive tunnelling.* Physics Letters, 1962. **1**: p. 251-253.
46. Bednorz, J.G. and K.A. Müller, *Possible high$T_c$ superconductivity in the Ba−La−Cu−O system.* Zeitschrift für Physik B Condensed Matter, 1986. **64**(2): p. 189-193.
47. Mousa, A. and N. Grimes, *A note on the preparation of the high transition temperature superconductor lithium titanate.* Journal of Materials Science, 1980. **15**(3): p. 793-795.
48. Sleight, A.W., J.L. Gillson, and P.E. Bierstedt, *High-temperature superconductivity in $BaPb_{1-x}Bi_xO_3$ system.* Solid State Communications, 1975. **17**(1): p. 27-28.
49. Michel, C., L. Errakho, and B. Raveau, *The oxygen defect perovskite $BaLa_4Cu_5O_{13.4}$, a metallic conductor.* Materials Research Bulletin, 1985. **20**(6): p. 667-671.
50. Wu, M.K., et al., *Superconductivity at 93 K in a new mixed-phase Y-Ba-Cu-O compound system at ambient pressure.* Physical Review Letters, 1987. **58**(9): p. 908-910.
51. Maeda, H., et al., *A new high-$T_c$ oxide superconductor without a rare-earth element.* Japanese Journal of Applied Physics Part 2-Letters, 1988. **27**(2): p. L209-L210.
52. Sheng, Z.Z. and A.M. Hermann, *Bulk superconductivity at 120 K in the Tl-Ca/Ba-Cu-O system.* Nature, 1988. **332**(6160): p. 138-139.
53. Hazen, R.M., *Crystal structures of high-temperature superconductors.* Physical Properties of High-Temperature Superconductors II, DM Ginsberg,(ed.), New Jersey, World Scientific, 1990: p. 121-198.

54. Schilling, A., et al., *Superconductivity above 130 K in the Hg-Ba-Ca-Cu-O system.* Nature, 1993. **363**(6424): p. 56-58.
55. Fossheim, K. and A. Sudbø, *Superconductivity: Physics and Applications, Wiley, The Norwegian University of Science and Technology, Trondheim, Norway*. 2004.
56. Hebard, A.F., *Superconductivity in doped Fullerenes.* Physics Today, 1992. **45**(11): p. 26-32.
57. Hebard, A.F., *$C_{60}$: Buckminsterfullerene.* Annual Review of Materials Science, 1993. **23**: p. 159-191.
58. Nagamatsu, J., et al., *Superconductivity at 39 K in magnesium diboride.* Nature, 2001. **410**(6824): p. 63-64.
59. Takahashi, H., et al., *Superconductivity at 43 K in an iron-based layered compound LaO1-xFxFeAs.* Nature, 2008. **453**(7193): p. 376-378.
60. Meissner, W. and R. Ochsenfeld, *Ein neuer Effekt bei Eintritt der Supraleitfähigkeit.* Naturwissenschaften, 1933. **21**(44): p. 787-788.
61. Sheahen, T., *Introduction to high-temperature superconductivity*. 1994: Springer.
62. Mourachkine, A., *Room-temperature superconductivity*. 2004: Cambridge International Science Publishing.
63. Tinkham, M., *Introduction to superconductivity*. Vol. 1. 2004: Dover Publications.
64. F. London and H. London *The Electromagnetic Equations of the Superconductor*. Proc. Roy. Soc. (London), 1935. **A149**: p. 71.
65. London, F., *Superfluids: Macroscopic theory of superconductivity. v. 2 Macrosopic theory of superfluid helium*. Vol. 1. 1961: Dover Publications.
66. Landau, V.L.G.a.L.D., *Phenomenological theory of superconductivity.* Zh. Eksperim. i. Teor. Fiz., 1950. **20**: p. 1064.
67. Cooper, L.N., *Bound electron pairs in a degenerate Fermi gas.* Physical Review, 1956. **104**(4): p. 1189-1190.
68. Bardeen, J., L.N. Cooper, and J.R. Schrieffer, *Microscopic theory of superconductivity.* Physical Review, 1957. **106**(1): p. 162-164.
69. Fermi, E., *Eine statistische Methode zur Bestimmung einiger Eigenschaften des Atoms und ihre Anwendung auf die Theorie des periodischen Systems der Elemente.* Zeitschrift für Physik, 1928. **48**(1-2): p. 73-79.

70. Müller, A., *Designer 3D Magnetic Mesostructures.* PhD thesis, Physics Department, Bath University, 2012.
71. Abrikosov, A., *Nobel lecture: Type-II superconductors and the vortex lattice.* Reviews of modern physics, 2004. **76**(3): p. 975-979.
72. Berezins.Vl, *Destruction of long-range order in one-dimensional and two-dimensional systems possessing a continuous symmetry group. II. Quantum systems* Soviet Physics Jetp-Ussr, 1972. **34**(3): p. 610-616.
73. Kosterlitz, J.M. and D.J. Thouless, *Ordering, metastability and phase transitions in two-dimensional systems.* Journal of Physics C-Solid State Physics, 1973. **6**(7): p. 1181-1203.
74. Bloch, I., J. Dalibard, and W. Zwerger, *Many-body physics with ultracold gases.* Reviews of modern physics, 2008. **80**(3): p. 885.
75. Esaki, L., *Long journey into tunneling.* Reviews of modern physics, 1974. **46**(2): p. 237-244.
76. Clarke, J., *The Josephson Effect and e/h.* Amer J Phys, 1970. **38**(9): p. 1071-1095.
77. Andreev, A.F., *The thermal conductivity of the intermediate state in superconductors.* Soviet Physics Jetp-Ussr, 1964. **19**(5): p. 1228-1231.
78. Pannetier, B. and H. Courtois, *Andreev reflection and proximity effect.* Journal of Low Temperature Physics, 2000. **118**(5-6): p. 599-615.
79. Beenakker, C.W.J., *Colloquium: Andreev reflection and Klein tunneling in graphene.* Reviews of modern physics, 2008. **80**(4): p. 1337-1354.
80. Heersche, H.B., et al., *Bipolar supercurrent in graphene.* Nature, 2007. **446**(7131): p. 56-59.
81. Oran Johansson, G., *Multiple Andreev reflection-a microscopic theory of ac Josephson effect in mesoscopic junctions.* 1998.
82. Borzenets, I.V., et al., *Pb-Graphene-Pb Josephson Junctions: Characterization in Magnetic Field.* Ieee Transactions on Applied Superconductivity, 2012. **22**(5).
83. Sato, T., et al., *Gate-controlled superconducting proximity effect in ultrathin graphite films.* Physica E-Low-Dimensional Systems & Nanostructures, 2008. **40**(5): p. 1495-1497.
84. Heersche, H.B., et al., *Induced superconductivity in graphene.* Solid State Communications, 2007. **143**: p. 72-76.

85. Ojeda-Aristizabal, C., et al., *Tuning the proximity effect in a superconductor-graphene-superconductor junction.* Physical Review B, 2009. **79**(16).
86. Shailos, A., et al., *Proximity effect and multiple Andreev reflections in few-layer graphene.* EPL (Europhysics Letters), 2007. **79**(5): p. 57008.
87. Jeong, D., et al., *Observation of supercurrent in PbIn-graphene-PbIn Josephson junction.* Physical Review B, 2011. **83**(9).
88. Kessler, B.M., et al., *Tunable Superconducting Phase Transition in Metal-Decorated Graphene Sheets.* Physical Review Letters, 2010. **104**(4).
89. Aslamazo.Lg and A.I. Larkin, *Influence of fluctuation pairing of electrons on conductivity of normal metal.* Physics Letters A, 1968. **A 26**(6): p. 238-239.
90. Minnhagen, P., *The two-dimensional Coulomb gas, vortex unbinding, and superfluid-superconducting films.* Reviews of modern physics, 1987. **59**(4): p. 1001-1066.
91. Allain, A., Z. Han, and V. Bouchiat, *Electrical control of the superconducting-to-insulating transition in graphene–metal hybrids.* Nature materials, 2012. **11**(7): p. 590-594.
92. Girit, C., et al., *Tunable graphene dc superconducting quantum interference device.* Nano Letters, 2008. **9**(1): p. 198-199.
93. Zhang, Y., et al., *Ambipolar $MoS_2$ Thin Flake Transistors.* Nano letters, 2012. **12**(3): p. 1136-1140.
94. Ayari, A., et al., *Realization and electrical characterization of ultrathin crystals of layered transition-metal dichalcogenides.* Journal of applied physics, 2007. **101**(1): p. 014507-014507-5.
95. Feigel'man, M.V., M.A. Skvortsov, and K.S. Tikhonov, *Proximity-Induced Superconductivity in Graphene.* Jetp Letters, 2008. **88**(11): p. 747-751.
96. Blake, P., et al., *Making graphene visible.* Applied Physics Letters, 2007. **91**(6).
97. Castellanos-Gomez, A., N. Agrait, and G. Rubio-Bollinger, *Optical identification of atomically thin dichalcogenide crystals.* Applied Physics Letters, 2010. **96**(21).
98. Levinson, H.J., *Principles of lithography*. Vol. 146. 2005: Society of photo optical.
99. Ishigami, M., et al., *Atomic structure of graphene on $SiO_2$.* Nano Letters, 2007. **7**(6): p. 1643-1648.

100. Zheng, C., *Micro-nanofabrication technologies and applications*, 2005, Beijing: Higher Education Press.
101. Venables, J.A., *Introduction to surface and thin film processes*. 2000: Cambridge University Press.
102. Venugopal, A., et al. *Contact Resistance Studies of Metal on HOPG and Graphene Stacks.* in *AIP Conference Proceedings.* 2009.
103. Nagashio, K., et al. *Metal/graphene contact as a performance Killer of ultra-high mobility graphene analysis of intrinsic mobility and contact resistance.* in *Electron Devices Meeting (IEDM), 2009 IEEE International*. 2009. IEEE.
104. Russo, S., et al., *Contact resistance in graphene-based devices.* Physica E: Low-dimensional Systems and Nanostructures, 2010. **42**(4): p. 677-679.
105. Nagashio, K., et al., *Contact resistivity and current flow path at metal/graphene contact.* Applied Physics Letters, 2010. **97**(14).
106. Nagareddy, V., et al., *High temperature measurements of metal contacts on epitaxial graphene.* Applied Physics Letters, 2011. **99**: p. 073506.
107. Klusek, Z., et al., *Graphene on gold: Electron density of states studies by scanning tunneling spectroscopy.* Applied Physics Letters, 2009. **95**(11).
108. Valencia, H., A. Gil, and G. Frapper, *Trends in the Adsorption of 3d Transition Metal Atoms onto Graphene and Nanotube Surfaces: A DFT Study and Molecular Orbital Analysis.* Journal of Physical Chemistry C, 2010. **114**(33): p. 14141-14153.
109. Custance, O., R. Perez, and S. Morita, *Atomic force microscopy as a tool for atom manipulation.* Nature Nanotechnology, 2009. **4**(12): p. 803-810.
110. Giessibl, F.J., *Advances in atomic force microscopy.* Reviews of Modern Physics, 2003. **75**(3): p. 949-983.
111. Wo, S.T., et al., *Structure of a pentacene monolayer deposited on $SiO_2$: Role of trapped interfacial water.* Journal of Applied Physics, 2006. **100**(9).
112. Schrader, B., *Infrared and Raman spectroscopy*. 2008: Wiley-VCH.
113. Edwards, H.G.M., D.W. Farwell, and S.E.J. Villar, *Raman microspectroscopic studies of amber resins with insect inclusions.* Spectrochimica Acta Part A: Molecular and Biomolecular Spectroscopy, 2007. **68**(4): p. 1089-1095.
114. Ferrari, A., et al., *Raman spectrum of graphene and graphene layers.* Physical Review Letters, 2006. **97**(18): p. 187401.

115. John, R., et al., *Single-and few-layer graphene growth on stainless steel substrates by direct thermal chemical vapor deposition.* Nanotechnology, 2011. **22**(16): p. 165701.
116. Lock, J., A. Pippard, and D. Shoenberg. *Superconductivity of tin isotopes.* in *Mathematical Proceedings of the Cambridge Philosophical Society.* 1951. Cambridge Univ Press.
117. Hall, E.H., *On a new action of the magnet on electric currents.* American Journal of Mathematics, 1879. **2**(3): p. 287-292.
118. Engbarth, M., *Hall Magnetometry of Electrodeposited Superconducting Pb Mesostructures,* 2010, University of Bath.
119. Bending, S.J., *Local magnetic probes of superconductors.* Advances in Physics, 1999. **48**(4): p. 449-535.
120. Dingle, R., et al., *Electron mobilities in modulation-doped semiconductor heterojunction super-lattices.* Applied Physics Letters, 1978. **33**(7): p. 665-667.
121. Malard, L., et al., *Raman spectroscopy in graphene.* Physics Reports, 2009. **473**(5): p. 51-87.
122. Tan, Y.W., et al., *Temperature dependent electron transport in graphene.* The European Physical Journal-Special Topics, 2007. **148**(1): p. 15-18.
123. Nouchi, R. and K. Tanigaki, *Charge-density depinning at metal contacts of graphene field-effect transistors.* Applied Physics Letters, 2010. **96**(25): p. 253503-253503-3.
124. Novoselov, K.S., et al., *Two-dimensional gas of massless Dirac fermions in graphene.* Nature, 2005. **438**(7065): p. 197-200.
125. Tikhonenko, F.V., et al., *Transition between Electron Localization and Antilocalization in Graphene.* Physical Review Letters, 2009. **103**(22).
126. Morozov, S., et al., *Strong suppression of weak localization in graphene.* Physical Review Letters, 2006. **97**(1): p. 16801.
127. Chen, Y.-F., et al., *Magnetoresistance in single-layer graphene: weak localization and universal conductance fluctuation studies.* Journal of Physics: Condensed Matter, 2010. **22**(20): p. 205301.
128. Tikhonenko, F., et al., *Weak localization in graphene flakes.* Physical Review Letters, 2008. **100**(5): p. 56802.

129. Wu, X., et al., *Weak antilocalization in epitaxial graphene: evidence for chiral electrons.* Physical Review Letters, 2007. **98**(13): p. 136801.
130. McCann, E., et al., *Weak-localization magnetoresistance and valley symmetry in graphene.* Physical Review Letters, 2006. **97**(14): p. 146805.
131. Berger, C., et al., *Electronic confinement and coherence in patterned epitaxial graphene.* Science, 2006. **312**(5777): p. 1191-1196.
132. Horsell, D., et al., *Mesoscopic conductance fluctuations in graphene.* Solid State Communications, 2009. **149**(27): p. 1041-1045.
133. Skocpol, W., et al., *Universal conductance fluctuations in silicon inversion-layer nanostructures.* Physical Review Letters, 1986. **56**(26): p. 2865-2868.
134. Staley, N.E., C.P. Puls, and Y. Liu, *Suppression of conductance fluctuation in weakly disordered mesoscopic graphene samples near the charge neutral point.* Physical Review B, 2008. **77**(15): p. 155429.
135. Gorbachev, R., et al., *Weak localization in bilayer graphene.* Physical Review Letters, 2007. **98**(17): p. 176805.
136. Prozorov, R., et al., *Anomalous Meissner effect in pnictide superconductors.* Physical Review B, 2010. **82**(18): p. 180513.
137. Curran, P.J., et al., *Geometry-dependent penetration fields in superconducting $Bi_2Sr_2CaCu_2O_{8+\delta}$ platelets.* Physical Review B, 2010. **82**(13): p. 134501.
138. Wang, Y., et al., *Vortex penetration into micron-sized $Bi_2Sr_2CaCu_2O_{8+\delta}$.* Physical Review B, 2002. **65**(18): p. 184506.
139. Zeldov, E., et al., *Geometrical barriers in high-temperature superconductors.* Physical Review Letters, 1994. **73**(10): p. 1428-1431.
140. Benkraouda, M. and J.R. Clem, *Magnetic hysteresis from the geometrical barrier in type-II superconducting strips.* Physical Review B, 1996. **53**(9): p. 5716.
141. Bean, C. and J. Livingston, *Surface barrier in type-II superconductors.* Physical Review Letters, 1964. **12**(1): p. 14-16.
142. Burlachkov, L., *Magnetic relaxation over the Bean-Livingston surface barrier.* Physical Review B, 1993. **47**(13): p. 8056.
143. Paltiel, Y., et al., *Surface barrier dominated transport in $NbSe_2$.* Physical Review B, 1998. **58**(22): p. R14763-R14766.

144. Burlachkov, L., A. Koshelev, and V. Vinokur, *Transport properties of high-temperature superconductors: Surface vs bulk effect.* Physical Review B, 1996. **54**(9): p. 6750.

145. Corcoran, R., et al., *Quantum oscillations in the mixed state of the type II superconductor 2H-$NbSe_2$.* Journal of Physics: Condensed Matter, 1994. **6**(24): p. 4479.

146. Stiles, J., D.L. Williams, and M. Zuckermann, *Dependence of the critical temperature for the formation of charge density waves in 2H-$NbSe_2$ upon impurity concentration.* Journal of Physics C: Solid State Physics, 1976. **9**(18): p. L489.

147. Berthier, C., P. Molinié, and D. Jérome, *Evidence for a connection between charge density waves and the pressure enhancement of superconductivity in 2H-$NbSe_2$* Solid State Communications, 1976. **18**(9): p. 1393-1395.

148. Iwaya, K., et al., *Electronic state of $NbSe_2$ investigated by STM/STS.* Physica B: Condensed Matter, 2003. **329**: p. 1598-1599.

149. Naito, M. and S. Tanaka, *Electrical transport properties in 2H-$bS_2$, $NbSe_2$, $TaS_2$ and $TaSe_2$.* J. Phys. Soc. Jpn, 1982. **51**(1): p. 219-227.

150. Volkenshtein, N., V. Dyakina, and V. Startsev, *Scattering mechanisms of conduction electrons in transition metals at low temperatures.* physica status solidi (b), 1973. **57**(1): p. 9-42.

151. Zhu, X., et al., *Upper critical field, Hall effect and magnetoresistance in the iron-based layered superconductor $LaFeAsO_{0.9}F_{0.1-\delta}$.* Superconductor Science and Technology, 2008. **21**(10): p. 105001.

152. Werthamer, N., E. Helfand, and P. Hohenberg, *Temperature and Purity Dependence of the Superconducting Critical Field, $H_{c2}$. III. Electron Spin and Spin-Orbit Effects.* Physical Review, 1966. **147**(1): p. 295.

153. Zehetmayer, M. and H. Weber, *Experimental evidence for a two-band superconducting state of $NbSe_2$ single crystals.* Physical Review B, 2010. **82**(1): p. 014524.

154. Xiao, Z., et al., *Observation of the Vortex Lattice Spinodal in $NbSe_2$.* Physical Review Letters, 2004. **92**(22): p. 227004.

155. Dean, C.R., et al., *Boron nitride substrates for high-quality graphene electronics.* Nature Nanotechnology, 2010. **5**(10): p. 722-726.